PAWEŁ KABACIK

RELIABLE EVALUATION AND PROPERTY DETERMINATION OF MODERN-DAY ADVANCED ANTENNAS

OFICYNA WYDAWNICZA POLITECHNIKI WROCŁAWSKIEJ
WROCŁAW 2004

Reviewers

Dr. Nicholas E. Buris – Motorola Labs, Schaumburg
Dr. John Huang – NASA/Jet Propulsion Laboratory
Prof. Lot Shafai – University of Manitoba

OFICYNA WYDAWNICZA POLITECHNIKI WROCŁAWSKIEJ
Wybrzeże Wyspiańskiego 27, 50-370 Wrocław

ISBN 83-7085-765-5

Drukarnia Oficyny Wydawniczej Politechniki Wrocławskiej. Zam. nr 369/2004.

CONTENTS

PREFACE

Driven by the demands of communication and informatics systems, the use of technologies featuring high scale of integration has become frequent in microwave and antenna techniques. The scale of integration achieved in electromagnetic devices is getting higher every year. High integration makes these devices applicable to many more uses, due to the enhanced performance and improved cost effectiveness. It is therefore no surprise that the development of reliable methods for the evaluation and determination of the overall properties of modern antenna arrays has recently taken on a sense of urgency. It goes without saying that the properties of antennas need to be determined with great care. But the evaluation of these properties must involve indirect techniques, as in many instances this is the only reasonable approach to the examination of highly integrated structures. A consequence of increasing the scale of integration is the tendency to raise the number of antenna elements and components. That is why preference must be given to experimental test methods enabling a quick detection of the components which are out of the permissible technical limits. Also, the ever increasing scale of integration accounts for the disappearance of clearly defined unit packaging. Although, in consequence, antenna investigations relying on the interim results obtained gradually at the subcomponent level seem to be of decaying use, the tracing of the antenna properties in the course of design or manufacture must still come under continuous scrutiny.

Periodicals and scientific conferences reflect the efforts towards establishing new integration and miniaturization technologies, as well as developing reliable antenna evaluation techniques. There is plenty of room for creativity and new techniques with the advent of miniaturized or highly integrated electrical and electromagnetic devices. Thus, the research on miniaturization and new lightweight materials is regarded as one of the most revolutionary breakthroughs in engineering nowadays. However, in order to overcome the problems that arise with the growing gridlock of complex interrelations, new or revised methods need to be implemented in measurement techniques and evaluation approaches have become indispensable.

New technological developments in modern communications and radar involve ten, or so, major subjects regarded as critical. Thus, without major yardsticks and advancements in these fields, any plans that aim at launching new generations of radio systems will fail. Antennas are ranked as a top priority. A far going revision of antenna functioning is frequently postulated by researchers working on new concepts of radio communication systems. The antenna is not only considered as the impedance

interface between the radio front-end unit and free space. The sophisticated systems under study commonly rely on a fine spatial access to radio channels and on an efficient spatial signal filtering. Despite the progress achieved to date, additional improvements in antenna technologies are needed. Emerging examples are smart antennas and arrays used in modern satellites, such as *Envisat* (a 10 meters long SAR radar antenna comprises more than a dozen thousands of miniature Tx/Rx modules and its total cost was € 80 million). The interest in modern antenna technologies has been strengthened by the belief that advantages of new antenna concepts are able to overweigh the benefits provided by improved modulation and coding methods.

For decades, antenna measurements have been regarded as being of vital importance both in research and manufacturing. Nowadays, these measurements have become more complex due to the presence of such features as multiband operation and broad frequency ranges, scanned or multiple beams, reconfigurability and adaptability. To make things more complex, the input signals in some of the emerging antenna concepts take the form of a binary stream or phase characteristics are of high importance. Problems with the reliability of measured data, the huge amount of data produced in the course of tests, as well as the processing of these data, are still amongst the major factors that impose constraints on the research capabilities, regardless of how talented and hardworking the human workforce would be.

In this monograph, we attempt to describe two evaluation methods developed on our own for the needs of the research on highly integrated lightweight antenna arrays. In contrast to conventional measuring methods which provide overall data, it is expected that the evaluation methods will enable instant pointing of non-conforming elements and modules. The capabilities of both methods have been upgraded as compared to those described in the literature. As in both methods use is made of indirect measured data, comprehensive data processing or simulations must be performed in order to achieve interpretable results. With one of the methods it is possible to carry out simulations of highly integrated arrays made of lightweight composites or other stratified dielectrics. The electrical properties of the materials are measured over a broad temperature and frequency range, and thereafter they are included into the simulations of the impedance characteristics for the components incorporated into microwave stratified antennas. This method does not neglect the factors which are blamed for the considerable discrepancies between the design and actual values of the electrical parameters. The other method explores the field distribution sampled in the near field zone of the antenna. Owing to the two-dimensional signal processing applied, the method provides highly accurate radiation patterns in the three-dimensional format. Such format is of great desire when analyzing antennas which make use of advanced beamforming or provide off-broadside beams. A major advantage of this method is the unique capability of revealing the field distribution in the antenna aperture. It must be emphasized that the coupling of the measuring equipment to the antenna under test is small.

These two methods are among the hot subjects in leading scientific centers. The author wishes to acknowledge the many companies and institutions which contacted him, discussed the results obtained with these methods, or requested more details. From Poland, the author would like to mention the scientists affiliated with Przemysłowy Instytut Telekomunikacji and Wojskowa Akademia Techniczna, who have shown much interest in the application of the two methods. The author also wants to acknowledge the contacts with the experts from the European Space Agency and several other internationally recognized institutions. It was a nice surprise to learn that our problems and our experience are consistent with theirs. The results presented in this monograph have been published in more than twenty papers, of which four journal papers have been published in the *IEEE Transactions on Antennas and Propagation* and *IEEE Antennas and Propagation Magazine*. Part of the research presented in this monograph was recognized by the Institute of Electrical and Electronics Engineers, Inc. (IEEE) when they praised it with the prestigious *2000 Harold A. Wheeler Applications Prize Paper Award Honorable Mention* (the *H.A. Wheeler Award* recognizes a paper considered to be the best applications paper in the *IEEE Transactions on Antennas and Propagation* for the past year).

* * *

The author would like to express his gratitude to the National Research Council (KBN), Warsaw, Poland for funding a major part of this research. Four generously funded Projects made it possible to accomplish the research and to present the results. Sincere thanks are due to Prof. Robert Hossa and Prof. Krzysztof Sachse, Wrocław University of Technology, for invaluable discussions and cooperation which markedly has influenced author's research. Many thanks go to Prof. Marek Białkowski, the University of Queensland, Australia for encouragement and inspiring discussions. I acknowledge the suggestions, corrections, and constructive criticisms of the reviewers: Dr. John Hunag of NASA/JPL, Dr. Nick Buris of Motorola Labs, Chicago and Prof. Lot Shafai of University of Manitoba, Winnipeg. Finally, I must recognize my family for the support and I shall commend their patience.

CHAPTER 1

DIAGNOSTICS OF ADVANCED ANTENNA ARRAYS

1.1. Introduction

In its essence, communication must overcome the constraints inherent to fixed line services and make the access to information and data exchange freely available to the users, regardless of where they are, and whether they are in motion or immobilized. The idea of seamless communication is getting more and more accountable basis. It is also important to develop a great awareness among engineering community that the long lasting split into the fixed and wireless systems, as well as differentiation between terrestrial and satellite networks, should cease possibly soon so as not to impede any visionary concepts in the future. Needless to say that these highly desired goals can be achieved with wireless and mobile communication technologies irrespective of how well developed the fixed line infrastructure is. Furthermore, there is an unquestionable rush to combine fiber links with the flexible wireless 'last miles' or 'last sections' of the communication link. Such systems are sometimes named 'radio over fiber' or 'info ports'. In order to provide the required capacity of the radio systems – and this includes the capability of hot spots handling – major attention must be focused on the following items: fine spatial access to radio channels, sophisticated spatial filtering and bandwidth considerations. These issues have become fundamental also in radar and remote sensing, as they make it possible to determine the specific characteristics of the targets, to investigate the surface properties, to provide three-dimensional weather data or to combat deliberate electronic countermeasures.

Communication and information technology has always had paramount importance in societies with a high position in world's economy or science. In the 1990s, communication and information technologies have developed there at a rate which was twice as fast as that of the average economic growth. However, to achieve the planned range of applications for the information technology in the comparatively near future, we must develop – as soon as possible – many of the techniques that now are beyond our reach. By definition, antennas are transitional structures between the radio space and signal guiding devices, so they are of vital importance when attempts

are made to achieve the desired performance of modern communication and radar systems. The interest in modern antenna technologies has been substantiated by the belief that the gains from new antenna concepts are likely to be most profitable, since well-organized spatial access to the radio channels competes successfully with many modern modulation and coding methods even then, they are applied together. Only techniques utilizing deliberate space-time coding with multipathly propagating signals (*e.g.* MIMO, MIMO-OFDM, V-BLAST) might need less focused radio wave transmission and reception. It is commonly agreed that the antenna technology must be ranked among the highest contemporary electrical engineering priorities. As a result, antenna research is essentially on a critical development path, so if it 'lags behind', antenna underdevelopment will expose the launch of new communication systems to jeopardy.

Modern antennas are expected to co-establish high-quality radio channels. So far, the available antenna technologies have not been able to cope with these ambitious goals. To make things even worse, there is a general lack of reliable engineering methods. Advanced antennas often take the form of arrays, or incorporate subarrays in their reflector illuminating systems. A prerequisite of their development is the use of advanced microwave circuits and materials, as well as the adoption of miniaturization. Fine adjustment of pre-defined or adaptive amplitude and phase values for array elements enables more sophisticated beam scanning and radiation pattern shaping but often calls for elaborated signal processing. Complex antennas may have more than one beam and possess reconfigurability or real-time adaptability. Input or output signals can take different forms, such as that of the binary streams in their baseband.

In order to cope with those challenging objectives, researchers must have not only a strong theoretical background and experience, but also elaborated simulation tools, as well as measuring and diagnostic systems at their disposal. In contemporary technology and science, the traditional split into two branches – theoretical and experimental work – must be regarded as inadequate since simulations has paramount importance. Nowadays R&D in electromagnetic combines three complementary activities: theory, simulation and experiment.

It is the complexity of new antenna techniques and new signal processing methods that makes conventional technical terms and measuring standards incapable of thoroughly assisting the researcher or designer. It follows that experimental methodology must be upgraded, new definitions formulated, and new measuring systems elaborated. The results obtained with these methods are expected to provide not only data on the performance of the Device Under Test (DUT), but also to allow a sufficiently deep insight into what is going on inside sophisticated technical systems. A lot of additional attention must be directed to the calibration and final tuning of the studied device.

1.2. Importance of measuring technologies in antenna engineering

The evaluation methods which gained interest in our studies are primarily to enable the development of

- modern lightweight phased arrays and active phased arrays,
- arrays referred to as smart antennas,
- multiband antennas, including small elements,
- highly integrated arrays.

The most inspiring trend is that a transmitting antenna should focus the propagation of the radiated energy, as much as possible, towards active receivers, whereas in the receiving mode, the antenna should synthesize permanent or instantaneous minima which ensure spatial filtering. Large-scale integration normally leaves no space for extensive housing, if at all (with maintaining low undesired couplings or providing indispensable shieldings). Therefore the circuits must be designed for non-connectorized operation. The increasing attention towards sophisticated radiation pattern shapes and irreversible integration must be supported by deeper insight into the actual electromagnetic phenomena occurring inside the antenna.

A successful development of such antennas is hard to imagine without accurate measuring techniques and diagnostic tools. Critical for the accomplishment of such emerging antennas are fast and sufficiently precise evaluation techniques focusing on the determination of (i) a comprehensive set of electrical properties at different levels of the integrated antennas, and (ii) the characteristics of microwave materials related to the major parameters (frequency, temperature, *etc.*). It is expected that with these techniques it will be possible to investigate the distribution of the excitation coefficients in both transmitting and receiving antennas, to observe the edge and scattering effects or any other spurious radiation induced by the feeding circuits, and – last but not least – to sort out the most probable sources of the discrepancies between design and model. Since the electromagnetic interactions between the investigated antenna and the test equipment affect the quality of the measurement, the testing method should be virtually a non-invasive one or the measuring probe and its manipulator must feature a negligible coupling to the DUT. The high quality *quiet zone* in the anechoic chamber and the sufficiently spacing between probes and the Antenna Under Test (AUT) is essential to the endeavors listed. If necessary, the results should give a basis for evaluating the design correction coefficients prior to the final assembly. Another important research task is the troublesome calibration of the antenna, and the decoupling of antenna elements (including signal processing methods that are preferred when use is made of digital beamforming).

1.3. Interdisciplinarity of modern diagnostics

One of the most challenging objective in contemporary engineering is to design possibly simple devices and manufacture them at a possibly low cost. Although it may sound strange at least at first glance, these objectives pave the way for many sophisticated methodologies into research laboratories. Owing to the continuing interest in the increase of the integration scale and improvement of miniaturization, measurements must be extended from electrical issues onto material characteristics. Present array designs tend to unify radio and structural functions into common parts. The importance of material technology increases when low losses become a key issue in the process of design. In these circumstances, the measurements of modern antennas have wrapped up many issues dealt with in the physics of dielectrics, as well as chemical and semiconductor engineering, and so the interdisciplinarity of modern antenna diagnostics has become a fact.

In contemporary antenna measuring and evaluation techniques, the following tasks have come to the forefront:

- determination of actual current distributions in the apertures of reflector and array antennas, which makes possible remote detection of manufacturing inaccuracies in the radiating or beamforming part of the antenna,
- detection of failure or unstable operation of antenna components, particularly in large and highly integrated arrays,
- development of failure compensation methods which enable array operation with broken components (less unscheduled servicing),
- compensation of parameter spread and drifts, which backs up the functioning of beamforming systems, both in the on- and off-line mode,
- prediction of effects related to temperature and humidity variations,
- inspection of reflector shape during manufacture and operation,
- measurement of systems for spatial signal formation with focus on reflectarrays and spatial power combining,
- investigations of antennas fed with binary streams,
- studies of human-antenna interactions encountered in handset and portable terminals.

1.4. Need for diagnosis of highly integrated arrays

The emerging high-scale integrated arrays set new standards, as their structure can not undergo full tests when the system is split into pieces. Until the entire array is fully packaged and integrated, it is difficult to say whether or not it will function according to the designer’s intention. The situation is similar to that in satellite communication.

Unless the satellite is placed in the orbit, no one can be sure if the communication subsystems will work in accordance with the technical specifications. Measuring the performance of the components prior to integration is of limited use – their design may take into account existence of particular interactions (*e.g.* couplings, or thermal effects). Large-scale integration normally does not leave space for extensive housing, and the circuits are designed for non-connectorized operation. Thus, the measured results for isolated or disconnected subcomponents might deceive the investigator; they may also become infeasible or, at least, seriously bounded. That is why the actual properties can be evaluated only after the assembling process has been entirely completed. In order to accomplish the integrated antenna array it is unavoidable to determine, by experiments and simulations, not only the properties of the AUT/DUT but also the sources of the discrepancies between measured and design values. The difficulty of diagnostics is further increased by the frequent use of advanced or tricky beam forming algorithms in highly integrated antennas.

1.5. Major advantages of near-field antenna measurements

While radio engineering was evolving, new designs of antennas and radar were developed, but not every radiation pattern test could be supported by outdoor far-field antenna ranges. The desire to house the antenna test facilities inside affordable chambers has directed the attention of the antenna research community to the investigations of the antenna properties with data recorded close to the radiation source. It must be said that the interest in near-field methods was also driven by the need of measuring the radiation pattern and gain of the antennas which were too bulky to be tested in outdoor far-field systems. The antenna size and its sidelobe level impose other unfavorable constraints on the required distance between the transmit and receive site. Last but not least, more and more communication and radar antennas should be measured indoor for environmental and security reasons. Furthermore, nowadays the extensive use of the radio spectrum has jeopardized much of the outdoor antenna measurement capabilities (there are not many remotely located test ranges). This is so because antennas are not designed for odd frequency ranges, but only for those which have already found applications. In developed countries, the radio spectrum below 5 GHz is heavily utilized. Thus, it is hard to think of outdoor antenna measurements when many strong, interfering signals propagate through the test site. Another constraint is the presence of test signals reflected from the ground in the far-field ranges. An example of a wise suppression of the reflected signals is the France Telecom facility in La Turbie, a mountainous area in *Cote de Azur* Region of France. The transmitting and receiving sides of the far-field system are deployed on two mountains separated by a deep valley.

The near-field measuring technique provides highly accurate results. These are of top importance to the aperture antennas, which are to meet the tough requirements of the communication and radar link budgets. It should be mentioned that even the lack of as little as 1 dB in the directivity of the antenna may really count for much. It is also the angular position of the nulls that should be precisely determined (*i.e.* no more than 0.1°). The AUT usually operates in the transmitting mode, while the probe receives the test signal. But the method applies both to transmitting and receiving antennas. In some complex arrays, use is made of non-reciprocity devices, like frequency conversion units, amplifiers and A/D converters. In such instances, the direction of the test signal propagation must be reversed in the near-field systems and due to reciprocity such change is without effect to the measurement results.

When research into the near-field technique geared up in the 1960s, the major objective was to provide accurate radiation pattern and gain measurements under indoor conditions. Anechoic chambers usually have floor dimensions not much greater than a dozen meters. The chamber height is generally between 40% and 60% of the longest floor side. Perhaps only a few anechoic chambers all over the world might be longer than 60 meters. University laboratories usually make use of the anechoic chambers that are 1.5 to 4 m high and have a floor surface area ranging from 8 to 40 m^2. When the development of the near-field technique achieved a mature stage, interests evolved towards the detection of failed elements and later towards the calibration of large phased arrays (Special Issue IEEE TAP 1988). Another application of the near-field method is in the investigations into the optimum arrangement of the antennas mounted on spacecraft or other platforms.

Near-field measurements are an indirect methodology of measuring patterns, and this means that the measured data must be processed in order to obtain useful results. The near-field method provides a three-dimensional view into the radiated fields. The data processing software operates with complex values of the field samples, taken in near proximity of the AUT. Furthermore, the near-field theory allows the derivation of an algorithm for backward projection. Owing to this algorithm, the near-field technique can be used to determine the actual current distributions over the entire or sliced apertures of the AUT (microwave holography) (Rahmat-Samii 1985).

Outdoor use of the near-field test systems is still waiting for acceptable technical solutions which in fact are urgently needed. In such applications, the scanning volume may be large and German researchers reported implementation of the outdoor system capable to scan within 100×100×100 meters space (Fritzel et al. 2002). The near-field technique is generally used to test high gain antennas. The microwave frequency range is preferred, as the probe sizes are reasonable (below 1 m) and the span of the scanning grid can be accommodated inside the anechoic chamber. There are several reasons why near-field antenna systems are only occasionally used in VHF/UHF. In these bands, the radiation patterns do not need to be accurately shaped. In such instances propagation is affected by a variety of factors (*e.g.* earth losses) and it is important to

provide the required field strength within the coverage area. In the VHF/UHF range there is greater need for impedance matching circuits than advanced beamforming. Owing to the influence of the earth, antenna platforms or other objects, the radiation pattern properties depend a lot on the actual location of the antenna (the effect of ground losses is difficult to reproduce in chambers), and so the extremely high cost of the large scanning equipment operating at VHF/UHF would be ineffectively spent.

1.6. Historical milestones

It is difficult to outline the milestones in the diagnostics of highly integrated lightweight arrays, as any major advancement is considered a proprietary information. The method relies on accurate dielectric measurements and numerical simulations of the antennas. Thus, a firm basis for such techniques emerged in the 1980s.

The interest in near-field antenna measurements dates back to the 1940s, but relevant theoretical analysis was lacking in those days (Yaghjian 1986). Around 1950, two scientists of the Air Force Cambridge Research Center – Barrett and Barnes – built an 'automatic antenna wave front plotter' (Barrett, Barnes 1952). They obtained full-size data of phase and amplitude values in front of microwave antennas. It was solely experimental work and there were no attempts to relate the near and far fields. In 1960, Gamara compared the measured far-field radiation patterns with those computed on the basis of the data recorded in the near field. He achieved a good agreement over the main beam and the first sidelobes. Some principal theoretical concepts can be found in the fundamental book by Stratton (plane-waves) (Stratton 1941). The first plane-wave analysis which involved a probe-corrected algorithm was published by Kerns in 1963 (Kerns 1963). Near-field measurements without probe correction can produce acceptable results within the main beam and the first sidelobes only and are much less accurate than the probe-corrected ones. The first application of probe-corrected procedure to near-field measurements on the cylindrical surface was at Georgia Institute of Technology (Leach, Paris 1973).

The development of compact antenna test method must be primarily attributed to Richard C. Johnson of Georgia Institute of Technology. Contrary is with the near-field technique which is not a single researcher invention. The development of near-field measurements is a collective work of researchers scattered in Europe and in the USA, the driving force being space and radar industries. Amongst the major contributors were the Technical University of Denmark, Lyngby (common efforts with the European Space Agency) (DTU web page), Georgia Tech, Atlanta and National Institute of Standards and Technology, Boulder, Colorado (NIST web page). The work performed under Prof. Jesper E. Hansen at the Technical University of Denmark has focused on spherical scanning (Hansen J. 1988), the research carried out at the National Institute

of Standards and Technology has concentrated on planar scanning in Cartesian coordinates (Newell 2002). Everywhere these projects turned out to be spanned over decades. For example, it took the Technical University of Denmark as long as 15 years of generously funded research work under the supervision of four principal researchers, before their laboratory was approved on a commercial basis.

Being aware of the possible incompleteness or inaccuracy of his own data, the author attempted to identify the milestones in the development of the near-field antenna technique (Table 1.1). Among the major sources of historical data acquisition are the AMTA symposiums (AMTA web page) and the antenna measurement workshops organized by the European Space Agency in European Scientific and Technology Center (ESTEC), in Noordwijk, the Netherlands, to name just a few of them. It should be pointed that due to the legal regulations on Technology Transfer, many results obtained with the near-field technique are not detailed published in openly circulating literature.

Table 1.1. Some milestones in the near-field antenna measurement technique.

the 1960s	Work on near-field to far-field transform, Technical University of Denmark, Lyngby and National Institute of Standards and Technology, Boulder, Colorado, USA
1968	Development of the spherical near-field laboratory at the Technical University of Denmark, Lyngby
	Development of the planar Cartesian scanning system, USA
1972	Probe-corrected measurements, Prof. Fleming Holm-Larsen, Denmark Probe compensated cylindrical near-field scanning, W. Marshall Leach, Demetrius Paris, Georgia Institute of Technology, USA
the 1970s	Development of the planar polar scanning system, NASA/JPL, Pasadena, California, USA
	High quality electrical field probes and elaboration of probe calibration techniques, Denmark, European Space Agency
turn of the 1970s	Advancements in computer technology – computer capabilities do not bound implementation of near-field technique any longer
1986	Invention of the bi-polar scanning system, Dr. Yurii Belov and his team, Nizhni Novgorod, Russia
1988	Publication of comprehensive book, *Spherical Near-field Antenna Measurements*, edited by Prof. Jesper E. Hansen
1992	Microwave holography technique becomes widely published
1994	Spherical near-field measurements performed in the time domain, Thorkild Hansen and Arthur Yaghijan
1999	Phaseless measurements adopted to various planar scanning systems Publication on the near-field calibration technique used in the manufacture of large phased arrays
2002	Scanning capabilities of outdoor systems approach 100×100×100 meters space

Presently, researchers concentrate on the following problems dealt with in the near-field technique:

- advancement of robotic scanner system allowing scanning on a very large surfaces,
- increasing the upper frequency of the measuring systems onto millimeter frequencies,
- mobile and outdoor scanning systems,
- broadening of the valid angle to make it suitable for the measurement of phased arrays or multibeam antennas,
- improvement of signal processing for the needs of transform calculations,
- dual-system measurements and convergence of results in the overlapping zone,
- concurrent multifrequency acquisition of data and further improvement of accuracy.

Nowadays, there are about 100 antenna laboratories worldwide using the near-field technique. Only some of them are able to provide microwave holography images. Except for the system operated at the Department of Electrical and Computer Engineering, The University of Queensland, Brisbane, Australia, all laboratories are on the Northern Hemisphere (locations in Europe, US and Canada, Asia and Japan, Russia and Israel). It is worthy to say that up till now no standards for near-field antenna measurements have been established, although such standards are available for far-field measurements (IEEE 1980). Presently, there are preliminary attempts to organize a group of experts which will undertake a great work on editing substantially upgraded antenna measurement standard book. However, no steps beyond general talks were undertaken in the last two years.

1.7. Outline of the presented research

Since the modern-day advanced antennas make use of broad ranges of state-of-the-art technologies, it is hard to summarize methods of their property determination in one monograph. That is why this monograph had to be focused on selected problems and well-defined issues. Furthermore, the monograph was concentrated on results of the author's personal work. Two main focus areas are related to highly integrated lightweight arrays: thermal effects attributed to variations of dielectric constant in microwave laminates and advancements in bi-polar near-field antenna measurements. Both subjects are investigated in order to improve evaluation techniques of advanced integrated arrays. The author presented also his original contribution to property determination of phased arrays with a sophisticated backward projection technique.

In the past five years the author's research has concentrated on the following major problems – antenna arrays and array integration techniques, near-field antenna measurements, temperature-dependence of stratified antennas, digital beamforming techniques, conformal antennas and multi-resonant small antennas. The monograph covers

author's research on accurate evaluation of electrical properties of highly integrated lightweight antenna arrays. In order to establish the relevant background, Chapters 2 and 3 outline the performed studies of highly integrated arrays and low-loss feeding networks, respectively. These efforts made the author sensitive to the problem of how a well-balanced definition of the technical parameters may help to accomplish a reliable and cost-effective antenna design. As the work involved theoretical issues, simulations, as well as experimental and technological aspects, it allowed the author to realize that there was a lack of adequate definitions to catch up with the advancements in antenna technology. These gave inspiration to the furtherance of the search for new and much more relevant antenna parameters and measuring methodologies.

Currently, many advanced electromagnetic CAD tools are being widely marketed. Furthermore, in each major engineering field there are two or more competing commercial software. Also computer platforms needed to run this software are easily available on the market. If there are some limitations, these pertain only to the most powerful computer models, which are not very often needed. However, several restrictions are encountered in the measuring technique and manufacturing technology. These are the primary areas which prevent bringing even the most promising ideas to implementation. When someone is prohibited from the access to up-to-date measuring and diagnostic methods, their work will be immediately hampered and thereafter discontinued (sooner rather than later). That is why those wishing to keep pace with the advancements in antennas must develop measuring and diagnostic technologies with great own efforts.

In cooperation with the University of Wrocław, a unique methodology for the simulation of the antenna performance over a wide temperature range has been elaborated. The method makes use of the precisely measured electrical properties of the dielectric materials that constitute the microwave and structural parts of the antenna arrays. These temperature-related data are put into the simulations of the impedance characteristics of stratified antennas. This research methodology, as well as the attempts to narrow the temperature dependence, is described in Chapter 4.

Chapter 5 deals with the bi-polar near-field antenna measuring system and addresses major development considerations. The bi-polar antenna measuring system designed and developed under the author's supervision at the Wrocław University of Technology in 1996 is the only near-field facility in Poland (Kabacik 1997a; Kabacik 1997c). The laboratory is one of the three bi-polar laboratories in the world. The customized scanner and its control system were made in Poland by two small firms (based in Wrocław).

In order to avoid lengthy numerical integration in the course of far-field computations, it is advisable to use the Fast Fourier Transform, provided that the sample points are arranged on one of the three fundamental coordinate systems. The near-field data acquired in another grid format can be interpolated onto the fundamental grids. The signal processing techniques used for the needs of the study are advanced. The methods used in our laboratory are presented in Chapter 6. It was a great success to elabo-

rate all the transformation procedures and relevant software for the needs of the laboratory on our own. Amongst the scientific and industrial laboratories whose experts showed an interest in the results obtained by our laboratory, it is worthy to mention the European Space Agency and Motorola.

With our laboratory system we tested planar antenna arrays with a broadside fixed beam and an electronically scanned beam. Examples of results are presented in Chapter 7. Holographic imaging implemented enabled us to identify various aperture blockages and impairments, as well as to derive the actual amplitude and phase distribution of the currents in the antenna aperture. The most remarkable results are discussed in Chapter 8. In order to broaden the available valid angle, research on a dual-system scanner was initiated in 1999. When the planar bi-polar and the conventional cylindrical grids of the sampling points are combined, the valid angle can reach hemispherical coverage, which satisfies the requirements of most antenna tests. This innovative approach, as well as the feasibility studies on the mobile outdoor scanning system are the major subjects of Chapter 9.

In the course of his research on the near-field systems, the author accomplished also a comprehensive study at two other near-field antenna laboratories:

- spherical scanning at the Technical University of Denmark, and
- planar, rectangular scanning at the University of Queensland, Australia.

One of the most accurate and well equipped laboratories in the world is the Danish laboratory (DTU web page), which handles the most demanding needs of the space industry. The results obtained there are regarded as references by other laboratories.

CHAPTER 2

HIGHLY INTEGRATED LIGHTWEIGHT ANTENNA ARRAYS

2.1. Increasing precision of beamforming in modern arrays

Contemporary antenna researchers have placed advanced beamforming techniques very high on their list of top priorities (COST260 web page; COST284 web page). It is of course understood that a useful test system must be capable of providing a fine resolution of the measured data, because the adopted beamforming involves small steps in the amplitude and phase values. If the resolution is not fine enough, we are very likely to face a gridlock in our investigations when measurement methods turn out to be too coarse and fail to evaluate the analyzed antenna designs. Only with small steps is the antenna able to offer fine spatial filtering, maintain suppressed interference, as well as provide reconfigurable radiation and polarization properties. Since the signals fed with the Beam Forming Network (BFN) are modified by actual loading, mutual coupling and edge effects, most of the experimental investigations into the performance of the array must rely on the data acquired with arrays assembled to a degree which enables normal operation. It does not infer that tests with partitioned arrays become obsolete, but put them into a proper context due to their incompleteness.

There are several major factors which emphasize demands on the precision of beamforming:

- precise focusing of the radiation towards the receiver or target,
- real-time adaptive shaping of the radiation pattern,
- mutlibeam radiation patterns,
- multiband operation spanned up to several frequency ranges,
- good coverage with low interference produced outside the served area.

Some of the advanced integrated arrays should have the capability of failure compensation without disrupting the operation of the antenna and without off-schedule servicing.

Owing to structural integrity it should be expected that highly integrated technology will be a favorable solution for antennas embedded into construction of moveable platforms (airplanes, ships or vehicles). The increasingly frequent use of information technology with core functions assigned to wireless communication is another factor enhancing interest in such arrays and in digital beamforming. However, it is typical of such antennas that much of the computational power must be used to maintain continuous calibration of the array. As a matter of fact, emerging antennas suffer from insufficient or inconsistent definitions of their parameters.

2.2. Technology of high-scale array integration invented in the framework of the author's research

The author's studies of lightweight arrays date back to the end of the 1980s. Initially, his research concentrated on fixed beam arrays only, but in a short time the work extended onto moderate gain phased arrays, and the author's efforts to minimize the losses in the BFN became a top priority. Sections of Chapters 2 and 3 present the outline of the research accomplished; more details can be found in the referred literature.

The technology invented in the framework of the author's research was applied to planar and conformal antennas. Several lightweight material concepts were thoroughly analyzed, but the author's interest concentrated primarily on the composites used in aerospace industry. The stability of antenna modules properties within a wide temperature range raised primary interest. Two important technological concepts developed in the course of the author studies are presented in Figure 2.1. A photograph of the basic antenna panel made according to the implemented honeycomb technology is shown in Figure 2.1b. An illustration of how the technology applies to conformal array panels is in Figure 2.2. With this technology, numerous antenna elements and subarrays were designed for different frequency ranges (800 to 2500 MHz) (Kabacik et al. 1999d). Figure 2.3 shows the calculated and measured return loss characteristics for the antenna element developed entirely in the honeycomb technology, where all RF parts were made in the form of printed circuits on dielectric skins (the antenna core being 25 mm thick). The element is dual polarized and is to operate in the 890 to 960 MHz frequency range (Kabacik, Białkowski 1998d). Two elements were manufactured in one piece of composite panel. The simulations were performed for an infinite ground with the *Ensemble* (Ansoft web page). The dual-polarized patch element was fed with through slot coupled microstrip line (the same concept as it is depicted in Figure 4.2). The difference between impedance match measured at orthogonal ports of the elements is primarily due to short length of microstrip feeding lines (connectors at

the edge of a ground plate). Another factor is a rectangular shape of the ground plate.

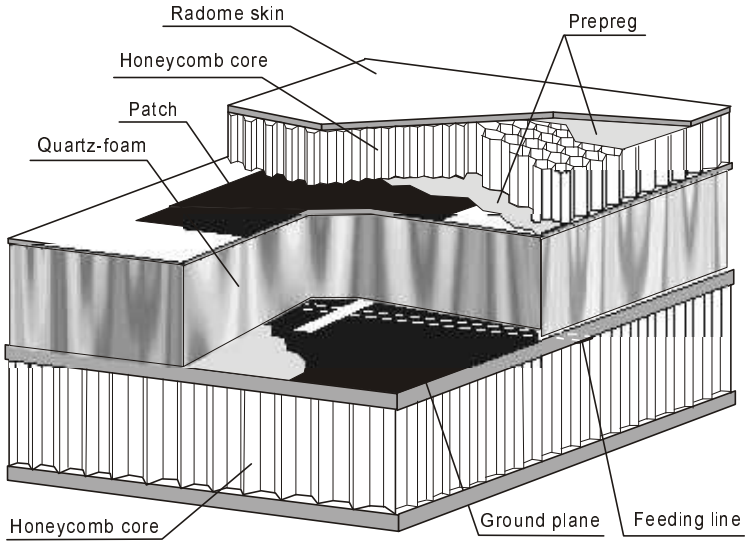

(a)

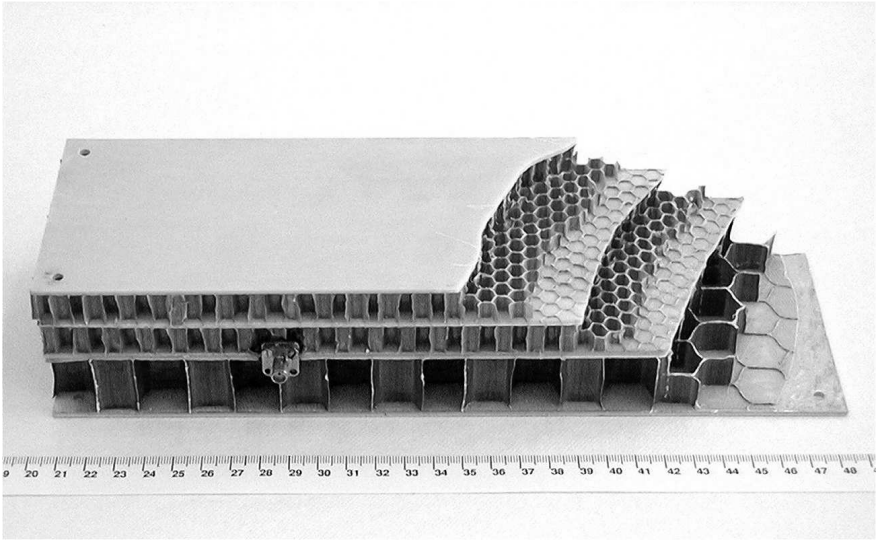

(b)

Fig. 2.1. Two forms of lightweight temperature resistant antenna modules developed in the course of the author's studies: (a) composite antenna involving quartz-fiber composite material and (b) three-layer antenna panel manufactured in the lightweight composite technology (Kabacik et al. 2000b).

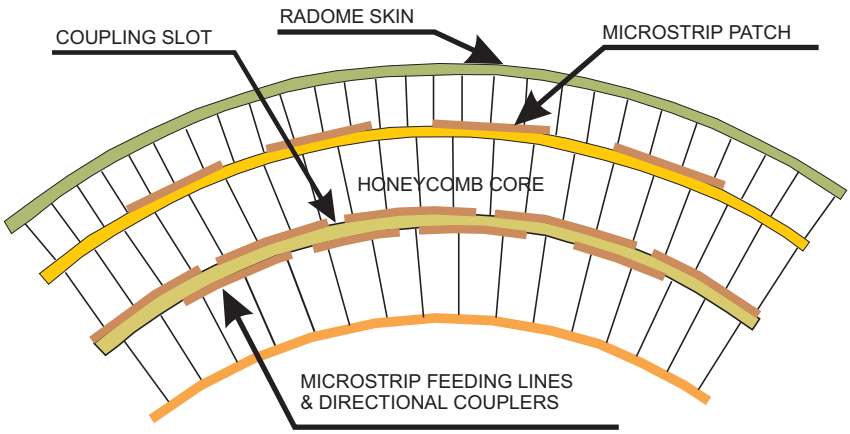

Fig. 2.2. Generic cross-section of the panel structure of the cylindrical array (Kabacik et al. 2001a).

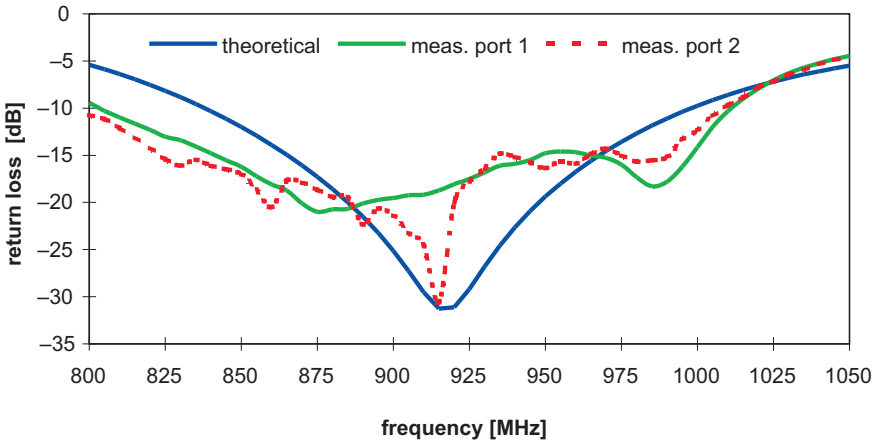

Fig. 2.3. Calculated and measured return loss characteristics of a dual-polarized GSM900 (890–960 MHz) antenna element made entirely of honeycomb composites and microwave laminates (Kabacik, Białkowski 1998d).

As two square elements were integrated into one panel, a ratio between lengths of the ground sides was 2:1. The measured plots reconstruct the calculated results with moderate accuracy – major features such as impedance bandwidth are on a good agreement. The most remarkable discrepancies are in terms of the best return loss, however for all measured cases the best values are below 20 dB. In such type of antennas, use is made of bonding films and composite cores with inhomogeneous physical and electrical properties. Initially, the consequences of such inhomogeneity were underestimated by the author, but with the progress of his research the problem received the attention it really deserved (the problem is remarkable at the antenna element level).

Honeycomb composites feature consists of many identical cells in their cores. Therefore, it is useful to investigate potential applications of the material in Photonic BandGap (PBG) structures. The PBG structure involves periodic dielectrics (rods, slabs, corrugations, etc.) which function as an substrate of the antenna or other microwave circuits. PBG structures can interact with electromagnetic waves in one or two dimensions. They make possible to control over propagation of electromagnetic waves to an extent that was not possible before. One of the important effects attributed to the PBG structures is frequency selective attenuation of surface waves (in such a way we can prevent scan blindness in arrays featuring wide beam scanning or suppress mutual couplings between elements). Preferred applications are at millimeter range (most often at 30 to 60 GHz) and submillimeter waves. These frequencies were beyond our interest – antennas at our studies were considered for frequencies up to 12 GHz.

Periodicity in the PBG is usually along one or two directions, but hexagonal honeycomb materials feature three major directions of periodicity. Typically, a width of periodic dielectric parts is comparable with adjacent air gaps (it is easy to ensure above 20 GHz). However, honeycomb cores used in our antennas (HRH-10 of Hexcell) have thin walls made of nomex and spacious air cells, so ratio between dielectric and air gap thickness is unfavorable, minimizing influence of dielectrics. I have not much experience with the PBG materials, but my feeling is that due to the thin thickness of dielectric walls any effect which may be attributed to the PBG structure is hardly to observe at 1 or 2 GHz. Furthermore, the PBG structures require remarkable large ground area extended outside the elements. In our antennas, the ground had to be truncated outside element outlines with little margin.

The numerical analysis should provide a good insight into the PBG phenomenon in our antennas. The two methods are most frequently used in the PBG analysis: Plane wave expansion (or spherical wave expansion) and the Transfer Matrix Method. However, they have not been investigated in our studies yet. Nevertheless, I think that in order to utilizes the PBG effects, special types of honeycomb cores should be developed (we had small experiences with polyurethane cores).

Another important issue pushing aside any effects which might be related to the PBG was significant influence of bonding layers on electrical properties in our antennas. Our research carried out on antenna arrays manufactured of honeycomb composites was concentrated on achieving repeatable properties and low losses. It was not easy, as bonding layers were modified and bonding thickness was hard to predict after curing (then thickness of a bonding film became nonuniform, thus making any prediction less accurate). Furthermore, the electrical properties of bonding layers such as dissipation factor and dielectric constant were not provided by their manufacturers. Unfortunately, they were hard to measure.

Assuring a low loss transmission of the microwave signals within an integrated array of a composite structure is another challenging task (Kabacik et al. 1998e). Major difficulties arise with the interlayer signal transmission through the bridges inside the array.

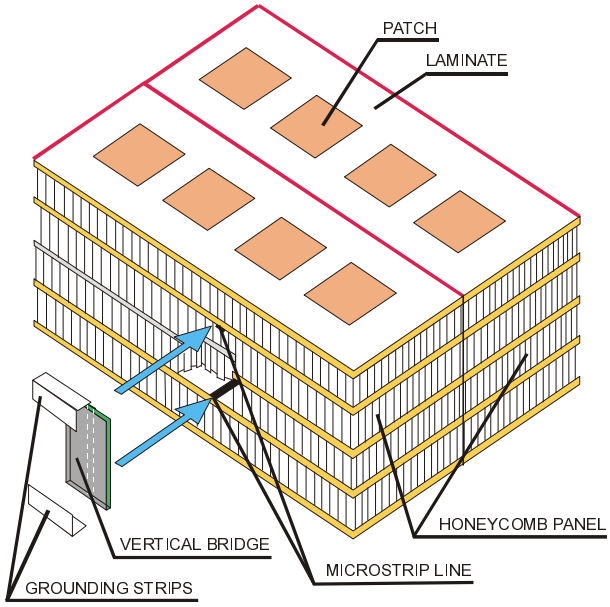

possible implementation

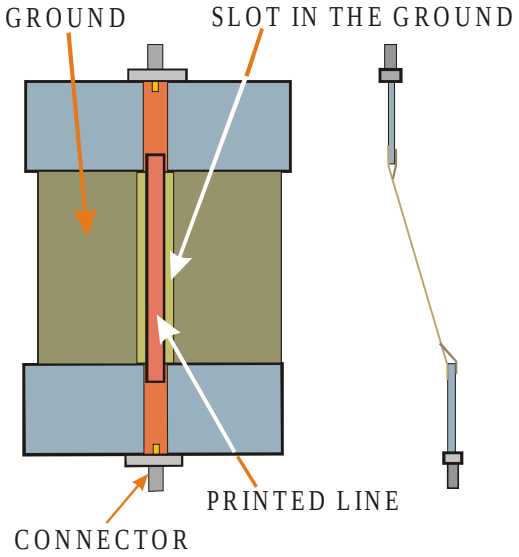

transmission line concept

Fig. 2.4. Interconnecting microwave transmission line printed on the membrane (thin dielectric film) invented in the course of our studies (Kabacik et al. 1998e; Kabacik et al. 2000d).

The air gaps required above the microstrip circuits or the spatial arrangement of the modular components accounts for the elongation of the bridges. However, their length takes inconvenient values for the passing of microwave signals. In our research we proposed and implemented vertical signal transmission through quasi co-planar lines printed on a membrane in the form of a flexible dielectric film (Kabacik et al. 2000d). The generic concept is described pictorially in Figure 2.4. Conceptual studies on the prototype membranes aimed at finding such a configuration of the printed line and the ground that would feature a favorable geometry and dimensioning. These requirements include a width of the line close to 2.5 mm for $Z_0 = 50$ ohm, and a width for any slot no narrower than 0.5 mm (due to the tolerances in typical photoetching). For these reasons, the transmission line has been placed above the wide slot in the ground. It is of prime importance that the metal cladding on the membrane side (top and bottom) be arranged consistently with the metal of the printed circuits on the laminates to which the interconnecting line has been soldered. The experimental studies were to verify the performance of the invented transmission line for several most likely arrangements of the circuit ports. It was promising that the return loss was always better than 22 dB and the measured impedance match varied slightly with the membrane profile shape.

Figure 2.5 presents the measured insertion losses for a membrane in a wide frequency range. The black line shows the measured values for the stretched membrane and the light line provides the measured values for a U-folded line (frequently en-

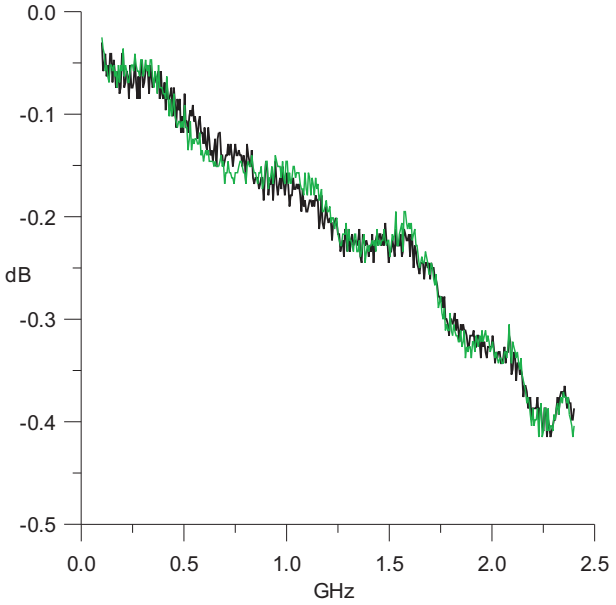

Fig. 2.5. Measured insertion losses of the interconnecting line printed on a membrane (green line – membrane U-shaped, black line – membrane stretched) (Kabacik et al. 2000d).

countered in engineering). Note that the insertion losses increase with frequency and are little affected by the actual membrane bending. The transmission losses of the 60 mm long membrane were measured and compared with the reference microstrip line made on a laminate. The losses of the reference microstrip line printed on a 60 mils thick GML 1000 laminate amounted to 0.14 dB at 1.6 GHz and were not much lower than those of the membrane (the provided loss data of the reference laminate do not include losses of discontinuity at the right angle connectors or microstrip ports).

2.3. Conformal integrated antennas

One of the most important innovations in modern antenna technology is the introduction of the conformal antenna design to many applications (Conformal 2001). The term *conformal antenna* is used to denote an antenna which conforms to the shape of the object on which it is attached (takes the form of non-planar surfaces for reasons other than electromagnetism). Later, the term *conformal* evolved to include antennas which are non-planar due to the beam forming requirements. Apart from other applications, conformal antennas can be used in mobile cellular base stations, as well as automotive and aerospace industries, and communication terminals. It is a general consensus that the aperture antennas utilized in these systems should be manufactured in a lightweight, highly integrated technology. The microstrip technology seems to be well suited for the conformal antenna structures.

Of the conformal antennas, cylindrical arrays have attracted the greatest attention so far (Löffler et al. 1999). There are three major reasons why cylindrical antennas have become so popular:

- the full angle field of view,
- radiation pattern properties almost independent of azimuth pointing (omni),
- a smaller number of components than in an equivalent system of planar arrays providing full angle coverage in azimuth.

The full field of view in the azimuth plane makes application of cylindrical arrays to outdoor base stations particularly advantageous. The most recent demand for cylindrical array antennas includes the Wideband Code Division Multiple Access systems (UMTS or CDMA 2000). In our research, a lot of attention has been given to the design of cylindrical element apertures for base stations servicing 3rd generation systems (1850–2200 MHz). A preliminary model of the module was manufactured and tested (Kabacik, Białkowski 2001d). The antenna elements consisted of a multilayer structure combining honeycomb composites and microwave laminates with printed circuits. The basic segment comprised four elements and is shown in Figure 2.6. However, the cylindrical array consists of many such or similar segments. A fully developed cylinder row may comprise 19 patches along the cylinder perimeter. The square patches are

probe-fed. The array has the form of a 680 mm diameter cylinder, what is equivalent to 4.2 and 5.0 wavelengths at 1850 and 2200 MHz, respectively. Center frequency was 2050 MHz and the element spacing was $0.7\lambda_0$. The number of rows depends on the required elevation radiation pattern.

Numerous applications in the field of terminal antennas are presently expected to fit curved surfaces, so that they can be flush mounted on a plane, ship or vehicle body. Good examples are the airborne terminals of the *Inmarsat* system. Having their uplinks and downlinks allocated in the upper L-band, the antennas that operate with the voice services of the *Inmarsat* system must have at least a 20 dBi gain, this corresponds to apertures which are more than half a meter in size. We developed a design of a terminal antenna which is formed with a cylindrical profile (Bem, Kabacik 1995; Kabacik et al. 2001a). The ground plane is a section of a cylinder (340 mm radius). The antenna has 32 elements arranged in eight rows. Its outline approaches 850 mm and 420 mm in length and width, respectively. The overall height of the antenna is 105 mm, of these 75 mm are counted by the cylindrical profile. The antenna elements and the feeding network are 30 mm thick. The elements which constitute the basic panel (four-element row) are excited with the equal power. The eight rows are fed with a non-uniform amplitude (30 dB modified Taylor) and phase distribution between these rows is electronically controlled with 22.5° steps.

The view of the developed antenna panel is presented in Figure 2.7. Since the system operates with circularly polarized waves, two orthogonal ports at each element are fed with signals in the quadrature phase. The directional coupler is responsible for feeding the orthogonal ports of the elements, so it must have an excellent phase characteristic (90°), a balanced power split, a small size and a thin profile (Kabacik et al. 2000b). In the course of our investigations, the best results were obtained with *three-strip* directional couplers made on polyimide films (about 50 μm thick). More details can be found elsewhere (Sachse, Sawicki 1999).

The measured return loss of the antenna element is plotted in Figure 2.8. The resonances measured at the element ports (without the directional coupler) are allocated close to the center frequency of the system band (1595 MHz). The measured and calculated bandwidths are in good agreement. Another plot included in Figure 2.8 shows the return loss characteristics measured at the input port of the antenna element which is integrated with the directional coupler needed to generate circular polarization. Owing to the good isolation maintained by the directional coupler, the combined element and coupler characteristic has also a wide bandwidth, but the best matching falls out of the *Inmarsat* frequency range.

As it can be seen from the radiation pattern plot in Figure 2.9, the main beam of the four-element antenna subarray is wide. The main beams of the conformal and reference planar subarray models (made with the same element dimensions and array spacing) are similar only within the center sector of the main beam. The standard beamwidth measured at the 3dB level is 25° and 22° for the conformal and planar

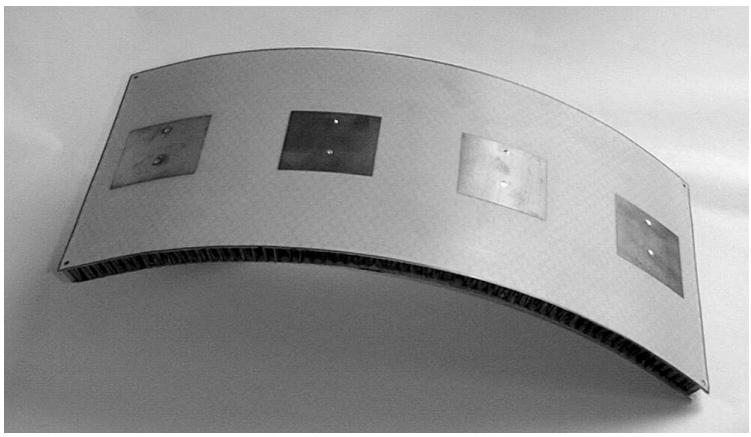

Fig. 2.6. Four-element basic subarray segment operating in the WCDMA frequency range designed and made within the author's studies (Kabacik, Białkowski 2001d).

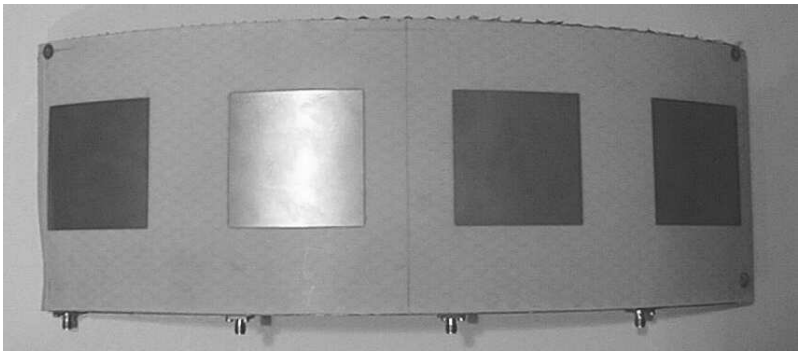

top view

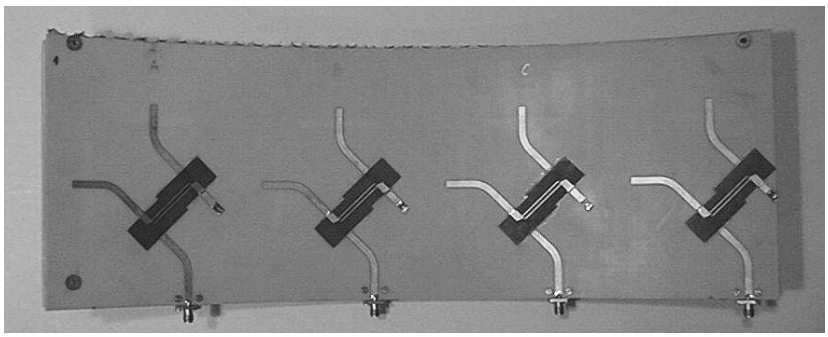

back view

Fig. 2.7. Model of the conformal subarray comprising four antenna elements for operation in the *Inmarsat* system (Kabacik 2001c).

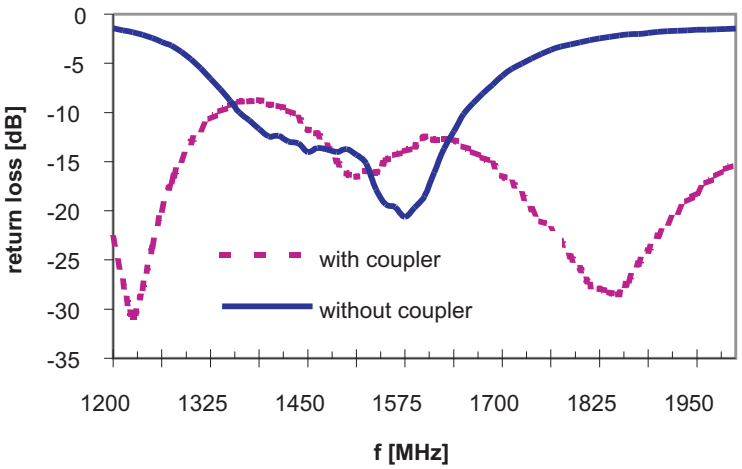

Fig. 2.8. Measured return loss of one center antenna element at the four-element panel, with and without the directional coupler (which was responsible for the generation of circular polarization).

subarray, respectively. With greater angles, the differences become considerable. It is important that the first nulls in the radiation pattern of the conformal subarray are pointed 65° to 70° off the broadside direction (compared to barely 26° in the planar counterpart). The 10 dB width of the main beam approaches 90° in the conformal design, while in the planar subarray it amounts to only 37°. The conformal design of the terminal antenna provides valuable improvements in the radiation pattern shape – the nulls in the radiation pattern are located much farther from the broadside direction than they are in the planar array. This effect reduces the hazard of signal loss during maneuvers of the antenna platform. A seatback of the reduced directivity in the conformal array is not additionally deteriorated by greater losses of the BFN.

As it can be seen in Figure 2.9, the radiation pattern exhibits ripples in the main lobe. To eliminate their occurrence, the phase excitation in the cylindrical array must be non-uniform even for a broadside beam. (Smooth beam slopes are achievable only with a non-uniform phase distribution.) Therefore conformal antennas establish tougher requirements for the diagnostic techniques, as non-uniform phase distribution are to be accurately synthesized in the array.

To provide a strong power taper between the subarray panels, an original bi-level 1:8 power distribution network was developed. One side of the highly integrated divider model is shown in Figure 2.10. The most impressive is the wide operation of the integrated power divider. It makes use of two substrates (teflon-type 30 mils laminates) bounded back-to-back on a common ground plane. The microstrip lines are coupled through slots in the ground (Sawicki et al. 1998; Kabacik et al. 2000b). The ports of the divider are on the same side of the coupler, but the microstrip lines are printed on both substrates. In order to compensate the phase velocity within the coupling zones, superstrate pieces of dielectrics are placed above the coupling slots.

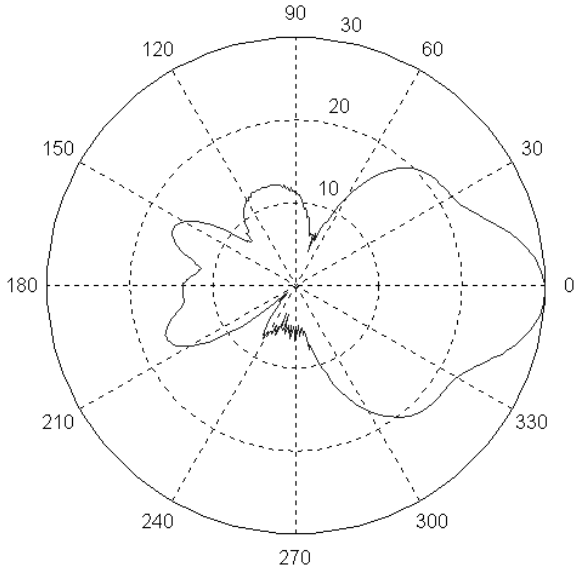

Fig. 2.9. Measured radiation pattern (level in dB) of the cylindrical antenna panel in the $\Phi = 90°$ plane at 1595 MHz (for one panel of *Inmarsat* antenna) (Kabacik et al. 2001a).

Another vital application of conformal antennas includes arrays offering a broad beam steering for the payload data downloading from the spacecraft. The extremely high value of the remote sensing data and communication signal calls for interception preventing measures. Among the weakest security issues are the broad beams of the satellite antennas transmitting payload data. A narrow satellite beam is the principal countermeasure preventing the danger of interception. Owing to the requirement of high data rates, the gain of the ground station antennas must be high and, at the same time, the beams should be adaptively pointed towards the lawful earth station. As the low-orbit satellite is flying over, the scan angle of the narrow-beam satellite antennas must be large. In order to achieve a broad beam steering, the aperture of the space-borne array must be conformal, when fully electronic beam steering is to be ensured (Martin et al. 2001).

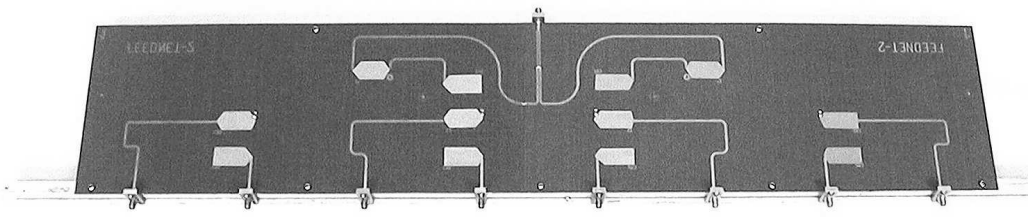

Fig. 2.10. Top-side view of the integrated 1:8 power divider (the outline approaches 850×200 mm) (Sawicki et al. 1998; Sachse, Sawicki 1999).

2.4. Antennas of future SAR radar

In order to obtain high resolution 3D images, spaceborne SAR radars with a scanned beam are needed. An unavoidable feature of such radars is the polarimetric capability in at least three bands (L, C and X) (Shafai 2000). The SAR technique is also promising for ITS systems. In one of the application the ISAR millimeter-wave radar will be mounted in front of the vehicle and provide data on the situation in the front of the driving car. The highly integrated lightweight arrays described in this Chapter may be considered for SAR applications. The objective of atmospheric remote sensing is to provide a comprehensive set of information on the actual environment of the Earth and on various forms of human activity on the Earth. The discipline is in front of its growing phase. Remote sensing combines expertise from dozens of scientific fields. Observation of the Earth's surface is performed from airborne and spaceborne passive and active sensors, amongst which microwave and millimeter-wave active equipment turns to be most productive. Passive sensors are capable of providing two-dimensional data, which are insufficient in advanced observations and do not support modern simulation techniques. That is why their use is expected to be less important in future. In order to improve the accuracy and resolution of weather remote sensing analysis, it is necessary to adopt a three-dimensional data format. Only in such a way it is possible to obtain a long term and highly accurate weather forecast (Desnos 2000).

CHAPTER 3

MULTI-ELEMENT ANTENNA ARRAYS FEATURING LOW-LOSS FEEDING SYSTEMS

3.1. Specifics of low-loss feeding systems

Research on lightweight antennas which feature a large number of elements (and therefore use of low-loss feeding systems is required) calls for evaluation methods suitable for handling densely packed arrays. This Chapter outlines some of the recent developments in arrays incorporating low-loss feeding systems which raise serious packaging problems. Owing to their low to moderate manufacturing costs, arrays with low-loss feeding systems are expected to be applied within mass markets. Thus, the diagnostic methods must be quick and easy to handle under production line conditions. A fundamental issue is how to maintain the tough tolerances of power distribution when large numbers of components are involved. In low-loss feeding systems, spatial power combining usually comprises precisely trimmed passive circuits or dispersed MMIC amplifiers. The propagation of electromagnetic energy inside air structures features very low losses, thus the application of any method based on this principle raises interest in low-loss array feeding systems. A characteristic of spatial feeding techniques is the lack of well defined ports and reference planes for measuring purposes. Further problems arise when analyzing the phase distribution inside such feeding circuits. It is therefore no surprise that antenna designers try to explore any form of symmetry (*e.g.* axial) as a guarantee of the aligned phase distribution. For experimental studies it is imperative to use methods where the amplitude and phase values are derived on the given spot of the array aperture. In this context, near field data gain in importance.

3.2. Radial line planar antennas

Many terrestrial and satellite communication systems require microwave planar antennas with a 30 dB or higher gain, which is very difficult to achieve using an array

with a conventional circuit-type feeding network (*e.g.*, a printed line corporate divider/combiner network). This difficulty is due to the excessive losses generated by the long microstrip transmission lines and multiple power combining steps which form the feeding circuit (Kabacik 1995). A loss in feeding by about 4–5dB makes the radiator inefficient. This problem further aggravates at upper microwave and millimeter frequencies (at the Ku-band). To overcome the problems of conduction losses in the circuit-type divider/combiner, a feeding structure in the form of a radial guide has been proposed and investigated by various researchers (Ando et al. 1985; Ando et al. 1988).

A radial guide with a central coaxial probe has been proposed as the feeding network for an array of slots located in the upper wall of a radial guide. This type of antenna, known as a radial line slot array (RLSA) antenna, has been successfully developed to receive DBS TV programs in Japan (Hirokawa et al. 1996). Another radial line planar antenna makes use of a radial guide including a central coaxial probe and a large number of peripheral probes arranged in concentric circles. Two parallel plates form the feeding network for an array with a curl, helix or microstrip patch as the radiating element (placed above the top plate of the waveguide structure). In the course of our studies we concentrated on such a type of planar radial antennas (Białkowski, Kabacik 2001). As it can be seen in Figure 3.1, the array comprises two circular plates and a large number of elements fed with short probes penetrating 'through hole' the radial waveguide structure at their open ends. To prevent propagation of waves which are non-uniform with respect to the guide height, the height of the radial guide has to be set smaller than a half waveguide wavelength. For that antenna, the usual design goal is to achieve a loss-free, uniform (amplitude and phase) aperture illumination. When achieved, the illumination allows each element of the array radiating in-phase the same amount of power. To achieve such illumination it is necessary to differentiate a length of the coupling probes between elements.

Crucial to the described design procedure is the availability of an electromagnetic model for the coupling probes in a radial guide. An approximate model describes only the interactions between the central probe and the probe under consideration. In the presented studies, a radial transmission line model has been established to obtain an accurate design of a radial line planar antenna which takes into account electromagnetic interactions between all the probes. In order to prevent the occurrence of grating lobes, the spacing between the elements (probes) must be sufficiently small, which increase the mutual coupling. On the other hand, to neglect the evanescent waves in the interactions between the rings, the spacing between the rings needs to be sufficiently large (a quarter wavelength or more).

An accurate modeling method for such feeding systems has been described by Białkowski and Kabacik (Białkowski, Kabacik 2003). By assuming that there is no

scattering and that the coupling probes gradually absorb the wave energy fed by the central probe, the amplitudes of the excitation coefficients or the lengths of the probes at an arbitrary tier can be determined. The model includes a center feed probe and a cascade of P circular rings of coupling probes (Fig. 3.1). The probes are assumed to be identical within one ring, but they may vary from one ring to another. Due to the interactions of radial waves (incident, scattered and reflected) and the probes, voltages V_1, V_2, …, V_P are established across equivalent admittances YA_1, YA_2, ..., YA_P representing antenna elements in the rings. Assuming that each antenna element sees an identical environment, these admittances can be made equal. Their values can be obtained from measurements or simulations.

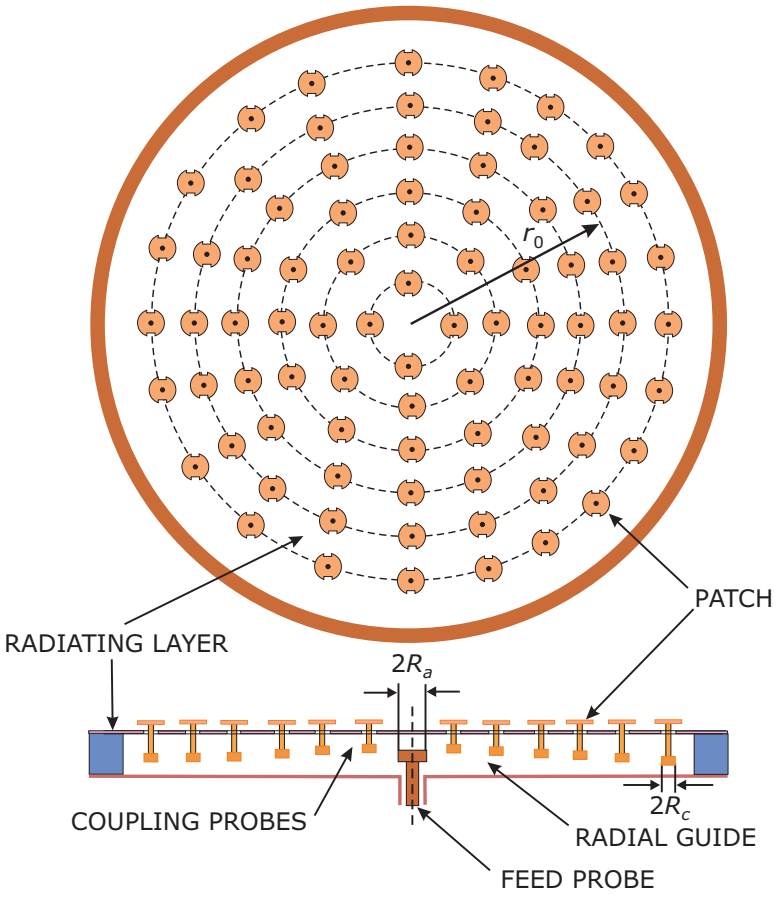

Fig. 3.1. Generic structure of the investigated radial line planar antenna (Białkowski, Kabacik 2001a; Białkowski, Kabacik 2003).

In order to solve such a problem, a field matching method, similar to that described in (Białkowski, Varis 1993), for the radial guide structure of Fig. 3.1 is applied. Here, the analysis is extended to the radial guide terminated at $r = R_2$ in an arbitrary wave admittance YR_2 while the probes are loaded in equivalent admittances YA_1. It is assumed that admittance YR_2 is experienced only by the propagating TEM radial wave. Higher order evanescent waves are assumed to see an infinite radial guide. The definition of admittance YR_2 with regard to the TEM radial wave is introduced as follows. By assuming that for the propagating TEM radial wave the *y*-component of the electric field $E_y(r)$ and the Φ-component (azimuth plane) of the magnetic field are given by (3-1)

$$E_y(r) = H_0^{(2)}(k\,r) - U_0 J_0(k\,r)$$

$$H_\Phi(r) = \frac{j}{Z_0}\left[H_1^{(2)}(k\,r) - U_0 J_1(k\,r)\right] \tag{3-1}$$

where k is a wave number, $j = \sqrt{-1}$, $H_0^{(2)}$, $H_1^{(2)}$, J_0, and J_1 are Hankel and Bessel functions of zero and 1st order and U_0 is some kind of reflection coefficient, the wave admittance YR_2 experienced by the TEM radial wave at $r = R_2$ is given by (3-2)

$$YR_2 = YR(r = R_2) = \frac{j}{Z_0}\frac{H_1^{(2)}(kR_2) - U_0 J_1(kR_2)}{H_0^{(2)}(kR_2) - U_0 J_0(kR_2)} \tag{3-2}$$

Due to the fact that $YR(r = R_2)$ used in the iterative process is assumed known, the coefficient U_0 shown in (3-1) can be determined and is given by (3-3)

$$U_0 = \frac{YR(r = R_2)H_0^{(2)}(kR_2) - X_0 H_1^{(2)}(kR_2)}{YR(r = R_2)J_0(kR_2) - X_0 J_1(kR_2)} \tag{3-3}$$

where $X_0 = j/Z_0$.

By using the above result the following expressions for the *y*-component of the electric field in the vicinity of the central probe, the peripheral probes and at the radial positions $r = R_1$ and $r = R_2$ are obtained when the axially symmetric TEM wave is terminated at admittance $YR(r = R_2)$ at $r = R_2$.

For the region close to the central probe $r \approx R_a$ (radius of a disc at the inner end of the central probe, which is used to improve operational bandwidth)

$$\begin{aligned} E_y(r \cong R_a) &= \sum_{n=0}^{\infty} \frac{\varepsilon_{0n}}{B} A_n\left[H_0^{(2)}(\Gamma_n r) - U_n J_0(\Gamma_n r)\right]\cos(k_{yn} y) \\ &+ M\sum_{n=0}^{\infty} \frac{\varepsilon_{0n}}{B} C_n\left[H_0^{(2)}(\Gamma_n r) - U_n J_0(\Gamma_n r)\right] J_0(\Gamma_n r_0)\cos(k_{yn} y) \end{aligned} \tag{3-4}$$

r_0 is a distance between the point of observation and a center of the radial line planar antenna.

For the region close to the peripheral probe $r_1 \approx R_c$ (radius of a disc at the inner end of peripheral probes)

$$E_y(r_1 \cong R_c) = \sum_{n=0}^{\infty} \frac{\varepsilon_{0n}}{B} A_n \left[H_0^{(2)}(\Gamma_n r_0) - U_n J_0(\Gamma_n r_0)\right] \cos(k_{yn} y) J_0(\Gamma_n r_1)$$
$$+ \sum_{n=0}^{\infty} \frac{\varepsilon_{0n}}{B} C_n \left\{ \left[\sum_{m=2}^{M} H_0^{(2)}(\Gamma_n r_{m1}) - M U_n J_0^2(\Gamma_n r_0) \right] J_0(\Gamma_n r_1) + H_0^{(2)}(\Gamma_n r_1) \right\} \cos(k_{yn} y) \quad (3\text{-}5)$$

where $\{A_n\}$ and $\{C_n\}$ are expansion coefficients for the field external to the cylindrical regions containing the central and the peripheral probes, and $\Gamma_n^2 = k^2 - (n\pi/B)^2$.

The first summation term in (3-4) and (3-5) represents the contribution from the central probe while the second term represents the contribution from the peripheral probes. During calculations infinite series in (3-4) and (3-5) are truncated. Ten to twenty terms are sufficient to produce accurate results for typical probes in a radial waveguide. Coefficients U_n appearing in (3-4) and (3-5) are given as follows. For $n = 0$ coefficient $U_n = U_0$, as defined by (3-3). For $n > 0$, U_n is assumed to be zero meaning that higher order radial waves produced by the central and peripheral probes have a negligible magnitude at $r = R_2$ and thus they are neglected.

The expressions (3-4) and (3-5) describe the electromagnetic interactions between the rings of peripheral probes, the central probe and the probes located in region $r > R_2$ only via the propagating axially symmetric TEM radial waves. However, the interactions between the probes within the ring are accounted for by both propagating and evanescent radial waves. The corresponding Φ-components of the magnetic field at locations $r \approx R_a$ and $r_1 \approx R_c$ are obtained by using the relationships, which are valid for the y harmonics in a parallel-plate radial guide. Assuming that the field expansion coefficients $\{A_n\}$ and $\{C_n\}$ are known, the y-components of the electric field of the propagating TEM radial waves at $r = R_1$ and $r = R_2$ are given by the following expressions.

At $r = R_1$:

$$E_{y\mathrm{TEM}}(r = R_1) = \frac{-VR_1}{B} = \frac{A_0}{B}\left[H_0^{(2)}(kR_1) - U_0 J_0(kR_1)\right]$$
$$+ M \frac{C_0}{B}\left[H_0^{(2)}(kr_0) - U_0 J_0(kr_0)\right] J_0(kR_1) \quad (3\text{-}6)$$

At $r = R_2$:

$$E_{y\mathrm{TEM}}(r = R_2) = \frac{-VR_2}{B} = \frac{A_0}{B}\left[H_0^{(2)}(kR_2) - U_0 J_0(kR_2)\right]$$
$$+ M \frac{C_0}{B}\left[H_0^{(2)}(kR_2) - U_0 J_0(kR_2)\right] J_0(kr_0) \quad (3\text{-}7)$$

The voltage transmission coefficient VR_2/VR_1 between $r = R_1$ and $r = R_2$ is given by

$$\frac{VR_2}{VR_1} = \frac{E_{y\text{TEM}}(r = R_2)}{E_{y\text{TEM}}(r = R_1)} \tag{3-8}$$

The wave admittance $YR_1 = YR(r = R_1)$ at $r = R_1$ (ring 1) is determined as

$$YR_1 = YR(r = R_1) = \frac{H_{\Phi\text{TEM}}(r = R_1)}{E_{y\text{TEM}}(r = R_1)} \tag{3-9}$$

where $E_{y\text{TEM}}(r = R_1)$ is given by (3-6) and $H_{\Phi\text{TEM}}$ by (3-10)

$$\begin{aligned} H_{\Phi\text{TEM}}(r = R_1) = \frac{j}{Z_0}\Bigg\{ & \frac{A_0}{B}\left[H_1^{(2)}(kR_1) - U_0 J_1(kR_1)\right] \\ & + M\frac{C_0}{B}\left[H_0^{(2)}(kr_0) - U_0 J_0(kr_0)\right] J_1(kR_1)\Bigg\} \end{aligned} \tag{3-10}$$

Without going into details of a number of mathematical conversions, the field expansion coefficients A_{0L} and C_{0L} for the case when the peripheral probes are terminated in admittance $Y_L = YA_1$ are

$$A_{0L} = A_0(V_0 = 1, V_1 = 0) - \frac{A_0(V_0 = 0, V_1 = 1)Y_{10}}{Y_L + \sum_{i=1}^{M} Y_{1i}}$$

$$C_{0L} = C_0(V_0 = 1, V_1 = 0) - \frac{C_0(V_0 = 0, V_1 = 1)Y_{10}}{Y_L + \sum_{i=1}^{M} Y_{1i}} \tag{3-11}$$

The above expressions can be used to determine VR_2/VR_1 and $YR_1 = YR(r = R_1)$ ((3-8) and (3-9)).

To complete the analysis, the voltage ratio V_1/VR_1 also has to be determined. The voltage ratio V_1/VR_1 does not depend on presence or absence of intermediate rings and thus it is more convenient to use. For configuration involving one ring of coupling probes excited by the center feed probe, this voltage ratio is determined by calculating VR_1 using (3-6) under condition (3-11) and is given by the following expression (3-12)

$$\begin{aligned} \frac{V_1}{VR_1} = \frac{V_1}{V_0}\frac{V_0}{VR_1} = \frac{-Y_{10}V_0}{Y_L + \sum_{i=1}^{M} Y_{1i}} \Big/ \Big\{ & A_{0L}\left[H_0^{(2)}(kR_1) - U_0 J_0(kR_1)\right] \\ & + MC_{0L}\left[H_0^{(2)}(kr_0) - U_0 J_0(kr_0)\right] J_0(kR_1)\Big\} \end{aligned} \tag{3-12}$$

The above procedure demonstrated for ring 1 is repeated for all the remaining rings and leads to obtaining a full set of voltage ratios $\{V_1/VR_1, V_2/VR_2, ..., V_p/VR_p\}$. Having determined ratios V_p/VR_p for $p = 2, \ldots, P$, and by using actual values of VR_p obtained for the cascade of rings, voltages $\{V_p\}$ can be calculated using the following formula: $V_p = VR_p (V_p/VR_p)$, $p = 2, \ldots, P$. The derived expressions for the fields, voltages and admittances complete the process of analyzing the radial line planar antenna feed network.

A comparison between the full electromagnetic model and the approximate model for the magnitude of the reflection coefficient for the two spacings of the cavity wall RD is presented in Figure 3.2. Even though a wall produces a strong reflection of the incident wave, it can be seen that the differences are in the range of less than 0.05.

Having determined probes excitation voltages $\{V_p\}$ or coupling coefficients $\{V_p/V_0\}$, the radiation pattern of the array formed by P rings positioned at radial locations $\{r_{0p}\}$ can be determined. Assuming that mutual couplings between the array elements are small and that the elements are co-polarized, the field radiation pattern can be obtained using the pattern multiplication principle applicable to circular arrays, as given by

$$F(\theta,\phi) = f(\theta,\phi)\sum_{p=1}^{P} V_p \sum_{m=1}^{Mp} \exp\left\{jk[r_{0p}\sin\theta\cos(\phi - m\Delta\phi_p)]\right\} \tag{3-13}$$

where $f(\theta, \phi)$ is the field radiation pattern of a single element and M_p, $\Delta\phi_p$ denote a number of elements and an angular spacing in the p-th ring and V_p is the voltage excitation coefficient for this ring.

Figure 3.3 shows the calculated array factor of a certain radial line planar antenna as a function of the elevation angle θ ($\theta = 0°$ represents normal direction to the antenna aperture). The antenna consisted of 90 elements arranged in five rings and generated linear polarization (Białkowski, Kabacik 2003).

3.3. Spatial solid-state power combining

The space-level combiners of solid-state power and low-noise amplifiers are of particular interest to the development of future millimeter-wave communication systems. Because of a gradual congestion at lower microwave frequencies, many future wireless communication systems will migrate to upper microwave and millimeter-wave frequencies. With such high frequencies, the communication systems are limited by the link budget (propagation losses takes a form $22 + 20\log(R/\lambda)$ [dB]). As the range of the service area is small and the wavelength is short, the application of cylindrical antenna systems (or spherical ones) is well suited both indoor and outdoor. Such systems are likely to be preferred in high-rate data transmission in the so-called 'air-bursts'. The author investigated the space-level combining of solid-state sources at millimeter frequencies in cylindrical antennas (Kabacik, Białkowski 2001d).

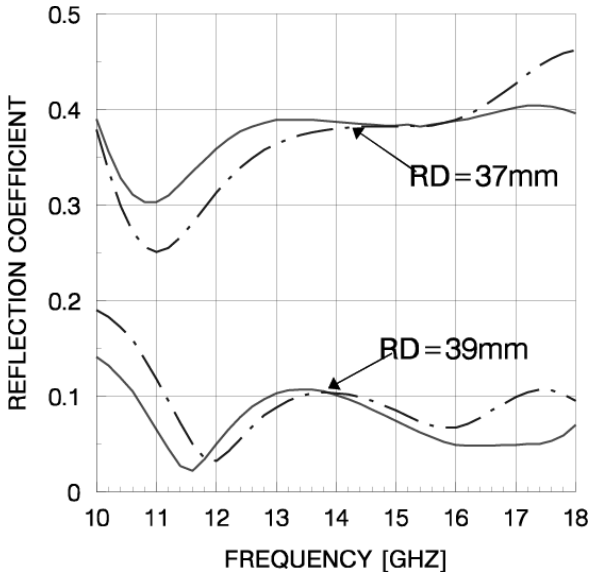

Fig. 3.2. Simulated input reflection coefficient for the radial cavity with one central probe and 20 peripheral probes: — the full electromagnetic model and – · – the simplified model. Two locations of the cavity perimeter wall RD = 37 mm and RD = 39 mm (Białkowski, Kabacik 2003).

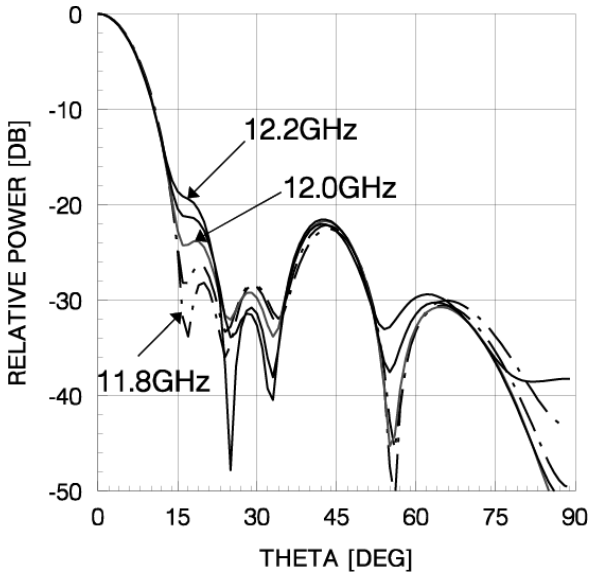

Fig. 3.3. Computed array factor for five-ring radial-line planar waveguide array at five frequencies: 11.8, 11.9, 12.0, 12.1 and 12.2 GHz (Białkowski, Kabacik 2003).

In order to avoid excessively large bias voltages, which are required when traveling wave tube (TWT) amplifiers are employed, future millimeter-wave base station transmitters will incorporate solid-state oscillators and amplifiers. Solid-state devices are lumped in form, their dimensions being only a tiny fraction of the operational wavelength. As the generated power depends on the size of the solid-state devices, the requirement for a small size to wavelength ratio is one of the factors that account for their limited power capability at millimeter-wave frequencies. In order to achieve power levels suitable for a proper operation of future millimeter-wave wireless systems, individual active stages have to be combined in clusters (Białkowski et al. 2001b).

In general, space-level combiners make use of tile or tray configurations to accommodate the active stages. Most of our attention has been given to space-level power combiners that use transmit-type tile configurations of patches. The reason for this choice is that these configurations are very convenient for integrating a large number of active stages with antennas made by monolithic manufacturing techniques. Since patch antennas radiate only on one side of the ground plane, two back-to-back tile arrays with a coupling arrangement between the two opposite sides are required to receive and transmit signals. Small holes or slots in the ground plane can be used for coupling purposes. With such arrangement, the inner side of the tile array can receive a signal and pass it to the active stage. Following the amplification stage, the signal can be delivered to the outer antenna for re-transmission. The development of MMICs on organic substrates enable the use of flexible matrixes of MMIC circuits.

Apart from power combining structures which rely on planar active antennas, the author studied a cylindrical array with an illuminating (feeding) system along the symmetry axis of the cylinder. The generic concept of the structure is depicted in Figure 3.4. The diameter of the cylinder is most likely to fall within 2 to 6 wavelengths. A great advantage of the cylindrical surface is the constant propagation loss and phase offset between the illuminating elements and the active stages. A customized illuminating system – difficult to design – is required to produce a tapered amplitude distribution along the axial direction (needed for vertical beam shaping).

An interesting emerging method which decreases the transmitting power makes use of the Ultra Wide Band (UWB) modulation method at microwave frequencies (Aiello, Rogerson, 2003). This method involves the so-called time domain modulation and produces signals which have at least 25% bandwidth at a relatively low center frequency (UWB, Ultra-wideband Laboratory web page). When the transmitting power is decreased by two or more orders, the requirements made on the antenna bandwidth are difficult to fulfil with active amplifiers. Furthermore, the antenna phase response over the operational band must be investigated (which is another new challenge to antenna engineering). In case of UWB pulses the instantaneous bandwidth is very large and antenna effects are extremely important. It turns out that the paradigm the transmit and receive antenna is equal in the frequency domain, is not any longer valid in time domain (Sarkar, Salzar-Palma 2003). Consequently, the transmit and

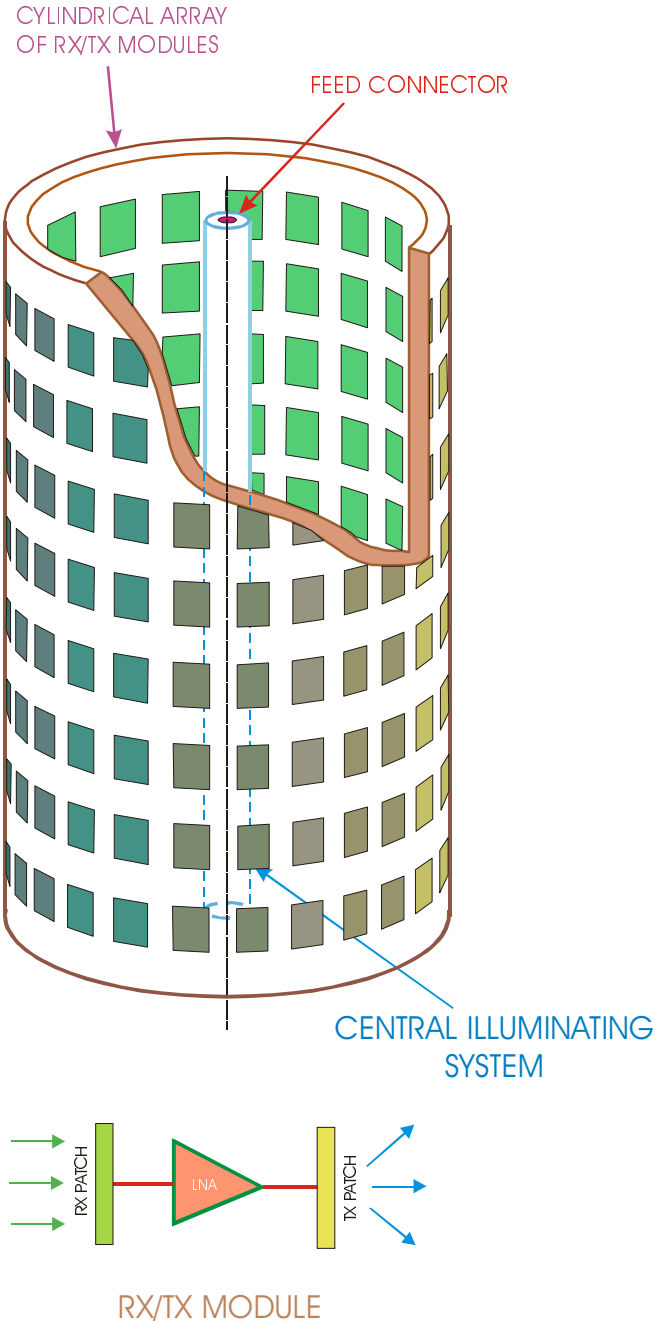

Fig. 3.4. Cylindrical array with a central illuminating system (Kabacik, Białkowski 2001d).

receive waveforms produced by the antenna are not equal in the case of very short pulses (the transmit waveform is related to the second derivative of the transient current in the antenna, while the received open-circuit voltage is approximately the derivative of incident field on the antenna).

3.4. Inflatable lightweight arrays

Contemporary mobile satellite communication systems can not compete with terrestrial systems in terms of price and performance (shadowing, constrained indoor penetration, *etc.*). Apparently small terminals are among the prerequisites to gain wide acceptance by the users. Small terminals must incorporate small antennas which feature a low gain. For this reason, a greater part of the link budget must be transferred to the satellite segment. To accomplish this goal, consideration is given to spaceborne antennas as large as several dozen meters (up to 60 meters). The focus is on inflatable arrays made of several membranes which support the printed circuits (Huang 2001). After having been put into space, the structure is inflated with gas from a tank.

The measurement of the antenna raises serious trouble. Firstly, the antenna is lacking a firm structural support. The result is that, after deployment on the earth, gravitational forces noticeably affect the geometry of the antenna (even though the weight of the membranes is very low). Parabolic flights are too short too suffice for structural experiments with such antennas. Secondly, the antenna is large and obviously bulky for testing. Since the antenna has a high gain and large dimensions, the near-field scanning must provide a very large scanning aperture and preserve the same direction of the gravitational forces in the course of measurements.

In space environment (earth orbits), antennas must sustain temperatures as high as +100 °C to +160 °C on their sun facing side (exact temperature depends on surface color, thermal conductivity within the structure, etc). On a shadow side or during eclipse phases, antennas must sustain temperatures as low as –100 °C to –150 °C. Good heat convection between a spacecraft and the antenna allow to avoid large temperature extremes. Anyway, temperature gradient may exceeds 200 °C or even 300 °C between sun facing and shadow side of antennas. When antenna is fixed to a wall of a spacecraft the gradient is much smaller. To reduce thermal gradient, a thermal protection layer under the antenna is used. Multilayer thermal blankets consisting of around 20 layers which are bonded in a 1 mm thick flexible panel are extremely important for good thermal protection of spaceborne antennas. The author believes such thermal blankets can be incorporated into inflatable antennas and planar antennas (as it is done with solar panels). However, large antennas still cause major problem in space technology.

CHAPTER 4

TEMPERATURE-DEPENDENCE OF MICROSTRIP ANTENNA PERFORMANCE

4.1. Introduction

In the technology of lightweight and integrated arrays, extensive use is made of dielectric materials to produce the array elements and the BFN subcomponents. However, the actual electrical parameters of the substrates may differ from those included in the manufacturers' specifications. Microstrip antenna designers generally rely on what the manufacturers say, although such specifications refer to standard environmental conditions only, neglecting a number of factors that are of prime importance to an accurate evaluation or design of antenna arrays. One such factor is the temperature-dependence of the materials, particularly when they are to be used in highly integrated structures (Kabacik, Białkowski 1998c).

In his studies of the diagnostics of antenna arrays, the author addressed the problem of how accurately the electrical properties of the material have to be determined. Samples of many microwave substrates were measured in a specialized laboratory for dielectric analysis. The measurements yielded characteristics of the dielectric constant and dissipation factor for temperature ranges equivalent to those occurring in the majority of airborne applications. Electrical performance and temperature-dependence were simulated for a variety of microstrip antennas (Kabacik, Białkowski 1999a). The results suggest that the attribution of the discrepancies between the design and actual properties to the inaccuracies of numerical analysis and geometry alone is not always justified (Kabacik et al. 2000c). One of the main reasons for the occurrence of such discrepancies lies in neglecting a thorough analysis of the material characteristics.

Of the various materials used in microstrip technology, teflon, ceramic and polystyrene laminates, dielectric foams, polyimide films, kevlar-type printed boards and honeycomb composites have found particularly wide acceptance. In the course of our diagnostic studies, we examined teflon-based laminates, ceramic-based laminates and quartz-fiber composite substrates. Using a precisely controlled laboratory setup, we obtained accurate temperature characteristics with different substrates offered by major manufacturers (*Rogers*, *3M-Arlon*, *Taconic*, *CuFlon*, *GIL*). On the basis of these

laboratory data, the substrates were divided into four categories according to their dielectric constant values and temperature dependence. We called these categories A, B, C & D and they are discussed in Section 4.3 and 4.4.

4.2. Temperature-related problems in integrated arrays

Only in some applications microstrip and other printed antennas, are to operate in an environment which is close to what is defined as standard conditions. In most applications, integrated antenna arrays are to work in harsh environments characterized primarily by temperature and humidity variations. Large-scale integrated microwave arrays are further thermally affected by the adjacent electronic active stages. In spaceborne arrays, there are additional constraints affecting heat dispersion.

In the course of our study we found that two major problems had not been clearly addressed in the antenna literature: the temperature-dependence of the electrical parameters of the substrates and the discrepancies between actual values and those quoted in the manufacturers' specifications (Kabacik, Białkowski 1998c). These aspects are evidenced by the common practices regarding the design and development of patch antennas where these problems are marginalized or even neglected.

In a typical approach to the design of microstrip antennas, the values of the dielectric constant and dissipation factor are assumed as they are quoted in the data sheets. There, the dielectric constant value (ε_r) is generally allowed a certain tolerance range, while the dissipation factor ($\tan\delta$) takes the highest possible value. The manufacturers usually emphasize the frequency-dependence and neglect the temperature drift of the material. Rarely do the data sheets provide the thermal coefficient of ε_r, which is of limited validity (*e.g.* for 0 °C to +100 °C). It is often the approximate nature of the theoretical models or the CAD tools used in the design process and the inaccuracy of the processes of model construction that are blamed for the discrepancies between the predicted and actual performances of the antenna elements. This judgment is misleading when the actual electrical and physical substrate parameters deviate from those of the data sheet or when they are both temperature- and frequency-dependent. It must be acknowledged that the electrical parameters of dielectric materials are difficult to measure accurately with rolling sheets at the running manufacturing system. This may be one of the reasons why the manufacturers' data are often incomplete or incorrect.

4.3. Effect of temperature on the microwave substrate properties

In the present study, substrate measurements were performed under the supervision of Prof. Hubert Kołodziej at the Laboratory of Dielectrics and Structure of Organic

Compounds, Chemistry Faculty of the Wrocław University. The laboratory has well-established facilities providing high quality measurements for solid and liquid materials. The material samples were disc-shaped and had diameters of 8 mm and 6mm for low frequencies and microwave frequencies, respectively. It should be pointed out that the measuring accuracy is significantly affected by the quality of sample preparation. Owing to the large frequency span (test frequencies, 800 kHz, 1 MHz, 1 GHz and 10 GHz), two measuring methods and three laboratory setups had to be used. The measuring system was calibrated using standard polypropylene or polystyrene samples of known parameters. Regardless of temperature, the accuracy of the measurements was quite good, with errors claimed to be smaller than 1.5% and 3% for dielectric constant and dissipation factor, respectively. Materials displaying very low losses (less than 0.001) could be measured with a poorer accuracy of the $\tan\delta$. Because of the anisotropy of many substrates, the measurement axis had to be clearly defined. In the presented analysis, the measurements were performed only in the *z* plane that was oriented along the laminate thickness.

The applied measurement method requires determination of sample thickness with high accuracy. Typically, thickness measurements are made at a room temperature, before inserting a sample into the microwave head. Strictly saying, the sample thermal expansion and dielectric constant thermal effect can not be separated. However, thermal expansion can be neglected if the value of thermal expansion is little. When thermal expansion coefficient value indicates, that thickness variations may become important, it is necessary to either make thickness measurements at both extreme temperatures (for in-between temperatures interpolation should be sufficient). Another approach is to recalculate thickness variations with the known thermal expansion coefficient of the material along the *z*-axis (sample thickness).

The investigated substrates were divided into four categories, A, B, C and D, according to the temperature-dependence of the dielectric constant. Categories A and B included teflon-glass microwave laminates. The substrates of Category A were characterized by dielectric constants decreasing with temperature, with an approximately constant slope gradient. Only when a phase transition in glass occurred, the curve became steeper over a narrow temperature subrange. Note that the phase transition phenomenon involves changes in molecular thermal mobility, which is associated with the transformations of the amorphous phase of the materials, from a glassy (low-mobility) to a rubbery (high-mobility) state. Phase transition in glass occurs between 20 and 30 °C and is accompanied by a variation in the dielectric constant and dissipation factor and by an increase in the thermal expansion coefficient.

Category B laminates were characterized by a dielectric constant with a gradient value differing remarkably in at least two large temperature subranges of the dielectric constant plot. Regardless of this effect, the laminates experienced phase transition. It is worthwhile to mention that Category B laminates had dielectric constant values which were almost independent of temperature in the lower subrange and showed a noticeable temperature dependence in the upper subrange.

The microwave laminates were made of woven or dispersed glass fibers and teflon fillers. Although there is a wide spectrum of glass types, only some of them, namely those having low losses at microwave frequencies (*e.g.* pyrex), can be used for the manufacture of microwave laminates. All of the laminates tested belonged either to Category A or Category B. Thus, good representative examples of Category A were Ultralam 2000 and CuClad 250 LX laminates, whereas good representative examples of Category B were RT/duroid 5880 and TLX-8 laminates. Unfortunately, it is impossible to classify a given laminate as A or B on the basis of data sheets, because the latter neither provide sufficient information about the chemical composition of the glass or material structure nor include the ε_r versus temperature plot. Category C and Category D materials were made of ceramic and quartz-fiber composites, respectively.

The complete measured temperature characteristics of the dielectric constant for the laminates representing Category A, Category B and Category C are published elsewhere (Kabacik 1995; Kabacik, Białkowski 1999a). Figure 4.1 presents dielectric constant and dissipation factor plots for one example of Category A and one example of Category B laminate, respectively. In one of the instances, the measured dielectric constant values for Category A material ranged from 2.82 at –60 °C to 2.56 at +80 °C (9.7% change). There was a noticeable phenomenon of glass phase transition, observed at 23 °C. (The occurrence of phase transition has not been mentioned in the manufacturers' specifications.) For one of the materials representing Category B, the measured dielectric constant ranged from 2.46 at –60 °C to 2.45 at +20 °C and 2.27 at +80 °C (this means 8% change within the upper 60 °C interval).

It was tempting to treat the problem by comparing the measured dielectric constant characteristics with the values specified by the manufacturers. The comparison revealed considerable discrepancies. The measured frequency-related variations in the dielectric constant (in the considered ranges) for these laminates were less noticeable – the change in the dielectric constant, as a function of frequency, was less than 0.15% for material A and less than 0.5% for material B. The measured dissipation factor values for these laminates were either much lower than the ones quoted in the manufacturer's specification or complied with the data sheets only over a limited temperature range.

Category C materials were laminates with a uniformly dispersed ceramic filler in a teflon matrix. Typical examples of this category are RT/duroid 6010 and AR1000. The measured dielectric constant value for one of the Category C laminates was changed by 6.9%. There was a negligible variation in the dielectric constant with frequency in the range of –60 °C to +25 °C and a slight variation with frequency in the higher temperature range, reaching a maximum of 0.8% at +80 °C. Only for temperatures below +10 °C did the dissipation factor comply with the value quoted in the specification. At high temperatures, the dissipation factor differed significantly from the one included in the data sheet (it was 5.2 times the value cited in the manufacturers'

specifications at +80 °C). The measured characteristics did not show any temperature-related hysteresis, as these changes were independent of sample cooling or warming in the course of data recording.

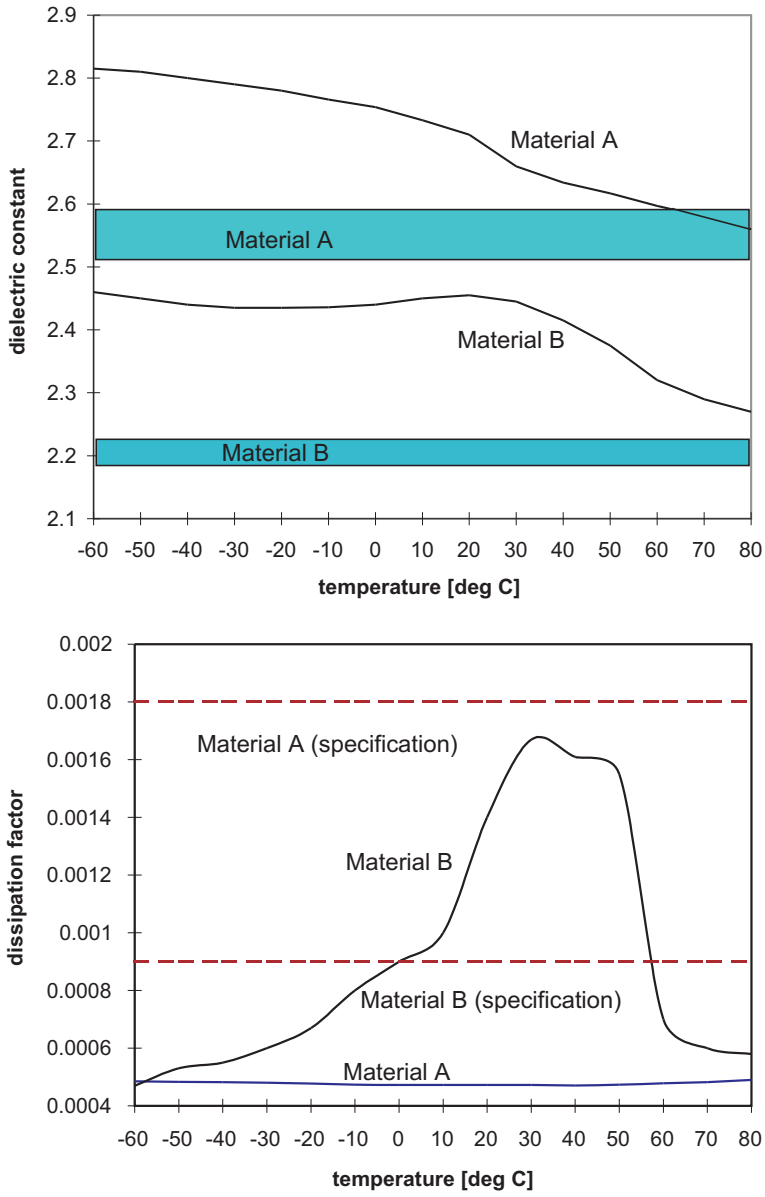

Fig. 4.1. Measured temperature characteristics of the dielectric constant and dissipation factor for one Category A and one Category B laminate (Kabacik, Białkowski 1999a).

4.4. Performance of microstrip elements over large temperature ranges

With the measured electrical parameters of the substrates, it is possible to simulate the impedance characteristics of various microstrip antenna elements exposed to large temperature variations. In the present section, our considerations are focused on a dual-feed, aperture-coupled microstrip antenna, which was designed for operation in the downlink of a personal satellite communication system. The downlink frequency band adopted for the purpose of the study ranged between 2483.5 and 2500 MHz (16.5 MHz bandwidth with center frequency f_0 = 2491.75 MHz). The dual-feed was to provide flexibility in polarization selection (horizontal, vertical, dual or circular).

A generic view of the investigated antenna is shown in Figure 4.2. The antenna consists of three different dielectric layers, a ground plane and printed circuits. On the top surface there is a square metal patch. Two orthogonal coupling slots are etched in the ground plane. On the bottom surface there is a microstrip feeding circuit comprising two separately excited microstrip lines and some space left for the directional coupler printed on a thin dielectric piece. In all the investigated cases, the patch substrate was chosen to be 3.18 mm thick (125 mils). The microstrip line and the feeding circuit substrate were 0.76 mm (30 mils) or 0.51 mm (20 mils) thick. Between the patch substrate and the ground plane there was a thin bonding film (40 μm). Note that in aerospace composite engineering the term 'bonding layer' is also referred to as *prepreg*. In spite of being thin, the bonding film generally raises serious problems when estimating the average dielectric constant and dissipation factor of the integrated composite panel. All circuits were printed on 17 μm (0.5 oz) copper foils.

In the investigations presented here, attention was focused on the return loss characteristic (S_{11} and S_{22}) as a function of frequency, and specifically on the temperature drift of the center frequency, defined in terms of the best impedance match (expressed by return loss). Although the isolation between the two ports is a key parameter in the design of dual- or circularly polarized antenna elements, its temperature dependence did not seem to deserve particular consideration. The reason is that for the dual- or circularly polarized antenna, there exists a trade-off between the return loss and isolation when broadband operation is required. In such a case, the return loss has to be decreased in order to achieve high feed isolation and, consequently, an increased polarization bandwidth. Nevertheless, in the cases investigated here, which had at the center frequencies maximized return loss, the isolation between the orthogonal ports ranged between 9.5 and 16.7 dB and they were moderately sensitive to temperature.

Impedance simulations were carried out with the *Ensemble* software package (*Ansoft*). The software involves a full-wave method and is suitable for analyzing printed antennas that are manufactured in stratified planar dielectrics (on infinite ground planes and infinite substrates). During calculations, the frequency step was set to

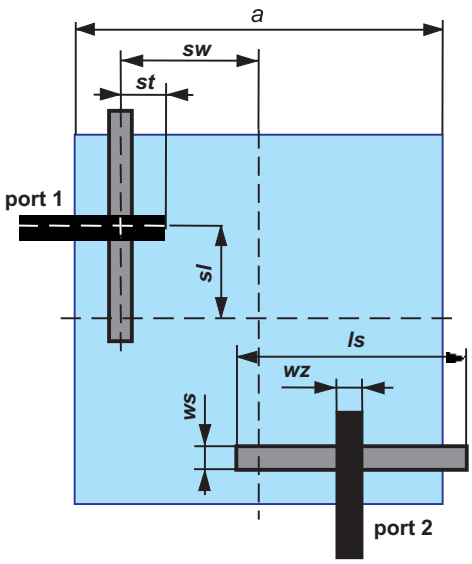

Fig. 4.2. Configuration of a dual-feed patch antenna with through-slot coupled microstrip lines. Metal cladding: 0.5 oz (17.5 μm) thick copper. Port 1 and 2 are located between branch coupler and coupling apertures.

2 MHz (with a few justified exceptions, when it was 1 MHz). The calculated results were slightly affected by the grid size (*e.g.*, the calculated center frequency was 2508 MHz and 2492 MHz for a coarse grid and fine grid, respectively). In the present analysis, a constant temperature across the entire antenna structure was assumed. In practice, the temperature distribution inside the antenna structure can be non-uniform, which makes a rigorous analysis troublesome.

Antennas with laminates A, B and C

We considered several antenna designs. For clarity, each antenna design under study was denoted by three letters. The notation reads as follows: the first letter (L or P) indicates the source from which the electrical parameters of the substrate were taken (L = manufacturers' data, P = our measurements). The second letter stands for the patch substrate category (A, B and D). The third letter denotes the category of the feeding line substrate (A, B and C). The return loss characteristics calculated for an LBB antenna is shown in Figure 4.3 (the patch and microstrip line substrates belonged to substrate category B). The lowest S_{11} (S_{22}) value was –52 dB at f_0 = 2492 MHz and the 10 dB return loss bandwidth was 108 MHz. It seemed interesting to recalculate the return loss characteristics of the LBB antenna by making use of measured electrical parameters of the laminate (and leaving aside the dimensioning of the LBB element).

Plots (b), (c) and (d) in Figure 4.3 present the results of such calculations for three temperatures, respectively. The plots of the antenna return loss for the measured ε_r values show a considerable shift downwards along the frequency axis. The center frequency at +20 °C amounted to 2384 MHz (being by 108 MHz lower than the design value). The 10 dB return loss bandwidth of the antenna was 97 MHz (which was associated with the decrease in the minimum return loss value). If the center frequency of an actual antenna falls below the design value, this may be an indication that the actual dielectric constant value of the substrate has been greater than the one assumed in the course of design. In our tests, the measured values of the dielectric constant were generally higher than the nominal ones. When temperature varied between –60 °C and +80 °C the drift of the center frequency amounted to 84 MHz and was several times the required operational bandwidth. The results imply that the designed LBB antenna will not cover the required frequency band over the considered temperature range. We also examined how the presence of the prepreg affected the return loss characteristics. The influence of the prepreg was found to be very small resulting in a frequency shift around 2 MHz only.

Figures 4.4 and 4.5 illustrate the calculated return loss characteristics for the PAA antenna and the PBB antenna, respectively (please note that dimensions of the PBB antenna differ from those of the LBB one). In both designs, use was made of actual electrical parameters, as obtained from the measurements at +20 °C. The center frequency drift caused by temperature variations was –42 MHz (at –60 °C) and +62 MHz (at +80 °C) for the PAA antenna, and –2 MHz (at –60 °C) and +88 MHz (at +80 °C) for the PBB antenna. The antenna bandwidth approached 7% and broadened slightly with temperature. For the PBB antenna, the f_0 frequency drift was only 22 MHz in the temperature range from –60 °C to about +40 °C. A major portion of the drift occurred at temperatures above +40 °C (due to the temperature-dependence of the dielectric constant in Category B substrates).

Since the use of the same substrates for the patch and for the feeding network may not necessarily provide an optimum patch design, we also studied antennas involving a combination of teflon-based (A or B) and ceramic-based (C) laminates. Figure 4.6 shows the plot of the S_{11} values calculated for the PAC antenna (material C, 0.51 mm thick). The center frequency offset due to temperature was –42 MHz at –60 °C and +50 MHz at +80 °C with respect to the center frequency value at +20 °C. The impedance bandwidth approached 110 MHz and increased slightly with temperature. The PAC antenna design was the first to comply with the return loss requirement (10 dB) over the specified frequency band and over the entire investigated temperature range.

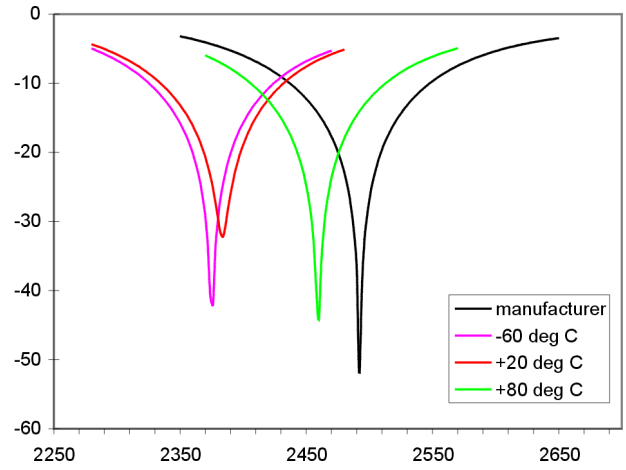

Fig. 4.3. Calculated return loss at port 1 and 2 (S_{11} and S_{22}) of a LBB patch antenna (both substrates were made of material B) having a structure of Fig. 4.2, with different sets of electrical parameters (e_r and tan$d$) of the substrates: (a) provided by the manufacturer, (b) measured at +20 °C, (c) measured at –60 °C and (d) measured at +80 °C.

a = 34.66 mm
ls = 23.2 mm, ws = 2.0 mm, sw = 12.4 mm, sl = 7.0 mm
wz = 2.42 mm, st = 6.0 mm
$\varepsilon_{r1} = \varepsilon_{r2}$ and $\tan\delta_1 = \tan\delta_2$
$\varepsilon_{r1} = \varepsilon_{r2} = 2.20$, $\tan\delta_1 = \tan\delta_2 = 0.0009$
d_1 = 3.18 mm (125 mils),d_2 = 0.76 mm (30 mils)
ε_p = 2.32, $\tan\delta_p$ = 0.0013, d_p = 40 μm

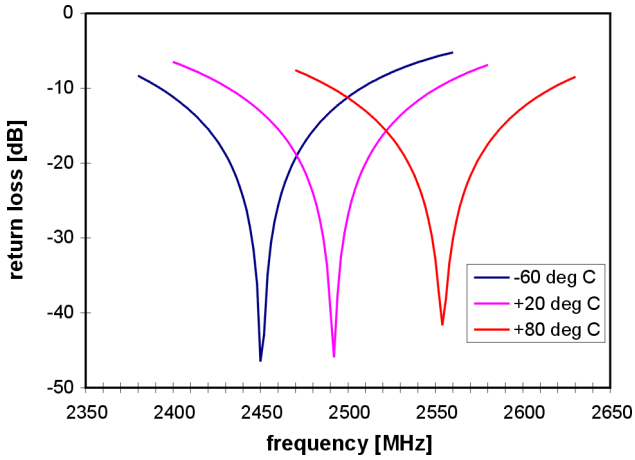

Fig. 4.4. Calculated temperature dependence of return loss (S_{11} and S_{22}) of PAA patch antenna (both substrates were made of material A), designed with the use of the measured material electrical parameters.

a = 31.1 mm
ls = 22.6 mm, ws = 2.0 mm, sw = 11.5 mm, sl = 6.5 mm
wz = 2.04 mm, st = 5.3 mm
$\varepsilon_{r1} = \varepsilon_{r2}$ and $\tan\delta_1 = \tan\delta_2$ are the mesaured values
d_1 = 3.18 mm (125 mils),d_2 = 0.76 mm (30 mils)
ε_p = 2.32, $\tan\delta_p$ = 0.001, d_p = 40 μm

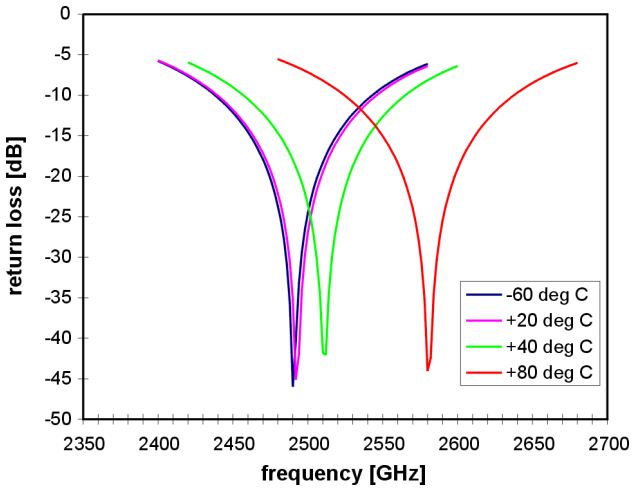

Fig. 4.5. Calculated temperature dependence of return loss (S_{11} and S_{22}) of PBB patch antenna (both substrates were made of material B), designed with the use of the measured material electrical parameters.

a = 31.1 mm
ls = 22.0 mm ws = 2.0 mm sw = 12 mm sl = 6.5 mm
wz = 2.18 mm st = 6.0 mm
$\varepsilon_{r1} = \varepsilon_{r2}$ and $\tan\delta_1 = \tan\delta_2$ are the mesaured values
d_1 = 3.18 mm (125 mils) d_2 = 0.76 mm (30 mils)
ε_p = 2.32 $\tan\delta_p$ = 0.0013 d_p = 40 μm

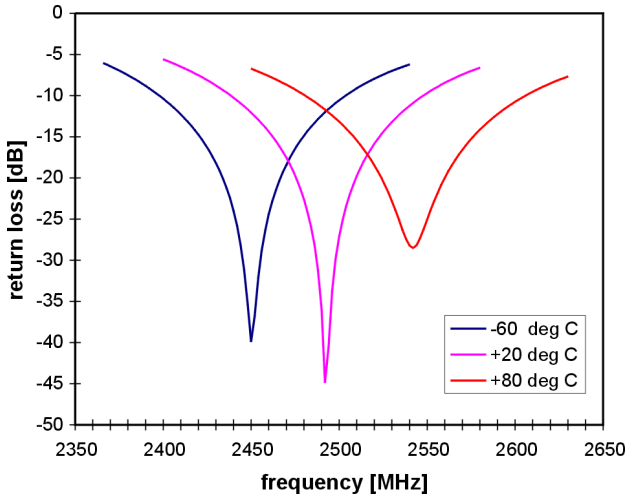

Fig. 4.6. Calculated temperature dependence of return loss (S_{11} and S_{22}) of PAC patch antenna, designed with the use of the measured material electrical parameters. Patch substrate: 125 mils thick material A, line substrate: 20 mils thick material C.

a = 39.8 mm
ls = 22.0 mm ws = 1.6 mm sw = 14.7 mm sl = 10.8 mm
wz = 2.04 mm st = 5.3 mm
$\varepsilon_{r1} = \varepsilon_{r2}$ and $\tan\delta_1 = \tan\delta_2$ are the mesaured values
d_1 = 3.18 mm (125 mils) d_2 = 0.76 mm (30 mils)
ε_p = 2.32 $\tan\delta_p$ = 0.0013 d_p = 40 μm

Antennas with material D

Summarizing the results obtained in the previous subsection, we can see that the use of glass-reinforced teflon substrates may be unacceptable in applications where the antennas are exposed to large temperature variations. Hence, it is worthwhile to look for materials with electrical properties less vulnerable to temperature. Advanced aerospace composite materials are promising candidates for consideration. There are two principal categories of such composites, one based on honeycomb fillers and the other one based on fibers (glass or quartz). The major advantages of these materials can be detailed as follows: low weight, very wide temperature range of operation, good electrical parameters, weak temperature-dependence of electrical parameters and small thermal expansion coefficient. The inner volume of the honeycomb composite panels is predominantly filled with air. The temperature-stable air properties moderate the temperature-dependence of the antenna impedance characteristics. In our study we also considered composites made of dispersedly bonded quartz fibers (Category D substrates). The drawbacks of the material were fragility, moisture absorption, and troublesome deposition of conductive circuits.

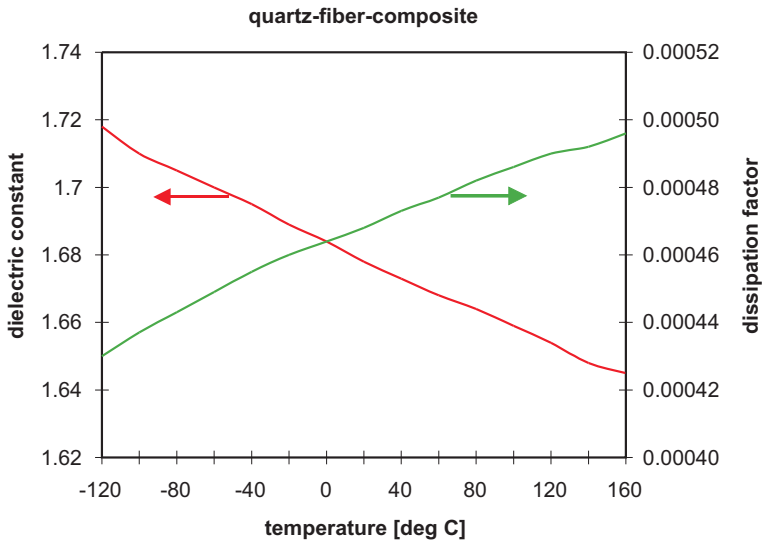

Fig. 4.7. Measured electrical parameters in a wide temperature range of quartz-fiber based composite (material D) (Kabacik, Białkowski 1999a).

One of the Category D materials recommended for use in microstrip antennas is the quartz-based composite, which consists of short quartz fibers bonded together (the fibers are randomly oriented). The development of this material was originally stimulated by the needs of thermal spacecraft engineering. The measured dielectric constant and the dissipation factor for this material are plotted in Figure 4.7 for test temperature

ranging from –120 °C to +160 °C (which is in compliance with the conditions of open spaceborne applications, but not in deep space or atmospheric re-entry flight). Compared to the materials of Category A, B or C, the dielectric constant value of the Category D material varied only slightly: from 1.718 at –120 °C to 1.645 at +160 °C (4.3%). The dissipation factor turned out to be ultra low, varying from 0.00043 at –120 °C to 0.0005 at +160 °C. Manufacturer's data were unavailable, because this material is marketed for other applications. It has to be added that frequency had little effect on the measured values and that there were no phase transition phenomena.

Using the Category D material, a new dual-feed microstrip antenna (PDB) was designed (the thickness of the Category B laminate being 30 mils). Figure 4.8 relates the calculated return loss to frequency, with temperature as a parameter. The maximum return loss, 56 dB, was achieved at 20 °C. The computed S_{11} at f_0 was always better than 24 dB within the entire operating frequency bandwidth. The center frequency drifted with temperature from 2480 MHz (–60 °C) to 2506 MHz (+80 °C). The PDB antenna return loss was never worse than 15.6 dB over the entire operating temperature (–60 °C to +80 °C) and frequency band.

Having achieved such promising results for the PDB antenna, we examined a PDC antenna in which the 30 mils teflon-based laminate had been replaced by a 20 mils thick ceramic laminate of Category C in the feeding line circuit. An illustration of the calculated return loss is in Figure 4.9. The center frequency is shifted by 22 MHz only (from –16 MHz at –60 °C to +6 MHz at +80 °C), and the return loss is even lower than that for the PDB antenna. It must be emphasized that the f_0 frequency drift achieved for the substrate combinations B + D and C + D was small (1% and 0.9%).

Thermal expansion effect

So far we have described the temperature-dependence of the electrical parameters of the substrates and their effect on the performance of the microstrip antenna element. However, there are other substrate-related factors that affect the performance of the patch antennas. One of them is the thermal expansion coefficient. Thermal variations account for a slight expansion or shrinkage of the antenna dimensions. A favorable coincidence is when the effect of thermal expansion and that of the ε_r temperature-dependence of the substrate may compensate each other.

The thermal expansion coefficient in the *x* and *y* directions (parallel to the laminate surface) generally ranges from 14 to 48 ppm/°C. Thus, in practice, the effect of the thermal expansion coefficient along the *x* or *y* axis is of little importance. Hence, in the present case, with temperature variations between –60 °C and +80 °C, the expansion in the *x* and *y* directions can be neglected. The values of the thermal expansion coefficient in the *z* direction for glass-reinforced teflon laminates generally range from

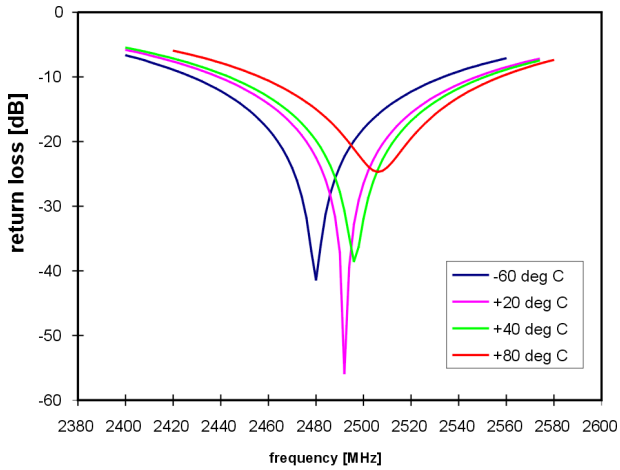

Fig. 4.8. Temperature drift of calculated return loss (S_{11} and S_{22}) of PDB patch antenna, designed with the use of the measured material electrical parameters. Patch substrate: 125 mils thick composite material D (Fig. 4.7), line substrates: 30 mils thick material B.

a = 39.14 mm
ls = 24.6 mm ws = 2.0 mm sw = 14.5 mm sl = 9.0 mm
wz = 2.18 mm st = 5.8 mm
$\varepsilon_{r1} = \varepsilon_{r2}$, $\tan\delta_1$ and $\tan\delta_2$ are the mesaured values
d_1 = 3.18 mm (125 mils) d_2 = 0.76 mm (30 mils)
ε_p = 2.32 $\tan\delta_p$ = 0.0013 d_p = 40 μm

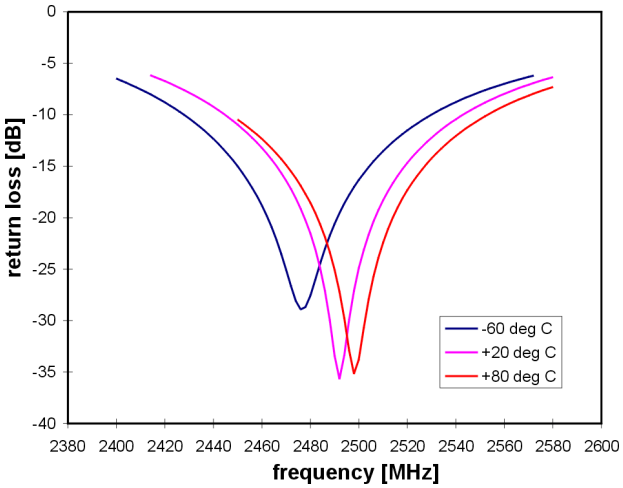

Fig. 4.9. Temperature drift of the calculated return loss (S_{11} and S_{22}) of PDC antenna, designed with the use of the measured material electrical parameters. Patch substrate: 125 mils thick composite material D (Fig. 4.7), line substrate: 20 mils thick material C.

a = 39.8 mm
ls = 22.0 mm ws = 1.6 mm sw = 14.7 mm sl = 10.0 mm
wz = 0.488 mm st = 3.2 mm
$\varepsilon_{r1} = \varepsilon_{r2}$, $\tan\delta_1$ and $\tan\delta_2$ are the mesaured values
d_1 = 3.18 mm (125 mils) d_2 = 0.51 mm (20 mils)
ε_p = 2.32 $\tan\delta_p$ = 0.0013 d_p = 40 μm

170 to 280 ppm/°C. For the value of 280 ppm/°C, the thermal expansion of a 0.76 mm thick laminate (at +20 °C) results in a 3.9% thickness change – from 0.7430 mm (29.25 mils) at –60 °C to 0.7728 mm (30.43 mils) at +80 °C. For a 3.18 mm thick board, thickness also changes by 3.9%, but the corresponding thickness value is 3.109 mm (122.39 mils) and 3.233 mm (127.30 mils) for –60 °C and +80 °C, respectively.

The thermal expansion coefficient of a quartz-fiber composite is approximately by two orders smaller than that of many foam types used in antennas. The quartz-fiber composite has an ultra low coefficient of thermal expansion, ranging from 4×10^{-7} to 7×10^{-7}. With a 3.18 mm thick board, this expansion coefficient produces 0.01% thickness changes, from 3.1798 mm (125.19 mils) to 3.18013 mm (125.20 mils) at –60 °C and +80 °C, respectively.

It is worth assessing how thermal expansion contributes to the overall antenna parameters. From the data of Table 4.1 (comparing the center frequency and maximum return loss with and without inclusion of the thermal expansion effect) it may be inferred that the change in the physical dimensions of the antenna is of little importance. The frequency step used in the simulations was 1 MHz. The plots of the calculated center frequency drift in Figure 4.10 illustrate the example of analysis when the thermal expansion effect was included. As shown by these plots, frequency drift due to temperature was 106 MHz for the PAA, 93 MHz for the PBB and 21 MHz for the PDC antenna.

Table 4.1. Calculated center frequency and maximum return loss with and without inclusion of thermal expansion effect.

Antenna	**Center frequency [MHz] return loss [dB]**			
	with thermal expansion effect neglected		**with thermal expansion effect included**	
	–60 °C	+80 °C	–60 °C	+80 °C
PAA	2450 46	2554 41	2449 38	2555 60
PBB	2490 46	2580 44	2489 32	2582 35
PDB	2480 41	2506 24	2478 53	2507 24
PDC	2476 29	2498 35	2477 27	2498 37

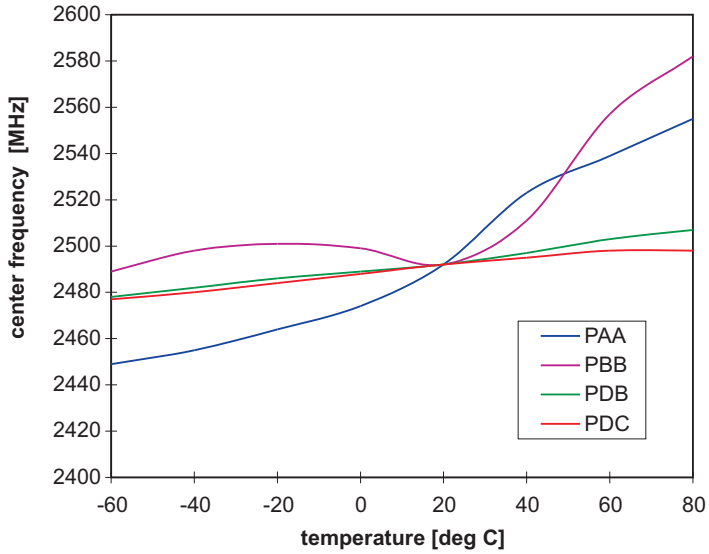

Fig. 4.10. Center frequency, defined in terms of the minimum value of S_{11} (S_{22}), versus temperature for antennas: PAA, PBB, PDB and PDC (Kabacik, Białkowski 1999a).

4.5. Design guidelines

The results obtained allow the formulation of some general design guidelines. For microwave laminates, the actual dielectric constant and dissipation factor values often differ from those listed in the data sheets. What is more, in all of the investigated cases, the measured dielectric constant value was greater than the one specified in the data sheets. In general, the manufacturers' specifications proved to be valid only for a limited temperature range. Hence, the values provided by relevant data sheets are inadequate when the substrate is exposed to large temperature variations. This deficiency is due to the temperature dependence of the dielectric constant of the microwave laminates studied. In consequence, the electrical characteristics of the microstrip antennas which involve layered dielectrics are considerably influenced by temperature. Two of these characteristics, resonant frequency drift and the return loss, may raise serious concern. A careful selection of the substrate dielectrics which are least sensitive to temperature is a prerequisite to accomplish a satisfactory antenna design. It has been shown that replacing the feedline substrates with ceramic ones can minimize temperature-related variations in the antenna performance. Further improvement can be achieved using quartz-fiber composites as a patch substrate. Investigations into the thermal expansion of the substrate have demonstrated that this phenomenon is of minor importance.

CHAPTER 5

NEAR-FIELD BI-POLAR ANTENNA MEASUREMENTS

5.1. Scanning methods and major related problems

So far, in near-field antenna measurement systems scanning has been performed on spherical, cylindrical or planar surfaces. With the spherical grid it is possible to measure a complete 3D radiation pattern. Cylindrical and planar scanning surfaces provide far-field results in the 3D format, though within a much narrower spatial angle as compared to the spherical system. But even then, the cylindrical and planar systems make it possible to determine the most important properties of the radiation patterns (*e.g.* main beam, primary sidelobes). The combination of these surfaces in one scanning system with the aim to enlarge the view angle nowadays is becoming a hot research subject. However, it is difficult to achieve consistent results provided by different scanning techniques.

Although there is a wide selection of sampling point grids for the scanning surfaces, the most frequent choice includes fundamental grids (rectangular, polar, spherical and spiral formats. The state-of-the-art interpolation algorithms enable the transposition of the nonuniformly scanned data onto other formats). Irrespective of the grid form, a key issue is the allowable spacing between two adjacent sampling points as less dense samples result in a smaller input data files. The formulas in algorithms of the near-field to far-field transform computation are closely related to the arrangement of the sample points. In order to improve near-field data processing, there are three challenging tasks for mathematicians to fulfill – more generalized transform methods, time-domain transform theory and faster convergence of results.

Table 5.1 summarizes the major features of the scanning systems which are mostly in use nowadays. Spherical scanning requires larger anechoic chambers than do other methods. Two of the most popular scanning systems are shown in Figure 5.1. The azimuth over elevation or the elevation over azimuth AUT revolving makes use of a two-axis positioner and are less space demanding than is the scanning system with a hemispherical strut. Changes of antenna orientation with respect to the gravity force direction usually require a firm structural part of the AUT. Cylindrical scanning is

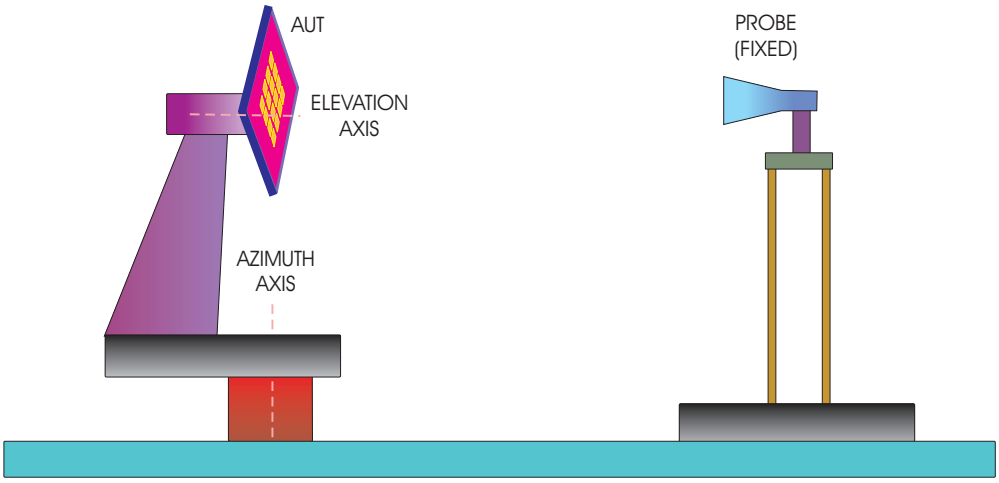

system with azimuth over elevation antenna positioning

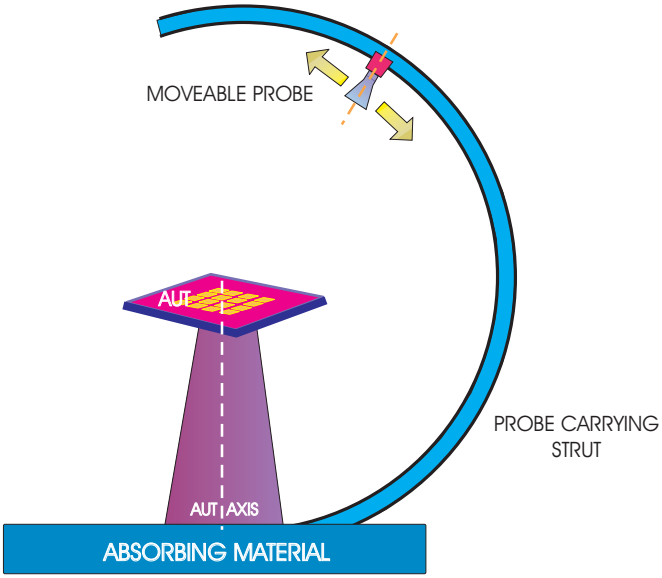

system with a hemispherical strut for probe movement

Fig. 5.1. Two most common scanning systems used in the spherical method.

well suited for applications in the tests of surveillance radar antennas (Astrium Technical Information). Planar scanning suffers from the narrowest view angle allowing measurements of the main beam and the closest sidelobes. Of the major advantages, the modest room requirements of the planar system and efficient data processing

methods are the most frequently quoted assets. With the plane-polar scanning system it is possible to obtain scanning areas larger than that of the anechoic chamber floor or a wall behind the scanner. Even though the view angle of the probe can reach ±70°, the accuracy of measurements is restricted by the non-ideal radiation pattern of the probe (beamwidth and slopes of the beam). It should not be missed by the investigator that for the far-off broadside angles, the probe correction may suffer from excessive inaccuracies.

Table 5.1. Major characteristics of five principal scanning methods.

Scanning	**Azimuth range**	**Elevation range**	**Space required**	**AUT positioning**
Spherical	360°	180°	large	rotation around two axes
Cylindrical	360°	±40°	large	fixed, or AUT revolves around one axis
Planar Cartesian	≤ ±40°	≤ ±40°	medium	fixed
Planar polar	≤ ±50°	≤ ±50°	small	rotation around one axis
Planar bi-polar	≤ ±60°	≤ ±60°	small	rotation around one axis

Presently, time issues do not raise serious concerns in processing measured near-field data. Standard processing of a single data file takes up to ten minutes with contemporary computers. Thus, the computation time is not likely to be a drawback even if many files have to be processed (but it was a problem in the 1970s). A factor which gains importance is the time needed for scanning, when multiple beam or multiple frequency data must be recorded. Of particular desire is the shortening of the measuring time for multifrequency data acquisition within one scanning cycle. The time of sample taking by the microwave receiver is an important limitation to data acquisition speed. There are no more than a dozen frequencies that usually raise the interest of antenna investigators (in RCS hundreds of frequencies are of interest). It is not often feasible to run multiple measurements for various beam positions during one scanning cycle because of the transition processes in the circuits of the BFN. That is why more attention should be given to faster scanning methods. In the majority of contemporary facilities with a single-frequency mode, data acquisition takes three to sixteen hours (so scanning in the single-frequency mode of a twelve-beam antenna at eight frequencies would take about a month of uninterrupted measurements).

Bi-polar scanning has a reputation of being suitable for a broad range of applications. Research on the bi-polar method dates back to the mid eighties. At that time, the Radio Physics Research Institute in Nizhny Novgorod received an inquiry regarding radiation pattern measurements for a reflector antenna with a diameter close to 40 meters. The application of this antenna was in radioastronomy and the antenna could be

measured on-site only (Belov et al. 1987). Such radioastronomical antennas can be partially measured using space radiation sources. In that case, the point was to measure the pattern with an earth based system in a broad angle. The adoption of the near-field technique was an obvious choice, but an acceptable scanning method and relevant far-field transform algorithm as well as software were lacking. In order to perform scanning, the scientists working under Dr. Yurii Belov proposed the use of a large construction crane. In such a way, they invented a new scanning method which soon gained a lot of interest. Presently, the method is referred to as the bi-polar one (Williams, Rahmat-Samii 1991; Rahmat-Samii et al. 1992). A specific feature of the method is the exclusive use of rotational movement during data acquisition. Owing to the use of the construction crane, the scientist could provide a large scanning aperture. As the AUT was pointed zenithally, the interferences propagating along the ground surface could have been mitigated (the space radiation floor was much below the test signal level). Unfortunately, the system of Nizhny Novgorod has never become fully operational. So far, three laboratories making use of the bi-polar concept have been developed worldwide:

- Radio Physics Research Institute, Nizhny Novgorod, 1986 (Dr. Yurii Belov and his team),
- University of California in Los Angeles, 1991 (Prof. Yahija Rahmat Samii and his students),
- Wrocław University of Technology, 1996 (Dr. Paweł Kabacik and his team).

In in-door application, the bi-polar method was first used at the University of California in Los Angeles (their scanner has an arm about 1.6 meter long). The UCLA research team developed the system up to its full operational capabilities within a few years. They adopted three different methods for the computation of the far field results (Williams et al. 1994b; Yaccarino et al. 1994). In Europe, the bi-polar method attracted the interest of several institutions. The research team headed by Dr. Paweł Kabacik developed a fully operational bi-polar system at the Institute of Telecommunications and Acoustics, Wrocław University of Technology (Kabacik 1992b). The scanner and all the software were developed in-house. Outstanding results in the interpolation theory have been achieved by Prof. Bucci's team of the University of Naples (Bucci et al. 1991). Their Optimal Sampling and Interpolation (OSI) algorithms derived for non-uniform sampled electromagnetic field can be used in many disciplines of applied electromagnetics (Bucci, D'Elia 1994b). The Katholike University of Leuven, Belgium also undertook research supported by the European Space Agency on the interpolation algorithms for applications in near-field laboratories in the 1980s.

5.2. Other major types of near-field electromagnetic measurements

In contemporary engineering, near-field measurements are applied to a broader group of problems than antennas only. Near-field electromagnetic measurements are used to determine radiation intensity in terms of both power density and field strength. The results are used to set warning signs or establish restricted zones in the proximity of the radiation sources. Other applications are in occupational medicine. Sooner or later such measuring procedures take the form of recognized standards. It goes without saying that when a parameter becomes a regulatory issue, its status receives closer attention amongst manufacturers and users.

Of the major electromagnetic measurements in the near field, worthy mentioning are those of the electric or magnetic field components in the vicinity of transmitting antennas or high power devices (Trzaska 2001). The engineering staff often wears miniature slim detectors as preventive measures signaling when the radiation level exceeds the safety or warning limits, but from time to time thorough measurements are carried out in order to verify whether or not the safety standards are met. In the course of such experiments, the specific electromagnetic field component is measured at discrete points. Measurements are performed for selected frequencies, which may be spread over a wide range. The method provides direct results which may require adjustment by a calibration procedure. Fundamental technical problems are linked to the probes. In order to avoid weighting of the results obtained with the waves propagating from different directions, the probe should have an omnidirectional pattern (Babij, Bassen 1986). After this issue has been overcome, there may still be some ambiguity due to the polarization issues. Troublesome is the definition of the polarization vector, which might have been differently defined off the main cut-planes. Last but not least, the correctness of the measuring procedures requires reference electromagnetic sources, which must generate precisely known radiation.

In the 1990s, the widespread use of cellular phones directed public attention towards human exposure to handset radiation. This gave rise to another category of near-field electromagnetic measurements. The fear of undesired side-effects from mobile phones inspired many investigations. Thus, the energy absorbed by human tissues, expressed as the Specific Absorption Rate (SAR), became a commonly accepted measure of exposure. The SAR values can be computed with the FDTD method, using an anatomically realistic model of the head, hand or neck, or a more elaborated human body model (1 mm resolution of tissue). The sophistication of numerical analysis can go so far that even tissue cooling caused by heat transfer due to blood circulation can be included (so the calculated rise in temperature induced by electromagnetic energy absorption is not overestimated in a pessimistic way). It must, however, be emphasized that while FDTD human tissue models need not be modified,

antenna and terminal models have to be customized for each simulation run. In order to validate the simulated results and verify the compliance of the terminal with the permissible upper limits of the SAR, the handsets undergo tests. The electrical components of the field are measured in the nodes of the dense 3D rectangular grid. The test volume is inside the human phantom filled uniformly with a special fluid (reproducing average electrical properties of the human body). The probe can be placed at an arbitrary spot inside the phantom. The duration of data acquisition usually varies from 4 to 12 hours, preceded by a calibration procedure. Thereafter the results are averaged and the SAR distribution is determined. With that technique the probes, the composition of the fluid and calibration are critical technical issues.

The interactions due to the proximity of the human body influence the shapes of the radiation patterns of the terminal antenna. It is advisable that the results be investigated in the 3D format. Fast 3D measurements of the terminal radiation pattern require systems using several dozens of probes (fifty or so) (Iverson et al. 2000). The probes are mounted on a semi-circular or a circular low-profile strut, and the whole strut revolves stepwisely around the measured object. Owing to the use of a sequential $1:N$ switch between the probes, the measuring time is short. These data may then be transferred to the far field. The wide bandwidth of the probes is of prime importance. A good example of other electromagnetic scanning systems developed for engineering purposes in the 1990s is the inspection of integrated circuits and printed boards.

5.3. Advantages of the bi-polar scanning method

The primary advantages of the bi-polar method are the integrity and the small space requirements of the scanner owing to the exclusive use of the rotational movement (Fig. 5.2). The AUT is placed on the turntable, and the probe is mounted at the end of the revolving back and forth arm. Thus, the microwave signals are transmitted over rotary junctions (revolving axes are more convenient than translation axes for microwave signal transmission). The varying layout of cables – unavoidable in the course of translation – affects the inserted phase shift in the signals transmitted through the cables. The integrity of the scanner construction backs up the reduction of the reflected wave level on the test site. The apertures of the measured antenna and the scanning area must be parallel. These planar apertures can be oriented horizontally or vertically. However, the horizontal arrangement is preferred as the weights of the revolving elements are then well balanced (so small motors are sufficient). Since the anechoic chamber floors are usually larger than their walls, the scanning area arranged horizontally can be possibly the largest available in the given chamber. One or two telescopic columns (pedestals) allow the adjustment of the spacing between the antenna and the scanning apertures over a wide range of values. The height of the telescopic columns is adjusted prior to measurements.

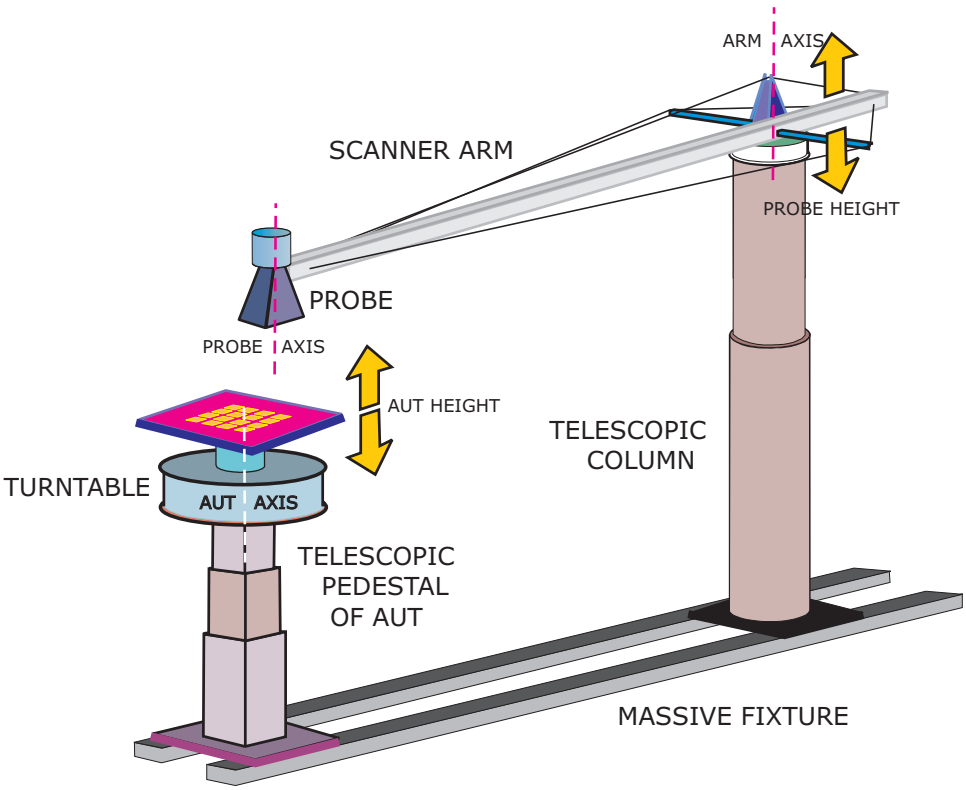

Fig. 5.2. Kinematic system of the bi-polar scanner.

Other advantages of the bi-polar method which are worth mentioning:

(i) the scanning aperture area of polar systems is larger than the area in the rectangular planar system involving a scanner of the same outline dimensions, so the valid angle of the results is comparatively wide, limited by the beamwidth not by the view angle of the probe (in normal case up to ±60°),

(ii) the scanning aperture area might be larger than the area of the anechoic chamber floor (increase up to 160%),

(iii) the scanner can be quickly dismantled and removed from the test site; in this way the anechoic chamber can be used for far-field measurements or other measuring set-ups can be installed,

(iv) owing to the zenithal pointing of radiation, the outdoor use of the method makes it possible to reduce the adverse effect of reflected waves,

(v) it is possible to develop a portable scanner allowing short deployment time,

(vi) the antenna maintains its position with respect to the direction of gravity force; a horizontal AUT position is preferred in laboratory models often involving simplified or ‘ad hoc’ structural support.

To establish a more balanced insight into the capabilities of the bi-polar method, a list of some major drawbacks inherent in this technique should be mentioned. The uncontrolled *z*-axis movement of the probe with respect to the antenna plane corrupts considerably the accuracy of phase measurements which are essential. The parallelism of the electrical axis is more difficult to maintain in a probe revolving system than in a translation system of probe movement (*e.g.* planar rectangular). A convenient method of far-field transform makes use of interpolation and FFT computation. However, the FFT data must be in a Cartesian (square area), not in a polar format (circular area). Two approaches are available to overcome this inconsistency – the square must be smaller and encompassed by a circle, or the circle must fit into a larger square. When Cartesian data must fill the square encompassed by a larger circle, the result is that no more than 64% of the circular scanning area can be effectively used for far--field computation. The remaining portion of the scanned surface with data is truncated. The measured data can be processed without any truncation, if the circular scanning area is entirely kept inside a square filled with the FFT input data. In that case, the pads outside measured data are filled with zeros.

5.4. Conventional bi-polar grid

With any planar scanning system it is possible to acquire the field sample at any point within the operational range of the scanner. Thus, the scanning grids take various forms which may considerably differ from the most common shapes. But the acquisition of data on an odd grid of the sampling points is not a constructive approach. It is known that the procedures of a transform to the far field can be applied to samples arranged only on few grid formats. Furthermore, the sampling grids should explore natural features of the scanning systems and provide results in a possibly short time. Worthy recommendation are those grids where the scanner determines the sampling point coordinates with small errors, of a systematic nature rather than of a random one. In order to reduce adverse effect of probe positioning, averaging of samples acquired in two-way probe movement over the same arc may be considered in the bi-polar method. Mixing without averaging the data acquired for different directions of the probe movement is not recommended and in such a case significant errors corrupt details of radiation patterns.

The shortest scanning times with the bi-polar scanner can be achieved when the samples are acquired during periodic revolution of either the AUT or the arm. Then, the other axis revolves stepwisely (small increments) in the course of the scanning process until the circular area is completely measured. The conventional bi-polar grid is shown in Figure 5.3. The sampling points are placed on the intersections of the arcs and concentric circles. In the most common scanning procedure, the probe mounted at

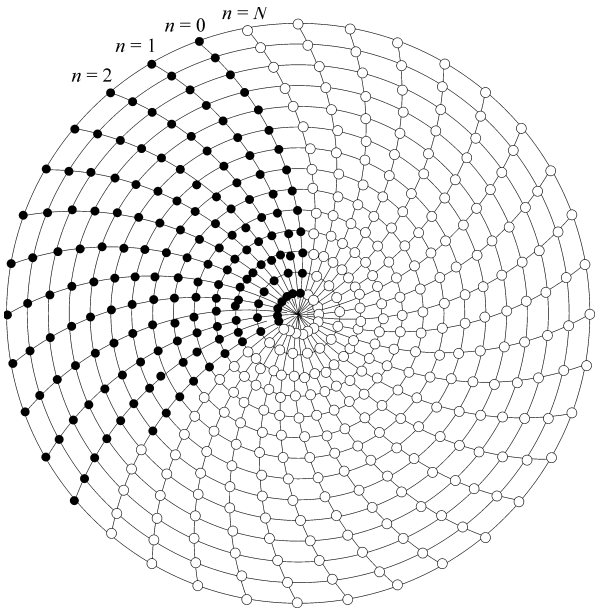

Fig. 5.3. Conventional bi-polar sampling grid where samples are acquired during successive revolvings of the arm (arm continuous tilt over AUT revolution).

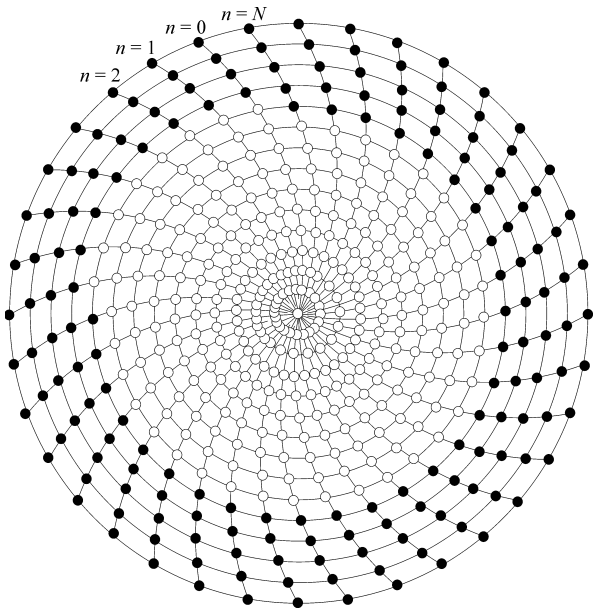

Fig. 5.4. Sampling grid where data are acquired in the course of multiple full-angle return revolution of the AUT while the arm is stepwisely tilted out the center to the outskirt of the scanning area only once (AUT revolution over arm tilt).

the arm end travels above the AUT following the arc trajectory, while the AUT revolves stepwisely by small angular increments (during each pause in the AUT revolution, the samples are recorded along one arc). In order to save time, samples must be taken when the probe *fly by* through sampling point. The other approach (Figure 5.4) in which the AUT revolves while the arm is tilted to the outermost circle by a small angular increment (during each pause in the probe movement, the AUT revolves by a full angle and sample are recorded at the grid nodes).

The return travel time of the arc (a forth and back tilt which ends at the point of origin) usually falls between 20 and 40 seconds (normally a tilt angle ranges from 20° to 60°), while a single full angle return revolution of the AUT takes 100 to 200 seconds. The number of arcs (ranging usually between 150 and 600) is considerably larger than the number of concentric rings (generally from 30 to 80) in a normal sampling grid. It is therefore hard to decide which of the two scanning methods should be recommended. When data are recorded during probe traveling, the synchronization of sample taking moments becomes critical.

In a conventional bi-polar grid all arcs meet at the central point of the grid. That is why the closer to the grid center, the larger the density of the sampling points. As it can be inferred from the data in Table 5.2, sample density variations on the grid are large. From the theoretical point of view, the minimum allowable density of points equals 4 samples/λ^2 on a Cartesian grid. In such a case, all the points must be uniformly distributed on a rectangular grid (the sample density is further increased due to oversampling, the ratio of which normally varies between 1.1 and 1.3). Any grid of a polar form with a constant number of points at each concentric ring shows a large redundancy. Our approach to overcome this drawback is described in Section 6.5.

Table 5.2. Density of samples for various distances with respect to the center point of the grid when a permissible spacing is the half-wavelength.

Diameter of the sampling grid [λ]	**Distance with respect to the grid center [λ]**	**Parameters of the sampling grid**		
		local density of points [samples/λ²]	**radial spacing between points [λ]**	**normal spacing between points [λ]**
40	1	98	0.0225	0.45
	10	10	0.225	0.45
	20	5	0.45	0.45
120	1	296	0.0075	0.45
	20	15	0.15	0.45
	40	7	0.3	0.45
	60	5	0.45	0.45

Duration of measurements with the bi-polar scanner

A typical diameter of the bi-polar scanning aperture ranges from 20 to 100 wavelengths. The actual diameter depends on the valid angle and on the spacing between the probe and the AUT planes. The duration of data acquisition is primarily influenced by

(i) the rotational speed of the arm,

(ii) the diameter of the scanning aperture,

(iii) the angular margins needed to accelerate and stop the arm.

On the basis of our experience, it is justified to say that the angular speed of the 1.5 to 3 m long arm securing a smooth traveling of the probe is not greater than 6º/sec. The choice of the angular speed and angular margins is a trade-off between several factors. In order to establish favorable conditions for accurate phase measurements, it is of prime importance to maintain a planar trajectory of the probe. Another important issue is sample recording and averaging in the microwave receiver. The knowledge of how the instant values are incorporated into the formulas for the averaged values at the microwave receiver becomes essential when setting the speed of the probe.

Accurate measurements can be performed only when the recording system avoids mixing the data acquired for different directions of the probe movement. When the electromagnetic field is sampled during two-way movement, the recorded values become alternately smaller and greater every second arc. This is due to the small displacement of the sample taking spot, irrespective of the accuracy of synchronization (the effect is the most distinct on the lobe slopes). In order to eliminate this systematic error, it is advisable to acquire data only during the outward or inward movement of the probe, or to average both values. As a result of one-way sample acquisition, the measuring system must remain idle during half of the sampling time. Reliable numerical smoothing of the recorded values, which allows the idle time to be avoided, requires thorough studies.

The data listed in Table 5.3 give the idea of the measurement duration in our facility. When orthogonal field components are to be recorded with a single-polarized probe, the values in Table 5.3 must be multiplied by two.

Table 5.3. Measuring time for data acquisition at the Bi-polar Laboratory, Wrocław University of Technology (valid angle up to ±50º; conventional bi-polar grid).

Diameter of scanning aperture [cm]	**Number of arcs**	**Measuring time for one arc [sec]**	**Overall measuring time**
146	428	38	4h 37 min
151	395	39	4h 17 min
271	700	47	9h 08 min
258	336	47	4h 25 min
128	165	38	3h 26 min
205	443	43	5h 19 min
384	900	57	14h 15 min

5.5. Bi-polar near-field systems: basic technical considerations

Of the various technical issues involved, three are of fundamental importance – the allowable ranges of antenna parameters, the limits of the frequency range and the valid angle of far-field results.

Allowable ranges of antenna parameters

The allowable ranges of the antenna parameters not only influence the choice of the scanning method but also determine the mechanical specifications for the scanning system. Before the design process starts, the values of the following antenna parameters should be specified:

(i) the minimum radius of the sphere encompassing the aperture of the AUT,
(ii) the smallest rectangular box where the tested antenna can be packed,
(iii) the maximum weight of the antenna,
(iv) the frequency range, and
(v) the permissible angular range for the antenna beam pointing.

The bottom level of the sidelobes and the null depth are also important.

Limits of frequency range

The 2 to 20 GHz frequency range needed by most of the near-field laboratories is covered by the majority of the marketed microwave equipment. It is worthwhile to consider the potential extension of this standard frequency range. Below 2 GHz, a wavelength is longer than 150 mm, and the minimum reasonable size of the scanning area exceeds 5 meters. The measurements of antennas operating between 800 and 2000 MHz are nowadays needed due to the continuing developments in mobile communication and radar. Below 800 MHz, the use of near-field laboratories is rarely advised. What can not be missed is the fact that at these low frequencies the antenna properties are remarkably influenced by the site of installation, by the properties of the soil, by the vehicle and other nearby antennas. Another shortcoming is the need for large and expensive absorbers in the anechoic chambers operating below 1 GHz.

The upper frequency limits in near-field systems can be ascribed to the short wavelength (above 20 GHz it becomes shorter than 15 mm), so the sample spacing is small and the phase measurements suffer from poorer accuracy. What is more, the recorded phase values are significantly corrupted by positioning errors, to say nothing of the equipment accuracy. Around 40 GHz, many absorbers loose their properties and cease to work as absorbing materials. At such high frequencies antenna research is focused

primarily on impedance characteristics and power efficiency, less consideration being given to the sidelobes in the radiation pattern (rare utilization of these frequencies and large propagation losses lead to weak interferences). At millimeter waves a compact and far-field technique are preferred methods of radiation pattern measurements.

Valid angle of the far-field results

From the mathematical point of view, computed far field data are organized in a matrix form. However, each element of the matrix must be assigned to the spherical coordinates prior to the presentation of the results. After such assignment, it is necessary to sort out the spatial angle within which the far field data can be regarded as accurate; this angle is referred to as a 'valid angle'. Owing to the truncation effects that occur close to the edges of the scanning area, the valid angle is narrower than the maximum view angle of the probe. Only spherical scanning can provide a valid angle which equals the full spherical angle and does not raise ambiguity as to how the far field results should be assigned to the spherical coordinates. The most common way of estimating the valid angle in planar scanning systems is depicted in Figure 5.5. This simple method proves in practice and shows a good accuracy, but the results close to the valid angle limit must be carefully treated. An additional validation in the limit area should be advised. Some of the validation methods rely on the comparison of the

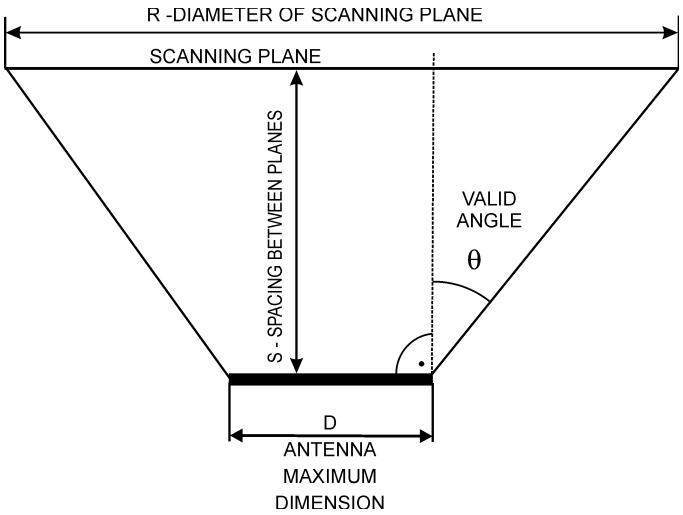

$$\theta_{\max} \approx \operatorname{arctg}\frac{R-D}{2\cdot S}$$

Fig. 5.5. The most common method of predicting the range of the valid angle in the near-field planar scanning system.

results obtained for different AUT-probe spacing. Usually inter-facility comparisons provide plenty of inspiring conclusions but involve many logistic issues due to the need of transporting the reference antenna. However, coupling between the AUT and the measuring system is different in each facility.

5.6. Scanner for the bi-polar system

Engineering recommendations for the bi-polar scanner

For the sake of maintaining an unchanged distribution of the waves propagating inside the anechoic chamber, we must try to avoid considerable displacements of the AUT in the course of measurements. In order to maintain the quality of the quiet zone, the probe, not the antenna, must travel during near-field scanning. Only in spherical scanning it is possible to keep both the probe and the AUT on the same spot during the scanning process. In the majority of techniques, the AUT pointing varies due to revolving around one or two axes.

In the bi-polar scanner, the probe and the revolving mechanism are mounted at one end of the arm (Fig. 5.6). The arm is mounted on the turntable, which is placed atop a supporting column. The rotational axes can be made of highly accurate robotic modules or elements of precise mechanic. The use of such somewhere-else developed components keeps the scanner costs at a moderate level. The experience gained so far shows that the development of a stable arm requires the application of advanced composites or some engineering methods. A common method of determining the coordinates makes use of angle measurements at two major scanner axes. That is why any deformation of the arm directly affects the accuracy of the sampling grid. More expensive methods of probe location must rely on linear measurements between the probe and the well-developed reference points. In this context, the laser interferometer has one impairment: the optical ray must be reflected back to the light source aperture. Only if the mirror moves along a straight line, the issue is not troublesome. However, if the probe travels along an arc, the specific pointing of reflection is hard to achieve. It is of paramount importance that the plane in which the probe travels be parallel with respect to the plane of the AUT aperture. Special attention should be given to dynamic phenomenons such as oscillations and yawing of the probe.

In the course of our research on array diagnostics we came to the conclusion that a scanner with two telescopic columns would be best suited for our needs. One of the columns would be a pedestal for the AUT, and the other one would support the probe-carrying scanner arm. Owing to such scanner kinematics, we achieved a valuable flexibility in the adjustment of the AUT-probe spacing with no further constraints on the height of the AUT location. The spacing between the sampling points usually

ranges from 10 to 100 mm (1.5 to 15 GHz). In our laboratory the probe travel speed must be set to values which enable recording no less than five samples (two complex components) at X-band frequencies. Thus, the corresponding translation speed of the probe generally does not exceed 80 mm/s.

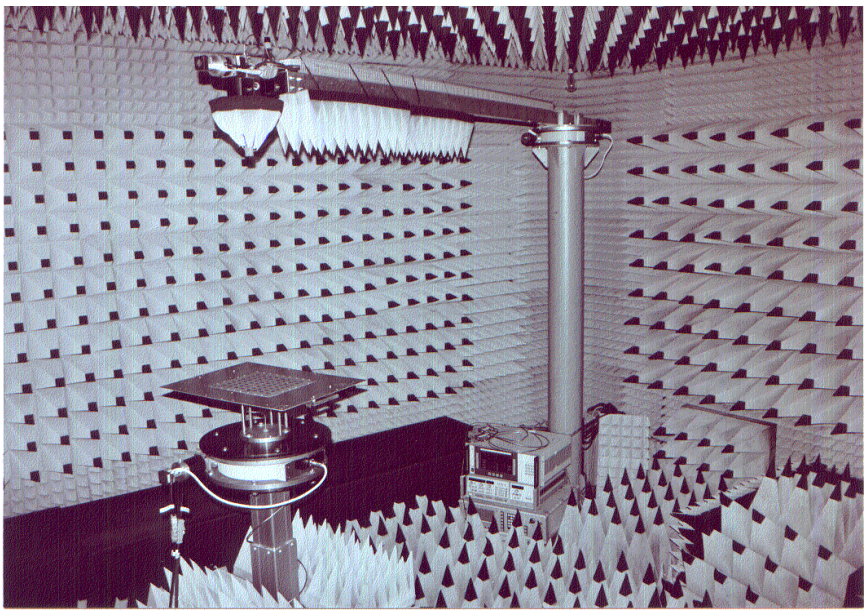

Fig. 5.6. Photograph of the 2.7 meter high and 3.3 meter long bi-polar scanner developed under the research presented in this monograph.

Critical technical issues related to the bi-polar scanner

According to our experience, the following technical problems must be regarded as critical when developing a high-quality bi-polar scanner:

- achievement of a planar trajectory of the probe, without yawing or horizontal oscillations,
- precise counter-rotation of the probe needed to maintain the same electrical axis orientation of the probe and the AUT,
- accurate determination of instantaneous probe coordinates in the course of scanning,
- low RCS and marginal influence on the electromagnetic coupling to the AUT,
- negligibly short delays of synchronization pulses generated by the scanner control unit.

A planar probe trajectory is a prerequisite to accomplish accurate phase measurements. One of two most dominant phase error sources are deviations of the probe movement observed along the *z*-axis. At 10 GHz, a 3 mm offset from the ideal probe

trajectory can produce phase errors up to 40°. When the arm is longer than 2 meters, special engineering efforts must be made to keep the probe on its track. The firm – but massive – arm can be accelerated up to slow speed only within an angular range typical in this scanning method, even though a high power motor is used. In consequence, the measuring time becomes extended by at least 60% compared to that of a low-weight arm traveling at a speed of 4 to 6 °/sec. Composite materials are recommended for arm development. Low-weight arms are generally stabilized with a proper profile of the arm or with guys or other dielectric ropes (inside or outside the arm). In our research, it was only the third design of the arm that met our basic expectations. The generic concept of the light (but strengthened) arm is shown in Figure 5.7. The total weight of the arm is kept low and there is no counterweight due to the use of a high-torque turntable. Another concept utilizes lightweight composite materials and generally calls for greater costs.

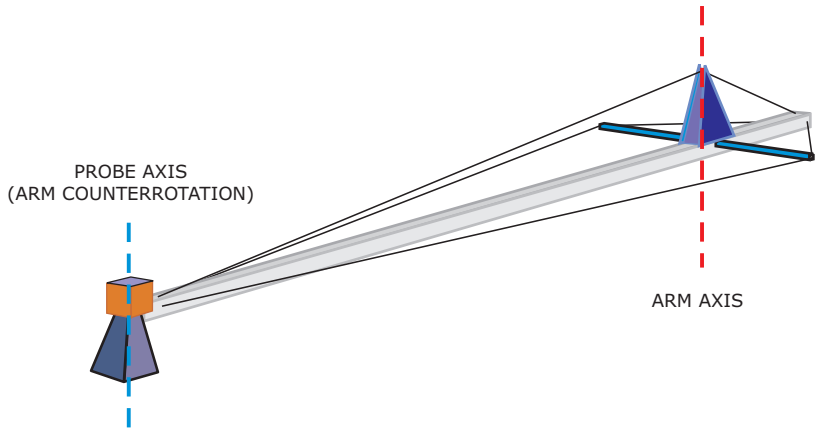

Fig. 5.7. Stabilization of the probe mounted at the end of the low-weight and flexible arm supported with three ropes (guys).

A tough accuracy of the probe counter-rotation is a must as otherwise uncontrolled leakage of signals between the orthogonal components of the electrical field will make the recorded data useless. If in the course of measurements the electrical axes of the probe do not follow the instantaneous electrical axes of the AUT, the orthogonally polarized field components corrupt each other. The tests of antennas with high purity polarization (high ratio of co-polar to cross-polar components at the principal axes) suffer particularly from the angular misalignment in the counter-rotation of the probe (even errors smaller than 0.1° result in a strong corruption of weak cross-polar field components). For some types of dual-polarized probes, there are quite accurate formulas of the radiation pattern. These expressions can be used in the numerical procedures of probe counter-rotation. However, the theoretical ‘rotation’ calls for main-

taining an accurate angular position of the probe with respect to the AUT. Otherwise, the procedure does not eliminate the inaccuracies normally encountered in mechanical counter-rotation.

In the bi-polar method, the AUT must be rotated by a 360° angle and, in consequence, at least the sidelobes (or even the main beam if tilted off the main geometrical axis) pass through the walls and ceilings of the anechoic chamber. When the wall incident waves are poorly absorbed, the spatial distribution of the radio waves varies, thus changing the conditions of the AUT measurements (the probe receives not only direct but also varying reflected and scattered signals). Furthermore, the intensity of the reflected signals depends on the polarization of the incident wave. The result of this undesired effect is depicted by the plots of Figure 5.8, which presents the excitation coefficient values of the first sample taken at all arcs. If the described effect were absent, the amplitude and phase would have constant values. It must be clarified that the presented variations are associated only with the angular position of the AUT and can not be attributed to the temperature drift of the equipment or the rotary junction properties.

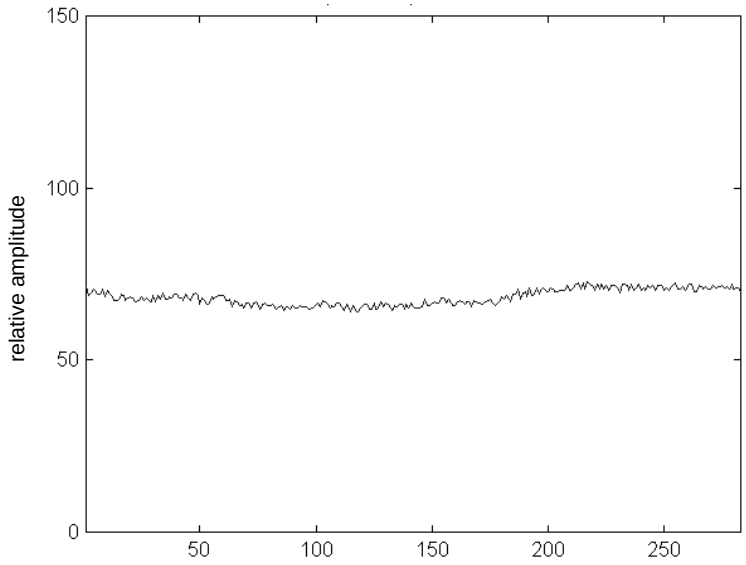

Fig. 5.8. Variation of amplitude arc number values for the first sample at all arcs recorded for the full revolution of the AUT (azimuth angle). The plot reveals 10% change of the amplitude value. At the same time, the phase values of these samples varied by up to ±6°.

The anechoic chamber at Wrocław University of Technology was constructed in 1993 with absorbers purchased in Belgium. The chamber has no air-condition since beginning of its operation. Uncontrolled air condition is a major shortcoming as local

climate features high humidity – many rains. Humidity is high as there are five major rivers and several canals in the city (the nearest two rivers pass barely 300 meters outside the building with the chamber). Thus, decay of absorbing properties progresses quite quick in absorbers, mostly due to the residual moisture kept inside cells of the foam materials. The reflectivity increases with frequency (the MC-8 phase array was measured at 5 GHz, while the other arrays were tested between 9 and 11.5 GHz). The properly maintained chamber should ensure reflectivity not worse than 40 dB at 5 GHz and 44 dB at 10 GHz (for 3 meter transmission length). Unfortunately, our anechoic chamber has much poorer reflectivity properties currently. Routine checks are not carried on, but last checks two years ago indicated, that reflectivity might have dropped below a critical level 20 dB in some spots (5 to 10 GHz).

Mechanical alignment

Prior to data recording, the geometry of the scanner must be checked and its elements must be correctly aligned with respect to the reference plane. This is a time consuming procedure which usually takes from two to five days. Once the AUT and the probe have been mounted their weight deforms the geometry of the scanner beyond the admissible tolerance. Thus, the mechanical alignment must compensate the major misalignments prior to the installation of the AUT and the probe; after the completion of the probe and AUT mounting, a fine tuning of the scanner geometry must be performed. Alignment is a customized procedure for each scanner type. While elaborating the mechanical alignment procedure for the bi-polar scanner, we should not miss that

- the revolving axes of the AUT, probe and arm must be parallel,
- the revolving axis of the AUT must be orthogonal to the scanning plane,
- deformations due to the weight of the probe and AUT must be compensated,
- the polarization planes of the AUT and the probe must be kept at the same angle,
- each actual turn of the AUT and the probe must equal 360°,
- the alignment procedure should not be wrapped into a plentiful iterations.

An efficient means of performing mechanical alignment is the use of optical instruments (narrow-beam light sources and mirrors). Optical elements are mounted to the adapters for the AUT or the probes. In order to detect the undesired drifts or misalignments of the microwave equipment, it is recommended that the last recorded arc repeats the first one (the same angular coordinate).

5.7. Microwave equipment

Signal source

The pictographic scheme of the basic microwave equipment needed in the antenna test near-field system is shown in Figure 5.9. There are two main devices – a signal source and a microwave receiver. An attenuator and a directional coupler are the main passive microwave accessories and they are used to properly feed the reference signal. A signal source generating up to +20 dBm output power is sufficient for the majority of measurements. If the measurements are performed at a single frequency (CW mode), remote control of the source is not required. The spectral purity and stability of the test signal is what primarily counts, regardless of how many frequencies are measured during one scan procedure. In some types of generators, small abrupt changes of frequency or amplitude which occur from time to time at the output signal impair a few hour lasting measurement (variation of frequency is usually associated with that of the amplitude). Occurrence of such microjumps is known in various types of generators – in a temperature-compensated crystal oscillator follows a cold soak (in order to notice microjumps, recording of an output signal over several hours is needed). Sweepers are particularly vulnerable to such undesired jumps. As a result, the recorded probe excitation coefficients remarkably change in-between two consecutive arcs or even samples. Examples of those highly undesired effects are illustrated by the plots in Figures 5.10 and 5.11. Both the plots are constructed by taking the first sample of each arc in the actual bi-polar data file. The noticeable discontinuities in the plots – even though they are small when expressed in decibels – makes utility of the recorded results questionable. Another possible source of these undesired abrupt changes is the impaired functioning of the microwave receiver.

Since the execution of multi-frequency measurements within one scanning procedure implies challenges to the microwave equipment, such mode is seldom used in near-field laboratories. In order to make the multi-frequency mode time-efficient, the signal source must be periodically tuned to the required measuring frequencies at the sampling points (usually no more than 25 frequencies). As the processing time at the receiver is relatively long, the initial phase value is of negligible importance. However, the microwave receiver requires a certain time to lock its Phase Lock Loop (*e.g.* 250 μs) in order to lock its circuits and measure amplitude/phase value. In the other periods between consecutive sampling points there is plenty of idle time in the normal single-frequency mode. Therefore when the microwave system is tuned in a cyclic mode, data on more frequencies can be recorded. Furthermore, if the offset in the coordinates of the sampling points in the grid is acceptable, the multi-frequency mode can be much easier to implement. Another form of multi-tone measurements is the time-domain method, attracting attention due to its wideband capabilities and

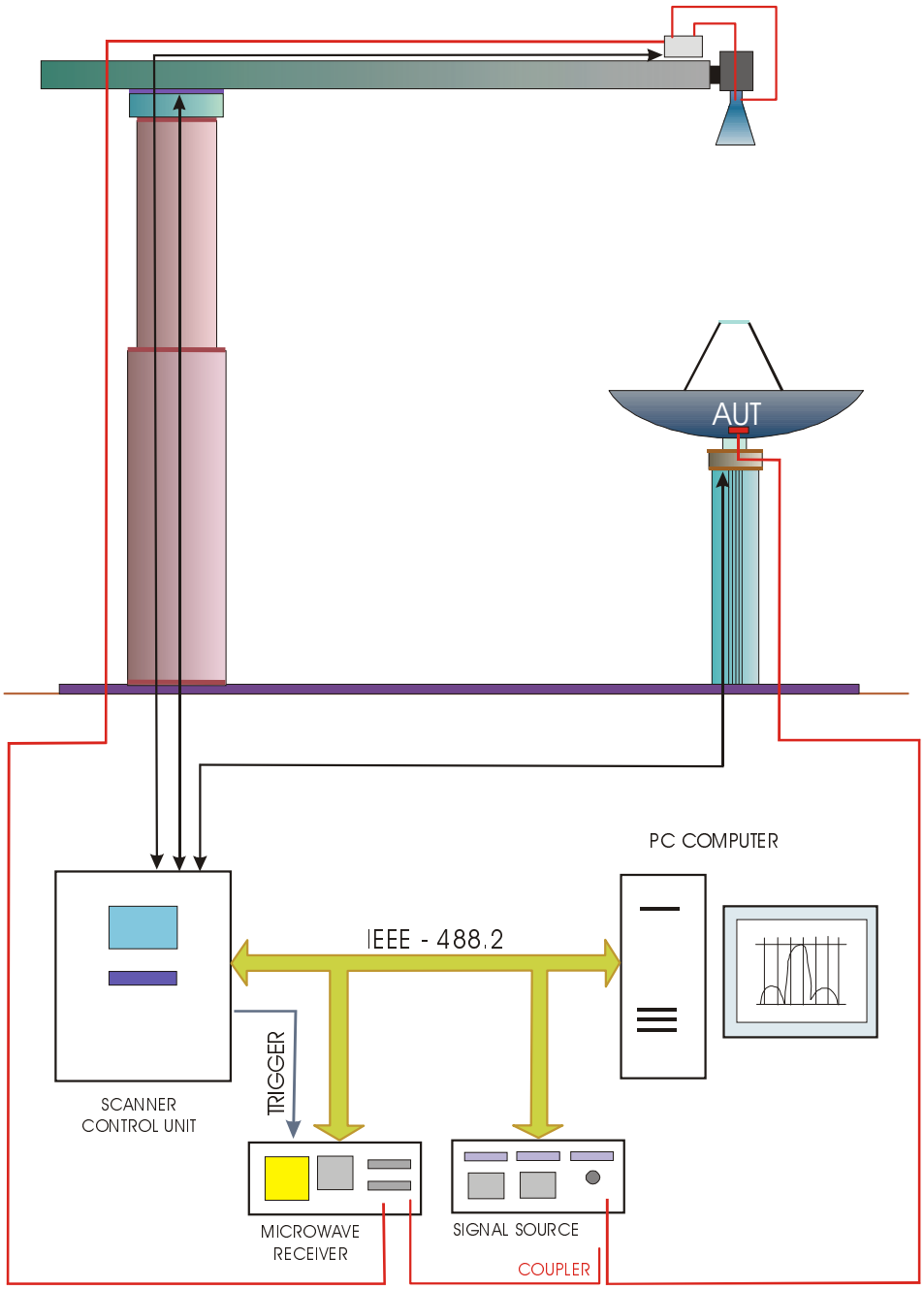

Fig. 5.9. Pictorial scheme of the microwave equipment and the data acquisition system used in a typical near-field laboratory.

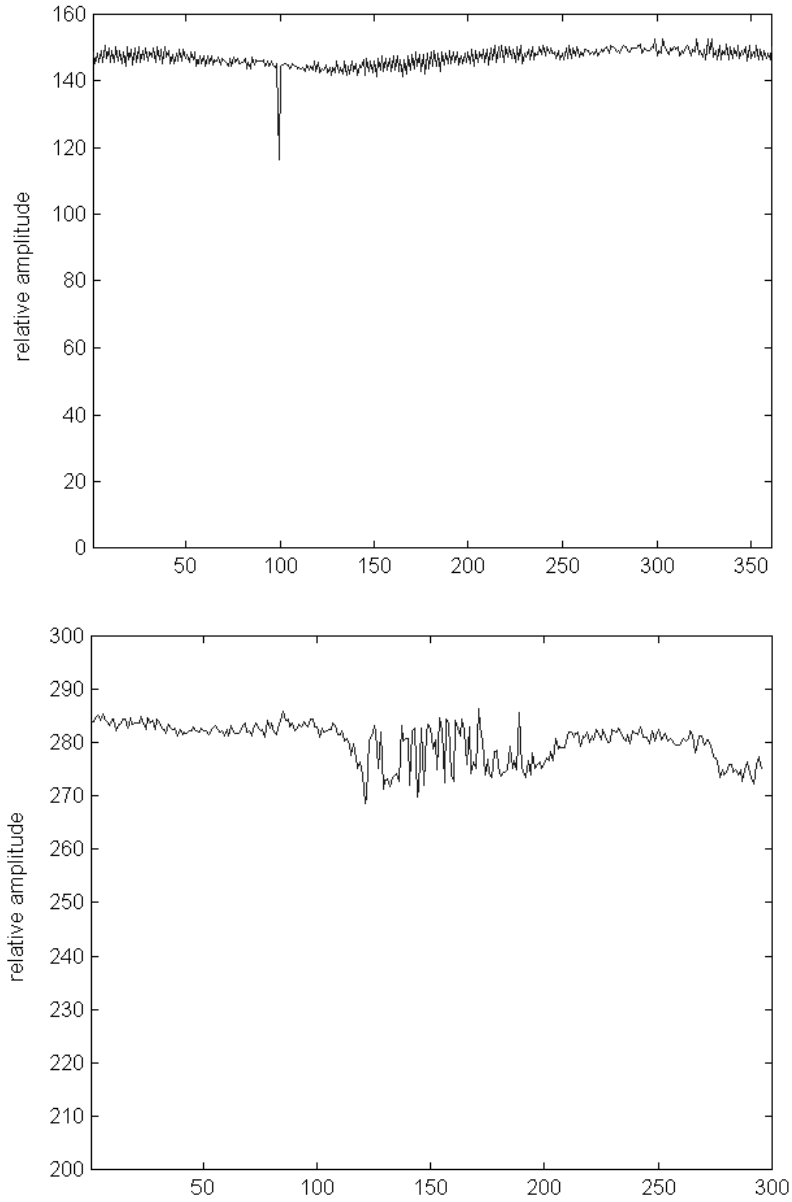

Fig. 5.10. Recorded amplitude taken for the first sample (located at the grid center) of 361 and 296 arcs of two different bi-polar grids.
The plots reveal effect of microjumps in the recorded values.

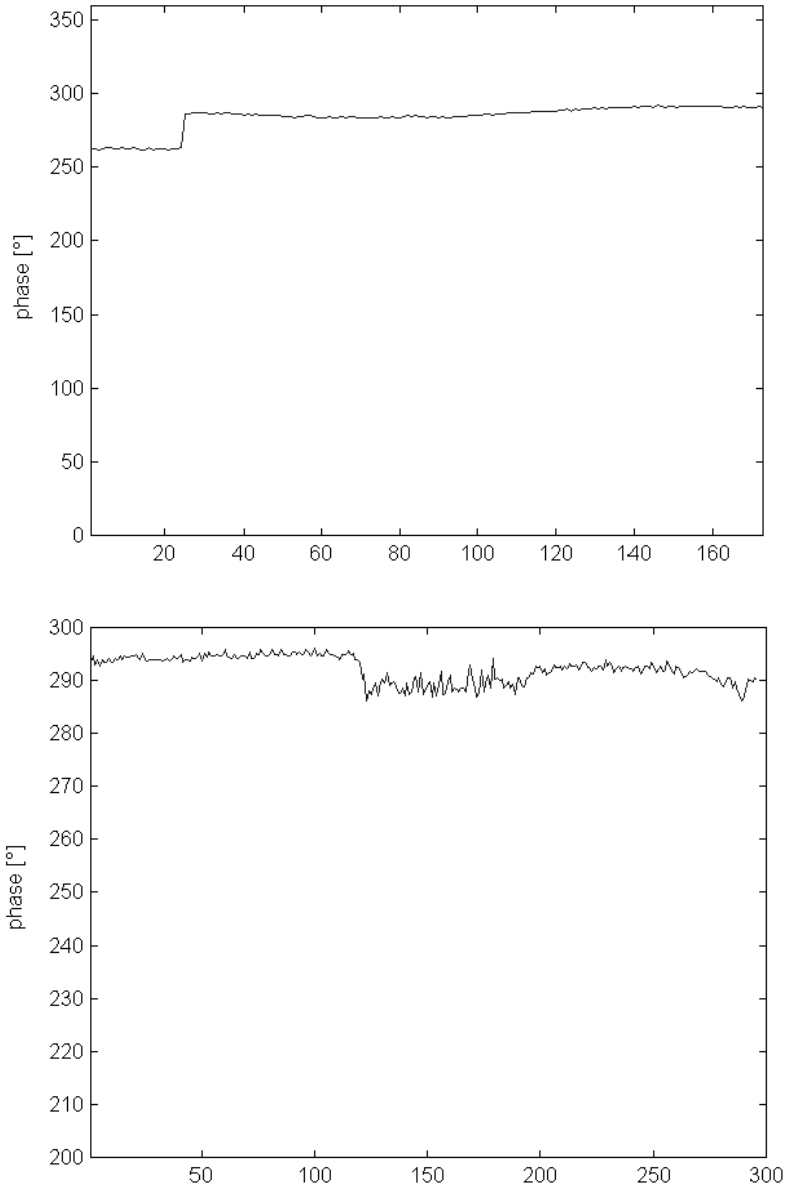

Fig. 5.11. Recorded phase taken for the first sample (located at the grid center) of 173 and 296 arcs of the different bi-polar grids.
Both plots reveal effect of microjumps.

improved immunity against the adverse effect of reflected signals (Hansen T. 1997). Measurements with multiple carrier signals generated at once are not considered very much yet. However, with the advent of broad uses of the OFDM systems, such a method may gain popularity.

In modern designs it might happen that an antenna includes a complete communication or radar signal source. In such circumstances, the final tests and diagnostics must utilize an internal signal source. On one hand, the quality of such signal sources is generally high but, on the other hand, the lack of a reference signal implies the use of statistical methods to verify the recorded near-field samples or picking up a signal radiated by the antenna (the designer of such antennas should remember that the spare output coupled to the internal source is of great help in antenna testing).

Microwave receiver

The microwave receiver measures the amplitude and phase values of the probe excitation coefficients, which are determined with respect to the reference signal. Usually the receiver has a few miniature frequency downconversion modules deployed outside the mainframe (MI-Tech web page; Agilent web page). It is well known that in the synthesis of the antenna radiation patterns the phase plays a more important role than does the amplitude. This means that phase variations influence the radiation pattern far more profoundly than the amplitude changes do. Thus it is not surprising that for the computation of the far-field results the recorded phase values must be of high accuracy (Janse van Rensburg, Hindman 2000).

To cope with the probe and reference signal measurements, the receiver must have at least two channels. Three channels are required to serve measurements involving a dual-polarized probe. The upgrade of the receiver to the three-channel standard and the probe to the dual-polarized standard raises the equipment costs by at least €50,000. As the microwave cables insert considerable losses at high microwave frequencies and in the millimeter range, the receivers are equipped with deployable mixers (downconverting units) operating remotely from their main unit. Mixers are placed closely to the probe and to the directional coupler which feeds the reference signal.

In the course of the author's near-field studies, use was made of the following three microwave receivers:

- Scientific Atlanta SA 1795 (presently MI Technologies),
- Agilent Technologies HP 8530 based on HP 8510,
- Orbit AL-8000-5 (its production has been discontinued) (Orbit 1998).

It is worthy to say that these models are amongst the most common in advanced antenna laboratories. Instead of the microwave receiver, a vector network analyzer can be considered for application (reduced cost solution and limited application range). However, in such a case frequency downconversion is generally impossible to perform

outside the mainframe. Thus, the losses of the test signals transmitted at the RF not at the IF frequency become the main impairment to the potential of the system. Other concerns are the details of the reference channel functioning (entirely inside the analyzer) and the way in which the CW mode is executed (vector analyzers are primarily for a sweep mode operation). As the microwave bridges (an integral part of the vector network analyzers) are costly and bulky, the utilization of the network analyzers in near-field systems adds further troubles.

Phase measurements of great accuracy are major problems at millimeter waves. A loss of accuracy is due not only to the capability of the microwave receiver but also to the errors in positioning of the probe. For these reasons, the development of phaseless measurements has been investigated for two decades. The retrieval of the phase values relies on amplitude measurements on two scanning planes, differently spaced from the AUT (Yaccarino, Rahmat-Samii 1999; Bucci et al. 1999).

Sample taking moment and its synchronization

As the probe travels in the course of measurements, the sample taking moment must be externally triggered. Furthermore, the trigger synchronization must not be affected to short delays occurring at the primary system interface – IEEE 488. Such delay spreads are due to the non-fixed bus access and processing time. In order to eliminate these error sources, the scanner control unit should be equipped with a module which traces the instantaneous coordinates of the probe and the AUT. The subsystem should operate in the background of the main processes and should trigger the receiver on time (for each of the predefined coordinates) even over a dedicated synchronization line (arranged outside the primary IEEE-488 control bus). Short advancements in triggering can be also adopted for the sake of better accuracy (such time advancement could approach 1 ms).

Averaging of measured data

For better accuracy, the communication and microwave test equipment commonly involves averaging. The averaging factor is set from 4 to 32 in the majority of instances. In near-field measurements, a basic impairment to averaging is the change of the probe excitation due to the probe movement above the radiation source. The largest changes of amplitude occur on the slopes of the main beam, around the nulls and on the slopes of high sidelobes. Fortunately, in the near-field region amplitude variations are much smaller than in the far field. Phase values undergo large changes in the sidelobe region (at least few times 360º over several first sidelobes) and only small ones in the space above the main beam (less than 90º). Unfortunately, the receivers

handle only one measured value (elementary sample) at a moment, so averaging must be extended in time needed to acquire several elementary samples (a receiver for the acquisition of many elementary samples in parallel is extremely difficult to construct even with complex calibration methods).

The modern vector network analyzers released by Agilent Technologies process one frequency point in 35 microseconds. Our AL-8000-5 receiver handles up to 1000 elementary samples a second (1 ms processing time for a sample). However, we discovered that when the averaging factor is greater than 16, it might happen that some values of the recorded elementary samples are wrapped up into calculation of two consecutive samples that are complete different in terms of their value. Figure 5.12 clarifies this drawback for three averaging factors. The lack of relevant documentation and the unwillingness of the manufacturer to clarify such technical parameter, did push us to study the problem in more detail on our own.

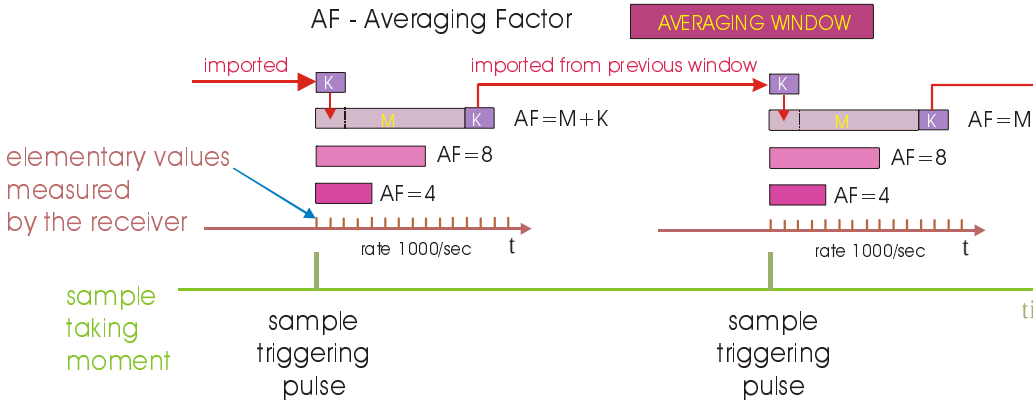

Fig. 5.12. Ambiguity of averaging for different averaging factors and sample windows (troubles with averaging factors greater than 8).

5.8. Probes of electromagnetic field

Primary probe parameters

The electromagnetic field radiated by the AUT is sampled with probes moving on the grid of the near-field scanning system. If the AUT is to operate in the receiving mode only, the probe must transmit a signal. The measured discrete values, referred to as probe excitation coefficients, are the product of the electrical field produced by the AUT (including the effect of undesired reflected waves) and the probe characteristics.

The voltage at the probe port must linearly depend on the strength of the illuminating electric field. This linearity must be provided over a moderate dynamic range of the electric field strength. As the probes are passive devices, the fulfillment of the linearity condition is not difficult to achieve, if the test signal is a carrier sinusoidal wave. The basic technical specification of the probe includes

- frequency range,
- width of the main beam,
- quality of signal discrimination outside the main beam,
- polarization purity and isolation between orthogonal ports,
- definition of polarization planes,
- weight and dimensions,
- mounting flange.

High-quality probes are expensive elements of the near-field measuring systems. The probes are of electrical type and have been designed to provide a linear relation between the incident electric field strength and the output signal of the probe. Measurements of only one field component are sufficient when the field scanning surface supports vector wave solution. Fortunately, planar surface is among six such surface shapes. As the electric field measurements are much more convenient than magnetic field measurements, the preferred choice in near-field laboratories are electric field probes. The sufficiency of measurements of only one electromagnetic field component is discussed in Section 6.3 (Far field determination with vector Kirchhof integrals).

The probe is to feed the input mixer of the receiver through a coaxial cable. The bandwidth covered by each probe is narrow – from 5 to 10%. The probes do not raise problems with the dynamic range. A highly desired dual-polarization operation are difficult to achieve. In the dual-polarized probes a tough tolerance of the phase balance between the orthogonal ports is critical.

In the near-field technique, there is no need to calibrate an absolute value of the signal at the probe output (this is another reason for denoting the sampled output signal as the probe excitation coefficient). Some mismatch between the probe and the free-space produces backward reflections of the waves inciding the probe. Because of the superposition of the back-reflected and direct waves, a standing wave is generated. As the distance between the probe and the AUT center varies in the course of scanning (*e.g.* a planar one), the sampled values are adversely influenced and their unwanted modulation follows the envelope of the generated standing wave.

View angle of the probe

The view angle at the outermost sampling points is larger than the valid angle of the far-field results. However, the view angle imposes requirements on the beamwidth of the probe. The choice of the allowable view angle depends on the AUT-probe spac-

ing and the size of the scanning aperture. These problems are more troublesome at lower than higher frequencies. Figure 5.13 illustrates the undesired effect which appears when the waves radiated by the AUT are not correctly measured by the probe due to the excessively large view angle. As a result weak, direct waves are corrupted by the reflected and scattered signals taking strong enough values.

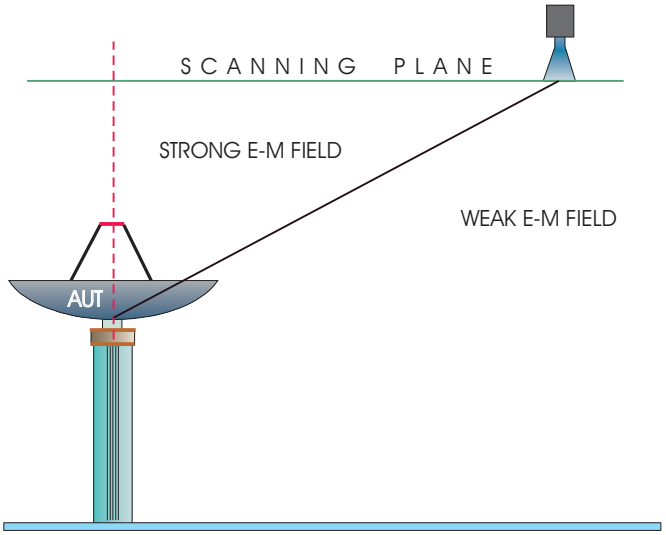

Fig. 5.13. Corrupting effect of a large view angle at which the probe overlooks the AUT.

The omnidirectional radiation pattern will equivalently sum up a direct wave and reflected waves – without any weighting. Needless to say that such a feature of the probe impairs accuracy of the measured values, which should include only the direct signal. It is a great advantage when the shape of the radiation pattern can significantly contribute to the suppression of all the incident signals other than the direct one. An ideal probe should have a directive main beam and sharp slopes at the beam as if it were a cut of a part of a sphere. The main beam of the probe should extend only over the required view angle. Owing to such a shape, the spatial filtering out of the interfering wave would be efficient. In real probes discriminating waves incident out of the main beam by at least a dozen dB is regarded as advantageous. When defining the technical specifications of the probe it is hard to overestimate the importance of the polarization properties. For the aforementioned two reasons, the monopole or wire probes have never found acceptance in near-field antenna measurements.

An ideal probe should have only a main beam focused within the specific view angle, but no sidelobes. Of the several major aperture antenna types featuring a directive main beam, horns and open-ended waveguides (low-cost option) have gained primary attention. When elaborating the technical specifications of the probe, the following issues deserve consideration:

(i) the AUT should always remain within a main beam in the course of the scanning procedure,
(ii) dominant reflected and scattered waves should be spatially filtered because of the low directivity of the probe (regardless of wave polarization),
(iii) it is necessary to achieve a high polarization purity, at least in the two principal cut-planes,
(iv) very low backward reflections of the incident waves should be provided.

Premium probes take the form of pyramidal horn antennas. The frequency range in which the probes are made varies from about 800 MHz to 40 GHz. But each probe cover no more than 10% bandwidth. Few firms specialized in probe manufacture have accurate CAD/CAM tools at their disposal (off shelf products are unavailable). It is worthy to say that these tools have been elaborated continually for three decades. It is therefore not surprising that the agreement between calculated and measured results is impressive. The most important probe manufacturers are MI Technologies (formerly Scientific Atlanta) (MI_Tech web page) and TICRA – Danish company founded in 1972 (Ticra web page).

Top quality probes are expensive and their cost ranges from € 45,000 to 95,000. A large portion of these costs is accounted for by the calibration procedure. Probes are calibrated by the manufacturer for the following parameters:

- amplitude and phase radiation patterns in two principal cut-planes for all ports,
- axial ratio at the main electrical axis, main beam slant angle and polarization properties for all ports,
- amplitude and phase balance between orthogonal ports,
- antenna gain.

Since some portions of the electromagnetic waves are reflected by the probe backward to the AUT, a standing wave is generated in the measuring zone. The standing wave can be easily observed when measuring the probe excitation values for different distances between the probe and the AUT. In the planar scanning, the effect must be suppressed as much as possible, as the distance between the probe and AUT varies, so measured values must be modulated by the standing wave phenomenon.

Open waveguide probes are low-cost items (price below € 1000). They feature a wide beam (±45°), but their polarization properties are moderate (particularly off the principal cut-planes). When needed, the range of the view angle is moderate or small, and the use of horn antennas manufactured as feeds for the reflectors can be considered. Their radiation patterns should be improved by corrugations (*corrugated feed horns*) and therefore the sidelobe level and spillover radiation should be suppressed. The cost of the feeds is only several times the cost of the open waveguides thus, it is still a low cost solution. Their use is limited due to narrow radiation patterns. Such corrugated horns are often designed for operation with two or more polarizations. However, they generally do not provide good phase and amplitude balance between their ports. Another serious disadvantage is the difference in the radiation pattern shape for different ports.

5.9. Automatic data acquisition and system operation

Since the number of measured data is overwhelming, the near-field laboratory must be entirely computerized. Before the advent of the powerful microprocessor technology, the computer techniques were the primary limitation to the development of near-field antenna test systems. Bi-polar data files usually comprise from 3000 to 50000 samples, each consisting of two or four numbers. It is widely agreed that the development of the software needed by data acquisition and data processing from scratches takes no less than 8 man-year. The major modules of the software are:

1. Control of measuring procedures
2. Interpolation, including normalization and merging of the measuring files, if necessary
3. Computation of the far-field transform
4. Correction procedures, such as that of probe or polarization correction
5. Visualization of far-field results, including assignment of spherical coordinates

Furthermore, for the purpose of antenna diagnostics it is necessary to develop additional specialized modules, *e.g.* for the computation of microwave holography.

For the sake of a well-organized file management, we introduced six primary categories of files denoted by the extensions (Kabacik et al. 2000e):

(i) measured data (*.msr),
(ii) normalized measured data (*.nrm),
(iii) interpolated measured data (*.int),
(iv) data transformed to the far field (*.far),
(v) far field data with inclusion of probe correction (*.fpr),
(vi) holographic imaging data (*.hgl).

All files have a rigorously defined format. The file headers contain about thirty lines of parameters, followed by data organized in lines. In order to simplify the file reading with a variety of programs the ASCII format is used, even though this format increases the size of the file. A typical size varies between 50kB and 400 kB, but some files with measured data are larger than 1 MB.

5.10. Our bi-polar scanning system

The bi-polar antenna test laboratory was designed and developed entirely in house, under three research projects with the author as the principal investigator (Kabacik 2003a). The scanning system operates in the anechoic chamber of the Institute of Telecommunications and Acoustics. Figure 5.6 presents the system and microwave equipment ready to operate (the computer is in a control room of the chamber). The scanner can be dismantled in two hours and installed in another chamber within two days (me-

chanical alignment may take three days). The dimensions of our 10-year old anechoic chamber are 5.25×5.25×2.70 m (width, length, height) measured between the tips of the absorbers. In order to reduce the costs of the anechoic chamber we used absorbers which differed in size. The anechoic chamber was analyzed with the optical ray tracing method, which revealed that the waves incident in the corner and edge areas are reflected twice before they reach the quiet zone. Thus, the absorbers in these areas can have poorer reflectivity. In engineering terms this means that they can be smaller (the largest absorbers are 66 cm and the smallest are 20 cm high). The chamber has been entirely shielded with a thick metal foil.

The fundamental technical parameters of our system are as follows:

- frequency range: 1–20 GHz,
- diameter of the scanning circle: 800 cm,
- diameter of the AUT: 280 cm (max),
- maximum AUT-probe spacing: 180 cm,
- allowable AUT weight: 160 kg,
- arm length: 270 cm,
- tolerance of the AUT position readout: +0.03°,
- tolerance of the arm position readout: ±0.005° (360000 quadrature pulses per each revolution).

All coordinates are calculated with the angular converters in our scanner. Since the arm length is 270 cm, the resolution of the angular converter connected to the arm must be small (the AUT angular converter does not require such resolution). The control unit of the scanner is centralized and the operation of the scanner is performed through the IEEE 488.2 control bus. (Currently a distributed control unit is being developed.) For triggering the receiver, a dedicated synchronization line is organized and the triggering pulses are generated by the scanner control unit. The computer which executes the measurements enables remote control of the AUT parameters. It can be helpful when phased arrays or other advanced antennas have to be measured. In our laboratory, we use the AL-8000-5 receiver and several signal sources (depending on the test frequency). The averaging factor is usually set to 4 or 8.

The subject of the bi-polar near-field measurements was treated in a generic way in the Ph.D. dissertation of Dr. Marek Barylak (2001) who wrote the Thesis on optimization of near-field scanning grids. Fifty pages of about total eighty, presents mainly information on near-field principles and discuss of sampling surfaces. Unfortunately this dissertation was not stored at the University library, thus the author had only limited opportunities to read it for some weeks in 2001. Dr. Barylak took a part in the work on mechanical alignment of our bi-polar scanner and contributed to the first control program executing measuring procedure (1996–1997). He left the Institute for good in summer 1998. In his Thesis he presented only one plot with a far-field radiation pattern. The plot was reprinted from the author paper which reported early results obtained with our bi-polar system (Kabacik 1997a). The above mentioned far-field

pattern was computed with the cubic spline interpolation method. As the third order spline functions display important shortcomings, the author ceased interest in their use in 1997. Therefore, the presented monograph has little common with Dr. Barylak Thesis – only a half page text on cubic spline interpolation covers a common technical point (part of section 6.2). All results showed in this monograph were computed with Optimal Sampling Interpolation. Furthermore, the scanning system consists of new major components and new control & data processing software presently (a new scanner arm, a new arm carrying column, a new 6.5 meter long scanner frame, a new probe rotator, a state-of-the-art real-time control computer and completely new software making use of new algorithms).

5.11. Examples of recorded data

All data presented in this Section were recorded with our measuring system. For the samples measured in the near field, the dynamic range of amplitude variations is much narrower than that observed in the far-field radiation patterns. Phase values undergo large changes in the sidelobe region, except the angular range of the main beam. The amplitude values recorded for the samples acquired along one arc are included in Figures 5.14 and 5.16 for the *EX* and *EY* field components. The frequency was 9.03 GHz. The phase values of these samples are shown in Figures 5.15 and 5.17. The microwave receivers return the phase value in the modulo 360° format, so the phase jumps in these plots are to be ascribed to the module format. Phase unwrapping (unfolding) can be performed if necessary.

The first samples in each arc are acquired for exactly the same position of the AUT with respect to the probe. The sample is located at the center of the grid and the polarization plane of the probe is parallel (for the *EX* components) or perpendicular (for the *EY* ones) to the polarization plane of the AUT. Thus, the values of the first arc sample should remain the same regardless of the arc number. The observation of the variations in the value at the first sample in each arc gives an insight into the drift of the microwave equipment or other similar disadvantageous phenomena (e.g. changes in the reflected wave distribution in the scanning zone). The data shown in Figures 5.18 and 5.19 are plotted with the value of the first sample (amplitude or phase) in the specific files of measured data (RMB-64 or TPA-256 antenna array).

The measured data acquired on the whole scanning grid are shown in Figures 5.20 and 5.21. The radiation source was a 256-element (16×16) TPA-256 array with a fixed beam (4.0° to 4.8° beamwidth depending on the cut plane). Visualization with the 3D format suits well the amplitude data, while the phase data images are hard to read (due to the modulo 360° standard). The *EX* component indicates that the antenna had one main beam, but the occurrence of a small slant angle is possible.

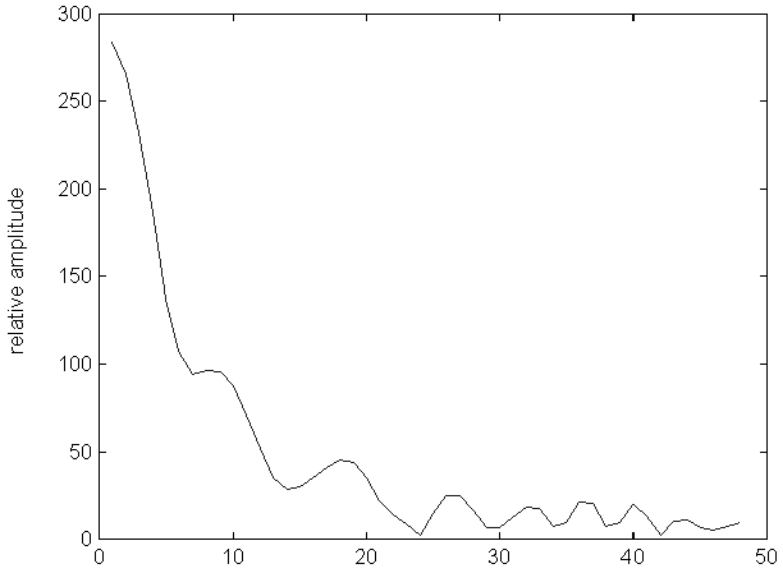

Fig. 5.14. Measured amplitude of 48 samples arranged along one arc with a normal sample spacing of $0.4\lambda_0$ (*EX* field components) at 11.25 GHz.

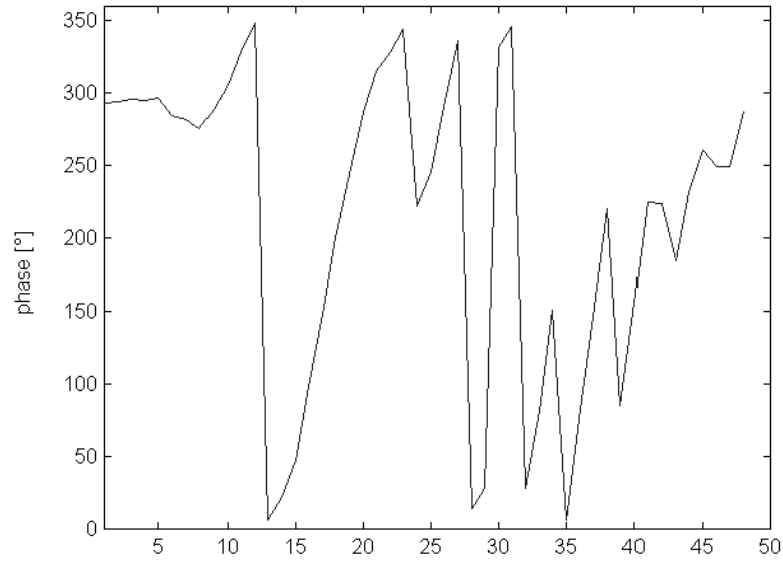

Fig. 5.15. Measured phase of 48 samples arranged along one arc with a normal sample spacing of $0.4\lambda_0$ (*EX* field components).

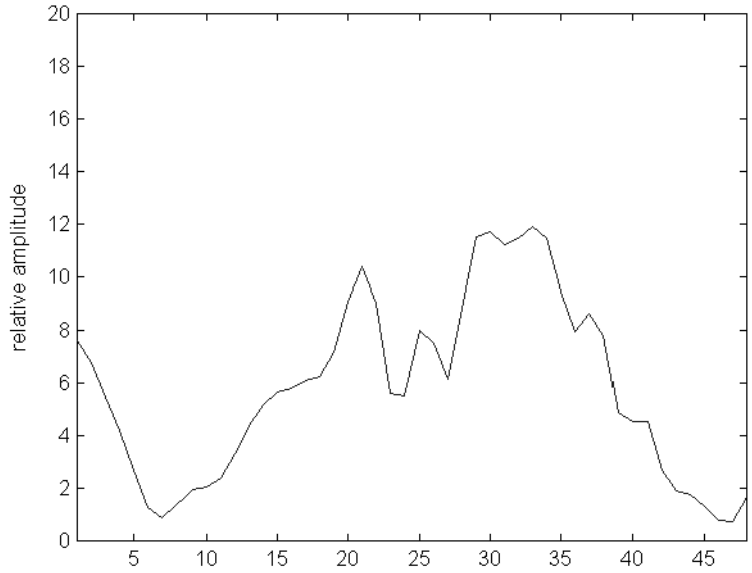

Fig. 5.16. Measured amplitude of 48 samples arranged along one arc with a normal sample spacing of $0.4\lambda_0$ (*EY* field components).

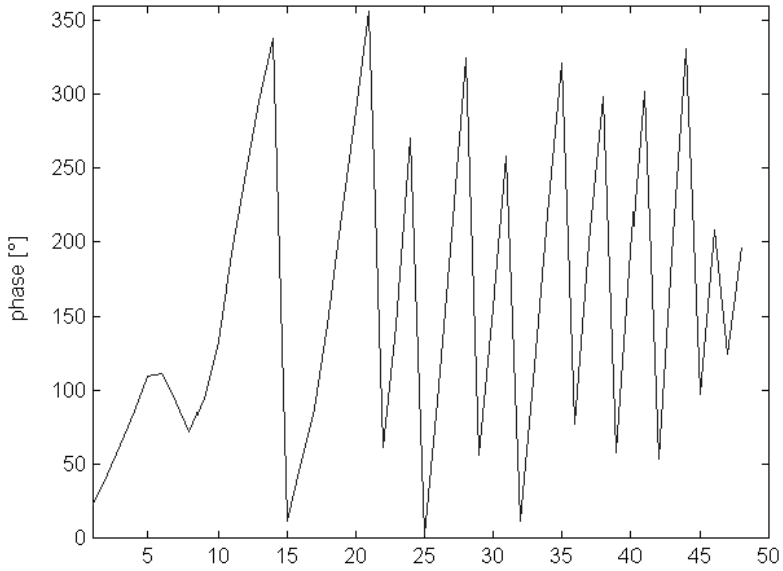

Fig. 5.17. Measured phase of 48 samples arranged along one arc with a normal sample spacing of $0.4\lambda_0$ (*EY* field components).

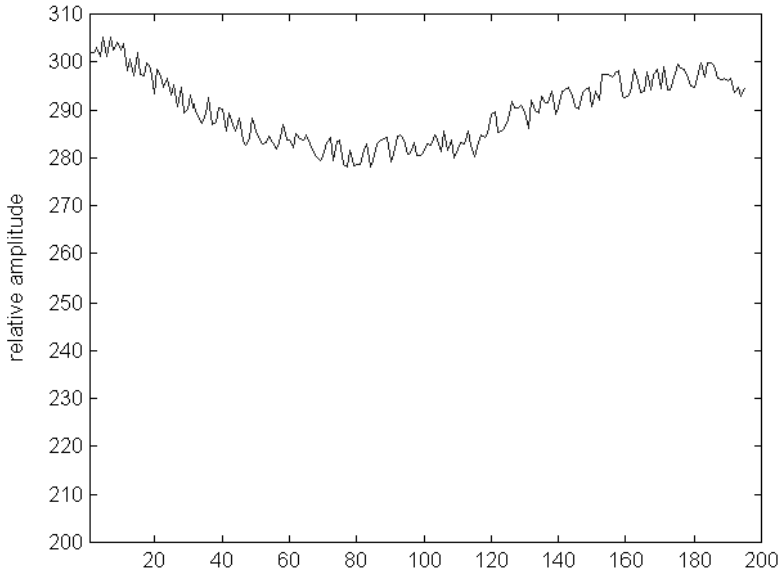

EX-component, f = 9030 MHz

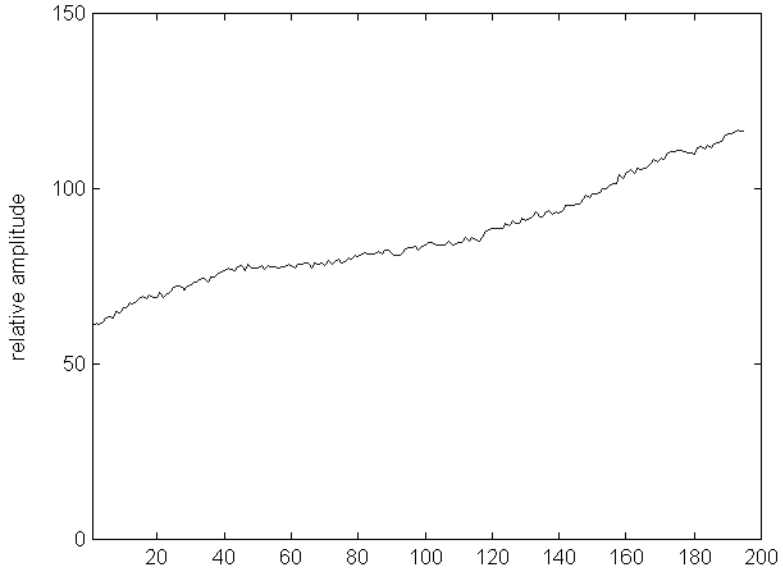

EY-component, f = 9030 MHz

Fig. 5.18. Recorded amplitude values of the first sample in each arc of the sampling grid comprising 194 arcs (the radiating source was the RMB-64 antenna).

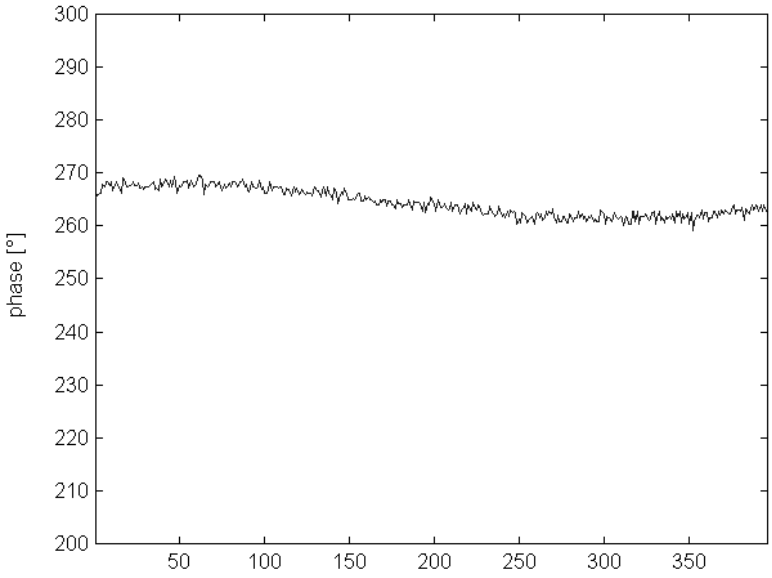

EX-component, f = 11250 MHz

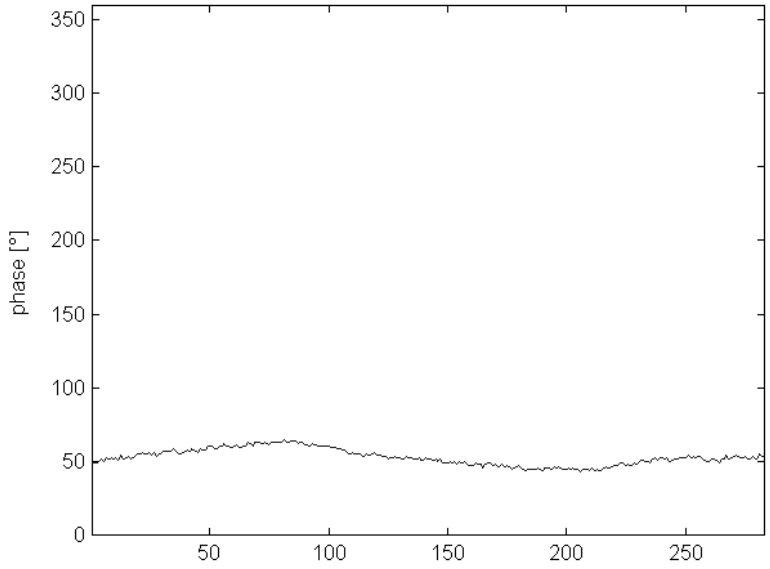

EY-component, f = 11250 MHz

Fig. 5.19. Recorded phase values of the first sample in each arc of the conventional bi-polar grid (the signal source was the TPA-256 antenna; *EX* and *EY* data taken at various scans).

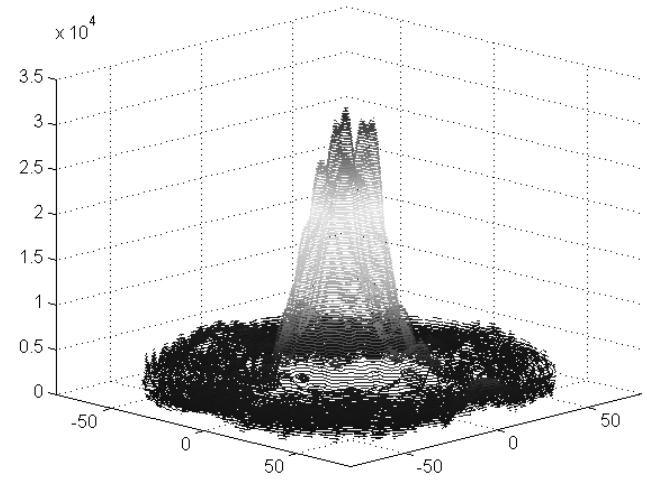

Fig. 5.20. Measured raw amplitude values for the samples located on the standard bi-polar grid (*EX*-field components). Sample spacing no greater than $0.45\lambda_0$ (12 mm at 11250 MHz) at the edge of the scanning circle (radius 75 cm). Spacing between the probe and the AUT (TPA-256) plane, 81.2 cm. Recording time, 4 hours 20 minutes. Averaging factor, 4.

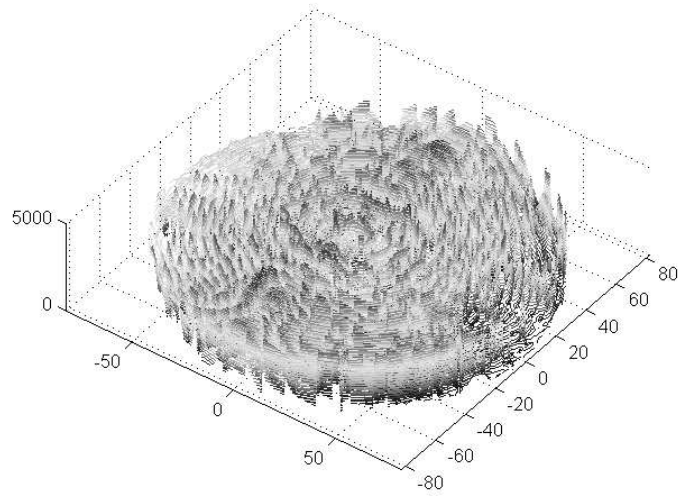

Fig. 5.21. Measured raw phase values for samples located on the standard bi-polar grid (*EY*-field components). Sample spacing no greater than $0.5\lambda_0$ (13.3 mm at 11250 MHz) at the edge of the scanning circle (radius 82 cm). Spacing between the probe and the AUT (TPA-256) plane, 59 cm. Recording time, 4 hours 20 minutes. Averaging factor, 4.

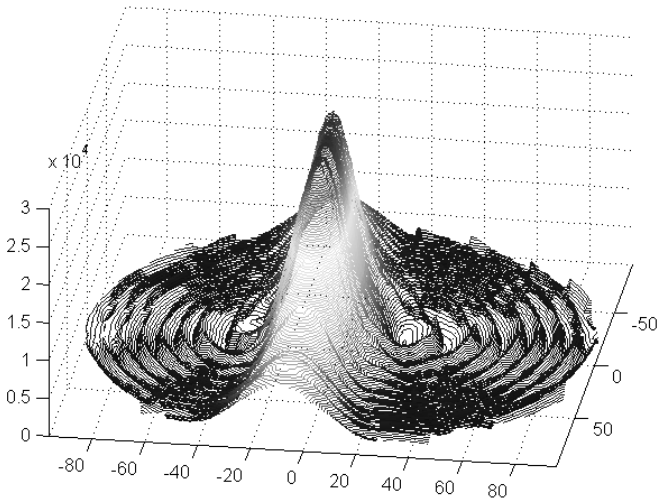

Fig. 5.22. Measured raw amplitude values of the e-m field radiated by the MC-8 phased array, for samples located on the standard bi-polar grid (*EX*-field components). A beam scanned by 7° off the principal geometrical axis (broadside direction). Sample spacing no greater than $0.4\lambda_0$ (24 mm) at the edge of the scanning circle (radius 95 cm). Recording time, 5 hours 30 minutes. Averaging factor, 4.

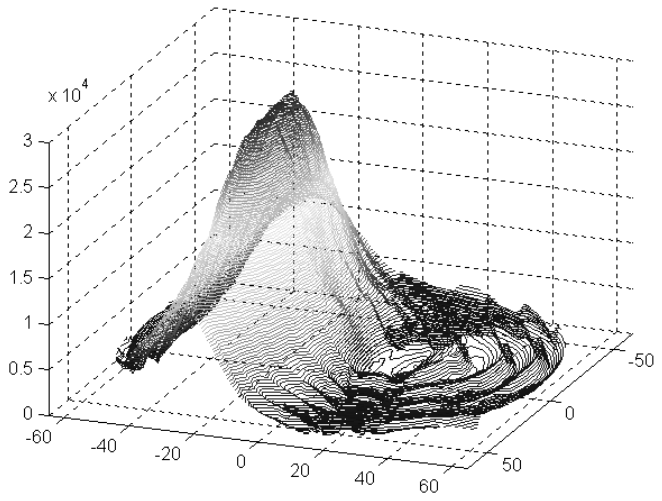

Fig. 5.23. Measured raw amplitude values of the e-m field radiated by the MC-8 phased array, for samples located on the standard bi-polar grid (*EX*-field components). A beam scanned by 21° off the principal geometrical axis (broadside direction). Sample spacing no greater than $0.4\lambda_0$ (24 mm) at the edge of the scanning circle (radius 64 cm). Recording time, 3 hours 30 minutes. Averaging factor, 4.

The images in Figures 5.22 and 5.23 depict the amplitude (without normalization) of the measured samples acquired for the phased array antenna for two beam positions: the broadside beam and the beam tilted by 21°. The radiation source was an 8-element (linear) MC-8 phased array operating with linearly polarized waves at 5000 MHz. The images show that the array is likely to be of linear type, as the recorded amplitude values are arranged in a strongly asymmetrical manner (much wider along one axis than along the orthogonal axis). Furthermore, the expected sidelobe level is likely to have been suppressed in the array. The main beam appears to be well formed. As the far-field radiation pattern develops when the observation point moves apart, the near-field data recorded for different probe-AUT spacing give the idea of how the amplitude pattern is evolving.

CHAPTER 6

SPATIAL SAMPLING AND NEAR-FIELD DATA PROCESSING

6.1. Sampling criterion

Introductory remarks

The commonly known sampling criterion that establishes the fundamentals of communication theory founded by pioneering works of Shanon and Wiener states that a band-limited signal $s(t)$ can be determined without any loss of information, when its discrete values are sampled over uniform time intervals T_s, and T_s is shorter than $1/(2f_{\max})$, where $f_{\max}$ is the upper frequency limit in $s(t)$. This principle is known as the *Shanon Criterion* and the minimum sampling rate $1/(2f_{\max})$ is called the *Nyquist rate*. A full reconstruction of the sampled field is possible when the chosen sampling intervals are such that an aliasing problem with their multiplied spectra can never occur (in the given domain). If the sampling rates were too slow, then periodical foldover regions would occur within the multiplied spectra, where some portions of the adjacent lobes would add and as a result the fidelity of the signal form would be lost. A signal can be reconstructed accurately from the sampled spectra, irrespective of whether the analyzed lobe is arranged in the original or in the inverse order. For sufficiently narrow bandlimited signals it is acceptable to determine sampling rates smaller than the lowest frequency of the signal, as the foldover regions will not occur due to the margins left between the multiplied spectra. When undersampling is feasible, the quantity of binary data may be reduced by many orders in the course of digital signal processing. The permissible undersampling rates are calculated with a simple inequality derived from the spectrum analysis of a sampled bandlimited signal.

In some instances, analysis of the field phenomenon concentrates on spatial-time signals, and then the determination of sampling intervals in the spatial domain instead of the time domain becomes indispensable. The determination of the spatial sampling criterion on the given scanning surface is vital for the near-field measurements of the antennas, because only methods operating with a discrete set of measured points have

a practical meaning (Joy, Paris 1972; Bucci, Franceschetti 1987). It is worth noting that the spatial samples can be regarded as a set of point sources generating an electromagnetic field identical with the original sampled field outside the surface which encompasses all the point sources.

Electrical engineers are generally less familiar with the criterions for spatial sampling of the electromagnetic field than with the well-known time domain sampling theory. Furthermore, the spatial sampling theory must address both uniform and non-uniform sample arrangements on various surfaces. In conventional analysis, consideration is given to bandlimited signals. However, when antennas are measured with ultra-narrow pulses, a wide spectrum of test signals must be taken into account, which makes the reconsideration of the permissible sampling intervals unavoidable (Hansen T. 1997).

In the most simple case of a plane wave signal propagating in homogeneous, lossless media, the electromagnetic field can be fully described at any point of observation with one-point data only. However, to enable the determination of the field at an arbitrary point, the time and point coordinates must be given. For other wave forms, more elaborated approaches must be established. The principle with which we can derive the maximal spatial separation of the samples obeys the rule that foldover lobes in multiplied spectra are never allowed to occur.

Sampling on an arbitrary planar grid

Without bothering with the fully 3D sampling arrangement at the moment, let us consider the sampling surface as being a plane oriented coincidently with the direction of spherical wave propagation. Then, the wave signal can be sampled instantly without any information loss, provided that the sampling points are spaced no farther than a half wavelength corresponding to the highest signal frequency. It is obvious that in the time domain such spacing is equivalent to sample intervals not greater than a half-period of the highest signal frequency (this observation is consistent with the *Shanon Criterion*). Please note that when the carrier signal is sampled and use is made of a reference channel, the recorded phase shift value is the same, regardless of the sample taking moment. Thus, the samples recorded sequentially (‘point after point’) by a measuring system with a reference channel will be equivalent to those acquired instantly at all points by a measuring system with no reference channel.

In a generalized approach, on the basis of the sampling theorem and Fourier Transform analysis (Papoulis 1977), it is known that the replacement of the continuous function $\mathbf{J}_s(\mathbf{r}')$ (expressing current or field strength) with discrete surface currents obtained in the course of sampling on the Cartesian grid (with sampling intervals Δx and Δy in x and y) produces a periodic replica of $\mathbf{U}_s$ with the following intervals in the Fourier space $\dot{\bar{k}}'$ (the prime denotes two-dimensional vectors) (Hansen J. 1988, Sec. 7.3.4]:

$$\Delta k_x = 2\pi/\Delta x \tag{6-1a}$$

$$\Delta k_y = 2\pi/\Delta y \tag{6-1b}$$

The periodic $\mathbf{U}_s$ replica is composed of a series of lobes. The main lobe is centered at $\vec{k}'$ equal to the projection $\vec{k}_0'$ of the ideal plane wave propagation vector $\vec{k}_0$ onto the Cartesian plane (*xy*-plane). Other replicas which enter the visible region are responsible for the occurrence of undesired grating lobes and for the foldover between the lobes. The visible space limits are defined by the condition $\left|\vec{k}'\right| \le k$ (where k is a wavenumber $k = 2\pi/\lambda_0$). Only if all lobes other than the main one remain in the invisible space, the replica $\mathbf{U}_s$ representing the sampled signal will reconstruct the original $\mathbf{J}_s(\mathbf{r}')$ current or field without any loss of information. (It is worthy to mention that a similar problem with grating lobes is frequently faced in antenna arrays and in sampling of bandlimited signals.) The undesired lobes will fall outside the visible region of the Fourier space $\vec{k}$, irrespective of the propagation vector $\vec{k}_0$, when $\Delta k_x \ge 2k$ and $\Delta k_y \ge 2k$. The two inequalities lead to the following criterion for the permissible intervals between the sampling points in *x* and *y*:

$$\Delta k_x = \frac{2\pi}{\Delta x} \ge 2k = 2\frac{2\pi}{\lambda} \tag{6-2a}$$

$$\Delta x \le \frac{\lambda}{2} \tag{6-2b}$$

$$\Delta k_y = \frac{2\pi}{\Delta y} \ge 2k = 2\frac{2\pi}{\lambda} \tag{6-3a}$$

$$\Delta y \le \frac{\lambda}{2} \tag{6-3b}$$

These formulas imply that the spacing between the sampling points can not be greater than a half-wavelength if the plane wave approaches the *xy*-plane from an arbitrary direction. In near-field measurements, this permissible spacing is known as the *half--wavelength criterion*. Only if the plane wave propagates perpendicularly to the source plane ($\vec{k}_0' = \vec{0}$), the replicas remain out of the visible region for $\Delta k_x \ge k$ and $\Delta k_y \ge k$. Consequently, the permissible spacing equals one wavelength in *x* and *y*. The spacing can be larger than a half-wavelength if limited occurrence of grating lobes is allowed. Such a case occurs when the spatial projection of the grating lobes passes off the measuring probe. Then, the grating lobe is unable to remarkably corrupt the sampled values when pointed far off the probe field of view in the outermost zone of the scanning aperture.

Sampling on polar and spherical grid

In polar and spherical grids, the introduction of angular sampling intervals seems to be feasible, as it can be inferred from the nature of the plane wave spectrum distribution. In that approach, larger scan radii of the scanning surface do not require a greater number of sampling points as it would be with the half-wavelength criterion. In polar and spherical coordinates, the following criteria were proposed and are used for angular sample increments in the azimuth ($\Delta\phi$) and elevation ($\Delta\theta$) angles

$$\Delta\phi = \frac{\lambda}{2(a+\lambda)}$$
$$\Delta\theta = \frac{\lambda}{2(a+\lambda)} \tag{6-4}$$

where a is a radius of the minimum sphere for the antenna.

Even though, there is a lack of mathematical proof, the (6-4) criterion is widely used in measurements. Then, the number of the sampling points is considerably smaller (*e.g.* for λ_0 = 32 mm and a = 270 mm, the number of samples in phi and theta is 119, giving the overall number of samples 14,161; at the same time the *half--wavelength criterion* gives the number of samples equal to 549 on the perimeter of the scanning sphere having a radius R = 1400 mm, and this may result even in a total number of 301, 401 sampling points).

Another approach which leads to similar results is the one described in Section 4.4.3 of (Hansen J 1988). The highest significant wave mode existing in the field radiated by the antenna is given by

$$N = ka + 10 \tag{6-5}$$

The minimum number of samples taken in a full angle in both azimuth (ϕ) and elevation (θ) directions is $2N + 1$. Thus the greatest permissible angular increment $\Delta\phi$ and $\Delta\theta$ is then

$$\Delta\phi = \Delta\theta = \frac{2\pi}{2N+1} \approx \frac{\pi}{N} \tag{6-6}$$

After simple conversions, (6-9) gives

$$\Delta\phi = \Delta\theta = \frac{\pi}{\frac{2\pi}{\lambda}a + 10(\approx 3\pi)} \approx \frac{\lambda}{2a + 3\lambda} \tag{6-7}$$

The studies showed that assuming an N value greater than the one given by (6-5) leads to inclusion modes (harmonics) which are very small, mostly below the noise

level. Increasing the N value can be justified only when the current distribution does not establish a well-defined minimum sphere. In many cases it is not obvious what size should be actually assumed for the minimum sphere. A dense oversampling is not advisable as it does not enrich the information about the radiated electromagnetic field. In practical near-field measurements, the oversampling ratio is small and accounts for a 10–20% increase in the number of samples.

In practical near-field measurements it is necessary to know a minimum spacing r_0 between the tested antenna and a scanning surface. It is worthy to mention that a minimum sphere of the probe must remain outside the r_0 limit surface all the time during scanning. Distance r_0 can be evaluated by deriving a sufficient number of propagating modes which are included into sampled fields. A sufficient number of terms for convergence of a series representation of spherical wave functions is for all practical purposes given by the empirical rule $N = [kr_0] + n_1$. According to Hansen, if the field point is more than a few wavelengths from the minimum sphere and four digits in the field computation are sufficient, an obvious choice is $n_1 = 10$. The same reference says, the value kr_0 between 15 and 22 is sufficient for practical measurements. Thus, the minimum scanning distance r_0 can be derived as $15 \leq kr_0 = (2\pi/\lambda) r_0 \leq 22$. Hence r_0 should not be smaller than 2.2 wavelengths.

6.2. Interpolation techniques

Interpolating non-uniformly placed samples

The major reason for applying interpolation to the processing of near field data is the desire to take advantage of the benefits offered by the FFT and in that way to escape from all those lengthy and abundant numerical integrations needed to compute the far-field patterns with near field data. When involving the FFT, the computation time can be reduced by a few orders (Rahmat-Samii et al. 1980) (FFT can be applied when the data matrix size N is different from the power of two). The transformation between near and far field is the most effective for the rectangular format of data arranged on a plane. For this reason, the conversion of the data in the bi-polar format into the Cartesian one is highly beneficial. However, the interpolation method and the selection of the interpolating values (exact recorded samples) strongly affect the accuracy of the transform method as a whole. Another interpolation-related issue is the non-uniform sample arrangement in the bi-polar grid and the two-dimensional arrangement of samples which are complex numbers. The probe excitation coefficients are complex numbers and can be presented either in the real/imaginary or in the amplitude/phase formats. Our microwave receiver returns the amplitude and phase values. In the polar format, the phase values are nonlinear (modulo 360°), but it is possible to

unwrap the phase and restore linearity. However, this mathematical process is difficult through presence of phase discontinuities and fast changes in the far sidelobe region (Carballo, Fieguth 2002).

Last but not least, the interpolation techniques might turn out to be of utility in improving the visualization of the far-field results. The resolution of the far-field results is improved in near-field laboratories with the zero-fill method (adding zero-pads to the FFT input matrix). However, when far field data are needed in an arbitrary cut-plane, the interpolation performed over the transform results yields a more accurate radiation pattern plot. Since the data points are nonuniformly spaced, particularly recommended for such a purpose is the OSI method (Ferrara et al. 2001).

Several interpolation methods were considered and three of them gained primary interest in our studies:

(i) the spline functions,
(ii) the four-point Lagrange interpolation,
(iii) the Optimal Sampling Interpolation (*OSI*).

The spline functions operate with data in the linear vector format. Methods (ii) and (iii) work with input data around the given interpolation node (of the first surrounding tier, the second one, *etc*.).

A specific feature of interpolating the samples arranged in the polar format is a better accuracy in the center than in the edge regions of the grid due to the following reasons:

(i) at the grid center interpolation is performed with densely packed sampling points,
(ii) phase variations, which are slow and small in the main beam region or in near field above the antenna aperture, become rapid and large over the sidelobes outside the antenna aperture,
(iii) the fields are usually stronger in the center of the grid and weaker at the far out sidelobes.

Redundancy at the grid center exists unless the bi-polar grid is modified by thinning (described in Section 6.5). Regardless of the method used, the validation of the interpolated results should be performed as a routine step in data processing. A checking procedure should evaluate the differences between exact and interpolated values, as it might happen that the interpolation unexpectedly fails – locally or globally – to follow up the measured data with a satisfactory fidelity.

Vector spline interpolation

At the beginning of our study, we made use of the third-order spline functions (*cubic* spline functions) (Kabacik, Maksimiuk 1997b). We chose this method, recalling the satisfactory experience gained in our earlier research. However, the spline method makes use of one-dimensional input data, and is far from being an optimum approach

to the interpolation of planar data. As the interpolation is performed on planar data, the spline functions must be calculated twice (along the *x*-axis and, thereafter, along the *y*-axis). The interpolating algorithm involves two steps: the choice of the interpolating nodes in the bi-polar grid for each interpolated linear vector (row or column of the rectangular grid) and the determination of the spline function coefficients. In the course of interpolation, we minimized the vector to vector distance defined by the following measure

$$d(V_i, Z) = \sqrt{\sum_{j=0}^{M} (V_{ij} - Z_j)^2} \tag{6-8}$$

for every i where $i = 0, ..., N$.

In our procedure, the spacing $(V_{ij} - Z_j)$ must not be greater than $1/4\sqrt{2}\lambda_0$ for every j (for majority of cases this spacing is much smaller). In the given interval $[a, b]$ having a partition u_i where $i = 0, \ldots, N$, and $u_0 = a$, $u_N = b$, the interpolating function is always a third-order polynomial. The spline interpolation requires that the unknowns in the set of linear equations be found.

Four-point Lagrange interpolation

A major advantage of the Lagrange interpolation formula is its simplicity and straightforward application to two-dimensional planar data. The method makes use of four sampled values in the proximity of the interpolating node. Weighting coefficients are calculated from ratios of the distances between the sampling and interpolated points. The distances can be expressed in terms of linear or angular measures as shown below:

$$\begin{aligned} f(\phi, \rho) = {} & \frac{\phi - \phi_2}{\phi_1 - \phi_2} \frac{\rho - \rho_2}{\rho_1 - \rho_2} f(\phi_1, \rho_1) \\ & + \frac{\phi - \phi_2}{\phi_1 - \phi_2} \frac{\rho - \rho_1}{\rho_2 - \rho_1} f(\phi_1, \rho_2) \\ & + \frac{\phi - \phi_2}{\phi_2 - \phi_1} \frac{\rho - \rho_2}{\rho_1 - \rho_2} f(\phi_2, \rho_1) \\ & + \frac{\phi - \phi_1}{\phi_2 - \phi_1} \frac{\rho - \rho_2}{\rho_2 - \rho_1} f(\phi_2, \rho_2) \end{aligned} \tag{6-9}$$

where $f(\phi_i, \rho_j)$ is one out of four sampled values taken in the vicinity of the (ϕ, ρ) point, and $f(\phi, \rho)$ denotes the interpolated value.

The values in (6-9) are complex and are represented in the real/imaginary format. The algorithm was implemented in the polar near-field system (Gatti, Rahmat-Samii

1988). Making use of the sampled values scattered around the interpolating node is the most reasonable selection method. However, the weighting algorithm applied here is one of the simplest possible and does not ensure control of the approximation error. Variations of the electric field of the antenna are associated with abrupt changes. Needless to say that the proportional method of calculating the weights does not enable such abrupt trends to be followed-up accurately. In order to overcome this drawback, smaller distances between the points can be suggested. However, the decrease of sample spacing is neither a wise nor a recommended approach in the measurement technique that operates on large data files. Furthermore, it was observed that increase of the sampling point density does not reduce interpolation errors.

Optimal Sampling Interpolation (OSI) of non-uniformly spaced samples

More suitable for the processing of the antenna fields are the algorithms of optimal reconstruction (Bucci et al. 1994a; Williams et al. 1994b; Kabacik et al. 2000a). Furthermore, the OSI method does not require greater sample density than the ones determined by the sampling spacing criterion. The method which has found the widest acceptance is the Central Interpolation Scheme (Bucci et al. 1991). Owing to the elaborated use of the Dirichlet and Tschebyscheff sampling functions, the OSI method yields interpolated values with great accuracy (Bucci, D'Elia 1994b; Bucci et al. 1998b). The understanding of the best approximation is in the sense of the Least Mean Squares (LMS). Since the sampling functions must be formulated for a given coordinate system of exact values, non-trivial efforts are required when making use of the method. Presently the OSI method supports the cardinal coordinate grids, including the plane-polar grid. Please note that with the formulas for the plane-polar grid it is possible to interpolate data in the bi-polar grid.

The geometry of point location in the interpolation procedure is shown in Figure 6.1. The interpolating values are taken in the nearest proximity around the interpolation node (which is in the Cartesian system).

For geometry of Figure 6.1 following normalized description of sample location was introduced

$$\xi = \frac{\rho}{d}$$
$$\eta = \frac{\rho\phi}{r_m} = \phi \sin\vartheta \tag{6-10}$$

where ρ is a radial distance of the point under consideration and d is a distance between AUT and the scanning plane with bi-polar samples.

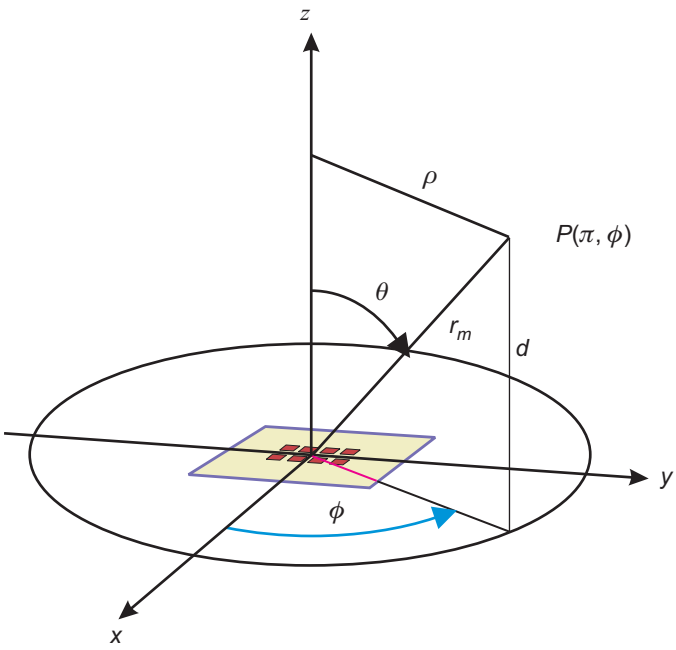

Fig. 6.1. Geometry of the bi-polar points and description of their coordinates.

In the interpolation procedure we applied the general equation

$$E(\xi,\eta)=\sum_{n=n_0-p+1}^{n=n_0+p}\left[\sum_{m=m_0(n)-q+1}^{m=m_0(n)+q}E(\xi_n,\eta_{n,m})\theta_n(\eta-\eta_{n,m})\right]\Omega(\xi-\xi_n) \tag{6-11}$$

Indexes $\{n_0, m_0(n)\}$ denotes the nearest sample to the observation point (ξ, η) in terms of normalized coordinates. $\Omega(\xi)$ is a product of the sampling function and the weighting function appropriate for the line η = const, wherein $\theta_n(\eta)$ is given by the sampling function times the weighting function applied for the observation line ξ = const. The interpolated value is obtained in two steps: firstly by interpolating the values along the lines $\xi = \xi_n$ and then by computing the final values along the line η = const. In the considered case the interpolating functions of (6-11) are given by

$$\begin{aligned}\Omega(\xi)&=\sin c(\chi_2 w\xi)\Psi(\xi)\\ \theta_n(\eta)&=D_{M_n'}(\eta)f_{N_n}(\eta)\end{aligned} \tag{6-12}$$

In our laboratory the calculation explores the formulas established for the data in the plane-polar coordinate system. For computation Φ_N either the Dirichlet or the Tschebyscheff Sampling Function may be applied. The Dirichlet Approximate Spheroidal Function (DAPS) is given by

$$f_N(\phi) = \frac{\sinh[(2N+1)\sinh^{-1}\sqrt{\sin^2(\phi_0/2) - \sin^2(\phi/2)}]\sin(\phi_0/2)}{\sinh[(2N+1)\sinh^{-1}(\sin(\phi_0/2))]\sqrt{\sin^2(\phi_0/2) - \sin^2(\phi/2)}} \tag{6-13}$$

The Tschebyscheff Sampling Function (TS) is expressed as

$$f_N(\phi) = \frac{T_N\left[2\left(\frac{\cos(\phi/2)}{\cos(\phi_0/2)}\right)^2 - 1\right]}{T\left[\frac{2}{\cos^2(\phi_0/2)} - 1\right]} \tag{6-14}$$

$$\phi_0 = p\Delta\phi \tag{6-15}$$

The Ψ can take a form of the Approximate Spheroidal Function (APS) or the Sampling Window function (SW). Both are defined by equations (6-16) and (6-17) respectively

$$\Psi(s) = \frac{\sinh[\pi\upsilon h\sqrt{1-\left(s/p\Delta s\right)^2}}{\sinh(\pi\upsilon p)\sqrt{1-\left(s/p\Delta s\right)^2}}$$

$$\upsilon = (\chi_2 - 1)/\chi_2 \tag{6-16}$$

wherein s is the rectilinear abscissa (x-axis coordinate of the point) normalized to d. $\Delta s = \pi/(\chi_2 w)$ is the sampling rate. In order to control the truncation error, Δs must be slightly larger than the minimum one *i.e.* π/w (w is the band of the approximating function).

$$\Psi(s) = \frac{\cosh[\pi\upsilon h\sqrt{1-\left(s/p\Delta s\right)^2}}{\cosh(\pi\upsilon p)} \tag{6-17}$$

The OSI interpolation method is also applied to the Singular Value Decomposition (SVD) technique. The application is to determine the uniformly reconstructed samples in some antenna problems. The OSI is used in order to determine the solution which is the best approximation of the linear equation system

$$\mathbf{A}\,\mathbf{x} = \mathbf{b} \tag{6-18}$$

where **b** is a vector of the known nonuniformly spaced samples, and **x** is a vector of unknown values to be calculated which are uniformly arranged. The number of ele-

ments in **b** can be greater than, or equal to, the number of elements in **x**. With the OSI expansion elements a_{km} of matrix **A** are determined as follows

$$a_{km} = \Omega_M(\eta_k - \phi_m) D_{M''}(\eta_k - \phi_m) \tag{6-19}$$

where Ω_M is the Dirichlet function and $D_{M''}$ is the Tschebyscheff function.

Interpolated near-field data recorded in our laboratory

The accuracy of the interpolation algorithm is a critical issue to the overall far-field results. In this Section, illustrative examples of interpolated data processed in the course of the studies with our computer codes are presented and discussed. The discrete values interpolated with the spline method were in good agreement with the original ones, as it can be inferred from the plots in Figure 6.2. The exact data presented the radiation pattern in the *H*-plane cut. A remarkable discrepancy between the interpolated and exact values was observed at two points located between –85º and –90º. The interpolation procedure started with those points and terminated on the opposite side of the radiation pattern. It should be noted that the discrepancies occurring at the surface edges deserve closer than just marginal attention, and that this sort of discrepancies are likely to occur in other interpolation techniques as well due to truncation. What is an edge point in the grid of measured samples can become an inner value after zero padding (in the FFT method, *zeros* are filled at the outskirt of the scanned area).

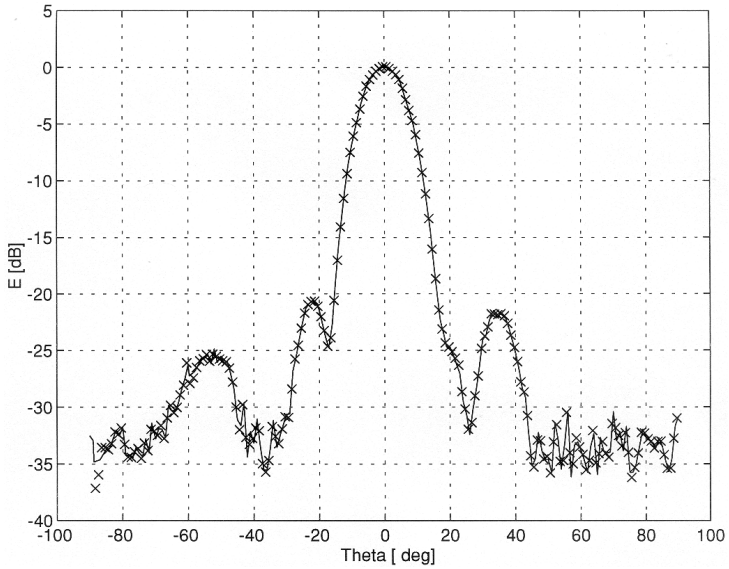

Fig. 6.2. Interpolated values computed with the spline method,
1° intervals between interpolated points (Kabacik, Maksimiuk 1997b).
solid line – exact values, crosses – interpolated values

In the spline technique, the interpolating coefficients are computed with all elements of the input data vectors which span from one edge to another. Thus, distant samples are wrapped up into the computation of the interpolated values. A more reasonable approach should concentrate on nearby samples and neglect the distant ones as irrelevant.

The remaining interpolation plots were computed by the OSI method implemented in our data processing software. Figures 6.3 through 6.7 show the interpolated amplitude values of the field recorded with our bi-polar system above the 16×15 cm, planar RMB-64 array (the measurements were at 9030 MHz). The plotted data showed that the quality of linear polarization was not very high. During scanning, the co-polar field components generated by the antenna were obtained in the *EX* plane, while the cross-polar components were in the *EY* plane of the scanning system. Closer inspection of the interpolated values allow us to conclude that the interpolation algorithm handled accurately the sidelobe concentration regions which are particularly difficult to process. Our research showed that the results obtained with the OSI method are most accurate of all three interpolation techniques analyzed.

The TPA-256 array consisting of 16×16 elements (33×33 cm) was four times as large as the RMB-64 antenna and thus had a narrower main beam and more sidelobes. Figures 6.8 and 6.9 show the interpolated amplitude values in the rectangular coordinates of the field recorded $22\lambda_0$ above the TPA-256 array. The antenna was measured at 11250 MHz in such a way that the co-polar field components were consistent with the *EX* plane and the cross-polar field components were arranged along the *EY* axis (on the principal axes of the system). As is evident from the surface plots in Figures 6.8 and 6.9, the OSI method proved its good accuracy and reconstructed the main features of the radiated field. The surface plots of the recorded phase values are hard to read in the printed version, as the microwave receivers return the numbers in the modulo 360° format and the phase undergoes rapid and large changes within the sidelobes. To visualize the phase values in a readable form it is strongly advisable to use computer animation or print several plots for various points of view.

Multi-beam and scanned-beam antennas have their beams pointed off the broadside direction, so the strongest intensity of the radiated field is outside the central region of the grid. In these circumstances, some setbacks of the interpolation method may emerge. We tested the OSI method by recording the sampled field values in front of the 8-element linear MC-8 phased array (Kabacik 1995b, Ch. 6).The interpolated amplitude surfaces for several beam positions are shown in Figures 6.10 through 6.14. The *dx* and *dy* spacing in the Cartesian grid was 24 mm ($0.35\lambda_0$), and the scanning plane was 52 cm ($8.6\lambda_0$) above the AUT. In some of these plots there is noticeable truncation of the data across the main beam because of the scanning aperture truncation.

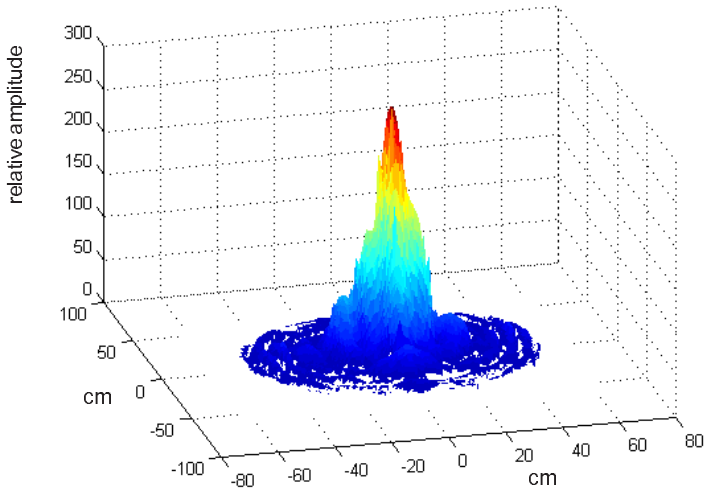

Fig. 6.3. Interpolated (with the OSI method) 3D amplitude surface of *EX* field components radiated (at 9030 MHz) by the 8×8 element microstrip RMB-64 array. Scanning aperture radius, r = 51 cm; AUT-probe spacing, d = 46 cm (13.8λ_0); dx and dy spacing in rectangular grid, 0.4λ_0; increment of concentric rings in bi-polar grid, 0.4λ_0. Averaging factor of recorded data, 4.

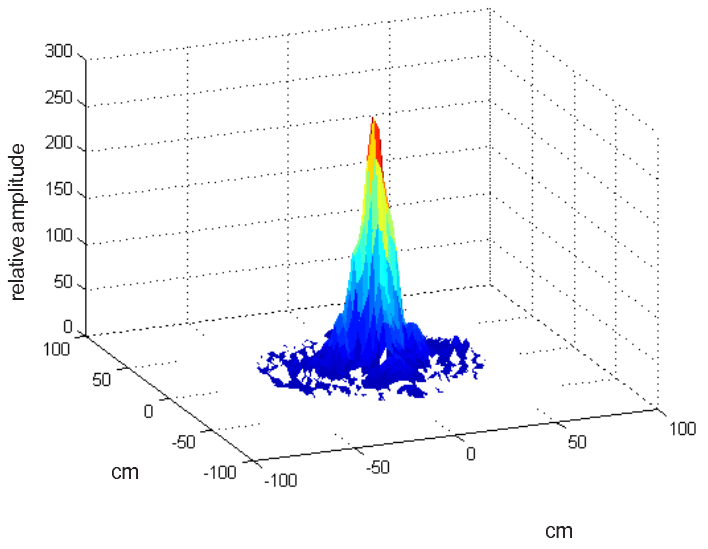

Fig. 6.4. Interpolated (with the OSI method) 3D amplitude surface of *EX* field components radiated (at 9030 MHz) by the 8×8 element microstrip RMB-64 array. Scanning aperture radius, r = 51 cm; AUT-probe spacing, d = 46 cm (13.8λ_0); dx and dy spacing in rectangular grid, 0.4λ_0; increment of concentric rings in bi-polar grid, 0.7λ_0. Averaging factor of recorded data, 4.

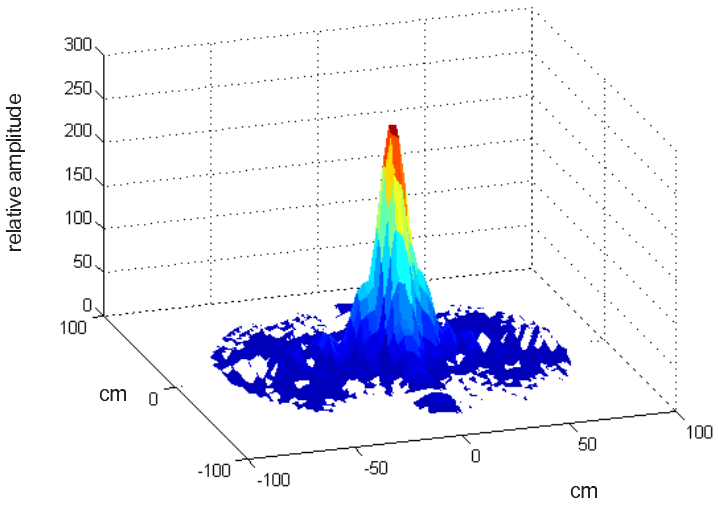

Fig. 6.5. Interpolated (with the OSI method) 3D amplitude surface of *EX* field components radiated (at 9030 MHz) by the 8×8 element microstrip RMB-64 array. Scanning aperture radius, r = 78 cm; AUT-probe spacing, d = 70 cm (21.1λ_0); dx and dy spacing in rectangular grid, 0.4λ_0; increment of concentric rings in bi-polar grid, 0.9λ_0. Averaging factor of recorded data, 4.

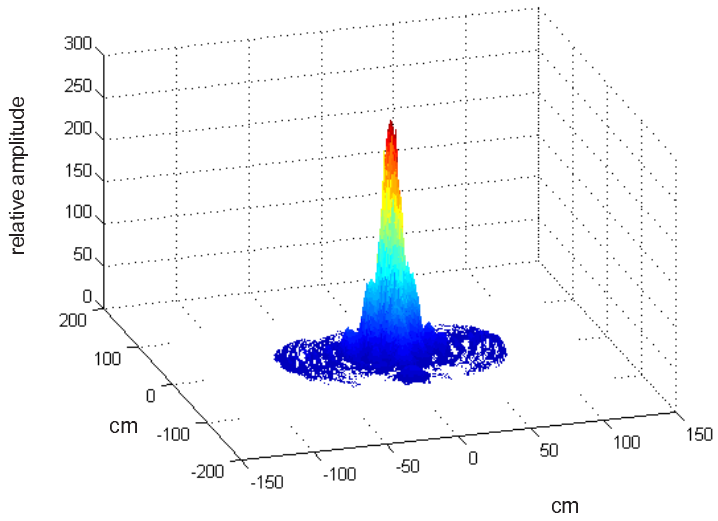

Fig. 6.6. Interpolated (with the OSI method) 3D amplitude surface of *EX* field components radiated (at 9030 MHz) by the 8×8 element microstrip RMB-64 array. Scanning aperture radius, r = 78 cm; AUT-probe spacing, d = 70 cm (21.1λ_0); dx and dy spacing in rectangular grid, 0.4λ_0; increment of concentric rings in bi-polar grid, 0.4λ_0. Averaging factor of recorded data, 4.

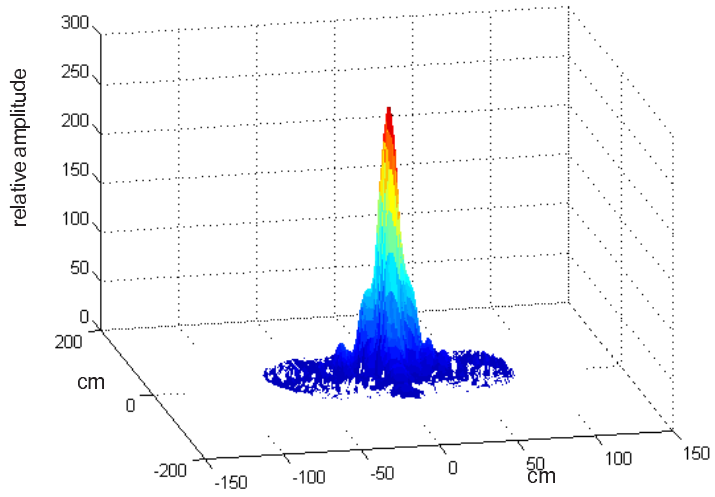

Fig. 6.7. Interpolated (with the OSI method) 3D amplitude surface of *EX* field components radiated (at 9030 MHz) by the 8×8 element microstrip RMB-64 array. Scanning aperture radius, r = 78 cm; AUT-probe spacing, d = 70 cm (21.1λ_0); dx and dy spacing in rectangular grid, 0.4λ_0; increment of concentric rings in bi-polar grid, 0.9λ_0. Averaging factor of recorded data, 4.

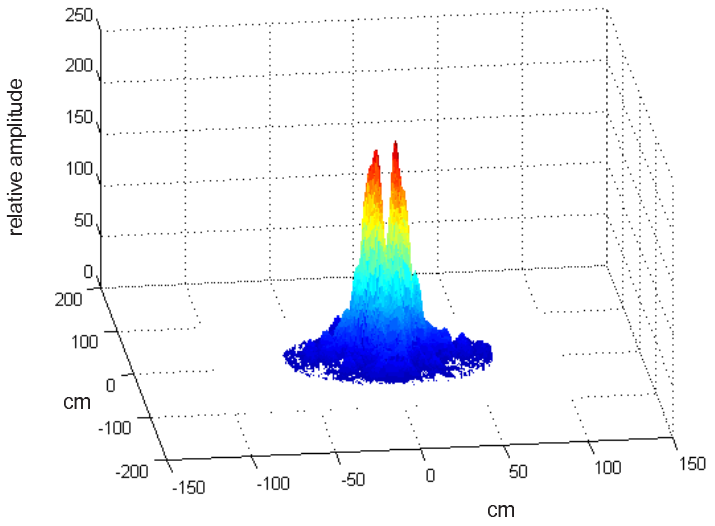

f_0 = 11250 MHz *EX* field components

Fig. 6.8. 3D surface of amplitude values interpolated with the OSI method, in front of the TPA-256 microstrip planar array. Scanning aperture radius, r = 60 cm; AUT-scanning aperture spacing, 59 cm (22.5λ_0); dx and dy spacing in rectangular grid, 0.4λ_0; radius increment of concentric rings, 0.4λ_0 (11250 MHz). Averaging factor of recorded data, 4.

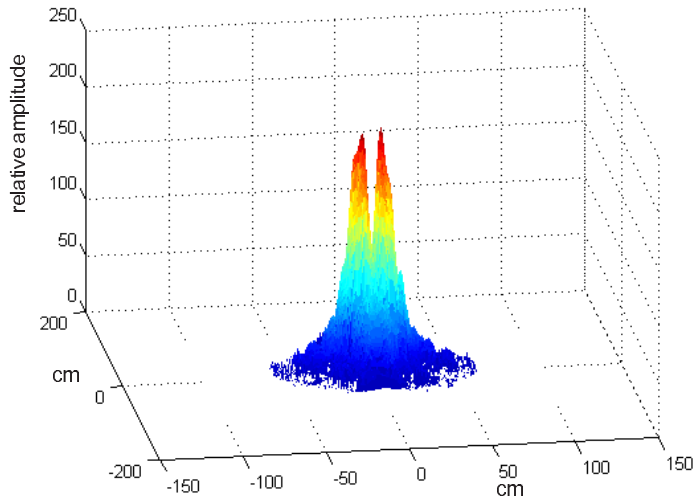

f_0 = 11250 MHz *EX* field components

Fig. 6.9. 3D surface of amplitude values interpolated with the OSI method, in front of the TPA-256 microstrip planar array. Scanning aperture radius, r = 60 cm; AUT-scanning aperture spacing, 59 cm (22.5λ_0); dx and dy spacing in rectangular grid, 0.7λ_0; radius increment of concentric rings, 0.7λ_0 (11250 MHz). Averaging factor of recorded data, 4.

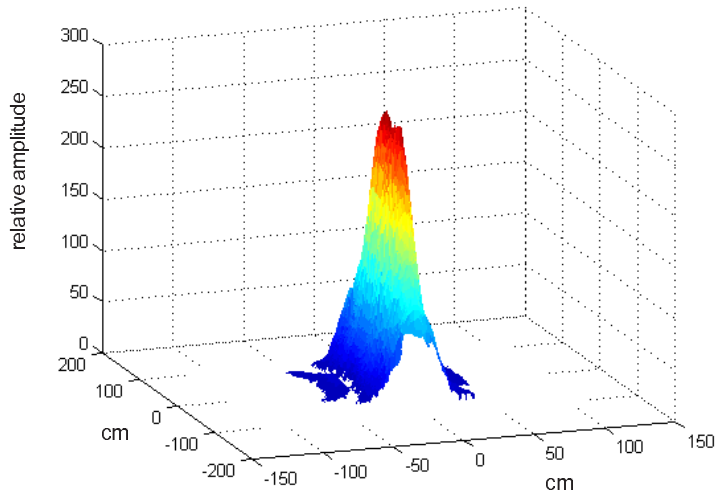

f_0 = 5000 MHz *EX* field components

Fig. 6.10. Interpolated amplitude surface in the Cartesian format (dx = dy = 0.35λ_0) of the *EX* field components, calculated with bi-polar data scanned on the plane 52 cm (8.6λ_0) above the MC-8 phased array for the broadside position of the beam (f = 5000 MHz).

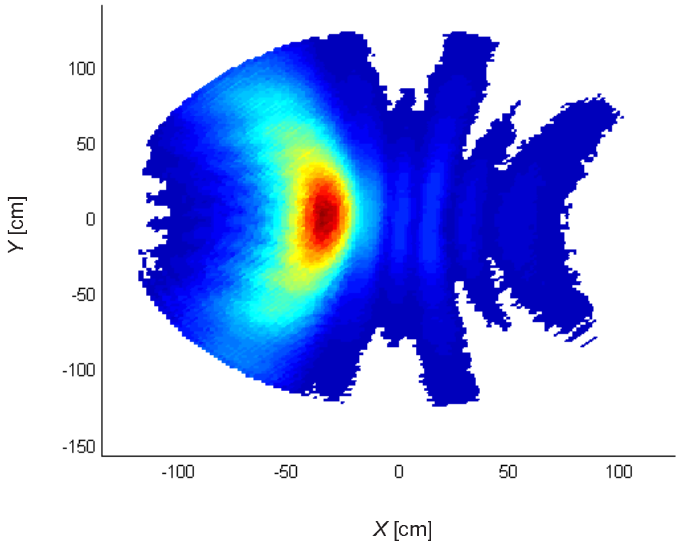

Fig. 6.11. Interpolated amplitude surface in the Cartesian format ($dx = dy = 0.35\lambda_0$) of the *EX* field components, calculated with bi-polar data scanned on the plane 52 cm ($8.6\lambda_0$) above the MC-8 phased array for the beam tilted by 34° (f = 5000 MHz).

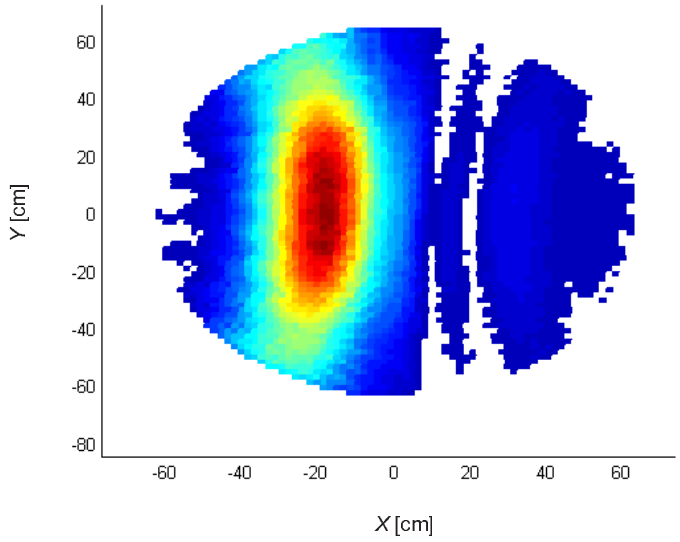

Fig. 6.12. Interpolated amplitude surface in the Cartesian format ($dx = dy = 0.35\lambda_0$) of the *EX* field components, calculated with bi-polar data scanned on the plane 52 cm ($8.6\lambda_0$) above the MC-8 phased array for the beam tilted by 20° (f = 5000 MHz).

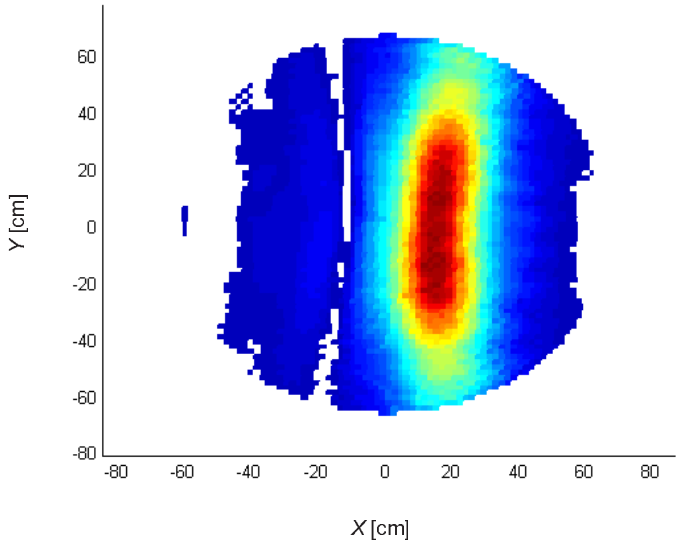

Fig. 6.13. Interpolated amplitude surface in the Cartesian format ($dx = dy = 0.35\lambda_0$) of the *EX* field components, calculated with bi-polar data scanned on the plane 52 cm ($8.6\lambda_0$) above the MC-8 phased array for the beam tilted by –13° (f = 5000 MHz).

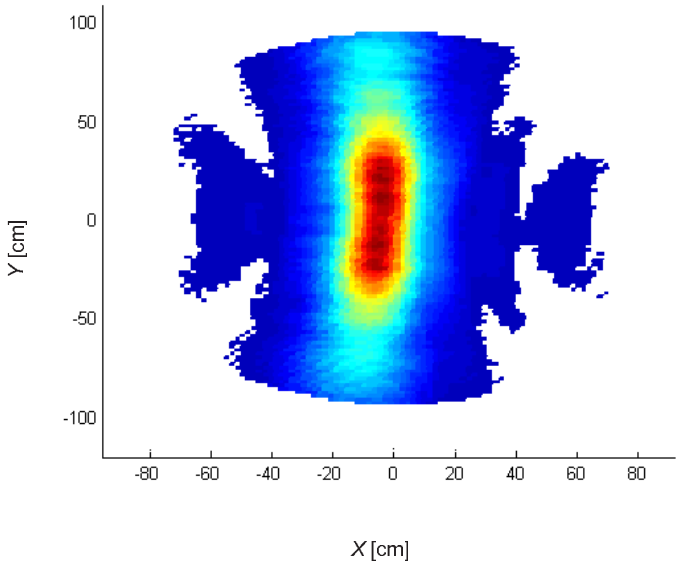

Fig. 6.14. Interpolated amplitude surface in the Cartesian format ($dx = dy = 0.35\lambda_0$) of the *EX* field components, calculated with bi-polar data scanned on the plane 52 cm ($8.6\lambda_0$) above the MC-8 phased array for the beam tilted by 7° (f = 5000 MHz).

6.3. Fundamentals of near to far-field transform

As the near-field technique creates a lot of difficulties, there is no need that each member of the research team be well competent in the theory – there are several more areas demanding proficiency. But at least one team member should possess a versatile knowledge of the theory on which the near-field technique is based. Since the near--field method is an indirect approach, the measured data do not provide insight into the antenna parameters and follow up data processing becomes indispensable. There are two general approaches making use of the FFT for the computation of integrals in the far-field transform:

(i) plane-wave spectrum,

(ii) convolutional expression of the probe fields and the AUT fields.

The plane-wave spectrum is identical with the far-field *E* component radiation pattern. The concept of plane-wave spectrum makes it possible to easy understand the development of antenna radiation pattern in the far field. In particular, the derivation of the far-field transform for the planar rectangular scanning is well supported by the plane-wave spectrum theory.

Near field and far field of antenna radiation

The strength and spatial distribution of the field radiated by any antenna evolves with distance from the source and the radiation pattern takes a practically stable shape for sufficiently large distances from the field source. For smaller distances between the antenna and the observation point, the following types of distinctive different regions should be introduced: reactive, near field and transition, the latter being followed by the far field zone. So far, the reactive region has been considered as useless in terms of antenna measurements. It occupies a space adjacent to the antenna structure, where propagating reactive field components vanish quickly. However, there are works aiming at establishing near-field reactive-field transformation (Appel et al. 1998).

The antenna can be considered as a whole radiation source outside its minimum sphere, *i.e.* the smallest one that encompasses the entire antenna structure. The first region extending outward from the minimum sphere is called the near-field region (actually, a well established near field starts between one to three wavelengths outside the minimum sphere). Talking about the near field makes sense in the case of antennas which are approximately at least $0.3\lambda_0$ large.

Intuitively the far field can be described as a zone where the shape of the radiation pattern does change negligibly. In order to establish a versatile definition of the far--field region it is assumed that the point of observation is in the far field when the phase offset between the waves generated by the edge parts of the antenna aperture is

small and does not exceed the permissible maximum value. The most widespread use definition takes the value of the maximum phase variations $\pi/8$ (22.5°). Such permissible phase difference leads to a conclusion that the far-field range extends from the Rayleigh distance R expressed as $R = 2D^2/\lambda$ (where D is the largest antenna dimension). But this Rayleigh distance is too small to properly evaluate the depth of the nulls and the sidelobe levels in antennas with suppressed sidelobes.

For antennas with low sidelobe levels or for those involving advanced beamforming methods (non uniformly illuminated reflectors or fed elements), greater far field distances are postulated (Kabacik 1995b). In such instances, the assumption that the phase variations will not be greater than 6° usually satisfies the designer's requirements (Kabacik 1998a) and the far field distance R can be expressed as

$$R \geq 5\, D^2/\lambda \tag{6.20}$$

Such R values must be necessarily applied to the sidelobe and null depth measurements (the antenna main beam, however, can be evaluated with shorter ranges). Typical symptoms of an underestimated far-field measuring range are: an increased level of the sidelobes, shoulder-like distortions of the main beam, smoothened nulls, or sidelobe mergers.

Plane wave propagating in lossless unbounded isotropic media

The electromagnetic field generated by an arbitrary source can be described by spherical waves; the total far field of any antenna is a spherical one. The objective of plane-wave-spectrum analysis is to describe how the spherical wave in the far field of the antenna transforms from the plane waves propagating in the near field (in the plane wave, the surface of a constant amplitude or phase is planar) (Kerns 1980; Rudduck et al. 1973; Johnson et al. 1973; Li et al. 2001). Perhaps the first published major work on the concept of an angular plane-wave spectrum was by Booker (Booker, Clemmow 1950). The plane-wave scattering matrix establish an excellent framework for determination of mutual coupling between two antennas (Yaghjian 1982).

Near-field analysis is based on the aperture integration method or on the plane wave spectrum approach. It turns out that the electromagnetic field in the proximity of the antenna radiating structure shows plane wave properties. Without being troubled at the moment by the problem of what kind of charge or current distributions are necessary to establish the plane wave which propagates in lossless unbounded isotropic media and coincides with the (ϕ_0 i θ_0) direction, it is worthy to study in more detail the plane wave properties and the phenomenon of its propagation (Stratton 1941; Booker, Clemmow 1950). Basically, the electromagnetic field of the plane wave is described by its electrical $\mathbf{E}_{\mathrm{pl}}$ and magnetic $\mathbf{H}_{\mathrm{pl}}$ components expressed as functions of three dimensional coordinates and time. For the (ϕ_0, θ_0) direction of propagation:

$$\vec{E}_{\text{pl}} = \vec{E}_0 \mathrm{e}^{i\vec{k}_0 \vec{r}} \tag{6-21a}$$

$$\vec{H}_{\text{pl}} = \vec{H}_0 \mathrm{e}^{i\vec{k}_0 \vec{r}} \tag{6-21b}$$

where

$\vec{k}_0 = -k\sin\theta_0\cos\phi_0\hat{x} - k\sin\theta_0\sin\phi_0\hat{y} - k\cos\theta_0\hat{z}$ (propagation vector)

$k = 2\pi/\lambda_0$ (free-space wavenumber).

It is interesting to evaluate the dimensions of the space in which quasi-planar waves propagate in the antenna vicinity. Without going into details it can be said that such space is similar to the minimum sphere of the given antenna. For the short dipole, the radius of a quasi-planar zone approaches $4.8\lambda_0$ (Hansen J. 1988, Sec. 7.2). The amplitude and phase nonuniformity along the *x*-axis ($x < 3.8\lambda_0$) is 0.001 dB and 0.04°, respectively.

The understanding of the plane wave spectrum produced by an arbitrary antenna is illustrated in Figure 6.15. The waves have different direction of propagation. The spherical field generated by the source is a superposition of these plane waves. Integration over the spatial spectrum produce the far-field radiation pattern of the radiation source. It must be noted, that the insufficiently large separation between the scanning and the AUT planes, led to a small number of spherical wave components, which decreased the resolution and accuracy of the measurements.

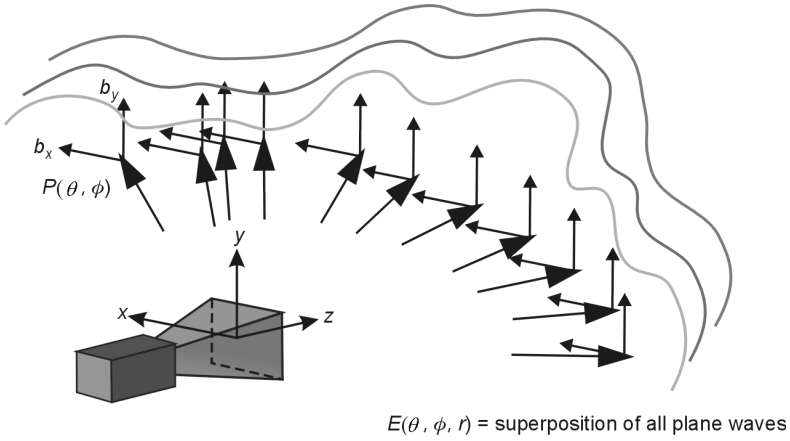

Fig. 6.15. Plane wave spectrum propagating outside the aperture radiation source.

Far-field determination with vector Kirchhof integrals

Knowing the current distribution, it is possible to determine the properties of antenna radiation at the given observation point. When the electromagnetic field components in the near field are known and the current distributions at the antenna aperture

are not, other methods of radiation pattern determination must be developed. There are techniques which rely on acceptable approximations of the fields recorded in the proximity of the antenna structure. One of these techniques is the *Field Equivalence Principle*. In electromagnetics it proves powerful when equivalent problems, yielding the same solution within a specific scope, are formulated. When adopting the equivalence principles, the field outside an imaginary closed surface (such as *S*) is obtained by introducing suitable electric and magnetic current densities onto surface *S* (Yaghjian 1984b). The introduced densities must satisfy the boundary conditions. Intuitively, the approach can be explained with reference to the Huygens's principle applied to continuous field sources. The Huygens's principle states that each point of a primary wave front can be regarded as a new source of a secondary spherical wave, and a secondary wave front can be viewed as the envelope of these secondary spherical waves.

Let us assume to be able to measure the electric and magnetic fields on an arbitrary surface *S* encompassing the measured antenna (Yaghijan 1986). The fields outside *S* can be expressed at any arbitrary point of observation by integrating the electric and magnetic fields tangential to *S* (*Kottler-Franz formula*). Our measuring system should be sensitive to different field components, so it is possible to provide a specific field type such as tangential or radial. The electric far field outside *S* – which is responsible for the radiation pattern – can be derived in terms of the so-called *vector Kirchhof integral*. The *vector Kirchhof integral* sets a cornerstone for the far-field computations with the integration method (another method makes use of the plane wave spectrum). In near-field measurements, *S* can be chosen as a scanning aperture, since in engineering there is generally no need to require that *S* be entirely closed. Although the *Kottler-Franz formula* and *vector Kirchhof integral* are simple in form, they need measurements of both tangential electric and magnetic fields on the entire *S*, and this is a serious drawback. Another impairment is the involvement of surface integration, which uses considerable computer resources and time.

It would be profitable if the *vector Kirchhof integral* could be derived using either the tangential electric or the tangential magnetic field. Then, the measuring equipment would record one physical quantity only. Preference should be given to the electric field as the measurements of the magnetic field components are much more troublesome. By utilizing the dyadic Green's function **G** it is possible to relate the outside electric field to the tangential electric field on the closed surface *S*. The problem can be solved when it is possible to find the **G** function. If the shape of *S* supports the orthogonal vector wave functions of *M*×*N*, the dyadic Green's function **G** can be provided in a convenient form. In such a case, **G** is given in terms of *M* and *N*. There are three cardinal coordinate systems which support the *M*×*N* vector wave solutions: planar, cylindrical and spherical. Three more coordinate systems support such vector wave solutions but they are difficult to implement in a scanning system (elliptic cylinder, parabolic cylinder or sphere in the conical format). With the *vector Kirchhof integral* and dyadic Green's functions, the following equation for the planar coordinates can be written for the non-probe correction transmission formula

$$\overline{E_t}(x,y,z)=\frac{1}{2\pi}\int_{-\infty}^{\infty}\int_{-\infty}^{\infty}\overline{T_t}(k_x,k_y)\mathrm{e}^{i\gamma z}\mathrm{e}^{ik_x x}\mathrm{e}^{ik_y y}dk_x dk_y \tag{6-22}$$

This is valid when assuming that the tangential electric field is measured with an ideal probe. Unfortunately, such probes do not exist – real probes have nonuniform directive and polarization properties. That is why the measured field must be corrected for the non-ideal performance of the probe if accurate pattern results are to be achieved not only within a fragment of the main beam (Joy et al. 1978). In planar scanning the probe remains along the same direction, usually coincident with the *z*-axis, which is parallel to the main geometrical axis of the AUT. Thus, the probe is pointed exactly towards the antenna only at the center of the scanning surface. Correction in planar scanning primarily compensates the directive radiation pattern of the probe. The vector response of the probe $\mathbf{b}_t$ is expressed by the transmission formula which incorporates the probe correction term then takes the form

$$\overline{b_t}(x,y,z)=\frac{1}{2\pi}\int_{-\infty}^{\infty}\int_{-\infty}^{\infty}\overline{\overline{R}}(k_x,k_y)\cdot\overline{T_t}(k_x,k_y)\mathrm{e}^{i\gamma\gamma}\mathrm{e}^{ik_x x}\mathrm{e}^{ik_y y}dk_x dk_y \tag{6-23}$$

In the case of spherical scanning, there is a less severe need for probe correction, as the probe is always pointed towards the AUT.

For nonreciprocal antennas, the radiation pattern properties can be determined by near-field measurements with probe transmitting and test antenna receiving. Generalization of transform techniques enabling adoption of arbitrary near-field geometry emerged as an interesting research subject few years ago (Sarkar, Taaghol 1999).

Reasons for applying the FFT

It is worthy to recall that the Fourier Transform is widely applied to the synthesis of aperture antennas. For non-uniform line-sources (current distribution along the length l), the space factor is a finite Fourier Transform relating the far-field pattern to the current distribution (Balanis 1997, Ch. 7].

Computation of far-field results involves integration which must be regarded as the most time consuming task in numerical data processing. A wise way of overcoming this trouble is the use of the Fast Fourier Transform. In order to materialize this idea, the integrals are derived in the form of FFT. In consequence, the computation time becomes shorter by a few orders. The use of the FFT for the computation of integrals in the far-field transform is feasible in both theoretical approaches: plane-wave spectrum and convolutional expression of the probe fields and the AUT fields. A Fourier transform is highly oscillatory, which makes it more difficult to integrate numerically than the less varying coefficients of Jacobi–Bessel integrals. Another issue is that the

FFT origin must be set to the corner of Cartesian data, while the maximum radiation is usually in the center of the Cartesian grid. However, the shift theorem of the Fourier transform makes it possible to shuffle the results of FFT and recover the proper arrangement of the radiation pattern values (by transforming the indices of the result matrix).

6.4. Far-field transform computation in our laboratory

The development of the software needed for data processing is out of reach for an average skilled research team. Teams with at least good scientific background spent approximately four man-year to develop computer far-field transform programs. That is why many laboratories turn to already developed software. The cheapest known to our team is a computer program, for 1000 USD, for the far-field transform in the Cartesian grid (Stubenrauch 1996). More reliable products cost around 20,000 USD. In our laboratory we use the software exclusively developed within our research work.

Far-field transform in the bi-polar method

Several methods can be utilized for computing the far-field transform in the bi-polar technique:

– interpolation/FFT,
– expansion methods (Jacobi–Bessel or Fourier–Bessel),
– quasi-Fast Hankel Transform (FHT).

In our research, it was the Interpolation/FFT method that received paramount attention. One of the two primary advantages of the Interpolation/FFT method is a very short computing time. It is also well suited for phased array and multibeam antennas. The Jacobi–Bessel and Fourier–Bessel methods make use of data in the original polar arrangement of the samples. In the expansion methods, near-field distributions are expanded into double series of expansion functions. These should be chosen in order that a simple analytical expression exists for the integrals to be calculated. In the Fourier–Bessel method, the expansion functions are Bessel functions. Orthogonalities of the functions should contribute at least to the improvement of the accuracy of the method. In the Jacobi–Bessel method, the expansion must be a polynomial and the functions must be orthogonal in the *xy* plane with a weight function one. Although the Jacobi polynomials fulfill these requirements, the analytical expressions for Jacobi

polynomials do not allow a fast computation. The recursion expressions are more efficient computationally and do not cause numerical difficulties. In the expansion methods, the choice of the expansion center is vital, if rapid convergence is to be achieved. The choice is optimal when the expansion center corresponds to the peak of the main beam in the radiation pattern. That is why the methods involving the expansion center are not a favorable choice in the far-field computation of antennas with off broadside beams. The accuracy of the two methods depends on the number of coefficients in the expansion series (Yaccarino et al. 1994). In the Fast Hankel Transform (FHT) the near-field is expanded into the azimuthal functions $\cos n\phi'$ and $\sin n\phi'$. The Hankel transform can be evaluated as the Abel transform, followed by the Fourier transform. In some instances, the Abel transform can be computed with the FFT algorithm. The FHT method needs an interim step to handle the uniformly spaced samples.

Data truncation and adjustment of data recorded on circular grid to square grid

Influence of truncation is observable in Figure 7.12 comparing the radiation patterns obtained with two near-field systems: at the Technical University of Denmark and our laboratory. Our bi-polar system suffers from data truncation. In such a case the sidelobes at the edge of far-field pattern, become lower than they actually are. Indeed, the sidelobes obtained with the spherical near-field system (which does scanning on a full sphere) are slightly higher than those provided by bi-polar system at edge of the valid data area.

In order to overcome the problem of data truncation, extrapolation of field outside the scanned area can be applied. We consider application of the method described by Italian researchers to estimate the outside samples (D'Agostino et al. 2003). The method requires acquisition of a limited number of extra samples.

In the bi-polar method the scanning area is circular, while the FFT method calls for data in the rectangular format. To solve this inconsistency, the square Cartesian grid can be circumscribed by the circular aperture. The square area can be filled with *zeros* outside the circular scanning area. In another instance (Fig. 6.16b), the parts of the outermost rings of the bi-polar grid are truncated. When the square is inside the circular area, only about 64% of the total scanning area might be utilized in far-field computing. In order to avoid acquisition of redundant samples, the scanning area can be set to a square instead of a circular shape (by trimming each arc length). Fortunately, the choice of the approach does not decrease the angle of view in the far-field results at both principal cut-planes. Outside the near-field results extrapolated values can be added and in that way truncation drawback is mitigated. The technique is addressed in Section 7.6.

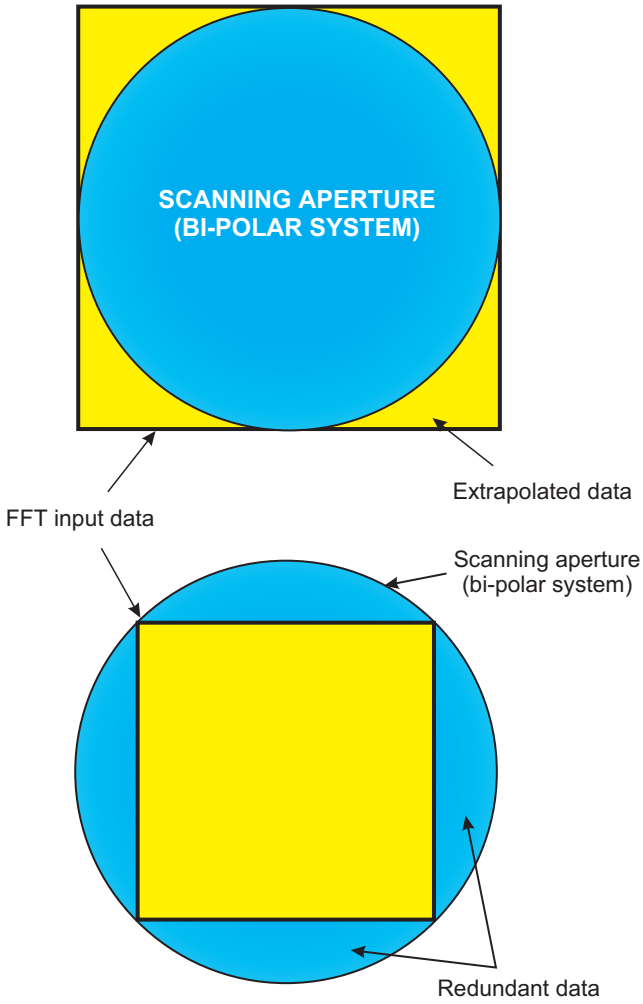

Fig. 6.16. Two possible transitions to a square data area from the circular data area in the interpolation/FFT transform method.

Determination of spherical coordinates in the far-field results

The matrix of the far-field results is the same as the matrix of the input values (near-field data plus zero pads). As shown in Figure 6.17, the assignment of the far-field data to the spherical coordinates is expressed in terms of the angle of view with respect to the origin of the coordinate system in the center of the AUT. In order to figure out the permissible angle at which the far-field results can be regarded as reliable (*valid angle*), the geometrical analysis illustrated in Figure 5.5 is used.

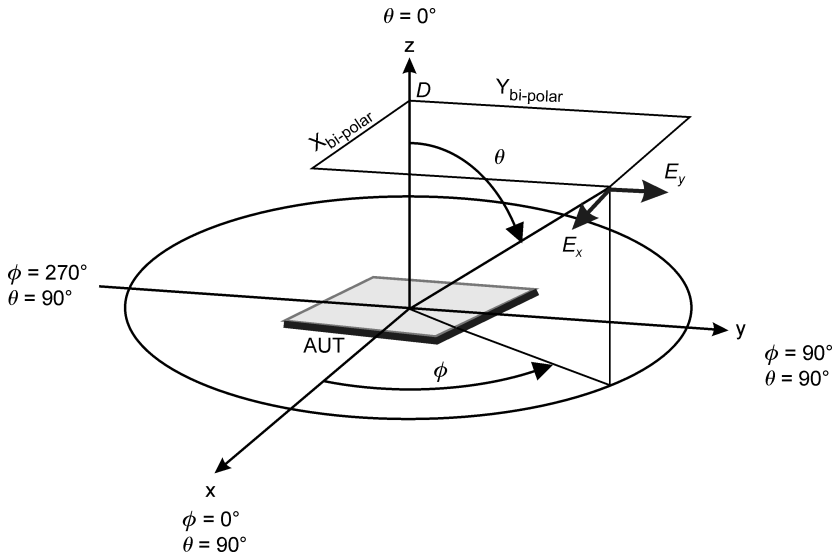

Fig. 6.17. Determination of spherical coordinates in the far-field results of the bi-polar measuring system.

6.5. Thinning of the bi-polar sampling grid

Sampling point redundancy in polar grids

As the scanning time is long and any further speeding up of the probe movement faces limits related to the accuracy of the sample taking process, other approaches towards a reduction of the measuring time must be taken into consideration. Particularly promising is the suppression of the sampling point redundancy in the grid center (Williams et al. 1994a; Kabacik et al. 2000a). Another approach involves the spiral grid (Williams et al. 1995). Even though the spacing criterion (6-4 and 6-7) relaxes the requirement for sample spacing at the outer rings, the number of sample arcs still must be large (the 6-4 or 6-7 criterion usually sets the outermost sample spacing within a half wavelength and a wavelength). Redundant points are concentrated in the bi-polar grid center (please refer to Figs. 5.3 and 5.4). It is worthy to point out that the redundancy of the sampling points should not be viewed exclusively as a drawback, since

(i) a large sample density in the central grid zone often covers a region of the strongest electromagnetic field,

(ii) the utilization of a redundant grid might be beneficial to the scanning system (compensate some of its shortcomings).

Some of the grid points can be reduced if the near to far field transform does not proceed all the points on the measured grid. For example, the *Jacobi–Bessel* and *Fourier–Bessel* transforms do not permit missing any point from the original scanning grid. But the Interpolation/FFT method – implemented in our laboratory – features a lot of flexibility in that respect (Williams et al. 1994b). The interpolation algorithm applied in our system is described elsewhere (Bucci, D'Elia 1994b). Owing to the interim interpolation step, the number of the bi-polar samples may be reduced and in this way redundancy is suppressed. Without changing the angular speed of the probe arm and the AUT, the thinning of the bi-polar scanning grid has the potential for shortening the measuring time even by 40%.

Thinning of the polar-grids

While investigating the thinning methods, we considered scans in theta (arm tilting) with steps in phi (AUT revolving) or scans in phi with steps in theta. We arrived at the conclusion that the first approach is more beneficial and we proposed a differentiation of the arc lengths as depicted in Figure 6.18 (Kabacik et al. 1998b). Arcs of trimmed lengths are grouped in identical clusters, each comprising even K number of arcs (K being an arc index). Generally, the arcs within each cluster are grouped in pairs which

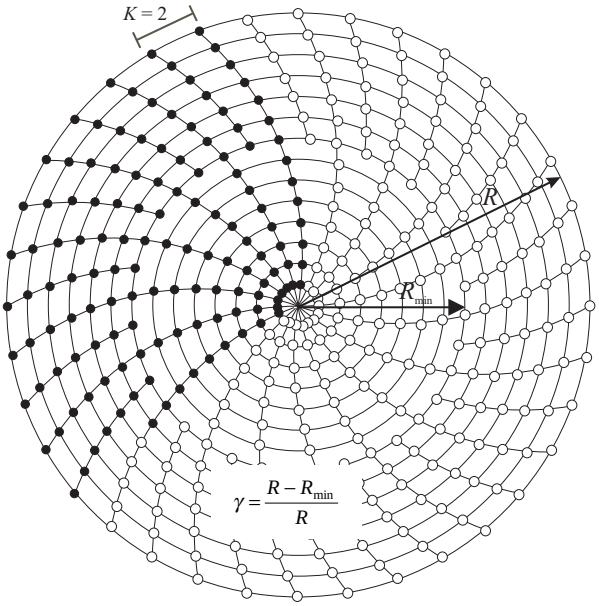

Fig. 6.18. A thinned grid with a reduced number of sampling points used in our bi-polar near-field facility (the K value and thinning coefficient γ is defined as well). Sequence of sample acquisition used in our laboratory is illustrated with black and white dots: recorded points are denoted with black dots, while those to be recorded are white (Kabacik et al. 1998b).

have the same length. The sequence of sample acquisition used in our system is also presented in the Figure. The idea of time advantages obtained with that approach can be drawn from Table 6.1. As it can be seen from the data itemized there, the reduction of the measuring time may reach 265 minutes as compared to the originally needed 445 minutes (measuring time reduction by 41%). It is worth noting that further minor improvements can be accomplished by allowing non-uniform angular steps between the arcs. The use of a spiral trajectory of the samples is another way of reducing the redundancy in the bi-polar grid, but the method does not necessarily shorten the measuring time.

Table. 6.1. Time needed to complete scanning on a circular bi-polar aperture for some values of the arc index (K) and the thinning coefficient (γ). For $K = 1$ and $\gamma = 0$ the grid does not involve any thinning.

K	γ	**Time [min]**
1	0	445
2	0.5	335
4	0.65	265
8	0.5	302

6.6. Determination of polarization properties in far-field results

When the radiation pattern properties are considered off the principal cut-planes, different definitions of the polarization plane can be introduced. A thorough definition of the antenna polarization properties in various coordinate systems was proposed by (Ludwig 1973). The use of three definitions of co- and cross-polarization properties is substantiated by the varying orientation of the polarization planes of the probe with respect to the AUT in each of the three cardinal scanning systems.

Analyzing the distribution of the phase shift between the *EX* and *EY* far-field results, the type of AUT polarization can be determined. Studying the phase advancements, it is possible to clearly distinguish the left- and right-hand circular polarization. Last but not least, the slant angle of the linear polarization plane can be straightforwardly evaluated.

CHAPTER 7

RADIATION PATTERN MEASUREMENTS

7.1. Probe used in the measurements

The major probe-related impairments influencing the accuracy of the near-field method are the shape of the radiation patterns and the quality of the polarization properties. Dual-polarized probes are much more expensive than single-polarized ones but they have the advantage of eliminating errors which result from the inaccuracies of the repeatability of the probe positioning. It is due to the excessive costs that dual-polarized probes are less commonly found in laboratories. Carefully designed, calibrated dual-polarized probes are regarded as being best suited for near-field scanning, but their price is high. As such costs are beyond the budget of many research projects, attention has been directed to the less expensive illuminating feeds of reflectors. However, the most common choice is a waveguide section open at one end or a low-gain horn antenna.

A typical probe utilizing an open waveguide is described pictorially in Figure 7.1. Such probes are used by our laboratory. The waveguide section should be long enough to allow propagation at least two and a half waveguide-wavelengths signal (our probe for the C band had a 205 mm long waveguide section which is equivalent to $3.4\lambda_0$ at 5 GHz). The measured radiation patterns of our open-waveguide probes for operation in the X-band are plotted in Figures 7.2 (*E*-plane) and 7.3 (*H*-plane). The width of the probe beam measured at a 3dB drop is narrower in the *H*-plane (±30°) than in the *E*-plane (±40°). It should be noted that the probe-AUT spacing increases as the probe travels out of the bi-polar grid center. It may occur that the probe will operate in its near field for the sampling points positions close to the grid center. In such instances, the width of the probe beam is broader than the one observed in the far field. When the probe reaches the outskirts of the scanning circle, the distance with respect to the AUT is usually far enough to consider the probe as operating almost in its far field. Thus, the use of the far field radiation is reasonable enough to determine the allowable view angle of the probe. The beamwidth value of the probes described by the plots in Figures 7.2 and 7.3 makes their use preferable with view angles not much greater than

30°. These plots reveal also that the signals received through the backlobe are 18 dB or more below the maximum of the main beam (what is further increased by absorber panel around the probe).

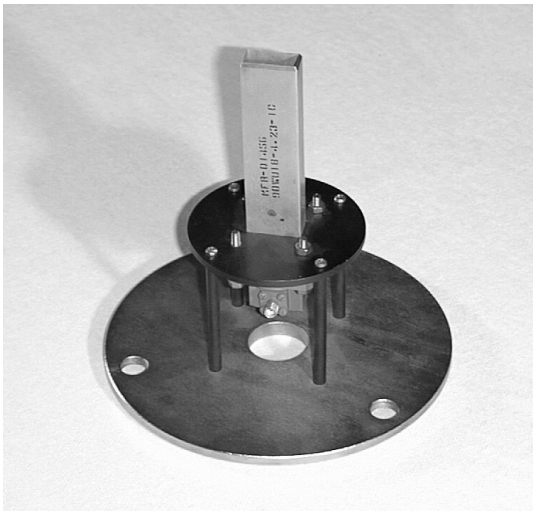

Fig. 7.1. Probe consisting of an open-end waveguide section for operation in the X-band. The chamfer form of the front side of the waveguide walls is needed to reduce wave scattering.

As the phase of the sampled data is an important factor affecting the calculated far--field results, the phase characteristics of the radiation pattern must not be neglected. The phase characteristics of the antennas change slowly within the main beam. As long as the drop in the directivity is lower than 10 dB with respect to the peak of the main beam, phase variations are small. The amplitude drop by 2 dB is paralleled by almost negligible phase changes. Normally, the cross-polar and co-polar field components corrupt each other at the waveguide to the coaxial adapter in the open waveguide probes.

In our laboratory, we tried to use a corrugated feed horn of the X-band reflector antenna which was priced below € 3,000. The photograph of the feed purchased from Taiwanese *Victory Industrial Corporation* is shown in Figure 7.4. The feed operates over the 1 GHz band centered at 11.2 GHz. The impedance match is good and the isolation between two ports is not worse than 35 dB.

A major shortcoming is the narrow beam of the radiation patterns for *X* and *Y* polarizations and this can be attributed to the corrugation in the horn, which has tapered illumination amplitude of the reflector. The measured radiation patterns for the two principal planes at both ports are plotted in Figures 7.5 through 7.8. Since the beam for port *X* is ±15° wide, the scanning range is limited to narrow view angles. The beam is also narrow at another port, and radiation pattern shape shows a noticeable frequency-dependence.

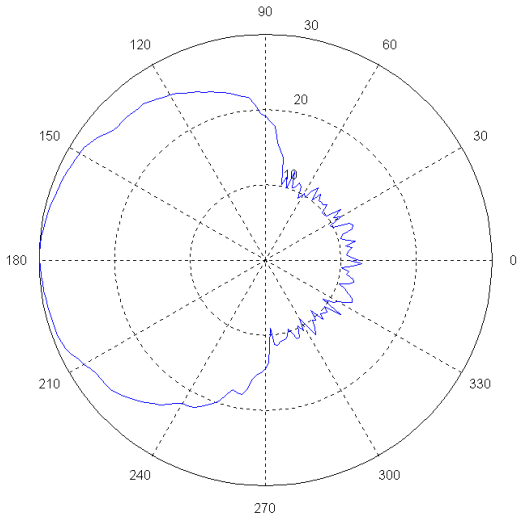

11400 MHz, *E*-plane

Fig. 7.2. Measured radiation pattern of the single-polarized probe made of a 110 mm long WG-90 waveguide section.

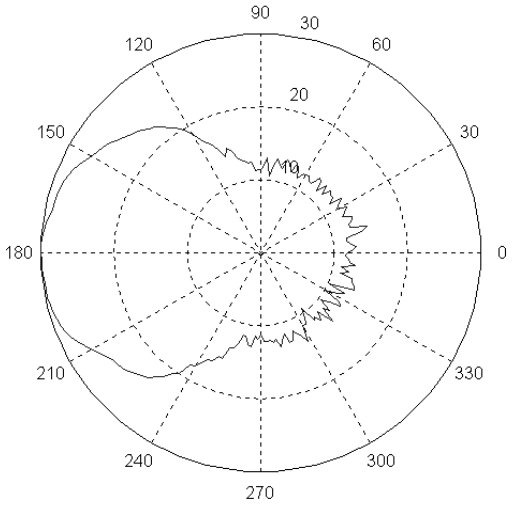

11400 MHz, *H*-plane

Fig. 7.3. Measured radiation pattern of the single-polarized probe made of a 110 mm long WG-90 waveguide section.

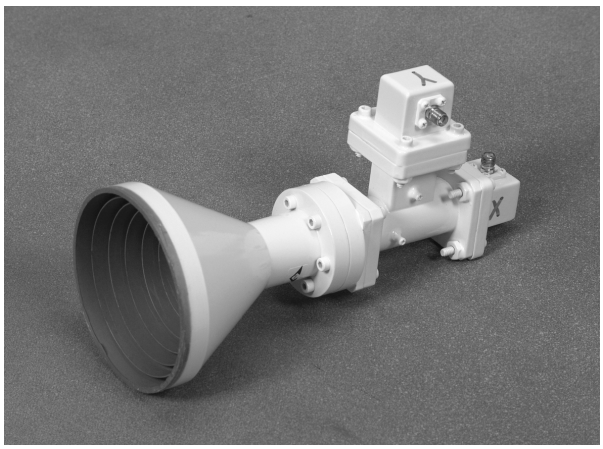

Fig. 7.4. Dual-polarized probe, made of antenna feed, for operation in the 10.7–11.7 GHz frequency range (*VIC*, Taiwan).

The difference in a shape of radiation patterns between ports 1 and 2 is remarkable. The explanation gave closer examination of differences between coupling of the X and Y ports to the horn. The signal coupled to the Y port has much bigger losses than that at the *X* port mounted at the end of a straight waveguide section directly facing the horn input. Indeed, the archive files with relevant calibration data of these measurements,

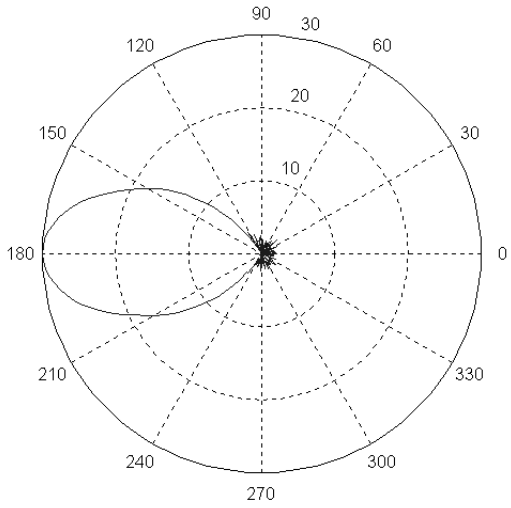

11701 MHz, *E*-plane

Fig. 7.5. Measured radiation pattern at *port 1* (*X*) of the dual-polarized probe.

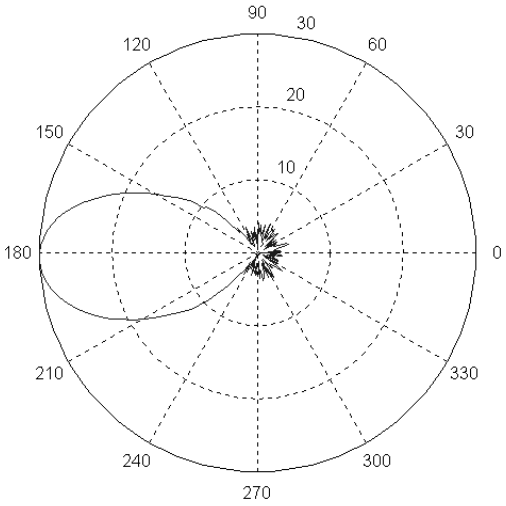

11800 MHz, *H*-plane

Fig. 7.6. Measured radiation pattern at *port 1* (*X*) of the dual-polarized probe.

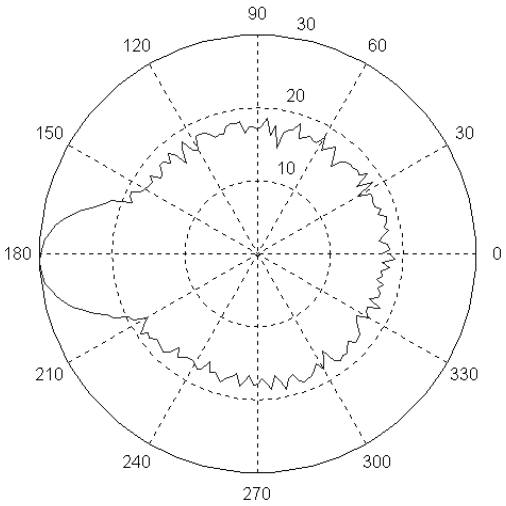

11800 MHz, *E*-plane

Fig. 7.7. Measured radiation pattern at *port 2* (*Y*) of the dual-polarized probe.

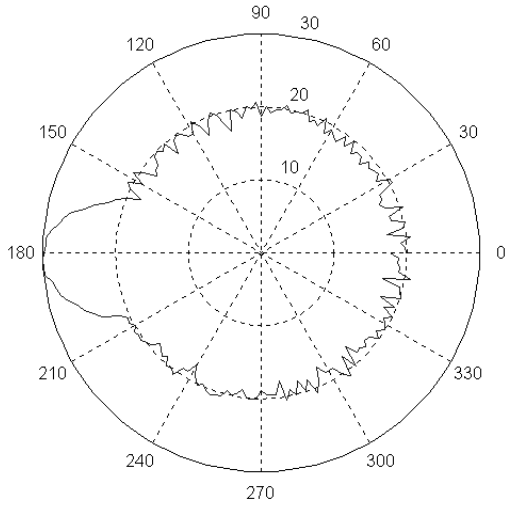

11800 MHz, *H*-plane

Fig. 7.8. Measured radiation pattern at *port 2* (*Y*) of the dual-polarized probe.

show that the signal level was almost 20 dB weaker at the *Y* port, than at the *X* input. The consequence was that the dynamic range of the *Y* port radiation pattern measurements was only 10 dB above noise.

7.2. Probe corrected measurements

Figure 7.9 depicts the difference in the shape of the radiation pattern between the ideal and real probe. As it can be inferred from the plots of Figure 7.9, spherical scanning requires a narrower view angle for the probe than does planar scanning. The broader is the probe view angle during scanning, the more desired becomes an accurate probe correction procedure due to the non-ideal probe pattern.

To eliminate the adverse influence of the non-ideal directivity patterns of real probes, the near-field results need to be recalculated with either the theoretical or the experimental correction method. The probe correction procedure is carried out with the results of the far-field transform. The advantage of the experimental method is that the details of the probe structure need not be exactly known. The series of the correction coefficients required to compute the probe-corrected results are basically obtained by measuring the radiation pattern of the probe in two principal planes. During this measurements, two identical probes are used, at the transmitting and at the

receiving side. Needless to say that the application of two probes is not always affordable or feasible, so the experimental method has been implemented in a few laboratories only. It should not be missed that the method compensates even little details in the characteristics of the actual probe (*e.g.* small asymmetry).

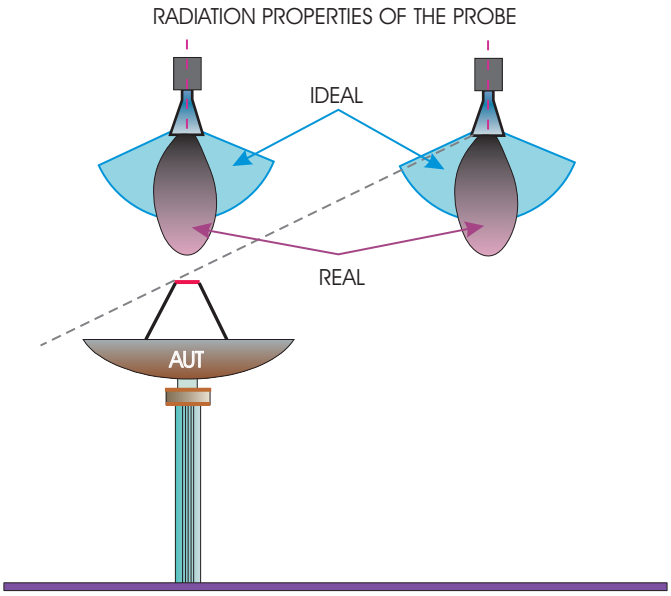

Fig. 7.9. Difference in the radiation pattern between an ideal and a real probe.

In the theoretical approach to the probe correction, the equalization of the adverse tapering is solely carried out with analytical formulas or numerical modeling of the probe. In order to perform one of such analyses it is indispensable to acquire accurate geometrical and dimensioning data describing the probe. The analytical formulas for the radiation pattern of the open-ended waveguide have been derived by Yaghjian (Yaghjian 1984; Repjar et al. 1988). Since in our laboratory use was made of waveguide probes and the accuracy of these analytical formulas had been well proved, we decided to use them in our procedure of probe correction. The presented method provided good results for the X-band waveguide but, unfortunately, we faced some problems when computing the correction for the C-band measurements (the expression for the open-ended waveguide yielded doubtful values).

In the theoretical probe correction, the compensation process is performed in the spatial spectrum. If use is made of a dual-polarized probe, correction consists in solving a straightforward set of equations (Paris 1978; Joy et al. 1978). With single-polarized probes, the probe correction formulas take the form

$$A_x(\theta,\phi)=\frac{k\cos\phi\cos\theta}{E_E(\pi-\theta)}\left(A_{m,x}(\theta,\phi)\cos\phi+A_{m,y}(\theta,\phi)\sin\phi\right)+ \\ -\frac{k\sin\phi}{E_H(\pi-\theta)}\left(A_{m,y}(\theta,\phi)\cos\phi-A_{m,x}(\theta,\phi)\sin\phi\right) \tag{7-1}$$

$$A_y(\theta,\phi)=\frac{k\sin\phi\cos\theta}{E_E(\pi-\theta)}\left(A_{m,x}(\theta,\phi)\cos\phi+A_{m,y}(\theta,\phi)\sin\phi\right)+ \\ +\frac{k\cos\phi}{E_H(\pi-\theta)}\left(A_{m,y}(\theta,\phi)\cos\phi-A_{m,x}(\theta,\phi)\sin\phi\right) \tag{7-2}$$

where:

$k=\frac{2\pi}{\lambda}$;

$E_s(r\to\infty)=E_E(\theta)\cos\phi\vec{e}_\theta-E_H(\theta)\sin\phi\vec{e}_\theta$;

E_s is the radiation pattern of the probe determined for the $\vec{e}_x$ polarization vector and $A_{m,x}(\theta, \phi)$, $A_{m,y}(\theta, \phi)$ are the components of the spatial spectrum derived by the Interpolation/FFT transform method.

7.3. Polarization correction

Our calculations performed with the theoretical method have shown that a tough maintenance of the polarization plane orientation for the probe is of absolutely critical meaning. This is so because even a slight polarization misalignment of the actual probe results in the leakage of energy between two orthogonal field components (especially undesired when the power of one component is much smaller than that of the other one). The goal of the polarization correction is to recover a proper assignment of the measured values to the *X* and *Y* field components. An illustration of the principles of signal leakage between the orthogonal components of the recorded probe excitation coefficients is in Figure 7.10. Probe polarization correction can be handled either theoretically or experimentally. As yet we have not implemented any procedure of probe polarization correction. In our investigations into the polarization alignment we focused on a precise counter-rotation of the probe in the scanner, thus trying to prevent significant signal leakage between *X* and *Y* components.

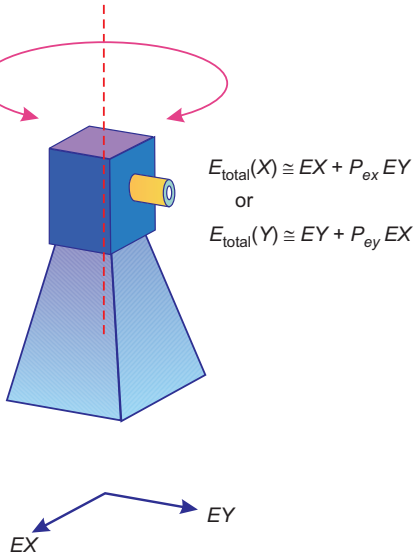

Fig. 7.10. Signal leakage between orthogonal ports (*X* and *Y*) of the probe which mostly corrupts far-field results in cross-polar pattern and for low-level sidelobes.

7.4. Measurements of fixed beam arrays

Measurements of the 8×8 microstrip array

The 64-element microstrip array (RMB-64) operating around 9 GHz was measured at our laboratory for various parameters of the sampling grid and distances to the probe. The antenna was placed on a larger ground plate than was the printed circuit alone. The extended ground plate is to provide well established conditions for the formation of the radiation pattern and to reduce the scattering of the surface waves from the edges of the ground. Figure 7.11 shows the RMB-64 antenna during tests at our laboratory. At the end of the scanner arm, there is a single-polarized probe, made in the form of an open-ended waveguide. X-band frequencies impose reasonably tough conditions on the test of the measuring system. The geometrical accuracy required at these frequencies is high, and the microwave equipment operates with a short wavelength. Furthermore, the spacing between the sampling points establishes sufficiently challenging conditions for the verification of the system run.

The radiation patterns measured for two spacings between the sampling points in the grid are depicted in Figures 7.12 through 7.14. The results show that the major features of the radiation patterns, such as the shape of the main beam, the number of sidelobes and their level, or the null pointings, are in a close agreement with the design values and furthermore, are in a good agreement with those obtained with other

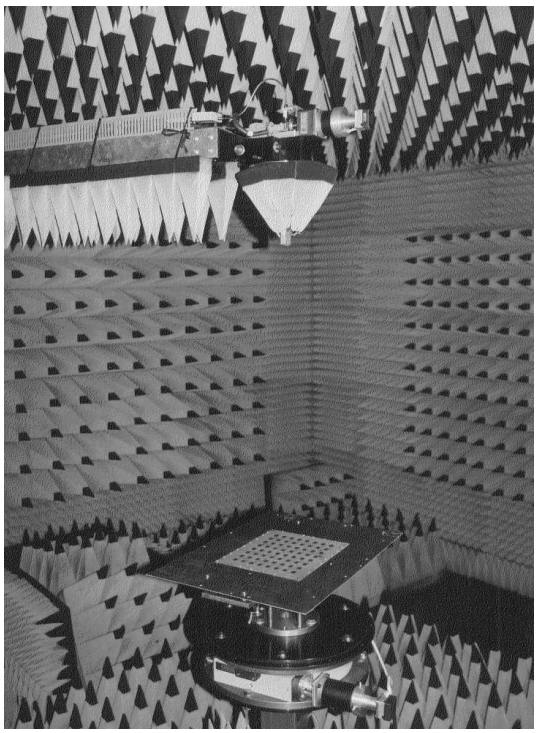

Fig. 7.11. Photograph of the RMB-64 array during tests with our near-field system.

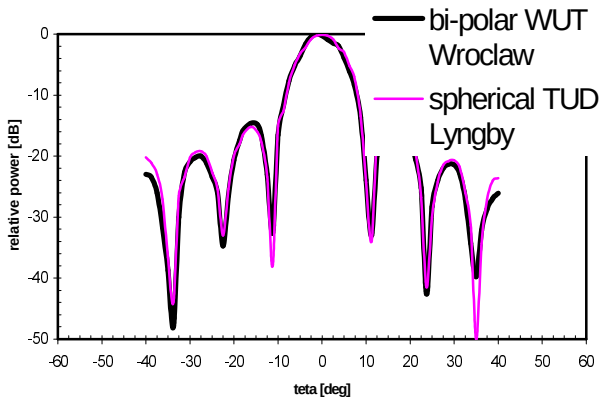

Fig. 7.12. Far-field E-plane radiation pattern (co-polar) of the RMB-64 array (linear polarization) measured at our near-field laboratory (WUT) and at the Spherical Near-Field Antenna Test System at the TUD, Lyngby, Denmark (reference plot). In the bi-polar scanning, spacing between the probe and the RMB-64 planes was 700 mm ($21.1\lambda_0$ at 9030 MHz), sample spacing, $0.4\lambda_0$. The reference radiation pattern was obtained with a highly accurate TUD spherical system (Kabacik 2003a).

antenna measuring systems (Kabacik 2003a). The reference data were obtained with a highly accurate spherical near-field facility operated by the Technical University of Denmark, Lyngby. The facility is part of the laboratories of the European Space Agency and is regarded as their validation measuring system. The far field data obtained for the RMB-64 array at that laboratory have been published elsewhere (Kabacik 1992).

The pattern in Figure 7.14 was derived from the measured data when the sample spacing was set to half wavelength and is in a good agreement with those obtained with a smaller sample spacing (the sample spacing in Figures 7.12 and 7.13 being $0.4\lambda_0$). However, the lack of even small oversampling in the near-field data sampled at half wavelength produced ripples in the radiation pattern plots at the third and farther sidelobes. There are also abrupt, though small, perturbations at the second sidelobes.

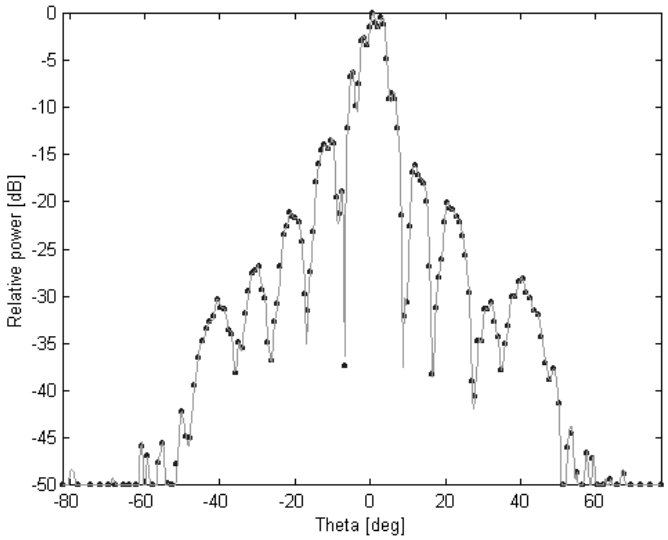

Fig. 7.13. Far-field *H*-plane radiation pattern of the RMB-64 array (linear polarization) measured at our near-field laboratory. Spacing between probe and AUT, 700 mm ($21.1\lambda_0$ at 9030 MHz). Sample spacing, $0.4\lambda_0$. Radius of scanning aperture, 78 cm. Data acquisition time, 8 hours 15 minutes.

In spite of some distortions in smoothness, the major points of the derived *H*-plane pattern are consistent with the reference data measured at the ESA facility. The possible explanation for the distortions mentioned is the incomplete summation of the *EX* and *EY* field components (particularly important at the *H*-plane).

One of the basic methods for verifying the accuracy of the near-field laboratory is the comparison of the far-field results which have been obtained with the near-field data scanned for different probe-AUT spacings. The radiation pattern presented in Figure 7.15 was derived for the RMB-64 array with an almost 1 meter distance between the scanning plane and the AUT. The results are consistent with those shown in Figures 7.12 and 7.14. The levels of the sidelobes are somehow underestimated. Even

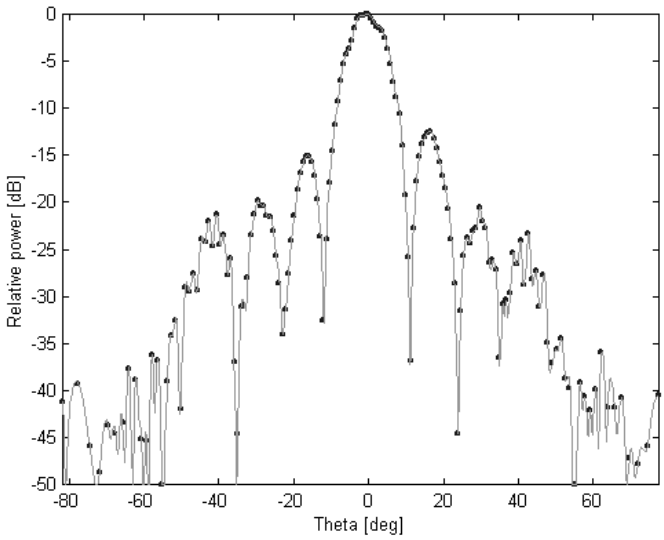

Fig. 7.14. Far-field *E*-plane radiation pattern of the RMB-64 array (linear polarization) measured at our near-field laboratory. Spacing between probe and AUT, 700 mm (21.1λ_0 at 9030 MHz). Sample spacing, 0.5λ_0. Radius of scanning aperture, 78 cm. Data acquisition time, 6 hours 40 minutes.

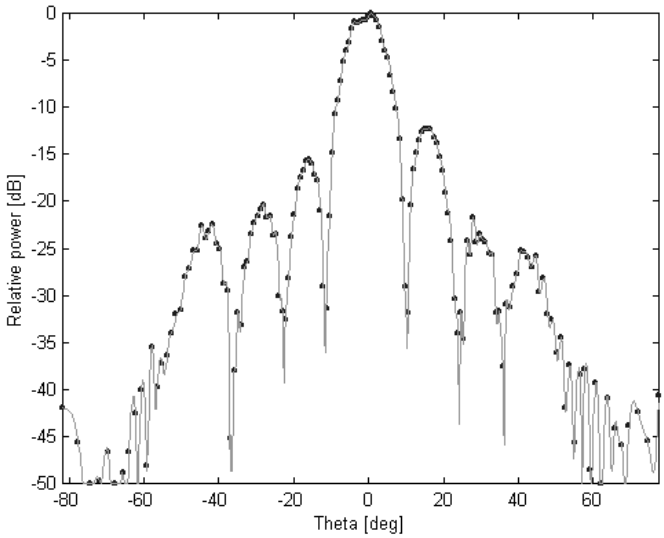

Fig. 7.15. Far-field *E*-plane radiation pattern of the RMB-64 array measured at our near-field laboratory. Spacing between probe and AUT, 945 mm (28.5λ_0 at 9030 MHz). Sample spacing, 0.45λ_0 at scanning circle edge. Radius of scanning aperture, 105 cm. Data acquisition time, 10 hours 40 minutes.

though the sample spacing was set with a small oversampling factor ($0.45\lambda_0$), the measuring time approached 11 hours. Comparing the three plots obtained for the *E*-plane of the RMB-64 antenna, it can be said that our laboratory provides far-field results which are independent of the actual probe-AUT spacing. Such consistency of the far-field results validates the implementation of the near-field method in our laboratory.

The near-field technique is sensitive enough to detect even slight changes in the AUT (*e.g.* a small failure of the feeding system, or a broken radiator). We experienced that one morning when our bi-polar facility detected a small distortion in the 64-element array (X-band, fixed broadside beam) instantly within the check procedure routinely held before scanning starts. What indicated that something went wrong was the value of the probe excitation coefficient at the center of sampling grid different that it was before. This value was always checked prior to scanning. The explanation for that distortion was in a scratch across one of the microstrip lines feeding basic clusters consisting of four antenna elements. A scratch probably made by a serviceman unintentionally while working on a main the day before.

Measurements of the 16×16 microstrip array

The 256-element microstrip array (TPA-256) – which is shown in Figure 7.16 – was developed in our earlier studies and underwent measurements at our near-field laboratory. The number of elements of the TPA-256 was chosen so as to obtain the gain required in DBS applications. As the main beam of the array is narrow (around 4° in both principal cut-planes), the antenna causes another kind of challenge for the measuring system.

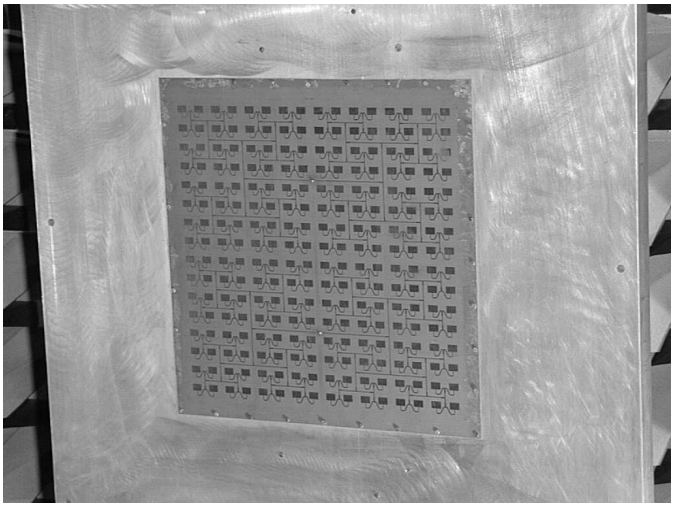

Fig. 7.16. Photograph of the linearly polarized TPA-256 array (31×33 cm) mounted on an extended ground plate (70×70 cm).

The radiation patterns of the TPA-256 antenna measured with our near-field laboratory are in Figures 7.17 and 7.18 for the *E*-plane and the *H*-plane, respectively. The number of sidelobes, their maximum pointing and the spherical coordinates of the nulls are in good agreement with the values obtained with another measuring system (far-field test range). Since the RMB-64 and the TPA-256 arrays make use of a rectangular element grid, the most important sidelobes are along two principal cut-planes; the sidelobes along the diagonal planes are less important. However, being composed of the cross-polar field, the sidelobes along the diagonal planes are often greater than the sidelobes which consists of the co-polar field components. The patterns determined with our measuring system are in good agreement with those measured directly with the far-field method at the Telecommunication Research Laboratory in Gdansk, Poland (this facility uses the time-domain technique in the far field).

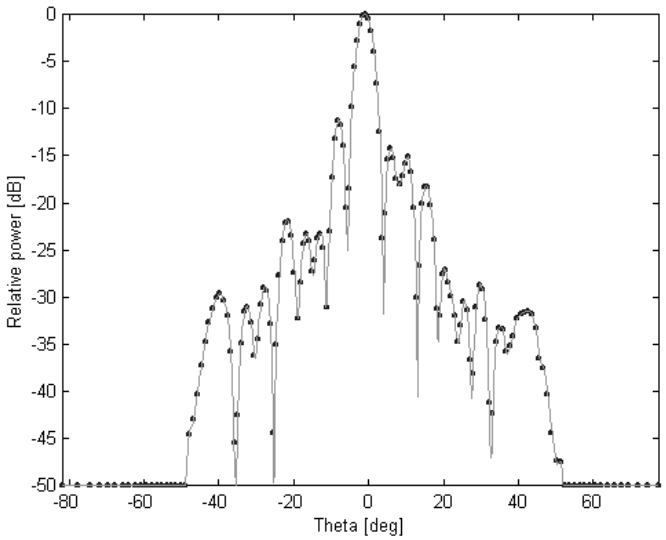

Fig. 7.17. Far-field *E*-plane radiation pattern of the TPA-256 array (linear polarization) measured at our near-field laboratory. Spacing between probe and AUT, 590 mm ($22.1\lambda_0$ at 11250 MHz). Sample spacing, $0.4\lambda_0$ at scanning area edge. Radius of scanning aperture, 59.8 cm. Data acquisition time, 7 hours 30 minutes.

Results obtained at various probe-antenna spacings are often compared in order to verify correctness of antenna near-field systems. Figure 7.19 shows the plots of the far-field results for the TPA-256 antenna, when the probe-AUT spacing has been increased by 222 mm ($8.3\lambda_0$) with respect to the spacing chosen for the measurements presented in Figures 7.17 and 7.18.

Verification of our system accuracy is comparison between Figures 7.17 and 7.19 (within the valid angle). These Figures were taken for the almost the same parameters, but only spacing between the scanning plane and the antenna aperture was

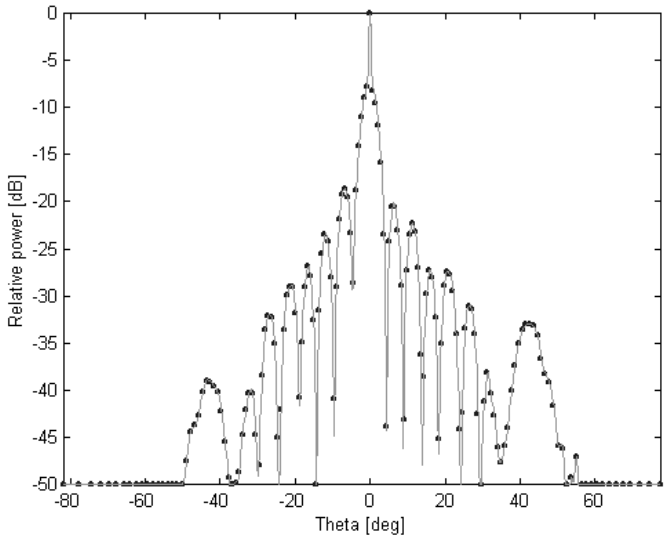

Fig. 7.18. Far-field *H*-plane radiation pattern of the TPA-256 array (linear polarization) measured at our near-field laboratory. Spacing between probe and AUT, 590 mm ($22.1\lambda_0$ at 11250 MHz). Sample spacing, $0.4\lambda_0$ at scanning area edge. Radius of scanning aperture, 59.8 cm. Data acquisition time, 7 hours 30 minutes.

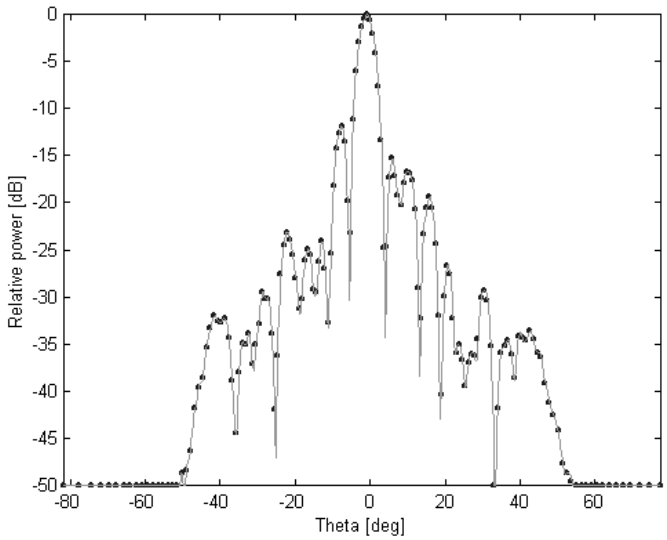

Fig. 7.19. Measured *E*-plane radiation pattern of the TPA-256 array (linear polarization). Spacing between probe and AUT, 812 mm ($30.4\lambda_0$ at 11250 MHz). Sample spacing, $0.37\lambda_0$ at scanning circle edge. Radius of scanning aperture, 75.5 cm. Data acquisition time, 10 hours 20 minutes.

different. Spacing was 590 mm ($22.1\lambda_0$ at 11250 MHz) and 812 mm ($30.4\lambda_0$) for data presented in Figure 7.17 and 7.19, respectively. Both radiation patterns are remarkably similar – the far-field plots for the TPA-256 antenna obtained with our laboratory display consistency irrespective of the probe-AUT spacing.

7.5. Measurements of arrays with a scanned beam

The results of measurements of phased arrays or other complex antennas are seldom reported in the literature. The main reason is that such antennas are designed under costly research projects, so their development involves a lot of efforts. Although the analysis of the radiation pattern properties for such antennas does not always need a complete 3D format, it is necessary to examine the radiation pattern shape in at least several cut-planes. Such flexibility in providing the results is offered normally by the near-field technique. Furthermore, the near-field technique ensures a high accuracy, which is desired in phased array tests. Because of beam tilting, the valid angle required for the near-field system must be much greater than the one needed in broadside antenna measurements.

In our laboratory, we measured the radiation patterns of the 8-element linear array capable of scanning the beam in the H-plane to 13 positions within ±45° (this array, referred to as MC-8, was developed in our earlier studies and is described in more detail in Section 8.5). The measured radiation patterns for several beams in the scan plane are plotted in three Figures 7.20, 7.21 and 7.22. The valid angle approached 40° in the case considered. As it may be concluded from the radiation pattern in Figure 7.22, our laboratory provided accurate results for the main beam when the scan angle was not greater than 30 degrees.

In all instances the results obtained with the near-field system was good in terms of the beam pointing for various scan angle. For comparison purposes, the MC-8 was measured with a simple far-field system. A close agreement between results was obtained in terms of the main beam shape. An excellent agreement was in terms of null pointing angles, irrespective of the scan angle. The measured level of sidelobes was below –20 dB in both measuring systems, which complies with the design values. However, some major discrepancies were observed in the shape of the sidelobes and the near-filed system provided results with irregular shape of sidelobes. The main reasons seem to be the undesired scattered waves and insufficiently accurate counter-rotations of the probe during measurements. Such inaccuracy produced leakage of the field between two polarization planes, as it was mentioned in Section 7.3.

Measurements of antennas with a beam tilted off the principal geometrical axis pose increased demands on the allowable level of reflected signals propagating inside the anechoic chamber. Since the AUT must revolve around its axis during scanning,

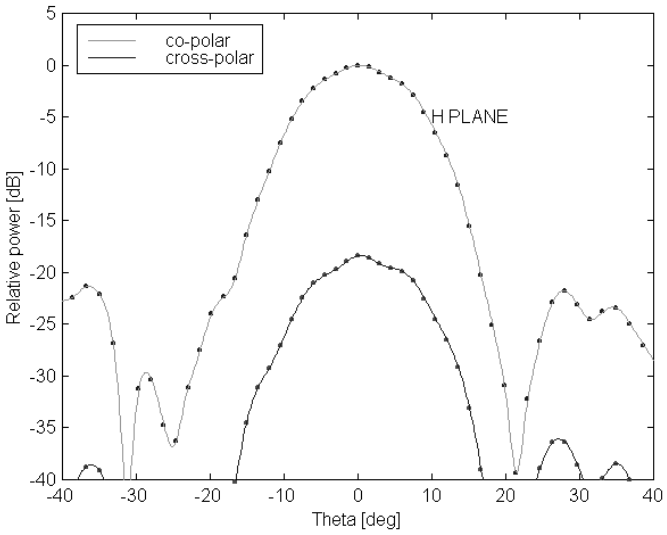

Fig. 7.20. Far-field radiation pattern (*H*-plane) for a broadside beam of the MC-8 phased array. Spacing between AUT and probe planes, 520 mm ($8.7\lambda_0$ at f = 5000 MHz).

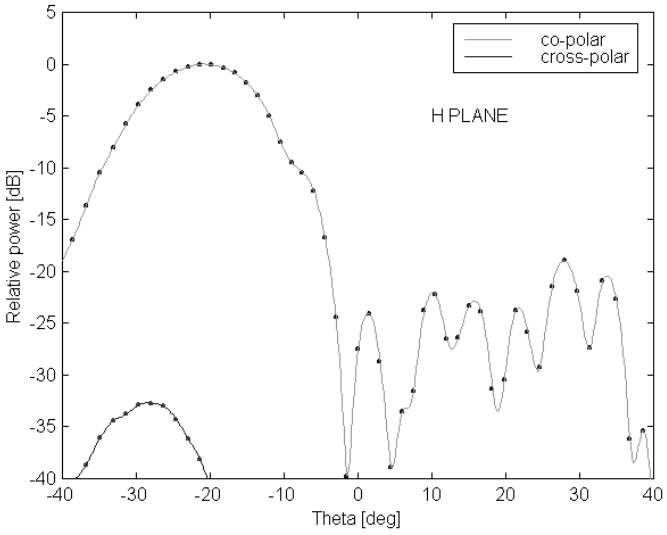

Fig. 7.21. Far-field radiation pattern (*H*-plane) for the MC-8 phased array with its beam scanned to 21°. Spacing between AUT and probe planes, 520 mm ($8.7\lambda_0$ at f = 5000 MHz).

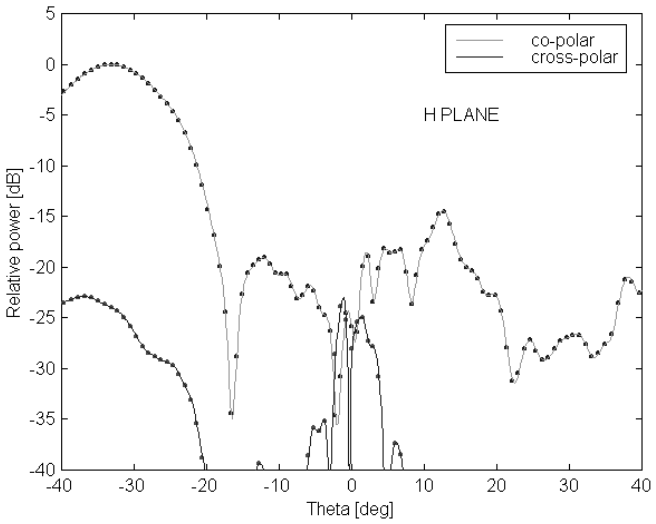

Fig. 7.22. Far-field radiation pattern (*H*-plane) for the MC-8 phased array when the beam was scanned to 33°. Spacing between AUT and probe planes, 520 mm ($8.7\lambda_0$ at f = 5000 MHz).

the main beam is not pointed at one spot all the time. In consequence, the distribution of reflected signals undergoes significant variations when the attenuation of reflected waves is moderate or poor. Undesired signals can become important, particularly in the zones where direct signals are weak. The recorded values of the excitation coefficients are considerably corrupted and far-field results are characterized by low accuracy in far sidelobe regions. The problem is even more serious with cross-polar field components (small signal power) than co-polar field components (stronger signal). Shortcomings due to poor absorption are a nightmare for many users of anechoic chambers. Sincerely saying, the chambers are not always thoroughly checked after the construction of the chamber has been completed. The scan angle, defined as the peak of the main beam, is usually derived with a high accuracy irrespective of the problems with anechoic chamber quality.

7.6. Truncation error

Due to truncation of a sampling surface, some portion of the radiation is missed in polar and cylindrical scannings. Limited scanning area seems to be of little adverse effect when directive antennas are measured. However, neglecting antenna radiation close to the limits of scanning area and outside it increases errors around the valid angle. Far-field results derived with truncated near field data show such specific inaccuracies as lower level and smaller number of sidelobe than actual ones, poorly developed nulls and unavoidable incorrect data on polarization purity. Figure 7.12

presents far-field radiation pattern obtained in our and in a reference laboratory for same RMB-64 antenna (the spherical near-field system does not suffer from truncation error). The results obtained with two measuring system are in good agreement. However, it is noticeable that outermost sidelobes in our results have lower level than these obtained with the spherical system. Such decrease of outermost sidelobe level must be primarily attributed to the truncation effect.

In order to overcome this drawback the data should may be artificially specified outside a scanning area. The most valuable method is extrapolation of data. Recently developed extrapolation techniques of electromagnetic field produce results which are highly accurate (D'Agostino et al. 2003). Such extrapolation techniques were unavailable until Italian researchers led by Prof. Bucci developed sophisticated interpolation and extrapolation algorithms utilizing the Dirichlet and Tschebyscheff sampling functions.

With such accurate extrapolation methods, it is possible to enlarge a set of input data taken into the far-field computation, thus the problem with truncation is shifted to the much farther angular regions. Usually, the data in bi-polar scanning are collected within no more than ±50° (view angle). An application of recently developed extrapolation method is comfortable, as it calls for sampling an electromagnetic field radiated by the AUT in a small number of additional points within the scanning aperture itself.

Estimation of the samples outside the circular scanning area $\rho \le R$ on the scanning plane, needs knowledge of the near-field samples on the K rings at radii ρk, uniformly distributed in the interval $[\rho(\xi_n), R]$. On each of these rings, the samples are azimuth angles $m\Delta\phi_{\min}$, where $\Delta\phi_{\min}$ is the azimuthal spacing between the samples on the last outside ring to be estimated. Fro each of the points to be estimated, p unknown outside samples are always involved in evaluation of reduced field at the point $P(\xi,\phi)$ located on a radial line. The reduced field is estimated by

$$\underline{F}(\xi,\phi) = \sum_{n=n_0-p+1}^{n_0+p} \underline{F}(\xi_n,\phi)\Omega_N(\xi-\xi_n)D_{N''}(\xi-\xi_n) \tag{7-3}$$

where the intermediate samples $\underline{F}(\xi_n, \phi)$ are given by:

$$\underline{F}(\xi_n,\phi) = \sum_{m=m_0-p+1}^{m_0+p} \underline{F}(\xi_n,\phi_{m,n})\Omega_{M_n}(\phi-\phi_{m,n})D_{M_n''}(\phi-\phi_{m,n}) \tag{7-4}$$

For each of the estimated points, K equations can be formed and the values can be determined with the OSI expansion

$$\underline{\underline{A}}\,\underline{x} = \underline{b} \tag{7-5}$$

where $\underline{b}$ is a sequence of the known terms, $\underline{x}$ is the sequence of unknown outside samples $\underline{F}(\xi_n, \phi_m)$ and $\underline{\underline{A}}$ is the $K \times p$ matrix whose elements are given by

$$A_{kn} = \Omega_N(\xi(\rho_k)-\xi_n)D_{N''}(\xi(\rho_k)-\xi_n) \tag{7-6}$$

CHAPTER 8

MICROWAVE HOLOGRAPHY AT OUR LABORATORY

8.1. Microwave holography in the bi-polar method

Since the near-field measurements need elaborated techniques and the development of the laboratory involves many efforts, it is strongly advisable to extend the range of deliverable results beyond the radiation patterns. As the far-field results obtained with the near-field method have a 3D format and comprise amplitude and phase data, it may be expected that the signal processing methods will make it possible to compute more information on the actual parameters of the antenna. One of most attractive capabilities of the method is the computation of the backward projection on an arbitrary plane, basically using the inverse Fourier Transform. Such technique is called microwave holography (Rahmat 1985; Junkin et al. 2000). With this method, we can determine the values of array element excitation (when the focus plane of the backward projection lies in the array plane). Furthermore, we can instantly sort out a failed element in the array provided that the resolution achieved is fine enough to distinguish unambiguously the elements in the array aperture. Accuracy of microwave holography on the planar surface is influenced by a variety of factors (Rose, technical information).

As microwave holographic imaging has been preferred in the tests of advanced medium- or small-sized arrays (*e.g.* phased arrays), the most desired scanning method is the one that offers a wide valid angle. A major technical impairment is that the resolution at the element level can not be easily assured when there is a subwavelength element spacing. It must be said that the longitudinal and latitude resolution obtained should not be worse than the pairs of array elements (*i.e.* the resolution along the principal planes). In microwave holography, phase values can be converged into geometrical parameters, which enables the evaluation of the actual reflector shape. One of the major advantages of the interpolation/FFT method implemented in our laboratory consists in that there is no need to define the expansion center, which must be consistent with the direction of the maximal radiation. When phased arrays or other electromagnetic systems radiating off the main geometrical axis are to be tested, the selection of the expansion center easily becomes ambiguous.

Another interesting use of the near-field holographic technique is in phase alignment. The application of this procedure to radar antenna arrays was recently described elsewhere (Patton, Yorinks 1999). The authors reported how to provide a coherent summation of the microwave signal power of all the waves radiated by the elements of the phased array in a given direction. For this reason, the compensation of the manufacturing inaccuracies is unavoidable and must be performed after the integration of the array. To reduce complexity of diagnosis systems many efforts have been undertaken in order to develop experimental methods relying on amplitude only values (Bucci et al. 2000b).

With our computer programs, it was possible to produce holographic images which disclosed the following four parameters:

- the amplitude for the *EX* field components,
- the phase for the *EX* field components,
- the amplitude for the *EY* field components,
- the phase for the *EY* field components.

Each image type provides valuable information, directing our attention to details which may have been unnoticed in other pictures. Since the magnetic field components represents surface currents, the conversion to the H_x and H_y field components can be advised in order to better evaluate surface currents. However, E_x and E_y values are good enough to give a right idea on distribution of surface currents.

For the linearly polarized AUT, the *EX* and *EY* field components are remarkably different along the principal axis. For the circularly polarized AUT, there is a $\pi/2$ phase shift between the *EX* and *EY* field components, the *EX* and *EY* amplitudes being of comparable magnitude.

The diagnostic capabilities of the test system developed in the course of our research were verified with a variety of antenna arrays (Hossa, Kabacik 2000; Kabacik 2003a). With some arrays, we face the crucial problem of where the holographic image should be focused, because the actual top surface of the elements is not clearly defined. This lack of clarity is often due to the presence of the radome and to the use of stacked patches which feature a non-negligible thickness.

Figures 8.1 through 8.15 show the holographic images obtained with the near-field data scanned at our laboratory and computed with the software developed in the course of our research. The holographic image of the amplitude distribution for the 64-element planar array (RMB-64) is presented in Figure 8.1. The image discloses significant differences between the *EX* and *EY* field components, which is an indication that the RMB-64 generates linear or strongly elliptical polarization (phase inspection may solve this ambiguity). The phase image for the *EX* field components (consistent with the polarization plane of the array) is illustrated in Figure 8.2. All the images are focused on the top plane of the antenna elements.

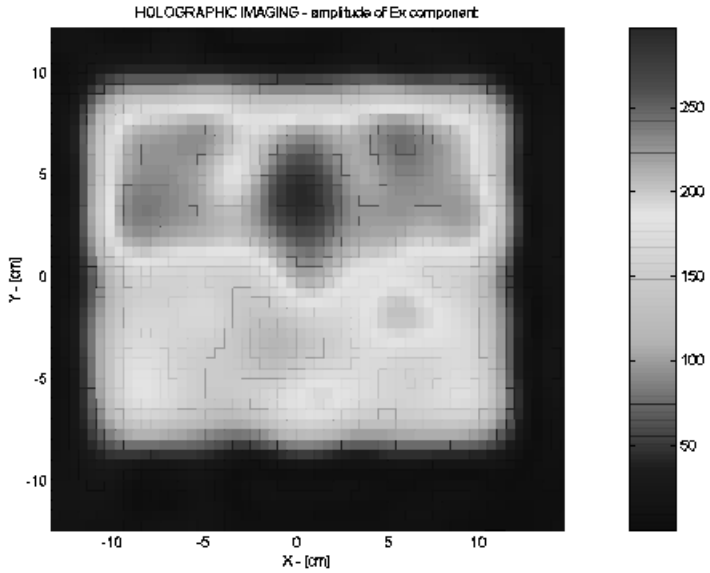

EX field components

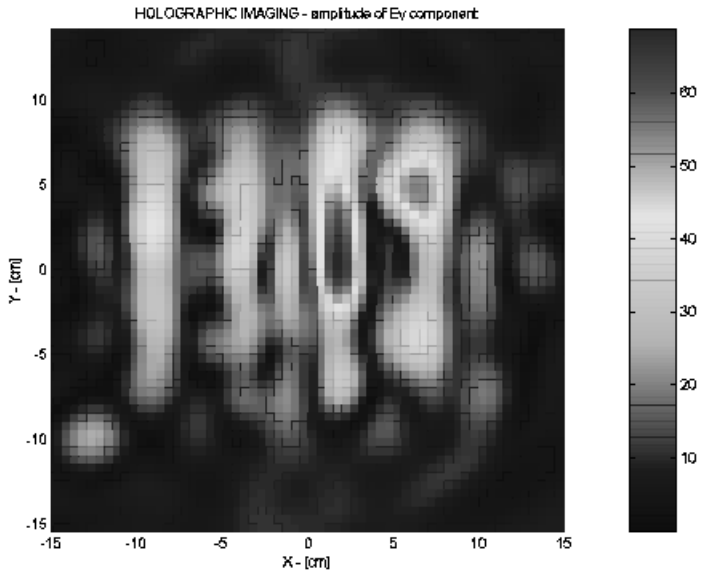

EY field components

Fig. 8.1. Amplitude holographic image focused on the surface of the printed circuits of the RMB-64 microstrip array (f = 9030 MHz) (Kabacik 2003a).

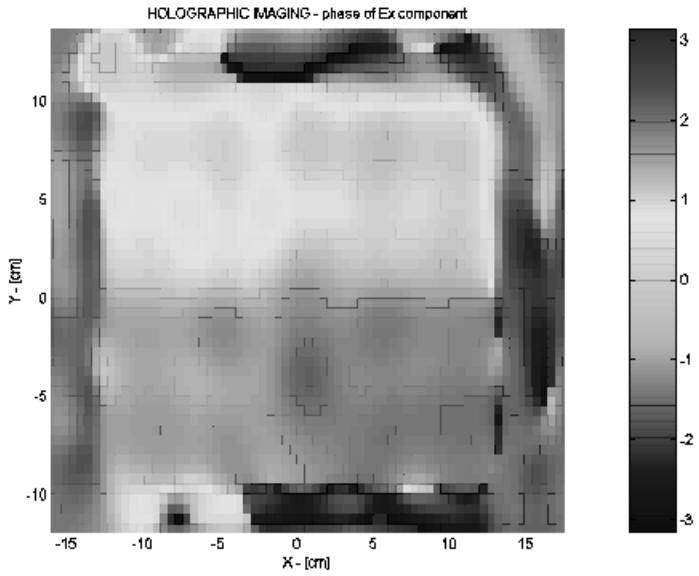

EX field components

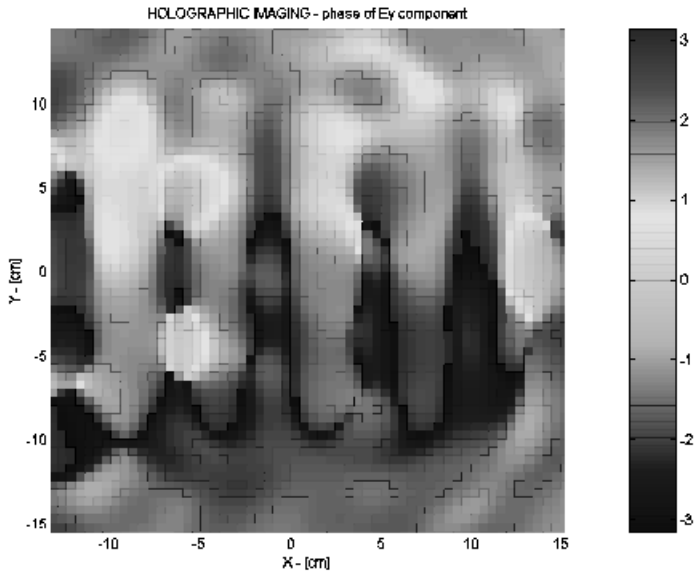

EY field components

Fig. 8.2. Phase holographic image for the RMB-64 array (f = 9030 MHz) which is focused on the surface of the printed circuits (Kabacik 2003a).

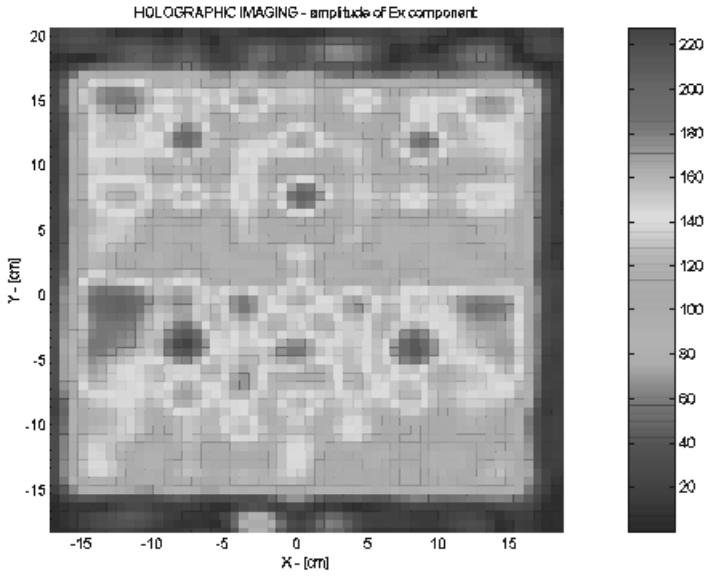

EX field components

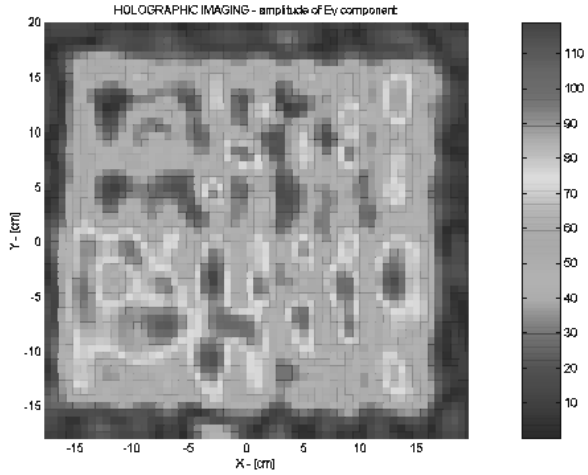

EY field components

Fig. 8.3. Holographic images (*EX* and *EY* amplitude at 11,250 MHz) disclosing a periodic geometry of the TPA-256 antenna. The resolution (~5 mm) allows the distinction of only basic array clusters comprising 2×2 elements (31×28 mm area). The spacing between the scanning and the antenna apertures was 27.8 λ_0. Both pictures prove that the TPA-256 consisted of the upper and lower half which actually were fed with some unbalance.

The holographic images of the magnitude distribution (*EX* and *EY*) disclosing a periodical geometry of the TPA-256 array are included in Figure 8.3. The TPA-256 array consisted of 256 patch elements which were fairly uniformly fed by the corporate feeding network, printed together with the rectangular antenna elements on the same side of the substrate. The array was linearly polarized, had a 11250 MHz center frequency and a subwavelength element spacing ($dx = dy = 20.36$ mm $= 0.76\lambda_0$).

The size of the pixels of which the presented image is composed approached 5mm. For comparison, the dimensions of the antenna elements were approximately 9×12 mm. As it can be inferred from the images in Figure 8.3, the achieved resolution made it possible to distinguish data at the level of the 2×2 element clusters. However, the quality of the pictures was insufficient to allow analysis at the element level. Unfortunately, a spacing shorter than the wavelength imposes physical constraints and, consequently, impairs the resolution of the holographic image. The achieved resolution revealed some major features of the array geometry, as well as disclosed the actual nonuniformity of excitation distribution between the elements. The image allowed us to distinguish clearly the outline of the entire antenna aperture (the edges were sharply depicted). The TPA-256 dimensions read from the holographic image were 340×330 mm, whereas in the antenna model the elements were arranged within a 320×320 mm area ($12\lambda_0$).

The comparison of the signal levels between the *EX* and *EY* field components suggests that the TPA-256 was actually linearly polarized. Furthermore, the image reveals that the array comprised two semi-arrays and that they were asymmetrically fed by the power divider next to the connector in the corporate feeding network. A rectangular mesh of the array is discernibly visible in the phase holographic images included in Figure 8.4. The evaluated phase distribution deviates somehow from the perfectly uniform arrangement. Interesting observations can be made on the basis of defocused images. The picture obtained for an intentionally defocused image with an offset equal to +40 mm ($1.5\lambda_0$ above the array) shows that the deformation of the amplitude undergoes less abrupt changes than does the deformation of the phase due to defocusing (Figure 8.5).

8.2. Detection of blockages in the antenna aperture

For the purposes of demonstration, in some of our experiments, selected antenna elements were intentionally covered with a shaped metal foil (blockage). In order to avoid shorts in the microwave circuit, the conductive blockage was isolated with a dielectric film (with respect to the antenna circuit). Figure 8.6 presents the reconstructed phase of the *EX* field components on the aperture of the TPA-256 array covered with a small rectangular piece of aluminum foil (the side length approaching $3\lambda_0$). The image made it easy to locate the square aluminum blockage and to evaluate its dimensions (the size read from the reconstructed image was ~70×80 mm, the actual dimensions being 65×72 mm).

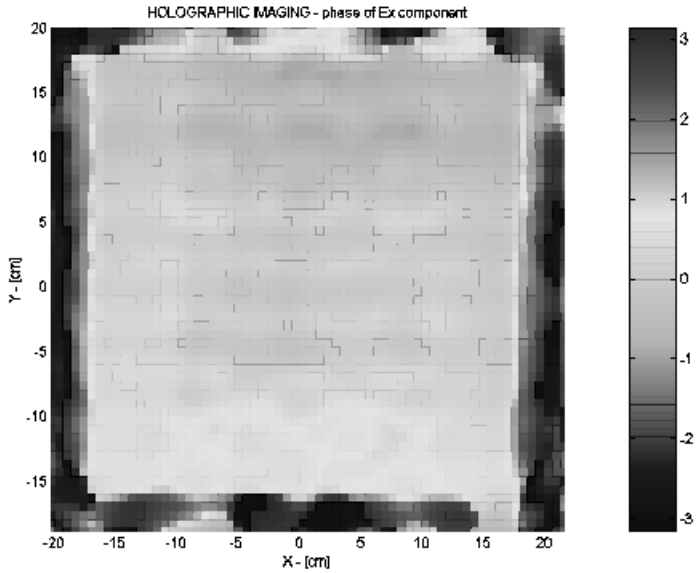

EX field components

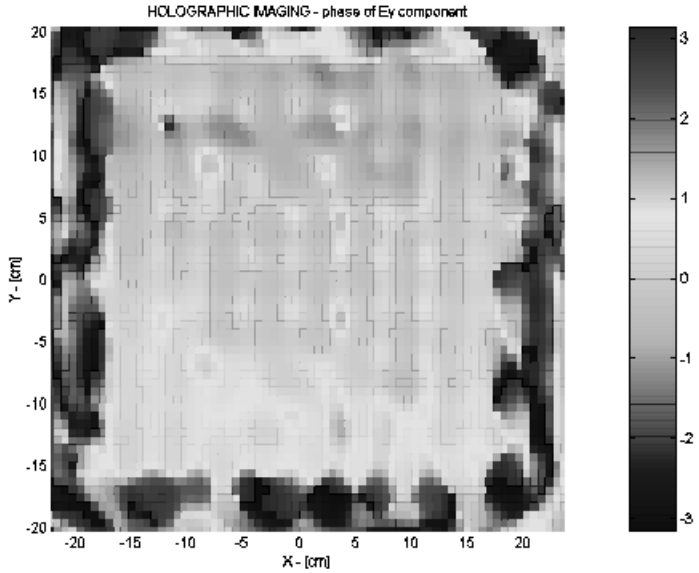

EY field components

Fig. 8.4. Holographic images (at 11.250 MHz) of the TPA-256 antenna. The pixel size (~5 mm) allows the distinction of only basic array clusters comprising 2×2 elements (31×28 mm area). A periodic geometry is mostly visible at the EY components. The spacing between the scanning and the antenna apertures was 27.8 λ_0.

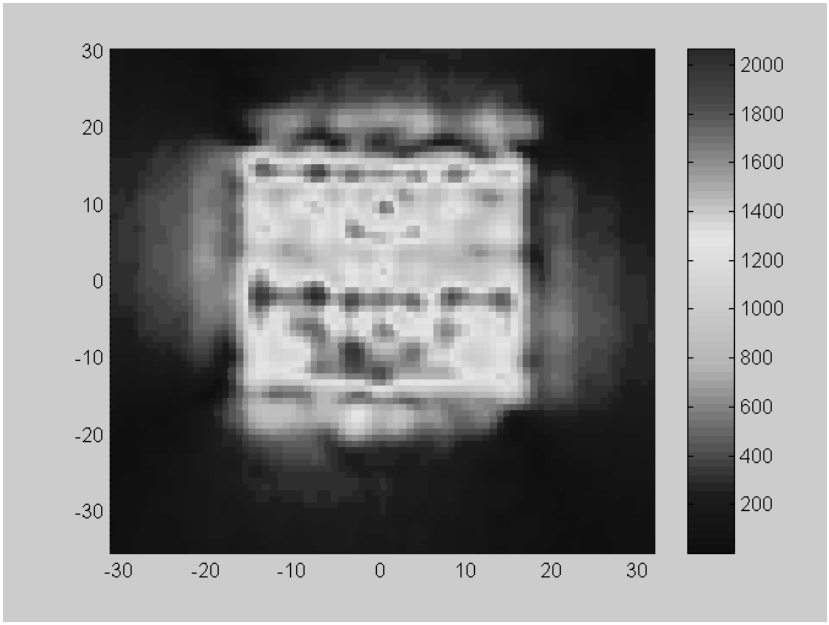

amplitude

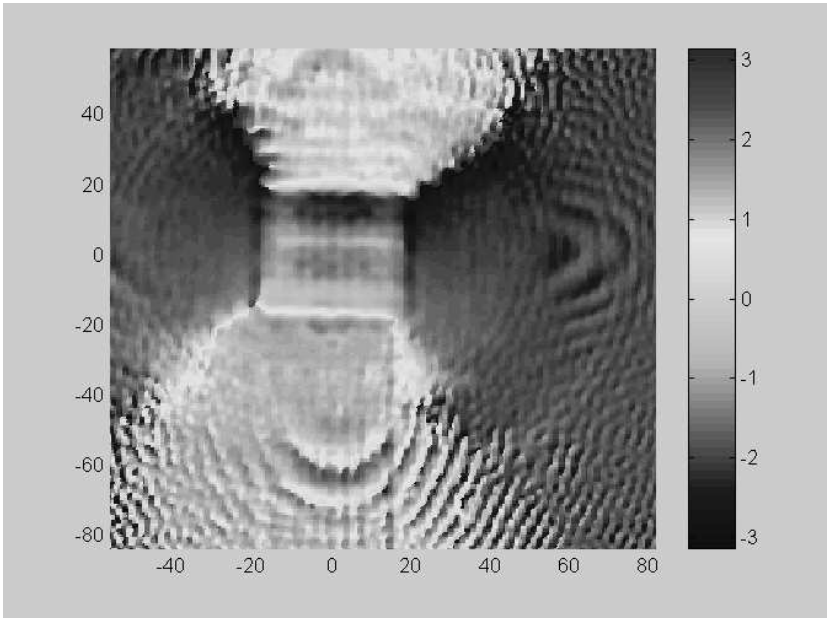

phase

Fig. 8.5. Defocused holographic image obtained for the TPA-256 array (f =11,250 MHz). The offset of the projection plane was set to +40 mm ($1.5\lambda_0$) above the antenna.

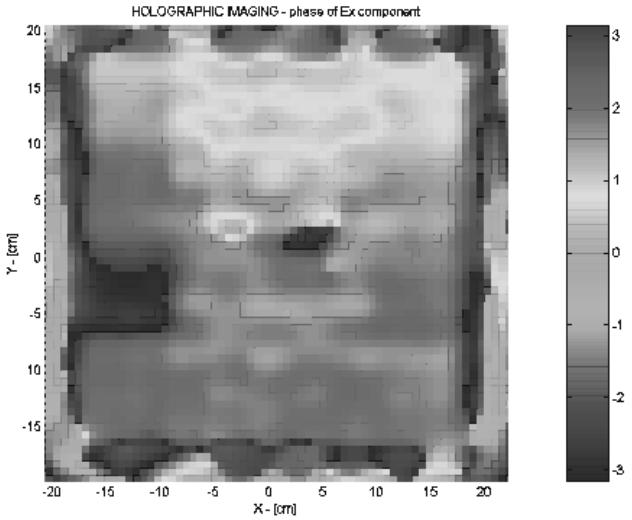

Fig. 8.6. Holographic image (5 mm pixel size) obtained with our near-field facility. The picture shows the actual *EX* phase distribution on the aperture of the TPA-256 microstrip fixed-beam array. A small part of the array aperture close to the left-hand edge was covered with a 65×72 mm (~3 λ_0) rectangular aluminum foil (galvanically isolated from the printed circuit). The spacing between the probe and the TPA-256 apertures was 27.8λ_0. The array patches were arranged in a 16×16 grid with a 0.76λ_0 (20.36 mm) element spacing. Data processing included probe correction (Kabacik 2003a).

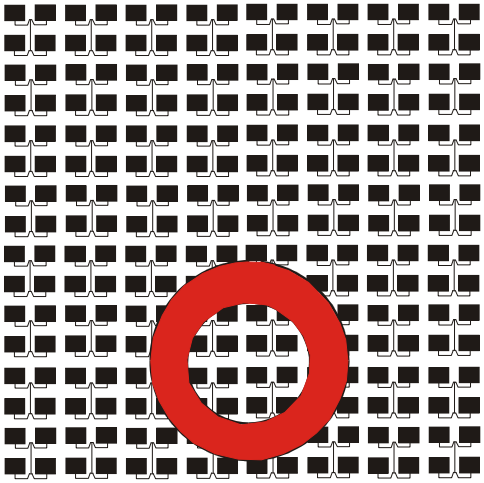

Fig. 8.7. Generic view of the TPA-256 microstrip array aperture and the ring-shaped blockage made of aluminum foil. The outline of the TPA-256 was 320×320 mm (12×12λ_0) and the outer and inner diameter of the ring was 4.5λ_0 and 2.5λ_0, respectively (at 11,250 MHz).

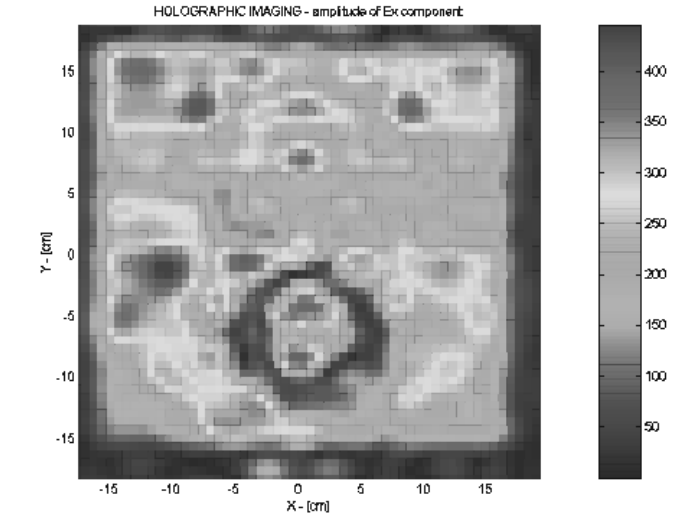

amplitude (*EX*)

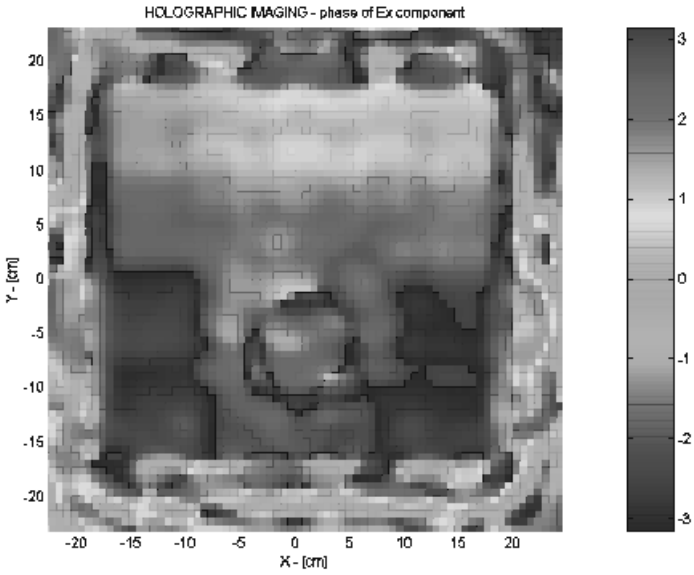

phase (*EX*)

Fig. 8.8. Holographic image of amplitude (a) and phase (b) for *EX* field components obtained with our facility for the TPA-256 antenna partly covered with an aluminum foil ring placed in the lower half of the array (Fig. 8.7). The aluminum-made ring was galvanically isolated from the antenna circuit with a 0.5 mm dielectric film. The outer ring diameter derived from the amplitude holographic picture (pixel ~5 mm) amounts to 12 cm and is consistent with the actual value (120 mm). The spacing between the probe and TPA-256 apertures was 27.8 λ_0 and test frequency was f = 11.250 GHz (Kabacik 2003a).

For the verification of the system, the ring-type blockage (depicted in Figure 8.7) was more demanding than the square-type one. The holographic images obtained for this case are shown in Figure 8.8 for the amplitude and phase of the *EX* field components. The value of the outer ring diameter determined in this way is consistent with the actual one (120 mm). In the presented experiments with blockages, the slot arrays (Litton technical information) provide more comfortable circumstances than do microstrip arrays. This is so because the slot arrays are less vulnerable to the extra load produced by the blockage in the antenna aperture. Waveguide-type power combining networks are robust to the blockages covering the slots.

8.3. Diagnostics of phased arrays

Our interest in phased arrays concentrates not so much on the amplitude distribution as on the phase distribution between the antenna elements, because the phase distribution has a much stronger influence on the shape of the radiation pattern than does the amplitude distribution (Kabacik 1998a). A typical spread of actual phase distribution values due to manufacture tolerances encountered in contemporary microwave beamforming circuits leads to a much greater deterioration of the design pattern shape than do the inaccuracies of the amplitude distribution values. In conventional microwave technologies, phase tolerance is not worse than ±6°, and amplitude tolerance is kept within ±0.7 dB in the majority of cases. Further tolerance improvements require the implementation of post-production circuit tuning or internal compensation of the inaccuracies in the beamforming network. When digital beamforming is involved, phase resolution takes smaller values than those for the conventional circuits; the near-field method allows a fine phase alignment after the integration of phased arrays (Bem, Kabacik 2000), which is a prerequisite to compensate the misalignment due to manufacturing tolerances.

With the developed laboratory system we obtained holographic images for several beam positions of the MC-8 phased array (Kabacik, Hossa 2001b; Kabacik, Hossa 2003c). The MC-8 array with eight elements arranged linearly (Figures 8.9 and 8.10) operates in the narrow band centered at 5000 MHz and generates linearly polarized signals (Kabacik 1995b). In order to reduce the sidelobe floor, the amplitude was tapered with a 25 dB cosine square distribution. Beam control was achieved with a passive circuit involving 4-bit phase shifters (22.5° step).

All the holographic images confirmed the non-uniformity of the power split between the elements of the MC-8. Figure 8.11 shows the amplitude image obtained for the co-polar field components (*EX*) of the broadside beam. The spacing between the scanning plane and the MC-8 aperture was set to $8.7\lambda_0$ (520 mm). The picture presents the actual asymmetry of element feeding with respect to the array center.

The white frames in the Figure denote the rectangular outlines of a laminate piece and of the element area. The frame dimensions read from all the holographic images examined are in good agreement with the actual values (280×60 and 237×18 mm for the laminate piece and for the elements, respectively, as depicted in Figure 8.9).

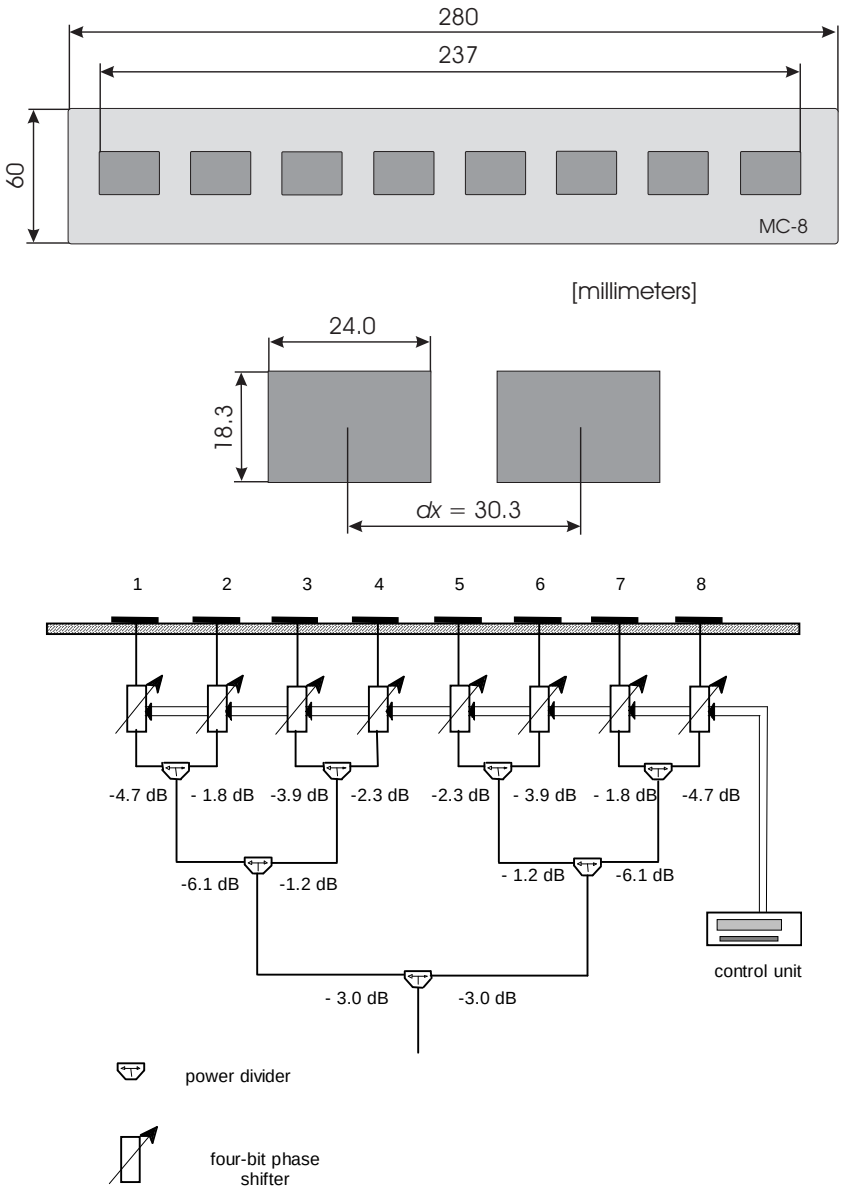

Fig. 8.9. Aperture and element layout, as well as a generic diagram of the beamforming network for the MC-8 phased array.

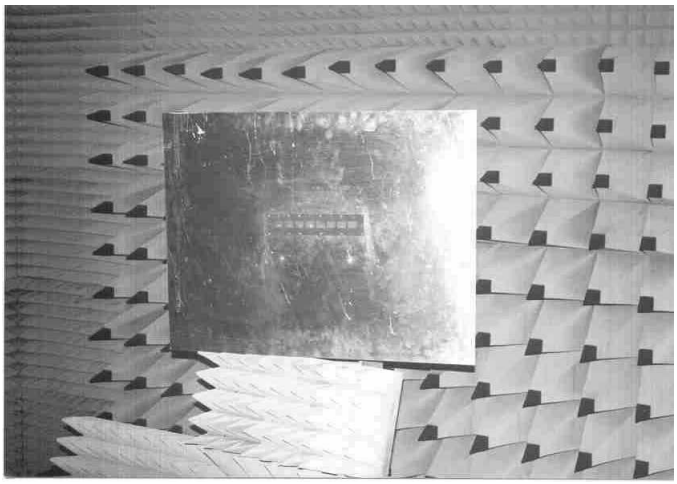

Fig. 8.10. Microstrip elements and extended 800×600 mm ground plate of the MC-8 phased array.

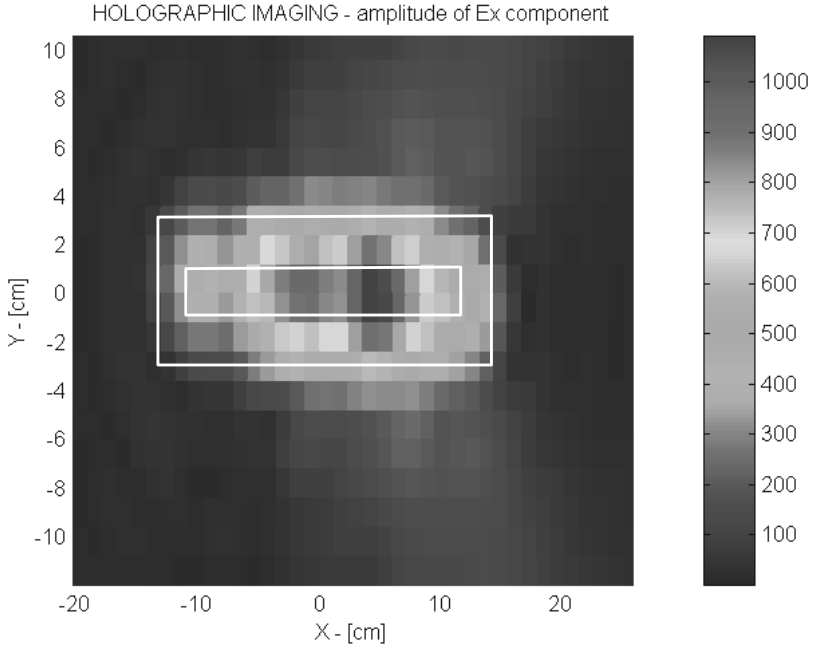

Fig. 8.11. Holographic image of amplitude (pixel size ~10 mm) for *EX* field components showing a non-uniform and a slightly asymmetrical amplitude distribution in the tested MC-8 linear array. The image was obtained for the broadside beam and reconstructed exactly at the element plane of the array (f=5000 MHz). The spacing between the scanning and the element planes was set to $8.7\lambda_0$ (520 mm). The image sharply outlines the edges of the antenna element substrate (28×6 cm) (Kabacik 2003a).

In order to verify the results obtained with the holographic diagnostic method, the scattering parameters at the beamforming ports were measured with a network analyzer. The amplitudes of the excitation coefficients measured with the network analyzer and those obtained by the holographic method are compared in Table 8.1 (normalized to element 4). It can be expected that when the microwave circuits are terminated with high-quality broadband loads (instead of antenna elements with varying input impedance), the design values will be better preserved. The data listed in Table 8.1 are in a good agreement, except those for element 5.

Table 8.1. Amplitude taper/distribution between the eight elements of the MC-8 phased array obtained with two measuring methods (broadside beam).

Origin of data	**Antenna elements**							
	1	2	3	4	5	6	7	8
Design value	0.186	0.363	0.692	1.0	1.0	0.692	0.363	0.186
Network analyzer method	0.17	0.34	0.70	1.0	0.88	0.66	0.32	0.17
Holographic method	0.18	0.39	0.67	1.0	0.64	0.67	0.32	0.13

It is interesting to note that the discrepancy between the designed and measured values for element 5 was detected regardless of the testing method used. Since the elementary power splitters of which the feeding network is composed were manufactured with a great care, this disagreement must be attributed to the differences in the loss values between the branches of the feeding network or to the impedance mismatch. Phase shifters are often responsible for excessive variations of insertion losses since their insertion loss depends on their settings. The measured total loss values ranged from 3.0 dB to 3.8 dB, which suggests that the undesired variation effect has been produced predominantly by the phase shifters. It may be concluded that the amplitude variations in any branch of the MC-8 array ranged up to $\pm$ 0.6 dB.

As near-field systems usually acquire data for two orthogonal probe polarizations, the holographic method can provide useful information on the polarization performance of the antenna arrays. Figure 8.12 shows a holographic image of the amplitude reconstructed for the *EY* field components. As it can be inferred from Figures 8.11 and 8.12, fields along the *x* and *y* axes differ by an order of magnitude. For determination the current values it is necessary to known H_x and H_y (it is possible to get H_x and H_y with some additional calibration as probe is of electric type because electrical field components are much easier to measure). This indicates that the AUT was linearly polarized. Another interesting feature is the deep field decay at the center line of the linear array observed for the *EY* field components. This shows that

the undesired currents responsible for the generation of the cross-polar radiation pattern are well compensated. But there is a stronger current flow along the diagonal semi-lines, which is likely to produce an asymmetrical cross-polar radiation pattern. It is interesting to note that the *EY* currents flowing on a certain part of the ground plane surface are of the same order of magnitude as those flowing within the element area.

The phase distribution in the array can be derived with the holographic images reconstructed on the basis of the near field data. The holographic image in Figure 8.13 (taken for the broadside beam and *EX* field components) shows that the phase values for all elements are almost equal. The maximum phase difference approaches 35°. The reconstructed data are consistent with those for the broadside beam when all array elements are fed in-phase. Like the image involving visualization of the *EX* components, this one also displays sharply outlined edges of the laminate piece and the outer border of the element area. The same holds for the ground plane.

An illustration of the phase distribution obtained for the beam tilted by 21° off the main axis is in Figure 8.14. To achieve this tilt angle, the phase progress between the elements was set to 67.5°, so the total theoretical phase shift between opposite edge elements was 472.5°. The overall phase difference between the edge elements read from the holographic results approaches 470° and is in an impressive agreement with the design value. The values for the beam scanned to 37.5° off the main axis were 787.5° and 720° for the calculated and the holographically measured total phase shift, respectively. Color pictures seem to be insufficiently accurate to enable an interpretation of the results obtained. That is why the numerical readout has become strongly recommended, besides image visualization. The phase distribution for a beam scanned only by 7° off the broadside axis is shown in Figure 8.15. The total phase shift within the array theoretically equaled 157.5°, but the reconstructed value was only slightly above 100°. This case discloses some problems which arise when small progressive changes are investigated.

The size of the smallest segment (pixel) in the holographic images of the phased array was set to ~10 mm. This value exceeded slightly that of the element size and was about one-third that of the element spacing. Since the element spacing was almost half-wavelength, the resolution at the element level was potentially achievable. However, it must be admitted that if the data are read from holographic images, problems will arise with the achievement of an unquestionable assignment of the element spot within the inspected picture area. The resolution achievable with near--field scanning for a subwavelength element spacing is discussed in detail elsewhere (Patton, Yorinks 1999). In order to overcome the problem of high resolution, the combined use of the data acquired for various scans was postulated.

Measurements of antennas with a beam tilted off the principal geometrical axis make greater demands on the allowable level of the reflected signals propagating inside the anechoic chamber. Since the AUT must revolve around its axis during

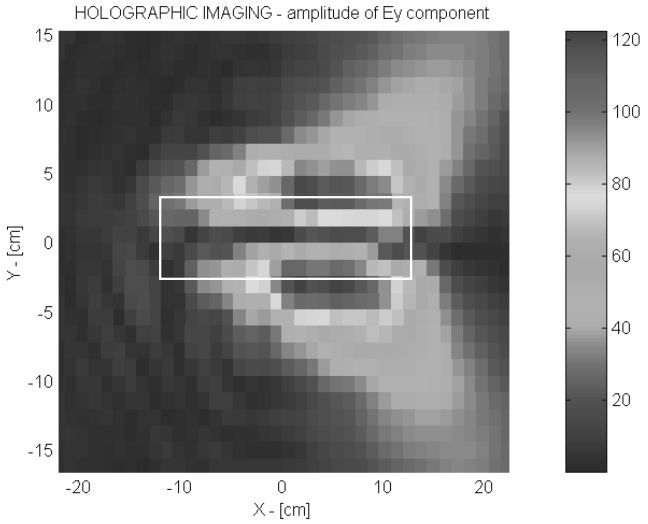

Fig. 8.12. Holographic image of amplitude for *EY* field components presenting the compensation of the cross-polar field components along the horizontal axis of the linearly polarized antenna. The field intensity on the ground plane is comparable to that on the aperture in the border zone. The image was obtained for the broadside beam at 5000 MHz. The spacing between the scanning and the MC-8 apertures was set to $8.7\lambda_0$ (520 mm) (Kabacik 2003a).

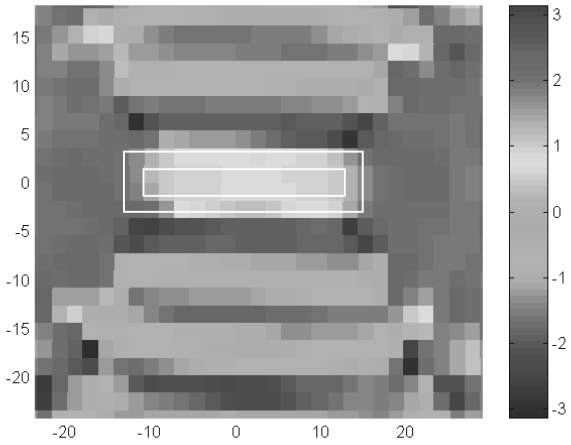

Fig. 8.13. Holographic image of phase for *EX* field components revealing an almost uniform phase distribution between the eight elements of the tested phased array. The image was obtained for the broadside beam and reconstructed exactly on the element plane of the MC-8 phased array. The spacing between the scanning and the antenna apertures was set to $8.7\lambda_0$ (520 mm).

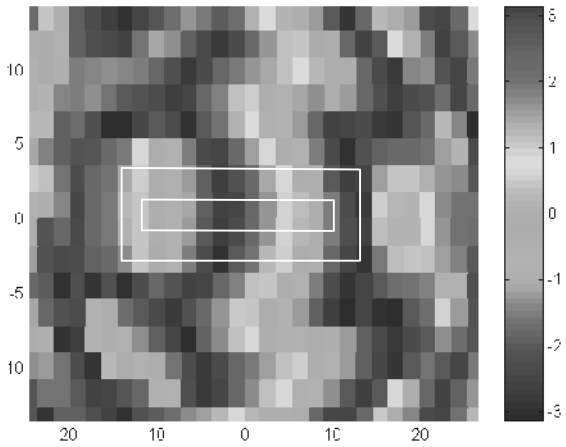

Fig. 8.14. Holographic image of the phase for *EX* field components revealing a progressive phase distribution between the elements of the tested MC-8 phased array. The total phase shift approaches 470° and is in good agreement with the design value of 472.5° (67.5° phase step). The image was obtained for the beam tilted 21° off the main axis and reconstructed on the top plane of the elements. The spacing between the probe and the MC-8 apertures was set to $8.7\lambda_0$ at 5000 MHz (520 mm). The currents flowing on the ground plane also follow a periodical pattern (Kabacik 2003a).

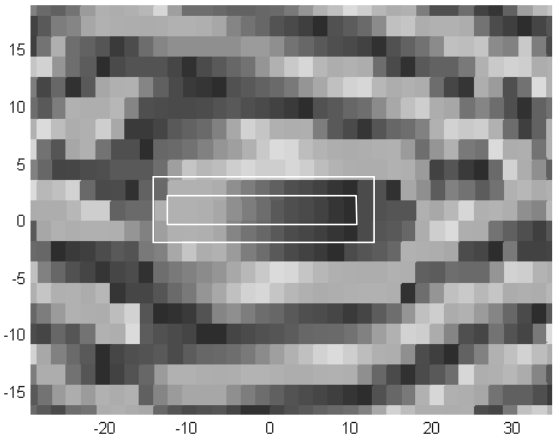

Fig. 8.15. Holographic image of the phase for *EX* field components revealing a progressive phase distribution between the elements of the investigated antenna array. The derived total phase shift approaches 110° and is considerably lower than the design value of 157.5° (22.5° phase step). The image was obtained for the beam tilted 7° off the broadside axis and reconstructed at the element plane of the MC-8 phased array. This spacing between the scanning and the MC-8 apertures was set to $8.7\lambda_0$ at 5000 MHz (520 mm).

scanning, the main beam is not pointed at one spot all the time. That is why the main beam and the sidelobes illuminate differently the ceiling and the walls of the anechoic chamber, thus changing the distribution of scattered radiation. As the AUT revolves during measurements, its polarization plane advances. The seatback is that the reflectivity of the absorber wall varies depending on the polarization plane squint. Consequently, the propagation of the reflected signals undergoes significant variations when the attenuation of the reflected waves is moderate or poor. In such instances, the undesired signals tend to influence the values of the recorded near-field samples, particularly in the zones featuring weak direct signals. Such superposition induces considerable variations in the measured signal with respect to the actual signal produced by the AUT. Consequently, the recorded values of the probe excitation coefficients are non-negligibly corrupted, and the far-field results are characterized by a low accuracy in the sidelobes. The problem is more serious with cross-polar than with co-polar field components (stronger signal).

CHAPTER 9

UPGRADE OF DIAGNOSTIC CAPABILITIES

9.1. Concurrent dual-method scanning

The accuracy of the results obtained with near-field systems, as well as the compactness of the measuring range, can not be overestimated, and researchers are convinced to use near-field measurements wherever possible and affordable. Despite a variety of advantages, near-field measurements suffer from some major constraints. Of these, the most troublesome (especially when hampering the test procedure) are:

- an insufficient valid angle for planar scannings,
- a lack of desired flexibility in the scanning aperture positioning,
- the gain measurements of large antennas.

Needing to maintain the deformation of large antennas within a tolerable range, a fixed direction of the gravity force might become a must when testing preliminary antenna models – usually equipped with insufficiently developed supporting structures.

A promising way to broaden the insufficient valid angle is the concurrent use of two methods at the measuring sites. Such approach has long been waiting for the chance to attract the attention of antenna engineers and scientists. When two concurrently used planar and cylindrical scanning systems provide complementary near field data, the capabilities of the facility will be remarkably improved by both broadening the valid angle and enabling measurements of a greater variety of antennas. The application of more than one scanning system at one location counterbalances the high costs that are to be borne for the construction of another anechoic chamber.

A broad valid angle, potentially achievable with hybrid techniques, is strongly desired when phased arrays are measured, as their beams are usually pointed within 45° off the broadside direction; those of conformal arrays can be pointed much wider. Just to recall, the bi-polar system alone is capable of providing a valid angle of up to 50° – too small to measure the patterns of all beams in typical phased arrays. We tried to solve the narrow valid angle problem by developing an appropriate hybrid scanning system (details are described pictorially in Figure 9.1). The system combines the planar bi-polar and the cylindrical scanning methods, so the view angle reaches the full

hemisphere. Cylindrical scanning can be performed by vertical linear scans with steps in azimuth or by scans in azimuth with vertical linear steps (the first approach seems better suited for a scanner concurrently involving bi-polar kinematic system). Other probe trajectories were studied by Italian researchers (Bucci et al. 2000c; Bucci et al. 2000a; Bucci et al. 1998a).

Taken alone, each of the scanning techniques considered can be regarded as already matured. The less privileged scanning will be a cylindrical one, which will handle data recorded over the sidelobes (even over the far ones). We expect that the achievement of satisfactorily consistent results in the overlapping zone will also be challenging. The overlapping zone most frequently falls within the spatial sectors of weak antenna radiation (generally there are far sidelobes or zones of low radiation). Thus, the accuracy of the measuring system is obviously lower. Furthermore, the results provided by the near-field methods are typically characterized by deteriorated accuracy at the edges of the scanning area.

The preferred interpolation/FFT method for the calculations of the far field data provide results on a square area. The inconsistency of the square and cylinder perimeters might result in incomplete radiation pattern outside two principal cut-planes. But when the perimeter of the cylinder is inside the square area or the cylindrical scanning terminates sufficiently high above the bi-polar scanning plane, the far field data are complete on the entire hemisphere.

The proposed system offers another unique asset when conformal antennas are to be diagnosed. In the conformal arrays, cylindrical antennas deserve particular attention. Unfortunately, the data reconstructed onto planar surfaces by microwave holog-

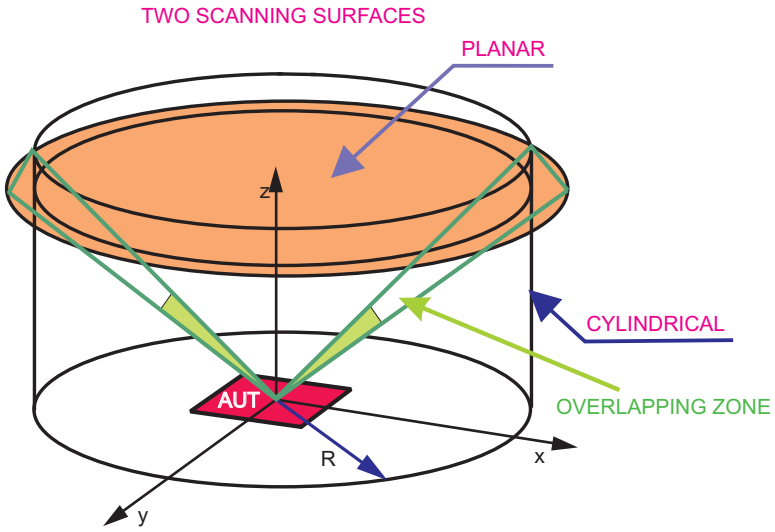

Fig. 9.1. The concurrent use of the planar and cylindrical scanning systems which may provide results over a very wide valid angle.

raphy do not fit the cylindrical surface of the antenna aperture. There is the potential for using the so-called "slices" approach when several holographic images are computed for a set of stacked planes (such approach combining data valid on narrow strips is not much reliable). The use of cylindrical scanning is a straightforward approach which helps to overcome this drawback, by enabling a backward projection focused exactly onto the surface of the cylinder.

9.2. Mobility of the scanner – on-site antenna evaluation

Until the 1990s, one of the primary constraints on the widespread use of the near-field technique was insufficient computational power of the mainframe computers. It is of course understood that mainframe computers were unsuitable for mobile applications and the same held for data communication. As a result, the attention towards mobile or outdoor deployable test systems generally dropped from the main stream of interest. Thus, the structure of the scanners presently in use makes them almost immobile. These days, however, accurate far-field patterns and holographic images obtained with on-site recorded data are of highest desire in both outdoor (operational site) and indoor (manufacturing site) environments. For these reasons, the mobility of the near-field system has become a key issue in recent years. Among the possible uses, the on-site diagnostics of sophisticated arrays mounted on vehicle platforms has come to the forefront. In this context, it is no surprise that of such portable scanning systems the most desired are those providing a large scanning area. It is a frequent situation that the large antenna aperture is in the vertical plane. Thus the main geometrical axis must remain in the horizontal plane. Furthermore, in some instances the large size of the AUT may impede any change in its position. For these reasons, a vertical scanning aperture with – an optional small tilt angle – appears to have really much to recommend it.

For such applications, a new scanner design and a new scanning method were developed in the course of our study. It was proposed that the new method be termed *uni-polar* (Kabacik 1999b). The term *uni-polar* method has been used here to parallel the widely known *bi-polar* and *polar* methods, though we are aware of the substantial differences among them, in spite of several common features. The major advantages of the uni-polar scanning method are the potentially large dimensions of the scanning apertures and the high mobility of the scanner. The proposed method is particularly convenient when applied to outdoor facilities. Furthermore, the deployment of the scanner in a remote AUT site can be performed quickly, without any laboratory infrastructure. *Uni-polar* scanners allow measurements on large planar apertures, irrespective of their orientation, but the vertical one is preferred.

A generic view of the measuring system is shown in Figure 9.2. The test range comprises a scanner, an RF system and scanner-carrying rails. The scanner consists of

a probe-carrying arm, a telescopic column and a railway carriage. The telescopic scanner column allows the adjustment of the angle of view and the scanning aperture dimensions to the actual needs. The AUT is mounted on a fixed pedestal and can rotate around its main geometrical axis. Owing to such geometry, the truncation area of the scanning aperture can be large enough to accomplish measurements of large AUTs and provide a wide valid angle.

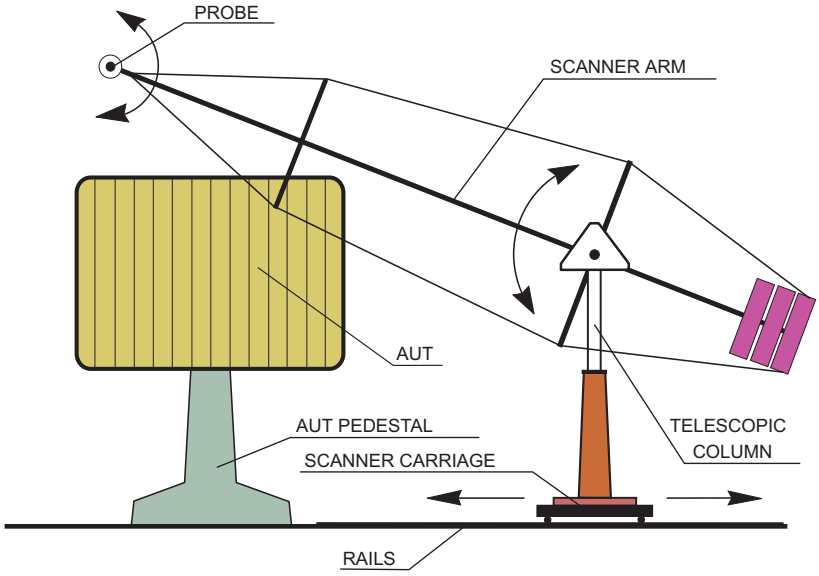

Fig. 9.2. *Uni-polar* scanning system suitable for on-site deployment (Kabacik 1999b).

The pattern of the sampling grid is in Figure 9.3. During *uni-polar* scanning, the probe travels in a uniform motion in the vertical plane, along the arc described by the end of the scanner arm. The RF system measures the probe excitation coefficients. When data acquisition on the arc is completed, the scanner rolls slightly to the next spot, and measurements are performed on a successive arc. In order to maintain a smooth translatory movement of the scanner carriage and to keep tight positioning tolerances, it is necessary to make the carriage roll on leveled rails. The AUT remains fixed during the entire measuring process. Alternatively, the AUT can be revolved around the horizontal axis, while the scanner carriage remains at the same spot during the entire measuring process (the samples are on the bi-polar grid). The scanning procedure is terminated once the samples have been acquired on all of the grid arcs. To provide a proper orientation of the polarization axes of the probe, it is necessary to revolve the probe around its electrical axis, counterwise to the arm, as it was with the bi-polar system. Owing to such a scanning arrangement, the troublesome impairment caused by cable bending can be substantially mitigated. When the on-site measuring

technique is involved, it might be of great utility if the data processing is capable to handle greater errors of sample locations. Studies on the measurements permitting such circumstances are carried on in some laboratories (Wittman et al. 1998).

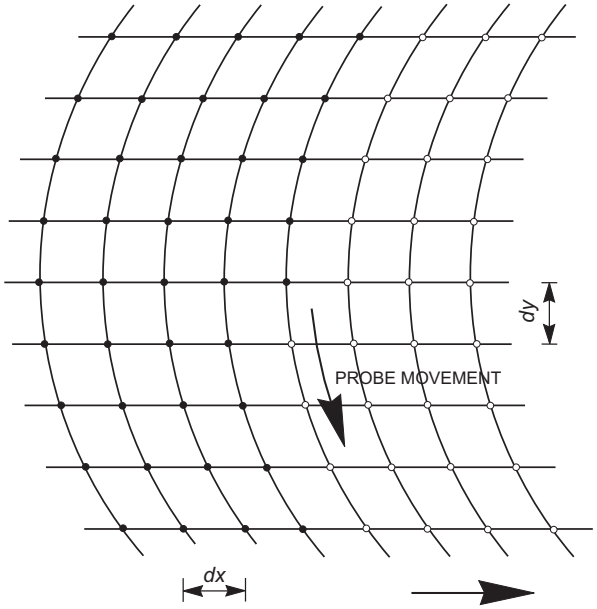

Fig. 9.3. Sampling grid typical of the *uni-polar* scanning technique.

The far-field transform can be calculated with well established algorithms, *i.e.* those used in bi-polar scanning. Of these, the far-field transform calculation which combines interpolation and Fast Fourier Transform (FFT) seems quite convenient (the milestones for this approach are outlined in Chapter 6). The *uni-polar* method does not feature a redundancy of the sampling points, as their density is uniform over the entire scanning aperture.

A major impairment of the scanner structure is the threat of oscillation at the end of the probe-carrying arm. The construction of lightweight, stiff and low-profile scanner arms has become feasible with the advent of composite materials. However, some engineering effort is still needed to stabilize the long, thin arm. The duration of the AUT measurements depends predominantly on the traveling speed of the probe (determined by the angular speed of the arm). Since the samples are taken while the probe moves, the synchronization of the sample taking moments is of paramount importance.

9.3. Tests of small multiband terminal antennas

Research on the interaction between terminals and operators includes two major issues, which are directly related to (i) the actual properties of terminal antennas in the presence of the operator and (ii) the absorption of the radiated energy by human tissue. The proximity of the operator, as well as the direct touch of the hand, leads to non-negligible changes in the electrical performance of the antenna (Byndas et al. 2001). Of these parameter changes, those of the input impedance and spatial distribution of radiation are of greatest concern. When the absorption of the RF energy approaches 50% of the transmitted power, this means that the available communication capabilities become reduced by half (potential data bandwidth or data rate).

For the needs of our research on terminal antennas we developed a human phantom with homogeneous filling, a gelly substance, which consisted of water, gelatin, dissolved salt and sugar (both 5 weight %) (Kabacik 2001c). The use of cold processed gel made the preparation of the phantom easy (but it must be noted that the overall phantom weight made its handling troublesome). From the viewpoint of the potential resonant phenomenon, the most important were the following dimensions: arm length (35 cm), forearm length (30 cm), head height (33 cm) and head diagonals (from 24 cm to 32 cm). The walls of the plastic shell were 1 cm thick. The listed values oscillated around a wavelength in the GSM900 system (in the air λ_0 = 32.6 cm at f_0 = 920 MHz).

In the course of our research, near-field systems were used to measure the density of the field radiated by mobile phones, both in isolation and in the operator's presence. Many experiments of ours were carried out with the system developed at the University of Queensland, Brisbane, Australia. The 200×200 cm scanning aperture was oriented vertically and the spacing between the scanning plane and the terminal antenna approached 1 meter. Whip or PIFA-type antennas were mounted on the metal mock-up of the cellular phone case. From the images obtained it can be inferred that the waves propagated by the PIFA-type antenna are much better focused than those radiated by the whip antenna. It is possible to modify the direction of major radiation generated by PIFA-type antennas (Kabacik, Kucharski 1999). However, such beam control adversely influences antenna efficiency.

Another testing system is being analyzed with the bi-polar scanner. The bi-polar near-field system is well suited for testing small antennas used in mobile terminals and in small satellite terminals (possible zenithal radiation, broad view angle). A generic concept of the measuring set-up considered in our laboratory is depicted in Figure 9.4. By adding a dielectric wheel on the scanner turntable it is possible to revolve the test object at the elevation over the azimuth format (full spherical coverage, the polarization plane can be adjusted with the dual-polarized or revolving probe).

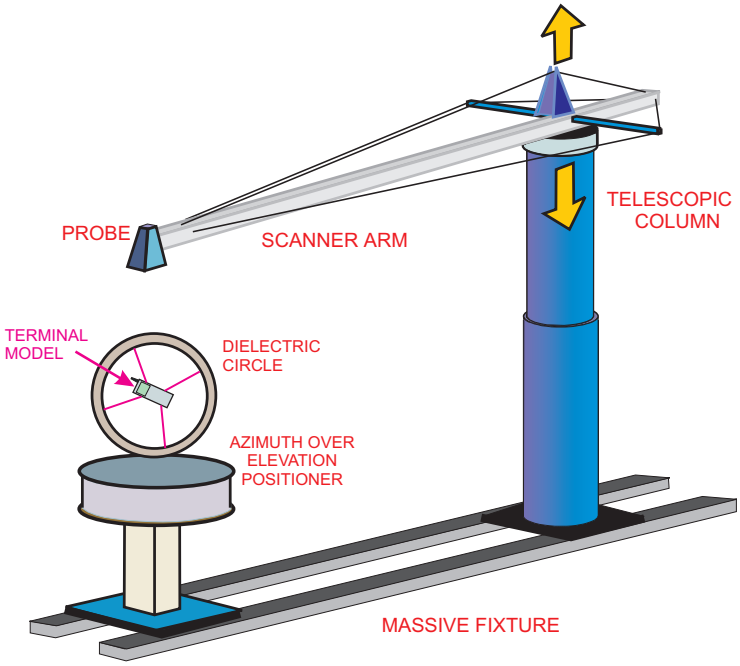

Fig. 9.4. Generic view of the measuring system based on the bi-polar scanner for testing antennas of mobile and wireless terminals, including small satellite terminals.

The method involves battery powered VCO generator integrated with the terminal antenna model. It is of paramount importance to ensure that the natural decrease of the battery voltage as a function of time does not affect the results. The procedure proposed by the author calls for choosing one or a couple of reference points (different spatial co-ordinates, possibly spread). In the course of scanning, samples are acquired at discrete points. In order to correlate the variations of a test signal level with time, measurements must be interrupted a few times in order to repeatedly record signals at the chosen reference points (always reference points are recorded at the beginning and at the end of the measuring procedure). Such procedure does not call for significant elongation of a measuring time. Computation of correction factors is straightforward and as far as amplitude is considered such method can provide acceptable accuracy.

A different approach relies on an optoelectronic converter with a sensor mounted in a proximity of the terminal antenna. Flexible fibers used to transmit optical signals should not much influence electromagnetic environment.

9.4. Fine alignment of antenna arrays

Antenna arrays which involve sophisticated beamforming methods impose tough tolerances on the excitation of their elements. Actual phase and amplitudes distributions must closely meet the design values, which fall much below the manufacturing tolerances (available when the production costs are kept at a reasonable level). Such order of tolerances can not be provided immediately after putting all components of the antenna together. The manufacturing inaccuracies can be reduced with the alignment technique. The problem is becoming even more complex presently, as the polarimetric technique requires antennas featuring dual-polarized or polarization reconfigurable performance. As a result, alignment analysis must be carried out for orthogonal field components. The near-field method offers a good insight into the amplitude and phase distribution in the antenna, and the antenna itself is well isolated from the interfering signals. As a rule, alignment is performed only once, namely at the manufacturer's. Another frequent use where the principles of this method can be applied is mutual coupling cancellation in arrays involving digital beamforming (Steyskal, Herd 1990).

9.5. Time domain measurements in the near field

Time and space domain measurements differ primarily in the form of the test signal and application of time gating. Space domain measurements are performed at one frequency at a time. In the time domain, measurements are carried out with short pulses (like in the emerging ultra wide band modulation techniques). There are two unique advantages that raise interest in time domain measurements: the reduction of the interfering signals, which corrupt the measured results, and the instant availability of results at arbitrary frequencies over a wide portion of spectrum. The reduction of the interfering signals is due to the time gating of the received signal. Furthermore, research on time domain measurements is driven by the investigations into broadband antennas as they emerged in modern radar and ultra-wideband communication systems (the bandwidth of the modulated signal is at least 10%).

In order to combat interfering signals and avoid troubles related to short pulses and time gating at a receiver input, two methods are investigated currently:

(i) use of phase-shift-keyed spread-spectrum test signals (Zeger et al. 1996),

(ii) application of equalizer (Leather, Parsons 2003).

Equalization is a technique which strongly combat effects of multipath propagation in radio channel. Both listed techniques can lead to reduced requirements on reflections at the measuring sites, both indoor and outdoor.

CHAPTER 10

SUMMARIZING COMMENTS

Presently we are witnessing great efforts which aim at soaring the role of the antenna and relevant signal processing in the concepts of radio systems in order to achieve the desired range of enhanced performances. It is the result of extensive search for new potentials of signal transmitting and processing in electrical engineering. In this context, modern antennas are expected to co-establish high-quality radio channels in both communication and radar systems by focusing electromagnetic radiation involving sophisticated modulation towards a receiving site or a target. A receiving antenna should ensure productive spatial filtering of the incoming radio waves. These challenging tasks placed the antenna technique in the critical spot of the development of new radio systems. Thus, the 'lagging behind' of the antenna designs exposes the launch of new systems to jeopardy.

Advanced antennas often take the form of planar or conformal arrays, or incorporate subarrays in their reflector illuminating systems. Highly integrated lightweight arrays and low-loss array feeding circuits raise principal interests. However, these techniques call for reliable testing procedures, tailored so as to respond to the constraints inherent in integrated or densely packed antenna structures. It is frequently witnessed that the lack of adequate evaluation techniques enforces the termination of the research on advanced and innovative concepts, even though the preliminary results were encouraging. As these measuring techniques are the prerequisite to accomplish any challenging R&D in the field of modern antenna arrays, the access to such techniques has been restricted. That is why references to their in-depth coverage are elusive. Needless to say that every institution aspiring to develop modern antennas must have proprietary testing methods developed with great own efforts.

In the course of my research on highly integrated lightweight antenna arrays, the reliable evaluation and determination of their properties have come to the forefront among other principal issues. I realized that the measuring and diagnostic methods deserved a lot of attention, as the available techniques did not include all the aspects which in my opinion were of crucial importance in terms of highly integrated microstrip arrays. In such antennas, the dielectrics and composites have a strong effect on the electrical properties, so an accurate evaluation of the actual material parameters

over a wide temperature range prior to the design of the antenna elements and microwave circuits becomes indispensable.

When highly integrated arrays undergo tests, the experimenters have no access to the partitioned beamforming and no instant access to the feeding ports of the antenna elements, as they have when handling less integrated conventional arrays. Thus, if we want to evaluate the component performance and to achieve the desired antenna design (as well as validate the model performance with the design parameters), we have to replace the conventional approach (which basically involves analysis of fragmentary data obtained at the functional BFN levels) with such a method that extracts the necessary information from the tests of completely integrated and operating antenna arrays (it is advisable to support these analyses with advanced simulations). It must be emphasized that such determinations rely on the experimental evaluation of the electromagnetic phenomenon, particular consideration being given to the current distribution (both amplitude and phase) within the antenna elements for all the beams and beam positions. Such a current distribution can be derived with advanced signal processing, preferably with sampled radiation in the near field of the antenna.

The monograph addresses the technical problems described above, and the major contribution of the author's personal research was within the following problems:

- investigations into highly integrated lightweight antenna arrays,
- studies of low-loss feeding circuits,
- investigations into the electrical properties of the microwave substrates over a wide temperature range,
- numerical simulations of stratified antenna performance over a wide temperature range,
- near-field measurements of antenna arrays, including derivation of microwave holography data,
- derivation of the current distributions at the phased array aperture,
- invention of near-field scanning systems for on-site antenna tests.

The most valuable author's contributions are included in Chapters 2–4 and 6–8. The scientific value and current importance of results presented is well documented with four comprehensive papers published by the author in the *IEEE Transactions on Antennas and Propagation* and *IEEE Antennas and Propagation Magazine* in last four years. The other results were presented at two dozen major international conferences on antennas. Analysis of great technical value is described in Chapter 4. This research work, featuring a lot of originality, found high evaluation of antenna experts and was commended with *2000 Harold A. Wheeler Applications Prize Paper Award Honorable Mention* of the IEEE Antennas and Propagation Society (the *H.A. Wheeler Award* recognizes the paper considered to be the best applications paper in the *IEEE Transactions on Antennas and Propagation* for the given year). Investigations into performance of phased arrays with holographic images are extremely rarely presented in literature. There are several reasons and among most important is complexity of such

a technique. Thus, the results presented in Chapter 8 should be regarded as important and new contribution to phased array measurements by the author.

The presented research on reliable evaluation and property determination of modern-day advanced antennas has been led by the author for years and has been performed within a small group of closely cooperating researchers. The investigations on the bi-polar technique has been carried on since 1992 and the author was a Principal Investigator to relevant research projects over this period. The bi-polar near-field system was developed in-house according to the author concepts and technical projects. The author established a framework for implementing Optimal Sampling Theorem, what turned out a milestone in accurate processing of measured data. Furthermore, he gave an idea for implementing a method of holographic imaging. Details of these concepts were comprehensively elaborated with Dr. Robert Hossa who implemented these algorithms into software. The results are published in four papers co-authored by them (Kabacik et al. 2000a; Hossa, Kabacik 2000; Kabacik, Hossa 2001b; Kabacik, Hossa 2003c).

The common research turned out to be advantageous for both researchers. On a basis of gained experiences, we undertook a work on a substantially improved measuring system in 2000. The scanner has been upgraded by a capability of performing cylindrical scannings. Nowadays it is controlled by a real-time computer. Presently we carried on pioneering investigations on concurrent use of the planar and cylindrical scanning systems, improvement of data processing by extrapolating values of some samples. Furthermore, phaseless near-field measurements are investigated by Dr. Hossa. The results of these studies will be published in another monograph written by Dr. Hossa. The preparation of materials for this work is in advanced stage presently.

In the last seven years, the author's interests have concentrated on his three original evaluating and testing methods:

(i) numerical simulation of antenna performance over a wide temperature range,
(ii) indirect determination of actual radiation patterns by scanning the field radiated by the antenna in its near zone,
(iii) reconstruction of the complex field distribution in the actual aperture of the array by backward projection of far field data derived with the near-field technique.

Other considerable efforts were spent on two hot issues in contemporary antenna research:

(i) interactions between terminal antennas and humans,
(ii) inner calibration of antenna arrays involving digital beamforming.

The techniques mentioned utilize sampled near field data and provide core information needed for the development of arrays, which make use of the most recent approaches to beamforming. The capabilities of the major presented methods are beyond those available with the conventional measuring techniques. The proposed methods not only feature high accuracy when determining antenna parameters, but

also may enable antenna researchers or manufacturers to quickly figure out the most likely reasons why the array performance deviates from the design parameters. Such evaluation technique is priceless in the course of research on integrated antenna arrays.

The investigations into the antenna performance over a wide temperature range are essential to bring the lightweight antenna technology up to many applications. With the presented simulation methodology based on the measured electrical properties of the materials and related numerical modeling it is possible to design highly integrated antenna arrays or low-loss feeding circuits. Considerable efforts spent on the measurements of the materials and their careful evaluation pay off the antenna design which can consist of a dozen substrates and be highly integrated. Such antennas are able to ensure a satisfactory overall performance even when exposed to the heat radiated by the active modules. A drawback is the difficulty with the experimental validation of the simulated results as the environmental test procedures are generally troublesome, when the testing conditions are far from normal.

The determination of the actual field distribution within the apertures of the reflector or array antennas is of vital importance to the research on advanced technologies. Our studies have shown that the proposed diagnostic method yields results consistent with those theoretically predicted. The method turned out to be capable of determining the actual performance of the element feeding in fixed or reconfigurable arrays. Holographic projection, essentially based on near-field measurements, should be regarded as a diagnostic tool which ensures the desired weak interaction between the measuring setup and the AUT. The use of the bi-polar scanning method has the inherent advantage of holding the AUT within the horizontal plane. Thus, the dominant radiation of the antenna is pointed upwards, while the gravity force acts in a constant direction.

There are two more major challenges – the accuracy of phase determination and the resolution of the reconstructed images. A high resolution is particularly desired when the array is composed of small elements which are closely packed, as it is expected to occur in the adaptive arrays of future base station antennas. Problems with providing fine resolution emerge when the element spacing is of a subwavelength, which is encountered in the majority of real arrays. Important factors corrupting the fine resolution of holography imaging are the adverse effects due to the presence of the scanner, as well as variations of the off-broadside beam pointing in the course of AUT revolving. The absorber wall reflectivity depends on the polarization as well. Scanner-related are the waves scattered on the scanner elements and a fixed orientation of the electrical axes of the probe. The advent of multiple-beam, reconfigurable or adaptive arrays requires many tests for the given AUT. A long measuring time with the single carrier systems is more troublesome than the tremendous amount of the data produced for analysis. The emerging conformal techniques will soon require the extension of the proposed diagnostic method firstly onto cylindrical antennas and later onto other non-planar arrays.

The author is investigating the application of the invented testing methods to some current research projects. One of them aims at developing a communication subsystem of the *SSETI-Express* and *ESEO* minisatellites under the *SSETI* Project (supported by the European Space Agency) (Kabacik et al. 2003b). In order to avoid the deployment of spaceborne antennas, we sorted out a highly integrated lightweight antenna array made of bonded stratified composites for on-board use. The same approach was selected for a bunch of telecommand and telemetry antennas, each made in the form of a single circularly polarized patch. The first minisatellite is scheduled for launch in April 2005.

REFERENCES

Aiello G.R. and Rogerson G.D., 2003, 'Ultra-Wideband Wireless Systems', *IEEE Microwave Magazine*, Vol. 4, No. 2, pp. 36–47.

Agilent Technologies, *Test and Measurement Catalog 2000*, Signal Sources, pp. 188–218, http://www.agilent-tech.com

AMTA – Antenna Measurement Techniques Associations, http://www.amta.org

Ando M., Sakurai K., Goto N., Arimura K., and Ito Y., 1985, 'A radial line slot antenna for 12 GHz satellite TV reception', *IEEE Trans. Antennas Propagat.*, Vol. 33, No. 12, pp. 1347–1353.

Ando M., Numata T., Takada J.-I., and Goto N., 1988, 'A linearly polarized radial line slot antenna', *IEEE Trans. Antennas Propagat.*, Vol. 36, No. 12, pp. 1675–1680.

Ansoft Co., http://www.ansoft.com

Appel-Hansen J., Johansen T., and Kristensen T., November 1998, 'Near-field reactive-field transformation and Huygens's Principle', *10th International Symp. on Antennas JINA '98*, Nice, pp. 193–196.

Astrium, Technical information on *Outdoor Cylindrical Near-Field Test Facilities (CNTF)*.

Babij T.M. and Bassen H., 1986, 'Broadband isotropic probe system for simultaneous measurement of complex E- and H-fields', US Patent Number 4,588,993.

Balanis C.A., 1997, *Antenna Theory – Analysis and Design*. John Wiley & Sons, New York.

Barrett R.M. and Barnes M.H., 1952, 'Automatic antenna wavefront plotter', *Electron.*, Vol. 25, pp. 120–125.

Belov Yu.I., Kalinin A.V., and Kalinina E.E., 1987, 'The use of Jacobi–Bessel series in processing of the field in near zone of antenna measured in points of quasi-radial lattice', *Radiophysics*, Vol. XXX, No. 10, pp. 1286–1288, (in Russian).

Bem D.J. and Kabacik P., June 1995, 'Microstrip phased array for mobile satellite terminals', *IEEE Antennas Propagat. Soc. Int. Symp.*, Newport Beach, California, pp. 1446–1449.

Bem D.J. and Kabacik P., May 2000, 'Smart antennas for mobile communications', *XIII International Conference on Microwaves, Radar and Wireless Communications MIKON*, Wrocław, Vol. 3, pp. 120–130.

Białkowski M.E. and Varis V.P., 1993, 'Electromagnetic model of a planar radial-waveguide divider/combiner incorporating probes', *IEEE Trans. Microwave Theory Tech.*, Vol. 41, No. 6, pp. 1126–1134.

Białkowski M.E. and Kabacik P., June 2001a, 'An equivalent circuit model of a radial line planar antenna with coupling probes', *IEEE Antennas Propagat. Soc. Int. Symp.*, San Antonio, Texas.

Białkowski M.E., Song H.J., and Kabacik P., 2001b, 'A broadband uniplanar quasi-Yagi antenna – parameter study in application to a spatial power combiner', *Journal of Telecommunications and Information Technology*, No. 4, pp. 41–47.

Białkowski M.E. and Kabacik P., 2003, 'An electromagnetic-field method modelling of a radial line planar antenna with coupling probes', *IEEE Trans. Antennas Propagat.*, Vol. 51, No. 5, pp. 1114–1120.

Booker H.G. and Clemmow P.C., 1950, 'The concept of an angular spectrum of plane waves, its relations to that of polar diagram and aperture distribution', *Proc. Inst. Elec. Eng. (IEE)*, Vol. 97, No. 1, pp. 11–17.

Bucci O.M. and Franceschetti G., 1987, 'On spatial bandwidth of scattered fields', *IEEE Trans. Antennas Propagat.*, Vol. 35, No. 12, pp. 1445–1455.

Bucci O.M., Gennarelli C., and Savarese C., 1991, 'Fast and accurate near-field–far-field transformation by sampling interpolation of plane-polar measurements', *IEEE Trans. Antennas Propagat.*, Vol. 39, No. 1, pp. 48–55.

Bucci O.M., Gennarelli C., Riccio G., and Savarese C., June 1994a, 'Fast and accurate far-field evaluation from a non redundant, finite number of plane-polar measurements', *IEEE Antennas Propagat. Soc. Int. Symp.*, Seattle, Washington, pp. 540–543.

Bucci O. M. and D'Elia G., June 1994b, 'Advanced interpolation techniques', *AMTA Workshop on Modern Imaging and Diagnostic Techniques for RCS and Antennas*, University of Washington, Seattle.

Bucci O.M., Gennarelli C., Riccio G., and Savarese C., 1998a,'NF-FF transformation with cylindrical scanning: an effective technique for elongated antennas', *IEE Proc. Microwave, Antennas Propagat.*, Vol. 145, No. 5, pp. 369–374.

Bucci O.M., D'Elia G., and Migliore M.D., 1998b, 'Advanced field interpolation from plane-polar samples: experimental verification', *IEEE Trans. Antennas Propagat.*, Vol. 46, No. 2., pp. 204–210.

Bucci O.M., D'Elia G., and Migliore M.D., 1999, 'An effective near-field far-field transformation technique from truncated and inaccurate amplitude-only data', *IEEE Trans. Antennas Propagat.*, Vol. 47, No. 9, pp. 1377–1385.

Bucci O.M., Gennarelli C., Riccio G., Sabino G., and Savarese C., April 2000a, 'Far-field reconstruction from probe compensated measurements on a cylindrical helix', *AP2000 Millenium Conference on Antennas & Propagation*, Special Invited Session, Davos.

Bucci O.M., Capozzoli A., and D'Elia G., 2000b, 'Diagnosis of array faults from far-field amplitude-only data', *IEEE Trans. Antennas Propagat.*, Vol. 48, No. 5, pp. 647–652.

Bucci O.M., Gennarelli C., and Riccio G., July 2000c, 'Field reconstruction over a cylinder from a non-redundant number of samples over a non-uniform circular helix', *IEEE Antennas Propagat. Soc. Int. Symp.*, Salt Lake City, Utah.

Byndas A., Kucharski K., and Kabacik P., July 2001, 'Experimental study of the interactions between terminal antennas and operators', *IEEE Antennas Propagat. Soc. Int. Symp.*, Boston, Massachusetts, pp. 74–77.

Carballo G.F. and Fieguth P.W., 2002, Hierarchical Network Flow Phase Unwrapping', *IEEE Trans. Geoscience and Remote Sensing*., Vol. 40, No. 8, pp. 1695–1708.

Conformal antennas, April 2001, 2nd European Workshop on Conformal Antennas, The Hague,

COST260 *Smart Antennas – CAD & Technology*, http://www.cost260.com.

COST284 *Innovative Antennas for Emerging Terrestrial & Space-based Applications*, http://www.cost284.com.

Desnos Y.-L., *et al.*, July 2000, 'The ENVISAT advanced synthetic aperture radar system', *IEEE International Geoscience and Remote Sensing Symp. – IGARSS*, Honolulu, Hawaii.

D'Agostino F., Ferrara F., Gennarelli C., and Riccio G., September 2003, 'Efficient outside data extrapolation in the plane-polar scanning', *International ITG-Conference on Antennas – INICA*, Berlin, pp. 89–92.

Departament of Electromagnetic Systems, Technical University of Denmark, http://www.emi.dtu.dk

Ferrara F., Gennarelli C., Ricccio G., and Savarese C., October 2001, 'A SVD based method for antenna far-field interpolation from nonuniformly distributed samples', *16th International Conference on Applied Electromagnetics and Communications*, Dubrovnik, pp. 250–253.

Fritzel T., Steiner H.-J., Hartmann J., and Habersack J., November 2002, 'Revolutionary new outdoor testing with a mobile airborne nearfield test facility (ANTF)', *24th Annual Meeting & Symposium, Antenna Measurement Techniques and Association AMTA*, Cleveland, Ohio, pp. 341–346.

Gatti M.S. and Rahmat-Samii Y., 1988, 'FFT applications to plane-polar near-field antenna measurements', *IEEE Trans. Antennas Propagat.*, Vol. 36, No. 6, pp. 781–791.

Hansen J. (ed.), 1988, *Spherical Near-field Antenna Measurements.* Peter Peregrinus, London.

Hansen T.B., 1997, 'Formulation of spherical near-field scanning for electromagnetic fields in the time domain', *IEEE Trans. Antennas Propagat.*, Vol. 45, No. 4, pp. 620–630.

Hirokawa J., Sakakibara K., Kimura Y., Ando M., and Goto N., May 1996, 'A two-beam slotted leaky waveguide array for mobile reception of dual polarization DBS', *IEEE Antennas Propagat. Soc. Int. Symp.*, Baltimore, Maryland, pp. 74–77.

Hossa R. and Kabacik P., July 2000, 'Holographic antenna diagnosis with a bi-polar near-field measuring system', *IEEE Antennas Propagat. Soc. Int. Symp.*, Salt Lake City, Utah.

Huang J., 2001, 'The development of inflatable array antennas', *IEEE Antennas Propagat. Magazine*, Vol. 43, No. 4, pp. 44.

IEEE Standard Test Procedures for Antennas, 1980, The Institute of Electrical and Electronics Engineers.

Iversen P.O., Garreau Ph., Englund K., Pasalic E., Edvardsson O., and Engblom G., April 2000, 'Real-time spherical near-field antenna test facility for personal communications applications', *AP2000 Millenium Conference on Antennas & Propagation*, Special Invited Session, Davos.

Janse van Rensburg D. and Hindman G., April 2000, 'Advancing near-field antenna measurements through error analysis and correction', *AP2000 Millenium Conference on Antennas & Propagation*, Special Invited Session, Davos.

Johnson R.C., Ecker H.A., and Hollis J.S., 1973, 'Determination of far-field patterns from near-field measurements', *Proc. IEEE*, Vol. 61, No. 12, pp. 1668–1694.

Joy E.B. and Paris D.T., 1972, 'Spatial sampling and filtering in near-field measurement', *IEEE Trans. Antennas Propagat.*, Vol. 20, No. 5, pp. 253–261.

Joy E.B., Leach Jr. W.M., Rodrique G.P., and Paris D.T., 1978, 'Applications of probe-compensated near-field measurements', *IEEE Trans. Antennas Propagat.*, Vol. 26, No. 5, pp. 379–389.

Junkin G., Huang T., and Bennett J.C., 2000, 'Holographic testing of terahertz antennas', *IEEE Trans. Antennas Propagat.*, Vol. 48, No. 3, pp. 409–417.

Kabacik P., 1992a, 'Measurement results for microstrip antenna arrays', Report of the Electromagnetics Institute, Technical University of Denmark, No. R-525, Lyngby.

Kabacik P., 1992b, 'Analiza koncepcji stanowiska do pomiarów anten w polu bliskim metodą dwuosiową', (Feasibility studies of a bi-polar near-field antenna measurement facility). Report I28/S-011/92, Institute of Telecommunications and Acoustics, Wrocław University of Technology, (in Polish).

Kabacik P., July 1995a, 'Active microstrip array for satellite communication applications', *SBMO/IEEE MTT-S International Microwave and Optoelectronics Conference*, Rio de Janeiro, pp. 626–631.

Kabacik P., 1995b, *Influence of Beam Forming Network Errors on the Performance of Microstrip Phased Arrays*. Ph. D. Dissertation, Wrocław University of Technology, Poland.

Kabacik P., April 1997a, 'Application of the planar bi-polar near-field method to antenna measurements and diagnostics', *10th International Conference on Antennas and Propagation, ICAP'97*, Edinburgh, pp. 1.95–100.

Kabacik P. and Maksimiuk D., April 1997b, 'Interpolating algorithm for far-field calculations in the bi-polar method', *10th International Conference on Antennas and Propagation, ICAP'97*, Edinburgh, pp. 1.101–104.

Kabacik P., September 1997c, 'Pomiary anten w polu bliskim metodą dwuosiową' (Antenna measurements with a bi-polar near-field method), *National Telecommunication Symposium*, Bydgoszcz, (in Polish).

Kabacik P., 1998a, 'Design constraints of low-sidelobe microstrip phased arrays', *Microwave and Optical Technology Letters*, John Wiley&Sons, pp. 107–111.

Kabacik P., Barylak M., and Maksimiuk D., June 1998b, 'Thinned-grid near-field bi-polar antenna measurements', *IEEE Antennas Propagat. Soc. Int. Symp.*, Atlanta, Georgia, pp. 1331–1334.

Kabacik P. and Białkowski M.E., June 1998c, 'Microstrip patch antenna design considerations for airborne and spaceborne applications', *IEEE Antennas Propagat. Soc. Int. Symp.*, Atlanta, Georgia, pp. 2120–2123.

Kabacik P. and Białkowski M.E., November 1998d, 'Microstrip base station antenna made of honeycomb composites', *IEEE-APS Conference on Antennas Propagat. for Wireless Communications*, Waltham, Massachusetts.

Kabacik P., Sawicki A., Sachse K., and Jaworski G., November 1998e, 'An advanced technology of integrating lightweight microstrip arrays', *10th International Symposium on Antennas JINA'98*, Nice, pp. 602–605.

Kabacik P. and Białkowski M.E., 1999a, 'The temperature dependence of substrate parameters and their effect on microstrip antenna performance', *IEEE Trans. Antennas Propagat.*, Vol. 47, No. 6, pp. 1042–1049.

Kabacik P., July 1999b, 'Uni-polar scanning method for near-field measurements of antennas', *IEEE Antennas Propagat. Soc. Int. Symp.*, Orlando, Florida, pp. 1806–1809.

Kabacik P. and Kucharski A., July 1999c, 'Planar handset antennas with electronically steerable parameters', *IEEE Antennas Propagat. Soc. Int. Symp.*, Orlando, Florida, pp. 2070–2073.

Kabacik P., Sachse K., Sawicki A., and Jaworski G., August 1999d, 'Highly Integrated Apertures of Base Station and Terminal Antennas', *SBMO/IEEE MTT-S International Microwave and Optoelectronics Conference*, Rio de Janeiro, pp. 233–237.

Kabacik P., Hossa R., and Grobelny M., April 2000a, 'Conventional and thinned-grid near-field measurements of antennas by the bi-polar method', *AP2000 Millenium Conference on Antennas & Propagation*, Special Invited Session, Davos.

Kabacik P., Sachse K., Sawicki A., and Jaworski G., April 2000b, 'Conformal antenna arrays manufactured in a highly integrated technology', *AP2000 Millenium Conference on Antennas & Propagation*, Davos.

Kabacik P., Sachse K., Sawicki A., Jaworski G., and Białkowski M., May 2000c, 'Airborne radar antenna modules using lightweight temperature-resistant materials', *IEEE International Conference on Phased Array Systems and Technology*, Dana Point, California, pp. 41–44.

Kabacik P., Sachse K., Sawicki A., and Jaworski G., July 2000d, 'Integrated multilayer arrays manufactured in lightweight technology', *PIERS 2000 – Progress in Electromagnetics Research Symp.*, Boston, Massachusetts, pp. 339.

Kabacik P., Hossa R., Grobelny M., and Świerczyński Z., 2000e, *Optymalizacja parametrów siatki pomiarowej w pomiarach anten w polu bliskim*, (Optimization of the grid in the bi-polar measurements). Report I-28/S-103/2000, Institute of Telecommunications and Acoustics, Wrocław University of Technology, (in Polish).

Kabacik P., Sachse K., Sawicki A., and Jaworski G., April 2001a, 'Conformal antenna panel for Inmarsat terminal', *2nd European Workshop on Conformal Antennas*, The Hague, The Netherlands.

Kabacik P. and Hossa R., July 2001b, 'Diagnostics of phased arrays with the near-field antenna measuring technique', *PIERS 2001 – Progress in Electromagnetics Research Symp.*, Osaka, p. 451.

Kabacik P., 2001c, 'Investigations into advanced concepts of terminal and base-station antennas', *IEEE Antennas Propagat. Magazine*, Vol. 43, No. 4, pp. 160–169.

Kabacik P. and Białkowski M.E., October 2001d, 'Cylindrical array antennas and their applications in wireless communication systems', *16th International Conference on Applied Electromagnetics and Communications IECom*, Dubrovnik, pp. 169–171.

Kabacik P., 2003a, 'The bi-polar near-field antenna measuring system at Wrocław University of Technology', *IEEE Antennas Propagat. Magazine*, Vol. 45, No. 5, pp. 74–83.

Kabacik P., Sachse K., and Hossa R., 2003b, 'Projekt SSETI i teleinformatyczne metody realizacji współczesnych minisatelitów (SSETI project and development of modern minisatellites with use of multimedia communication systems)', *Przegląd Telekomunikacyjny i Wiadomości Telekomunikacyjne*, No. 12/2003, pp. 562–568, (in Polish).

Kabacik P. and Hossa R., October 2003c, 'Alignment of the phased array beamforming with the bi-polar near-field measuring system', *25th Annual Meeting & Symposium, Antenna Measurement Techniques and Association AMTA*, Irvine, California.

Kerns D.M., 1963, 'Analytical techniques for the correction of near-field antenna measurements made with an arbitrary but known measuring antenna', *Abstracts URSI-IRE* Meeting, Washington, DC, pp. 6–7.

Kerns D.M., 1980, 'Plane-wave scattering-matrix theory of antennas and antenna-antenna-interactions', *National Bureau of Standards* Monograph 162.

Leach Jr. W.M. and Paris D.T., 1973, 'Probe compensated near-field measurements on a cylinder', *IEEE Trans. Antennas Propagat.*, Vol. 21, No. 7, pp. 435–432.

Leather P.S.H. and Parsons D., 2003, 'Equalization for antenna-pattern measurements: established technique – new application', *IEEE Antennas Propagat. Magazine*, Vol. 45, No. 2, pp. 154–161.

Li L-W., Kang X-K., and Leong M-S., 2001, *Spheroidal Wave Functions in Electromagnetics Theory*. John Wiley&Sons.

Litton Airton Co., *Microwave Components, Waveguide & RF Susbsytems*, Airton Series of X-Band Weather Radar Flat Plate Array Antennas.

Löffler D., Wiesbeck W., and Johannisson B., July 1999, 'Conformal aperture coupled microstrip phased array on a cylindrical surfaces', *IEEE Antennas Propagat. Soc. Int. Symp.*, Orlando, Florida, pp. 882–885.

Ludwig A.C., 1973, 'The definition of cross polarization', *IEEE Trans. Antennas Propagat.*, Vol. 21, No. 1, pp. 116–119.

Martin Polegre A.J., Roderer A.G., Crone G.A.E., and de Maagt P.J.I., April 2001, 'Applications of conformal array antennas in space missions', *2nd European Workshop on Conformal Antennas*, the Hague.

MI Technologies, http://www.mi-technologies.com

Newell A.C., 2002, Near-field antenna measurements, *AMTA – Antenna Measurement Techniques and Association, Educational Seminar*, Cleveland, Ohio.

National Institute of Standards and Technology, http://www.nist.gov

Orbit/FR – Microwave Test and Measurement Product Catalog 1998, Chapter D: *Microwave Receiver*, http://www.orbitfr.com

Papoulis A., 1977, *Signal Analysis*. McGraw Hill, Inc., New York.

Paris D.T., Leach Jr. W.M., and Joy E.B., 1978, 'Basic theory of probe-compensated near-field measurements', *IEEE Trans. Antennas Propagat.*, Vol. 26, No. 5, pp. 373–379.

Patton W.T. and Yorinks L.H., 1999, 'Near-field alignment of phased-array antennas', *IEEE Trans. Antennas Propagat.*, Vol. 47, No. 3, pp. 584–591.

Rahmat-Samii Y., Galindo-Israel V., and Mittra R., 1980, 'A plane-polar approach for far-field construction from near-field measurements', *IEEE Trans. Antennas Propagat.*, Vol. 28, No. 2, pp. 216–230.

Rahmat-Samii Y., 1985, 'Microwave holography of large reflector antennas – simulation algorithms', *IEEE Trans. Antennas Propagat.*, Vol. 33, No. 11, pp. 1194–1203.

Rahmat-Samii Y., Yaccarino R., and Williams L., November 1992, 'A novel indoor bi-polar antenna near-field measurement and diagnostic facility at UCLA', *7th International Symposium on Antennas JINA '92*, Nice, pp. 129–134.

Repjar A.G., Newell A.C., and Francis M.H., 1988, 'Accurate determination of planar near-field correction parameters for linearly polarized probes', *IEEE Trans. Antennas Propagat.*, Vol. 36, No. 6, pp. 855–868.

Rose Ch.A., 'Accuracy estimation of microwave holography from planar near-field measurements', www.mi-technologies.com/Product Literature/Technical Papers

Rudduck R.C., Wu D.C.F., and Intihar M.R., 1973, 'Near-field analysis by the plane-wave spectrum approach', *IEEE Trans. Antennas Propagat.*, Vol. 21, No. 3, pp. 231–234.

Sachse K. and Sawicki A., 1999, 'Quasi-ideal multilayer two- and three-strip directional couplers for monolithic and hybrid MIC', *IEEE Trans. Microwave Theory Techniques*, Special Issue on Multilayer Circuits, Vol. 47, No. 9, pp. 1873–1882.

Sarkar T.K. and Taaghol A., 1999, 'Near-field to near/far-field transformation for arbitrary near-field geometry utilizing an equivalent electric current and MoM', *IEEE Trans. Antennas Propagat.*, Vol. 47, No. 3, pp. 566–573.

Sarkar T.K. and Salzar-Palma M., October 2003, 'Widebandwidth baseband communication: fact of fiction?', *IEEE Topical Conference on Wireless Communication Technology*, Honolulu, Hawaii.

Sawicki A., Sachse K., Jaworski G., and Kabacik P., May 1998, 'Comparision of planar antenna feed networks with Wilkinson and coupled-line power dividers', *12th International Microwave Conference*, MIKON 98, Kraków, pp. 423–427.

Shafai L.L., Chamma W.A., Barakat M., Strickland P.C., and Seguin G., 2000, 'Dual-band dual-polarized perforated microstrip antennas for SAR applications', *IEEE Trans. Antennas Propagat.*, Vol. 48, No. 1, pp. 58–66.

Special Issue on near-field scanning techniques, *IEEE Trans. Antennas Propagat.*, Vol. 36, No. 6, 1988.

Steyskal H. and Herd J.S., 1990, 'Mutual coupling compensation in small array antennas', *IEEE Trans. Antennas Propagat.*, Vol. 38, No. 12, pp. 1971–1975.

Stratton J.A., 1941, *Electromagnetic Theory*. McGraw-Hill, New York, Section 5.

Stubenrauch C., 1996, *Planar near-field processing software*, National Institute of Standards and Technology, Boulder, Colorado.

Ticra Co., http://www.ticra.com. Near-field probes.

Trzaska H., 2001, *Electromagnetics Field Measurements in the Near-Field*. Noble Publishing.

University of Southern California, Ultra-wideband Laboratory, http://ultra.usc.edu/New_Site/

Williams L.I. and Rahmat-Samii Y., June 1991, 'Novel bi-polar planar near-field measurement scanner at UCLA', *IEEE Antennas Propagat. Soc. Int. Symp.*, London, Ontario, pp. 1446–1449.

Williams L.I., Yaccarino Z.G., and Rahmat-Samii Y., June 1994a, 'Polar, thinned-polar, linear sprial sampling using the UCLA bi-polar planar near-field measurement system: a comparatively study', *IEEE Antennas Propagat. Soc. Int. Symp.*, Seattle, Washington, pp. 548–551.

Williams L., Rahmat-Samii Y., and Yaccarino R.G., 1994b, 'The bi-polar planar near-field measurement technique, Part I: Implementation and measurement comparisions', *IEEE Trans. Antennas Propagat.*, Vol. AP-42, No. 2., pp. 184–195.

Willliams L.I., Rahmat-Samii Y., and Yaccariono R.G., November 1995, 'A comparision of polar, thinned-polar, linear spiral sampling using the UCLA bi-polar planar near-field measurement system', *17th Annual Meeting & Symposium, Antenna Measurement Techniques and Association AMTA*, Williamsburg, Virginia, pp. 358–363.

Wittman R.C., Alpert B.K., and Francis M.H., 1998, 'Near-field antenna measurements using nonideal measurement location', *IEEE Trans. Antennas Propagat.*, Vol. 46, No. 5, pp. 716–722.

Yaccarino R.G., Rahmat-Samii Y., and Williams L., 1994, 'The bi-polar planar near-field measurement technique, Part II: Near-field to far-field transformation and holographic imaging methods', *IEEE Trans. Antennas Propagat.*, Vol. 42, No. 2, pp. 196–204.

Yaccarino R.G. and Rahmat-Samii Y., 1999, 'Phaseless bi-polar near-field measurements and diagnostics of array antennas', *IEEE Trans. Antennas Propagat.*, Vol. 47, No. 3, pp. 574–583.

Yaghjian A.D., 1982, 'Efficient computations of antenna coupling and fields within the near-field region', *IEEE Trans. Antennas Propagat.*, Vol. 30, No. 1, pp. 113–128.

Yaghjian A.D., 1984a, 'Approximate formulas for the far-field and gain of open-ended rectangular waveguide', *IEEE Trans. Antennas Propagat.*, Vol. 32, No. 4, pp. 378–384.

Yaghjian A.D., 1984b, 'Equivalence of surface current and aperture field integrations for reflector antennas', *IEEE Trans. Antennas Propagat.*, Vol. 32, No. 12, pp. 1355–1358.

Yaghjian A.D., 1986, 'An overview of near-field antenna measurements', *IEEE Trans. Antennas Propagat.*, Vol. 34, No. 1, pp. 30–45.

Zeger A.E., Burton S., and Abrams B.S., 1996, 'Antimultipath system measurement of ultralow sidelobe level antenna patterns', *18th Annual Meeting & Symposium, Antenna Measurement Techniques and Association AMTA*, Seattle, Washington, pp. 44–49.